UNIVERSIDADE DE SANTIAGO DE COMPOSTELA

FACULTADE DE FÍSICA

Departamento de Física de Partículas

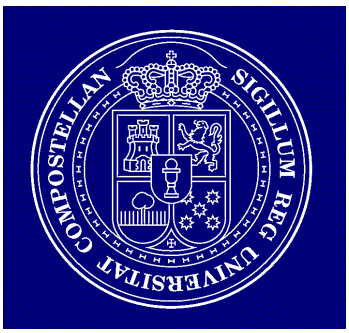

CERN-THESIS-2002-035
30/04/2002

The Detector Control System of the ATLAS experiment at CERN: An application to the calibration of the modules of the Tile Hadron Calorimeter.

Fernando Varela Rodriguez
Santiago de Compostela, Abril 2002

UNIVERSIDADE DE SANTIAGO DE COMPOSTELA

FACULTADE DE FÍSICA

Departamento de Física de Partículas

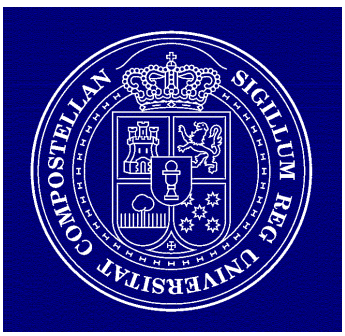

The Detector Control System of the ATLAS experiment at CERN: An application to the calibration of the modules of the Tile Hadron Calorimeter.

Memoria presentada para
optar al Grado de Doctor
en Ciencias Físicas por:

Fernando Varela Rodriguez

Abril 2002

Ignacio Durán Escribano, Profesor Titular de la **Universidad de Santiago de Compostela**,

CERTIFICO: que la memoría titulada **"The Detector Control System of the ATLAS experiment at CERN: An application to the calibration of the modules of the Tile Hadron Calorimeter"**, ha sido realizada, bajo mi dirección conjuntamente con la del **Dr. H. J. Burckhart**, por **Fernando Varela Rodríguez** en el **Departamento de Física de Partículas** de esta Universidad y consituye la Tesis que presenta para optar al grado de **Doctor en Ciencias Físicas**.

Santiago de Compostela, Marzo de 2002

Dr. H. J. Burckhart **Prof. Ignacio Durán Escribano** **Fernando Varela Rodríguez**

Acknowledgments

The PhD work here presented, was carried out in the framework of a collaboration USC-CERN, supported by the Doctoral Student Fellowship programme, under the joint supervision of H. J. Burckhart (CERN) and I. Durán Escribano (USC).

I would like to thank m*y* joint supervisors H. J. Burckhart and I. Durán Escribano for their support *a*nd guidance during *t*he past years. I thank Helfried for his clear and precise comments and explanations over the years, which have been very much appreciated. I also thank Nacho for his help and advise on the countless occasions when I have needed assistance.

I would also l*i*ke to acknowledge the ATLAS Tilecal co*m*munity for giving me the opportunity of joining to the team in the last p*a*rt of this thesis. I am in particular g*r*ateful to A. Gómes, G. Montarou, I. Hruska, R. Stanek and M. Vassent and, very in special, to A. M. Henriques Correia, P. Grenier, R. Leitner and G. Schlager.

I would like to *t*hank H. Boterenbrood, J. Cook, V. Filimonov, V. Khomoutnikov, B. I. Hallgren, R. Hart and Y. Ryabov for h*a*ving been a constant help with their support and fruitful discussions.

I would also like to thank to all the friends over the years who taught me to never give up.

Finalmente, me gus*t*aría expresar mi más sincero agradecimiento a mi familia por el constante apoyo y aliento *q*ue me han dado durante todos estos años.

.

A mis padres y
a mi hermano.

A la memoria de mis abuelos.

Contents

Resumen

El proyecto principal del CERN (Centro Europeo para la Física de Partículas) para la presente década es la construcción del LHC (Large Hadron Collider). El LHC es un colisionador *p-p* con una energía en el centro de masas de 14 TeV y una luminosidad de 10^{34} $cm^{-2}s^{-1}$, que operará con un intervalo entre cruces de haces de 25 ns (*bunch-crossing*). El LHC está siendo instalado en el actual tunel del acelerador LEP (Large Electron Positron collider) y comenzará su operación en la primavera del 2007.

Actualmente cuatro zonas experimentales están en fase de construcción. En una de ellas se intalará ATLAS (A Toroidal Lhc AparatuS). ATLAS es un detector de partículas multi-propósito diseñado para explorar completamente el potencial de descubrimiento del LHC. El detector está siendo optimizado simultáneamente para el amplio rango de procesos conocidos e hipotéticos en el LHC, incluyendo la búsqueda del bosón de Higgs en el marco del Modelo Standard, supersimetría, estudios de la hipotética estructura interna de quarks y leptones, asi como la física de quarks *b*.

ATLAS será el espectrómetro de particulas más grande construido hasta la fecha. El detector tendrá forma cilíndrica con una longitud total de 42 m y un radio de 11 m. En la parte interna se encuentra el sistema de reconstrucción de trazas (*tracking*), tambien llamado *inner detector*, que combina diferentes tecnologías para obtener alta resolución espacial y en momentos, así como un elevado número de puntos de *tracking*. La alta resolución viene dada por los detectores de silicio (*pixels* y *strips*) mientras que el *Transition Radiation Tracker* proporciona alta estadística para la rescontrucción de la trayectoria de las partículas. Un campo magnético de 1.5 T es creado por el solenoide central que comparte la misma cámara de vacio que el *inner detector*.

A continuación se encuentra el calorímetro electromagnético que se caracteriza por el empleo de Argon líquido como material activo. Al igual que en el sistema de tracking, en el calorímetro hadrónico también se emplean diferentes tecnologías dependiendo de los niveles de radiación a los que estarán expuestas. Así, en la parte central, se utilizará el llamado *Tilecal*, en el que se intercalan láminas de hierro que actúan como absorbente, con planos centelleadores que actúan como material activo. La tecnología de Argon líquido empleada en el calorímetro electromagnético se empleará también en los llamados *end-caps* del calorímetro hadrónico y en los calorímetros *forward*.

El espectrómetro de muones se caracteriza por disponer de un campo magnético creado por un imán toroidal. Esto permitirá la operación del sistema de muones de ATLAS de forma independiente del resto del detector, a la vez que proporciona una

alta resolución en la reconstrucción de la trayectoria de muones. Un eficiente trigger de muones será proporcionado por cámaras específicas con una respuesta rápida.

ATLAS será instalado en el punto de interacción 1 del LHC a una profundidad de 100 m, siendo inaccesible durante la operación debido al alto nivel de radiación y la presencia de campos magnéticos de hasta 1.5 T.

El sistema de control del detector (*Detector Control System*, *DCS*), debe garantizar la operación segura y coherente del detector, así como servir de interfaz homogénea a todos los subdetectores e infraestructura técnica del experimento. El sistema de control tiene que monitorizar todos los parámetros operacionales del detector, notificar cualquier posible malfuncionamiento y tomar acciones automáticas correctivas en caso necesario. El sistema de control es también responsable de la comunicación entre el experimento y los sistemas externos como el de control del acelerador LHC y los servicios generales del CERN.

Contrariamente al sistema de adquisición de datos (*Data AcQuisition system*, DAQ), el DCS es necesario antes del comienzo de la operación del experimento, durante la construcción y ensamblaje de los subdetectores. Por esta razón, la colaboración ha decidido separar las tareas de adquisición de datos y las de control en dos sistemas independientes. Sin embargo, esta separación no debe limitar el funcionamiento del detector y la comunicación bi-direccional entre ambos sistemas garantizará la operación coherente del experimento.

El sistema de control de ATLAS está basado en la experiencia adquirida durante el desarrollo y mantenimiento del sistema de control del experimento OPAL en el predecesor acelerador LEP. Sin embargo, las características del LHC y las dimensiones del experimento suponen nuevos retos en la implementación del sistema de control.

El DCS reproduce la organización jerárquica del detector en subdetectors, sistemas y subsistemas. La arquitectura del sistema de control está basada, por tanto, en particiones independientes, consistentes en aplicaciones de control y monitorización autónomas, organizadas en una estructura en forma de árbol de varios niveles. Este sistema de control será implementado a partir de una serie de componentes bien definidos, previamente seleccionados o diseñados para satisfaccer los requisitos funcionales y ambientales en ATLAS.

El DCS consta de dos subsistemas: un software distribuido de *Back-End* (BE) que será ejecutado en PC y los subsistemas de *Front-End* (FE). El producto comercial SCADA (*Supervisory Control And Data Acquisition*) PVSS-II ha sido selecionado en el marco del *Joint COntrols Project* (JCOP), para la implementación del BE de los cuatro experimentos del LHC.

Los subsistemas de FE son específicos de cada subdetector y por tanto han sido diseñados bajo la responsabilidad de los distintos grupos encargados. Sin embargo, con el objetivo de promover la homogeneidad y reducir esfuerzos durante el

desarrollo y mantenimiento de los detectores, el equipo central del DCS ha desarrollado un módulo de I/O genérico llamado *Embedded Local Monitor Board* (ELMB). El ELMB es un módulo del tamaño de una tarjeta de crédito, que puede ser instalado directamente en la electrónica de los subdetectores para la supervisión y control del equipo. EL ELMB está basado en la normativa industrial CANbus y CANopen ha sido implementado como protocolo de comunicación de alto nivel. El módulo representa una solución compacta que dispone de 64 canales analógicos de entrada, 16 líneas digitales de salida y 8 de entrada, en la configuración básica. La parte analógica es opcional y está basada en la utilización de un ADC (*Analog to Digital Converter*) de bajo coste de tipo Δ–Σ de 16 bits de resolución.

El ELMB posee dos microprocesadores:

- el procesador principal realiza las funciones de entrada y salida, y se encarga de la comunicación CANopen. Este procesador posee 128 kBytes de memoria *flash* de la que tan solo 20 kBytes son utilizados por la aplicación básica. El usuario puede cargar y ejecutar sus propios programas escritos en *C* en este procesador en caso necesario.
- el segundo procesador es más pequeño (4 kBytes de memory *flash*) y se encarga de las tareas de supervisión (*watch-dog*) del funcionamiento del procesador principal y permite su reprogramación vía el CANbus.

Debido a su versatilidad y bajo coste, el ELMB satisface los requisitos de la mayoría de las aplicaciones de control en ATLAS. El módulo ha sido ampliamente aceptado por todos los subdetectores y constituirá un elemento clave en la implementación de sus sistemas de *FE*.

Durante el desarrollo de esta tesis, el ELMB ha sido cualificado para operación en presencia de radiación de acuerdo con la *ATLAS Policy on Radiation Tolerant Electronics*. El objetivo de este proceso es la cualificación del ELMB para ser utilizado en la región central del subdetector de muones *Monitor Drift Tubes* (MDT) en ATLAS, es decir, fuera del sistema de calorimetría.

Dependiendo del tipo de radiación, pueden inducirse diferentes efectos en la electrónica. Así, por ejemplo, las partículas cargadas y radiación γ, pueden ionizar los semiconductores originando pares electrón-hueco que alteran el funcionamiento normal de los componentes electrónicos o bien modificar el valor de bits en memoria. Los neutrones, si bien no alteran la distribución de carga, pueden destruir la red interna de los semiconductores, influyendo en ciertas características del dispositivo. En este trabajo se presentan los diferentes tests realizados para:

- dosis total ionizante (*Total Ionizing Dose, TID*) con radiación γ y protones,
- pérdidas de energía no-ionizantes (*Non-Ionizing Energy Loss, NIEL*) con neutrones, y
- *Single Event Effects* (SEEs) realizado con protones.

Los resultados obtenidos para cada tipo de efecto cumplen, muy por encima, los llamados *Radiation Tolerance Criteria (RTC)* en la región antes indicada para la utilización del ELMB. Los RTC definen la dosis de radiación mínima que debe ser soportada por los componentes electrónicos para una localización dada en ATLAS. Estos RTC han sido calculados a partir de los niveles de radiación simulados aplicando diversos factores de seguridad que consideran las incertidumbres en las simulaciones, efectos debidos a radiación de tasa baja, y la tolerancia de los componentes pertenecientes a lotes no homogéneos. Este tipo de ensayos también ha permitido comprender como se manifiestan los distintos tipos de efectos debidos a la radiación en el ELMB y servirán para implementar mecanismos de corrección automática a nivel de hardware y software.

El número aproximado de módulos ELMB en ATLAS es de 5000, siendo el subdetector MDT el mayor usuario con aproximadamente 1200 nodos. El número máximo de ELMB por bus está limitado a 64 nodos por razones de hardware ya que tan solo son utilizados 7 bits para la identificación de los modulos. Los aspectos de integración de la llamada *Vertical Slice* del DCS de ATLAS y su escalabilidad han sido estudiados en esta tesis, habiendo operado un bus CAN de 200 m de longitud con 16 nodos ELMB desde una aplicación SCADA. El número de canales de I/O en este dispositivo experimental ha sido del órden de algunos subsistemas en ATLAS. La alimentación remota de los nodos a través del bus CAN y distintos aspectos de sistema, como puede ser la ocupación del bus y otras carasterísticas operacionales, han sido estudiados. Los resultados muestran unas buenas prestaciones del sistema, siendo posible leer más de 1000 canales analógicos en menos de cuatro segundos. Las medidas aquí descritas han constituido el primer paso para definir la topología de la red CANopen en ATLAS y para optimizar la distribución de taréas realizadas por los distintos elementos que conforman la *Vertical Slice*.

El DCS también constituye una herramienta muy útil para la comprensión del comportamiento y la respuesta de los detectores. En la segunda parte de este trabajo se describe el sistema de control implementado para la calibración de los módulos del calorímetro hadrónico de ATLAS (Tilecal) y los distintos estudios realizados. El detector Tilecal es un calorímetro hadrónico de muestreo no compensado, cuya característica más sobresaliente es la disposición de las fibras ópticas utilizadas para la lectura de las señales, ya que contrariamente a otros calorímetros del mismo tipo, los centelleadores y fibras están orientadas radialmente. Esto facilita la lectura de calorímetro a la vez que permite una buena hermeticidad del detector.

El calorímetro hadrónico está consitituido por un total de 256 módulos organizados en tres secciones: una central que cubre el rango de pseudorapidez $|\eta| < 1$ y dos, llamadas *extendidas*, que comprenden $|\eta| < 1.6$. Los módulos del calorímetro están a su vez subdivididos en celdas que se organizan en tres regiones de muestreo. Cada celda es doblemente leída utilizando dos fotomultiplicadores (PMT). Las distintas secciones del calorímetro están estructuradas en octantes. Todos los módulos del calorímetro serán calibrados utilizando una fuente de ^{137}Cs, mientras que, al menos un módulo perteneciente a cada octante, será calibrado empleando haces de partículas.

Durante el verano del 2001 fueron calibrados un módulo perteneciente a la sección central y cuatro de las secciones extendidss en distintas pruebas con haces de partículas. El procedimiento general de calibración, así como el dispositivo experimental utilizado en la linea de haz H8 del acelerador SPS (*Super Proton Synchrotron*) del CERN, se describen en los capítulos 5 y 6 de esta memoria.

Los distintos elementos de la *Vertical Slice* del DCS de ATLAS han sido utilizados en la implementación del sistema de control que se ha desarrollado para la calibración de los módulos. Esta aplicación ha permitido la integración en un marco común, dado por el software SCADA, de los distintos subsistemas de control del calorímetro: el sistema de refrigeración, y los de alta y baja tensión.

Los sistemas de control de la refrigeración y de la baja tensión estuvieron basados en la utilización del ELMB para la monitorización de las temperaturas y los parámetros de las fuentes de alimentación. En el caso del sistema de refrigeración, la funcionalidad básica del ELMB resultó ser suficiente. Sin embargo, en el caso del sistema de baja tensión, la funcionalidad del ELMB tuvo que ser extendida para controlar circuitos externos con salidas analógicas (*Digital to Analog Converter, DAC*). La estructura del software del ELMB, en la que se separa el protocolo CANopen de las funciones especificas para acceder al hardware, facilitó esta tarea en gran medida. El trabajo realizado se presenta en el capítulo 6 de esta memoria y los esquemas de la placa madre para la ELMB, desarrollada para este trabajo se muestra en el apéndice A.

Contrariamente a los sistemas de control de la refrigeración y de la baja tensión, el sistema de control de la alta tensión había sido desarrollado con anterioridad. Este sistema de control está basado en la utilización de un módulo VME para la monitorización, control y regulación de la alta tensión aplicada a los fotomultiplicadores (PMT). El DCS accedió a la información del sistema de alta tensión a través de una DLL (Dynamic Link Library), que actuó de interfaz entre ambos sistemas. Esta librería ha sido implementada por el autor de esta tesis y su código está listado en el apendice B de esta memoria. Este interfaz permitió el almacenamiento de esta información en la base de datos de la aplicación SCADA, permitiendo mostrar al operador el estado global del sistema de calibración.

El prototipo de DCS implementado ha proporcionado gran parte de la funcionalidad de control requerida en ATLAS. Además de la obvia supervisión y control de los parámetros operacionales de los módulos, el DCS también proporcionó la comunicación con el sistema de control del acelerador SPS y la comunicación bidireccional con el sistema de adquisición de datos mediante el software de comunicación DDC (*DAQ-DCS Communication*).

El sistema de control del SPS suministra la información correspondiente a la linea de haz H8 en un fichero, llamado *Non-Standard-Block,* a intervalos regulares de dos minutos. Este fichero contiene la información referente al tipo de haz, su energía y demás características, así como el estado de los distintos elementos de la linea de haz, tales como imanes, colimadores, etc. Esta información fue directamente

importada en la aplicación SCADA, de forma que los parámetros relevantes fueron presentados al operador y almacenados en la base de datos.

Todos los parámetros del sistema de control relevantes para el análisis *off-line*, provenientes tanto de los distintos subsistemas de control del Tilecal como del acelerador, fueron transmitidos mediante el software DDC al sistema de adquisición de datos para su posterior almacenamiento en una base de datos común. Ésta ha sido la primera utilización del DDC y la experiencia adquirida ha servido para mejorar la funcionalidad y las prestaciones de este interfaz.

La aplicación desarrollada tambien permitió determinar la estabilidad y características operacionales del sistema de refrigeración utilizado durante la calibración de los módulos. Los diferentes ensayos realizados y los resultados obtenidos son presentados en este trabajo. Los objetivos de estos estudios han sido determinar las características operacionales de la unidad de refrigeración. Los resultados muestran una estabilidad del sistema de refrigeración de 0.1 ^{o}C en las condiciones normales de operación (T=18 ^{o}C y ϕ=60 l/ min).

La influencia de los parámetros del sistema de control, en particular el valor de la alta tensión aplicada a los fotomultiplicadores utilizados para la lectura de los módulos, así como de su temperatura operacional, sobre la respuesta del calorímetro ha sido también objeto de estudio en este trabajo. Con este objetivo, fueron realizados barridos sistemáticos de la temperatura del sistema de refrigeración y de la alta tensión aplicada a los PMT. En todos los casos, la respuesta del detector fue estudiada a partir de datos tomados con un haz de electrones con una energía de 180 GeV incidiendo sobre la celda A14 del calorímetro, y los distintos sistemas de monitorización *online* del calorimetro: el sistema de laser, y el sistema de inyección de carga.

El análisis de los datos tomados con el haz de partículas muestra una contaminación del haz de electrones con piones y muones. Los distintos tipos de partículas son claramente identificados en el calorímetro debido a su peculiar deposición de energía. Las distintas técnicas aplicadas para la separación de partículas son descritas. El análisis de datos para electrones y piones es presentado.

- **Estudios de temperatura:** Debido a las dimensiones de calorímetro hadrónico, se espera una diferencia de aproximadamente 3-4 ^{o}C entre módulos situados en la parte superior e inferior del detector. El objetivo de este tipo de estudios ha sido determinar la dependencia de la respuesta de los PMT en función de su temperatura.

  En este trabajo se ha estudiado la evolución de la temperatura de los componentes electrónicos dentro de los módulos, en función de variaciones de la temperatura y del flujo del líquido de refrigeración. La temperatura del sistema de refrigeración fue incrementada desde 16 ^{o}C hasta 26 ^{o}C en intervalos de 2 ^{o}C. La dependencia de la temperatura de los fotomultiplicadores con la variación de la temperatura del sistema de refrigeración, viene dada por la siguiente expresión:

$$\Delta T_{PMT} = \frac{1}{2}\Delta T_{Cooling}$$

Los datos tomados para electrones en el barrido de temperatura efectuado con el sistema de refrigeración muestran una dependencia de la variación de señal reconstruida con la temperatura como:

$$\Delta E = 0.2\% \, \Delta T_{Cooling}$$

Este resultado coincide con el obtenido en previos estudios realizado en el laboratorio por la colaboración.

- **Estudios de Alta Tensión:** Durante la fabricación de los modulos del Tilecal, la producción de luz (*light yield*) de los centelleadores fue optimizada conduciendo a un incremento de ~20% de la carga inducida en el sistema de lectura del calorímetro. Por otro parte, las simulaciones realizadas recientemente indican a posibilidad de encontrar algunos sucesos de *jets* de partículas en el LHC en los que se depositarán varios TeV en una única celda del calorímetro. Con el presente factor de conversión de energía a carga en el detector, 1.13 pC/GeV, este tipo de sucesos producirán la saturación de la electrónica de lectura. En este estudio se ha investigado la posibilidad de atenuar la cantidad de carga inducida en función de la energía de las partículas incidentes, mediante la reducción de la alta tensión aplicada a los PMT, y se ha determinado la influencia sobre la resolución del calorimetro.

  La alta tesión aplicada a los PMT fue disminuida 150 V con respecto a los valores operacionales normales, en intervalos de 25 V. Los resultados obtenidos para electrones indican que es posible reducir la ganancia de los PMT disminuyendo la alta tensión aplicada 25 V, sin deteriorar significativamente de la resolución del calorímetro. Una reducción de la alta tensión de 150 V con respecto los valores nominales, conlleva una pérdida de la resolución de energía de 2.5% hasta un 7.5%. Sin embargo, la carga medida por cada PMT individualmente reproduce los valores esperados. Además, medidas de la linearidad de la respuesta del calorímetro, utilizando el sistema de monitorización laser, indican que los PMT permancen en el régimen lineal en todo el rango de alta tensión estudiado.

  La pérdida de resolución del calorímetero, como consecuencia de la reducción de la alta tensión aplicada, es debida a asimetrías introducidas entre los dos PMT utilizados en el sistema de lectura. Durante estas medidas, la alta tensión fue igualmente reducida a ambos PMT cambiando de forma diferente sus ganancias. Estos resultados sugieren que es posible recuperar la resolución del calorímetro en todo el rango de alta tensión estudiado mediante correcciones *offline*.

  Como consecuencia de este análisis, y de medidas complementarias realizadas por la colaboración, se ha decidido ajustar los valores de la alta tensión del calorímetro para conservar el factor calibración de 1.13 pC/GeV excepto para la

región longitudinal de muestreo más externa. Los muones atraviesan el calorímetro depositando tan solo una pequeña parte de su energía. La señal debida a muones es pequeña y se superpone con el ruido de la electrónica. La segmentación del detector permite mejorar la capacidad de trigger para muones del calorímetro incrementando el valor de la alta tensión aplicada tan solo en esta región particular y por tanto aumentar la señal reconstruida para esta región. El efecto sobre el trigger hadrónico es insignificante debido a que tan solo un 3% de la energía de jets es depositado en esta región de muestreo.

Finalmente, en este trabajo también ha sido estudiada la fotoestadística de los PMT, es decir, el número de electrones producidos en la conversión de fotones en electrones en el fotocátodo en función de la energía de la partícula incidente habiéndose determinado 70 fotoelectrones por unidad de energía (GeV). Este resultado coincide con estudios anteriores realizados por la colaboración.

En el último capítulo se exponen una serie de conclusiones generales del trabajo presentado en esta memoria.

A lo largo de esta memoria se pone de manifiesto la importancia del DCS de ATLAS debido a la enorme complejidad del experimento y a la diversidad de los componentes utilizados. El trabajo aquí presentado ha contribuido al diseño del DCS de ATLAS, así como a su aplicación a una terea concreta que permitido la calibración final del calorímetro hadrónico Tilecal.

Introduction

The principle subject of this thesis work is the design and development of the Detector Control System (DCS) of the ATLAS experiment at CERN. The DCS must ensure the coherent and safe operation of the detector and handle the communication with external systems, like the LHC accelerator and CERN services. A bidirectional data flow between the Data AcQuisition (DAQ) system and the DCS will enable coherent operation of the experiment.

The LHC experiments represent new challenges for the design of the control system. The extremely high complexity of the project forces the design of different components of the detector and related systems to be performed well ahead to their use. The long lifetime of the LHC experiments imposes the use of evolving technologies and modular design. The overall dimensions of the detector and the high number of I/O channels call for a control system with processing power distributed all over the facilities of the experiment while keeping a low cost. The environmental conditions require the utilization of magnetic field and radiation tolerant equipment. Homogeneity throughout the system, despite of the diversity of equipment and the number of people involved, is a key concern in the design of the DCS. For these reasons, the DCS will be implemented using well defined building blocks to reduce the design work, to ease commissioning and integration and to minimize the maintenance effort required during the lifetime of the experiment.

This thesis is divided into two main parts. In the first one, the requirements of the DCS are analyzed and the overall architecture of the system is designed. The building blocks of the system, and the different tests performed for their qualification for operation in ATLAS are presented. In the second part, the different technologies of the DCS are used to implement the control system for the final calibration of the modules of the ATLAS Tile Hadron Calorimeter. In addition, the effect of the DCS controlled parameters on the calorimeter response (e.g. the energy resolution and the linearity of the response) have been studied.

In the first chapter, the LHC accelerator and the ATLAS detector are described. The LHC is a *p-p* collider with an energy in the centre of mass of 14 TeV with a design luminosity of 10^{34} $cm^{-2}s^{-1}$ with a challenging bunch-crossing time of 25 ns. It will start operation in 2007. ATLAS (A Toroidal Lhc AparatuS) is a general-purpose particle detector designed to exploit fully the discovery potential of the LHC.

The design of the DCS for the ATLAS experiment is presented in the second chapter. The ATLAS DCS will follow the decomposition of the ATLAS experiment into subsystems. The DCS architecture will map the natural hierarchical organization of the detector. The main information flow, both data and commands,

is purely in the vertical direction. This leads to an arrangement of the system into *vertical slices*.

In the third chapter, the building blocks of the DCS are described in detail. The DCS consists of two major components: a distributed Back-End (BE) software system and the Front-End (FE) systems. The BE system will be implemented using a commercial Supervisory Control And Data Acquisition (SCADA) product running on PC. For the implementation of the FE systems, ATLAS DCS central team has developed a plug-on I/O module for detector control, called *Embedded Local Monitor Board* (ELMB). The ELMB satisfies the requirements of most applications in ATLAS, hence reducing the number of dedicated I/O systems needed. A total number of 5000 ELMB nodes is estimated to be needed, the Monitor Drift Tubes (MDT) subdetector being the major user with 1200 modules.

Chapter 4 is dedicated to present the different tests performed for the radiation qualification of the ELMB and the scalability aspects of the *Vertical Slice*, which comprises the ELMB and the SCADA interconnected by a CANopen OPC server.

In chapter 5 the Tile Hadron Calorimeter, as well as the different calibration and DCS subsystem of this subdetector are described.

The DCS developed for the calibration of the Tile calorimeter in the beam line H8 of the SPS accelerator at CERN in summer 2001 is described in chapter 6. The DCS implemented has allowed the performance of the cooling system to be determined. The different tests carried out and the results obtained are presented.

In chapter 7, a study of the effects of the parameters controlled by the DCS, namely the temperature of the cooling system and HV applied, on the calorimeter response to electrons and pions has been carried out. The physics analysis and the different techniques applied for particle separation are described.

In the last chapter, the conclusions of this thesis are given. Appendix A shows the schematics of the ELMB motherboard developed for the implementation of the DCS for the low-voltage system of the Tile Hadron Calorimeter. In appendix B, the source code of the Dynamic Link Lybrary (DLL) implemented to interface the high voltage system for this subdetector is listed.

Chapter 1

The ATLAS Experiment

ATLAS is a general-purpose particle detector designed to exploit the full discovery potential of the LHC. In this chapter, the main characteristics of the collider are outlined. The physics program of the ATLAS experiment is summarized. In section 1.3 the main design requirements of the detector and its organization are presented, followed by a detailed description of the different subsystems of the detector.

1.1 The Large Hadron Collider

The Large Hadron Collider (LHC) is a two counter-rotating proton beams each with an energy of 7 TeV giving a total collision energy in the centre of mass of 14 TeV. It will be built in the existing 27 km tunnel where the LEP collider was situated and it is scheduled to start operation in 2007. The LHC will have a dynamic range of discovery from energy scales of 5 MeV, in the case of *b*-physics, to a few TeV for the discovery of new vector bosons or quark compositeness.

The upper limit of the energy which can be reached at LHC, is imposed by geometrical and magnetic constraints. The magnetic field strength required to force the particle beams around the collider increases linearly with the beam energy. The highest operational magnetic field for affordable super-conducting magnets is 8.65 T which together with the requirement that the LHC has to fit inside the existing LEP tunnel gives the maximum energy of 7 TeV per beam.

The beam energy being limited, another way to increase the rate of events of interesting physics is to increase the luminosity. The event rate of a specific process is given as:

$$n_x = \sigma_x L \tag{1.1}$$

where L is the luminosity and σ_x the cross section of the process. The cross section is is in general a function of the energy and depends on the specific process. The luminosity is related by the parameters of the collider and is given as:

$$L = \frac{1}{4\pi}\frac{N^2 f}{tA_T} \tag{1.2}$$

where N is the number of protons in each bunch, t the time between individual bunches, A_T the transverse dimension of the bunches at the interaction points and f the fraction of bunch positions actually containing protons.

The time between bunches is limited by the requirement that there should be no additional interactions on each side of the interaction region and the time resolution of the experiment. For the LHC the bunch crossing time will be 25 ns corresponding to approximately 23 interactions per bunch. The transverse dimensions of the beam can at the interaction point are of a few μm. To be able to fill new bunches into the LHC and to operate the beam dump it is necessary to order the proton bunches in bunch trains followed by some empty bunches. In total 2835 of the 3557 available positions with 25 ns separation will contain protons corresponding to f=0.80. The only remaining way to increase the luminosity is to increase the number of protons per bunch but this is limited by electromagnetic forces.

The nominal luminosity is fixed at 10^{34} $cm^{-2}s^{-1}$ but for the first years of operations it is foreseen to run at a lower luminosity $L_{low}=10^{33}$ $cm^{-2}s^{-1}$ and increase it gradually to the nominal value. The requirements on the luminosity from physics can be seen from figure 1.1. The number of observed events is given as

$$n_{obs} = L\sigma B_r T\varepsilon \tag{1.3}$$

with T the effective time the machine is running, B_r the branching ratio of the detected decay and ε the detection efficiency.

The high requirement on luminosity is the reason for the choice of a proton-proton collider. While a proton-antiproton machine has the advantage that both counter-rotating beams can be kept in the same beam pipe, producing the enormous amounts of antiprotons required for the high luminosity is not realistic and it would be more expensive than the proton-proton solution with separated beam pipes.

1.2 Physics goals

The primary physics goal at LHC is to search for the Standard Model Higgs boson. The Higgs mechanism allows the electroweak symmetry to be broken explaining how particles have mass. The mass of the Higgs boson, which is unspecified by the theory, is expected to be in the range 50 GeV<m_H<1 TeV. Some of the best experimental signatures for observing the Higgs are expected to be:

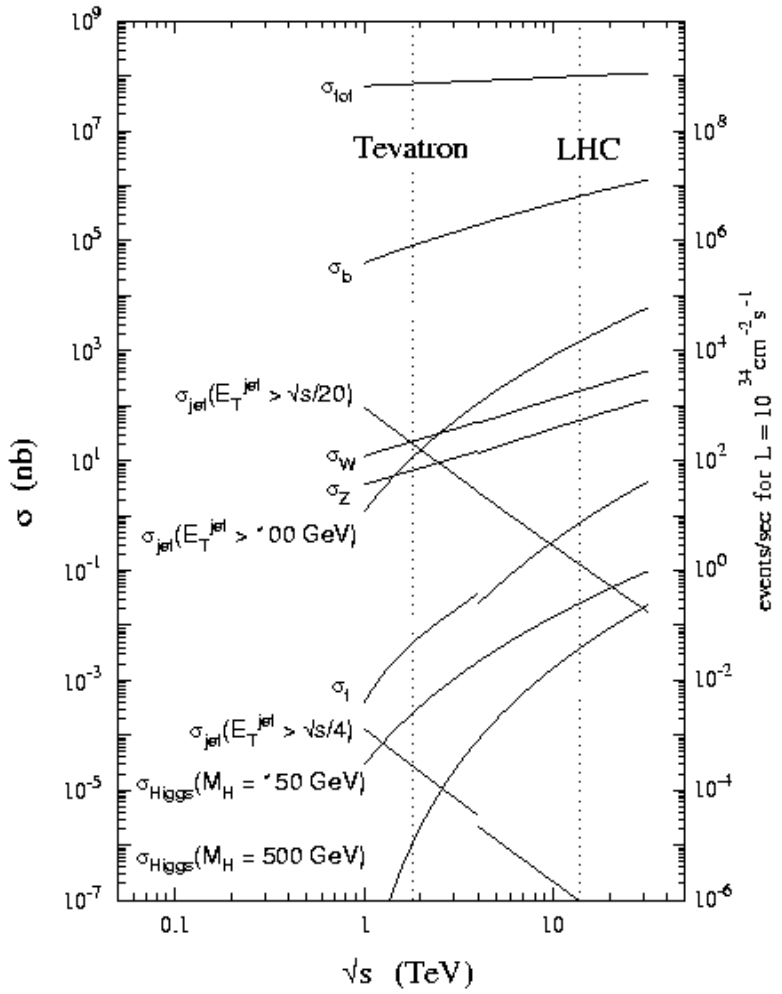

Figure 1.1: *Expected proton-proton cross section as a function of the energy in the centre of mass system.*

$pp \to H \to \gamma\gamma$	if $m_H < 150\ GeV/c^2$
$pp \to H \to Z(Z^* \to 4\ leptons)$	if $120 < m_H < 180\ GeV/c^2$
$pp \to H \to WW^* \to l\bar{\nu}\ \upsilon\nu\bar{l}$	if $m_H > 150\ GeV/c^2$
$pp \to H \to WW \to l\nu q\bar{q}$	if $m_H > 300\ GeV/c^2$

Other physics topics that will be investigated include:

- Supersymmetry: an extension of the Standard Model where every particle has a supersymmetric partner. Many of the supersymmetric particles are expected to have masses in the discovery range of the LHC.
- Compositeness of quarks and leptons substructures.
- B-physics

1.3 The ATLAS Detector

The ATLAS ("A Toroidal Lhc ApparatuS") is a general-purpose *p-p* espectrometer designed to exploit the full discovery potential of the LHC. The detector concept and its physics potential have been presented in the Technical Proposal [1] in 1994 and in different Technical Design Reports [2, 3]. The overall detector layout as shown in figure 1.2, has a cylindrical symmetry with a total length of 42 m and a radius of 11 m.

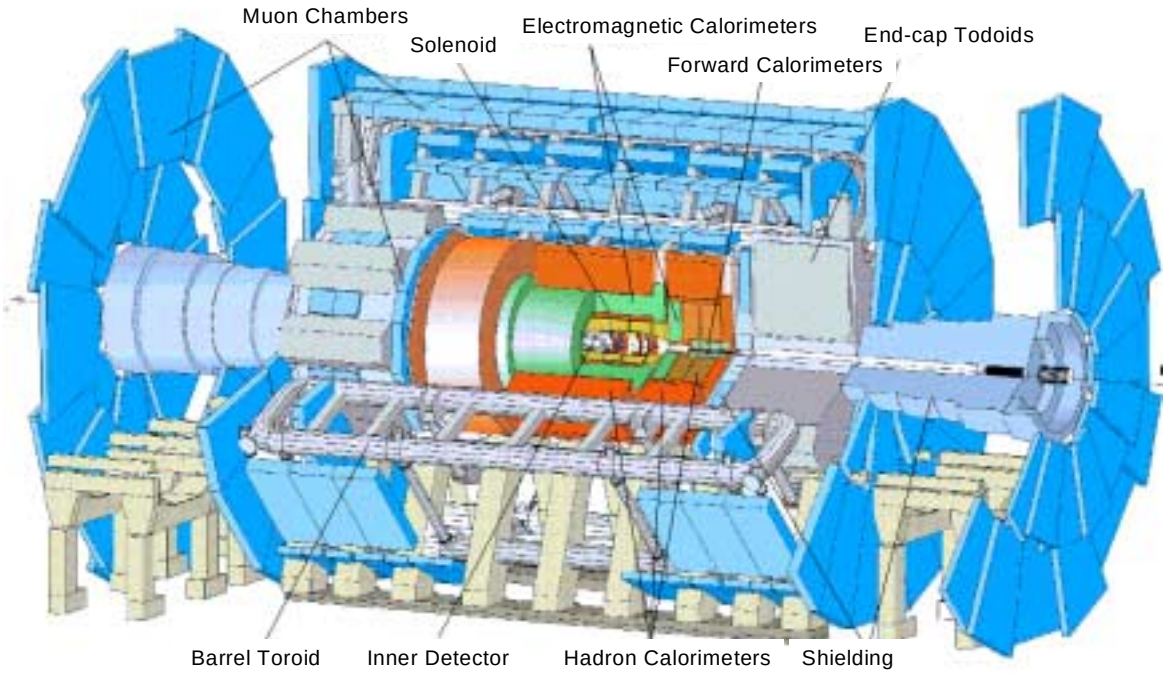

Figure 1.2: *General overview of the ATLAS Detector*

The detector will be installed 100 m under ground level in the cavern Ux15, at the interaction point 1 of the LHC. The underground facilities of the experiment are shown in figure 1.3. The figure also shows the co-ordinate system with the x-axis pointing towards the centre of the LHC tunnel, the z-axis laying along the circumference of the tunnel. The tunnel plane is slightly tilted with respect to the horizontal plane. This causes small deviation of the y-axis with respect to the original. The pseudo-rapidity of the particles from the interaction vertex is defined as:

$$\eta = -\log \tan\frac{\theta}{2} \tag{1.4}$$

where θ is the polar angle measured from the positive z-axis. The transverse momentum of the particles (p_T) is defined as the component of the momentum perpendicular to the LHC beam axis.

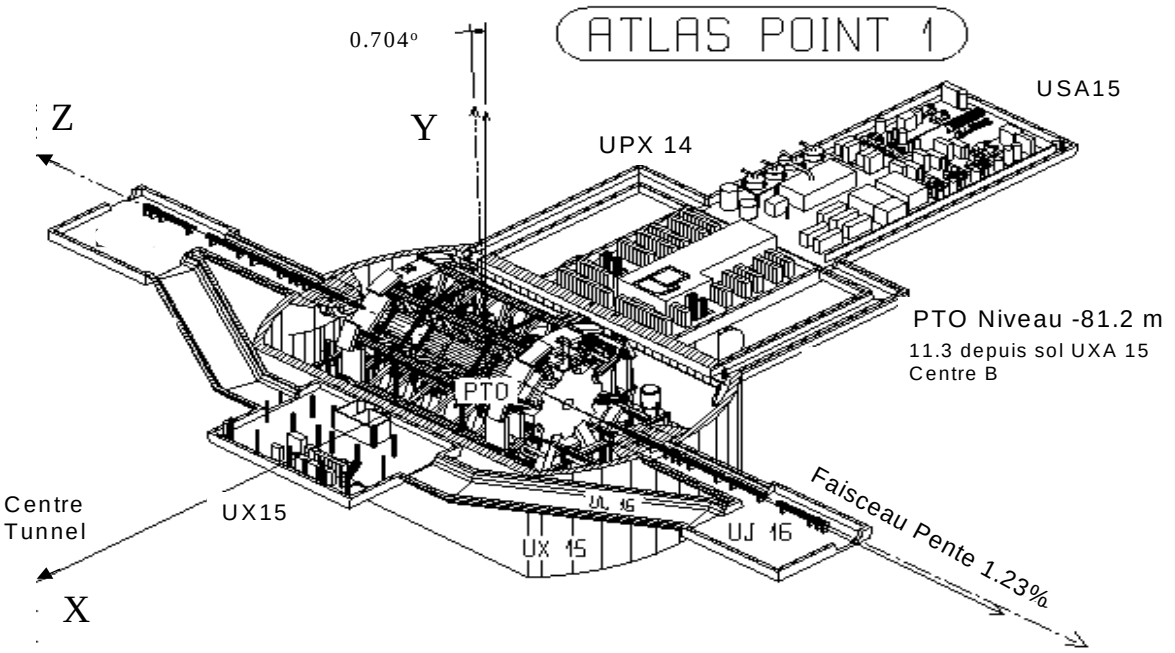

Figure 1.3: *Right-handed co-ordinate system of the ATLAS detector.*

The detector is optimized for a long range of known and hypothetical process. The observable cross-section for most of the processes is small over a large part of mass range, hence it is an important design consideration to operate at high luminosity and to maximize the detectable rates above backgrounds by high resolution measurements. The basic design criteria of the detector include the following:

- Very good electromagnetic calorimetry for electron and photon identification and measurements, complemented by full-coverage hadronic calorimetry for accurate jet and missing transverse energy (E_{Tmiss}) measurements.
- High-precision muon measurements, with the capability to guarantee accurate measurements at the highest luminosity using the external muon spectrometer alone.
- Efficient tracking at high luminosity for high-p_T lepton-momentum measurements, electron and photon identification, τ-lepton and heavy-flavour identification, and full event reconstruction capability at lower luminosity.
- Large acceptance in pseudo-rapidity (η) with almost full azimutal angle (ϕ) coverage everywhere. The azimuthal angle is measured around the beam axis.
- Triggering and measurements of particles at low-p_T thresholds, providing high efficiencies for most physics processes of interest at LHC.

ATLAS is characterized by two different magnetic field systems required for particle identification and momentum measurements. A super-conducting solenoid, providing a magnetic field of 2 T, will be installed around the Inner Detector cavity, whereas a large super-conducting air-core toroid system, providing a magnetic field of 1.5 T, will be arranged outside the calorimetry. The latter permits for high-resolution, large acceptance and robust muon spectrometer with excellent stand-alone capabilities. The total weight of the detector is ~7000 Tons, mainly due to the calorimetry system.

The inner detector (ID) is contained within a cylinder of length 7 m and a radius of 1.15 m. Pattern recognition, momentum and vertex measurements, and electron identification are achieved with a combination of discrete high-resolution semiconductor pixel and strip detectors in the inner part of the tracking volume, and continuous straw tube tracking detectors with transition radiation capability in its outer part.

Highly granular liquid-argon (LiAr) electromagnetic (EM) sampling calorimetry, with excellent performance in terms of energy and position resolution, covers the pseudorapidity range $|\eta| < 3.2$. In the end-caps, the LAr technology is also used for the hadronic calorimeters, which share the cryostats with the EM end-caps. The same cryostats also house the special LAr forward calorimeters which extend the pseudorapidity coverage to $|\eta| < 4.9$. The LAr calorimetry is contained in a cylinder with an outer radius of 2.2 m and extends longitudinally to ±6.6 m along the beam axis.

The bulk of the hadronic calorimetry is provided by a novel scintillating-tile calorimeter, which is separated into a large barrel and two smaller extended barrel cylinders, one on each side of the barrel. The outer radius of the scintillating-tile calorimeter is 4.25 m and its half length is 6.10 m. The overall calorimeter system provides the very good jet and E_{Tmiss} performance of the detector.

The calorimeter is surrounded by the muon spectrometer. The air-core toroid system, with a long barrel and two inserted end-cap magnets, generates a large magnetic field volume with strong bending power within a light and open structure. Multiple-scattering effects are thereby minimized, and excellent muon momentum resolution is achieved with three stations of high-precision tacking chambers. The muon instrumentation also includes as a key component trigger chambers with very fast time response. The muon spectrometer defines the overall dimensions of the ATLAS detector. The outer chambers of the barrel are at a radius of about 11 m. The half-length of the barrel toroid coils is 12.5 m, and the third layer of the forward muon chambers, mounted on the cavern wall, is located about 23 m from the interaction point.

The ATLAS experiment has entered the construction and calibration phase for many of its detector components. The following sections summarize the physics scope, performance and design of the individual subdetectors.

1.4 Inner Detector

The Inner Detector (ID) [4, 5] is designed to reconstruct tracks and decay vertices in any event with high efficiency. Using additional information from the calorimeter and muon systems, the inner detector also contributes to electron, photon, and muon identification, and supplies extra signatures for short-lived particle decay vertices. Important physics considerations for the design of the inner detector are:

- excellent momentum and impact parameter resolution for tracks with $p_T > 0.5$ GeV up to very high momentum,
- tracking coverage over the range $|\eta| < 2.5$,
- high efficiency keeping high noise rejection,
- identification of the charge of high-p_T tracks,
- tagging of *b*-jets originating from *b*-quarks,
- reconstruction of soft electrons and secondary vertices from *b*- and τ-decays,
- identification of the primary vertex,
- electron identification capability,
- identification of a high p_T track to reduce the level-1 electromagnetic cluster trigger rate from jet events.

The magnetic field configuration of the ID is based on an inner thin super-conducting solenoid surrounding the inner detector cavity with a radius of 1.2 m and a length of 5.3 m. It provides an axial magnetic field of 2 T in the centre of the tracking volume.

The momentum and vertex resolution requirements from physics call for high-precision measurements to be made with fine granularity detectors, given the very large track density expected at the LHC. The layout of the Inner Detector is shown in figure 1.4. The outer radius of the ID cavity is 115 cm. It consists of three units: a barrel section extending over ±80 cm, and two identical end-caps covering the rest of the cylindrical part. In the barrel region, high-precision detector layers are arranged on concentric cylinders around the beam axis, while the end-cap detectors are mounted on disks perpendicular to the beam axis.

The highest granularity around the vertex region is provided by semi-conductor pixel and strip detectors, the latter employed in the Semiconductor Tracker (SCT). The basic principle of the semiconductor detectors is that the passage of ionizing radiation creates electron-hole pairs in the semiconductor which are collected by an electrical field. The difference between strips and pixels is mainly geometry, pixels being closely spaced pads capable of good two dimensional reconstruction while strips give a better spacial resolution in one co-ordinate than the other.

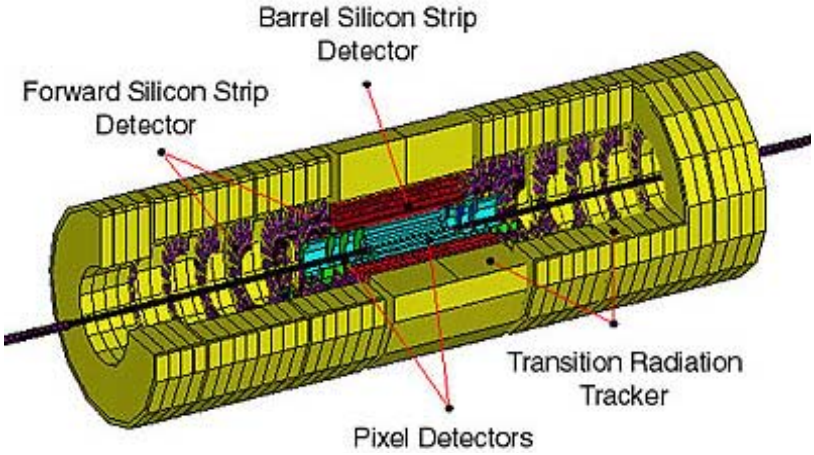

Figure 1.4: *Inner detector layout*

The pixel layers are segmented in Rϕ and *z*, while SCT detector uses small angle (40 mrad) stereo strips to measure both coordinates, with one set of strips in each layer measuring ϕ. The pixel detector is much more radiation tolerant than the silicon strip tracker.

The number of layers of the semiconductor detectors must be limited due to the material they introduce and their high cost. A larger number of tracking points is provided by the straw tube tracker also called Transition Radiation Tracker (TRT), which provides continuous tracking with much less material per point and a lower cost. The barrel TRT tubes are parallel to the beam direction. The continuous tracking consists of radial straws arranged into wheels.

The three different detector technologies are summarized below:

1.4.1 Pixel detector

The pixel detector [6] is designed to provide a very high-granularity, high-precision set of measurements as close to the interaction point as possible. Figure 1.5 shows the layout of the pixel detector. The system consists of three barrels at average radii of ~4 cm, 10 cm, and 13 cm respectively, and five rings on each side, with 11cm inner radius and 20 cm of outer radius, which complete the angular coverage. The thickness of each layer is expected to be about 1.7% of a radiation length (X_0) at normal incidence. It provides three precision measurements over the full acceptance, and mostly determines the impact parameter resolution and the ability of the Inner Detector to find short-lived particles such as B hadrons and τ leptons.

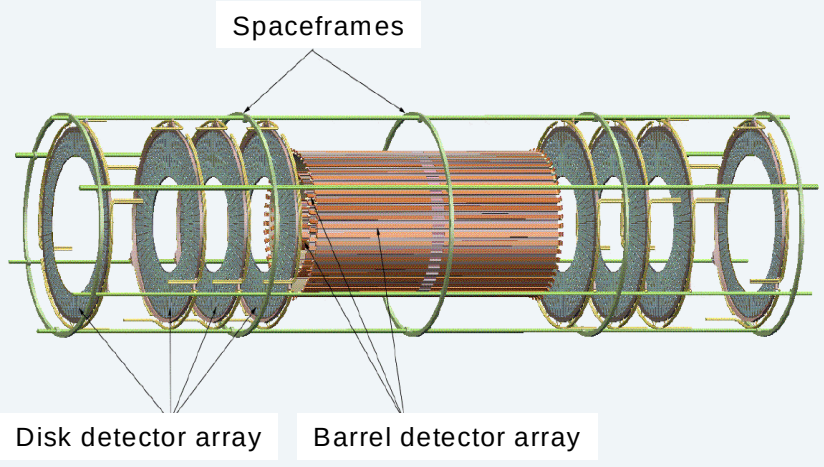

Figure 1.5: *Pixel detector*

The system contains a total of 140 millions of detector elements, each 50 μm in the *r*ϕ plane and 300 μm in *z*. The very fine granularity pixel detector provides a resolutions of about 10 μm in the *r*ϕ plane and 50 μm in *z*, allowing the track origin to be reconstructed and secondary decay vertices to be found. This has a crucial importance in the identification of short-lived particles such as b quarks and τ leptons, which requires the inner detector to reconstruct the decay point inside the beam pipe by extrapolating the tracks back to their origins. Good impact parameter resolution for low luminosity B-physics studies and is greatly improved by the presence of the inner- most pixel layer at 4 cm, also called B-layer.

The readout of the pixels requires the use of advanced techniques. The readout chips cover a large area, with individual circuits for each pixel element, including buffering to store the data while awaiting the level-1 trigger decision. In addition each chip must be radiation-hard to withstand over 300 kGy of ionizing radiation and over 5×10^{14} neutrons per cm^2 over ten years of operation of the experiment.

1.4.2 Semiconductor Tracker

The SCT system [5] is designed to provide eight precision measurements per track in the intermediate radial range, contributing to the measurement of momentum, impact parameter and vertex position, as well as providing good pattern recognition by the use of high granularity.

The barrel SCT uses eight layers of silicon micro-strips (80 μm pitch) to provide precision points in the *r*ϕ plane and *z* coordinates, using small angle stereo to obtain the z measurement. The two SCT end-caps, similar in construction to the barrel, are placed at each end of the module.

The detector contains 6.2 million readout channels. The spatial resolution is 16 μm in Rϕ and 580 μm in *z*, per module containing one *r*ϕ and one stereo measurement. Tracks can be distinguished is they are separated ~200 μm.

1.4.3 Transition Radiation Tracker

The Transition Radiation Tacker (TRT) [5] consists of thin proportional drift tubes (straws) with a diameter of 4 mm. The detector is divided in a barrel part containing about 50000 straws and two identical end-caps having about 320000 radial straws with the readout at the outer radius. Each of these straws is equipped with a 30 μm diameter gold-plated W-Re wire. The detector can be operate at the very high rates expected at the LHC due to the small diameter of the sense wires and their isolation within the individual gas volumes. The TRT is operated with a non-flammable gas mixture optimized for the detection of X-rays created as transition radiation in stacks of thin radiators between the tubes. This technique is intrinsically radiation hard, and allows a large number of measurements, typically 36, to be made on every track at modest cost. A good pattern recognition is also assured by the continuous tracking.

Each channel provides a drift-time measurement, giving a spatial resolution of 170 μm per straw and the efficiency >50% even for the highest rates (15 *MHz*). The TRT provides additional discrimination between electrons and hadrons.

1.4.4 Combined performance

The combination of the three techniques gives a very robust pattern recognition and high precision in both ϕ and z coordinates. The combined system covers a range of ± 2.5 in η and gives a momentum resolution of about 20% for low-η tracks with 500 GeV of transverse momentum. This is sufficient to identify the charge sign for particles at the highest energies. The coverage is very uniform, with around twelve space points measured on each track from the precision layers and 30-40 measurements in the straws.

The momentum resolution is limited by several factors: the strength of the magnetic field, the intrinsic precision of the detector elements and the radial space available in the inner detector cavity. At high momenta, the impact parameter of the track at the primary vertex can be measured with a precision of <15 μm. At lower momenta, multiple scattering of the tracks reduces the precision to > 60 μm. Tracks with p_T < 0.5 GeV will loop in the magnetic field and cannot be reconstructed. Increasing the magnetic field strength would improve the charge identification but would also raise the value of the minimum reconstructible track p_T.

1.5 The Calorimeters

Unlike other detector subsystems, the intrinsic energy resolution of calorimeters improves with increasing energy, making them suitable for use at high energy colliders. Physics requirements on calorimeters at the LHC include:

- the accurate measurement of the energy and position of both electrons and photons,
- the measurement of the energy and direction of jets,
- particle identification including the separation of electrons, photons and hadronic τ decays from jets,
- the measurement of the missing transverse energy of events,
- event selection already at the first trigger level.

The system is divided into an electromagnetic sampling calorimeter with high resolution closest to the interaction point and a larger hadronic calorimeter behind with a coarser resolution. The electromagnetic calorimeter uses liquid Argon as active medium whereas in the hadronic calorimeter different technologies are employed depending on the environmental constrains like radiation dose. The ATLAS calorimeters are shown in figure 1.6.

The position of the central solenoid in front of the electromagnetic calorimeter demands a careful minimization of the material in order to achieve the desired calorimeter performance. As a consequence, the central solenoid and the LAr calorimeter share one common vacuum vessel, thereby eliminating two vacuum walls. The cryostat covers covering a pseudorapidity range of $|\eta| < 1.7$. The central solenoid is designed to be as thin as possible without sacrifying the operational safety and reliability. Two end-caps cryostats enclose the electromagnetic ($1.5 < |\eta| < 3.2$) and hadronic calorimeters ($|\eta| < 3.2$) as well as integrated forward calorimeters ($3.1 < |\eta| < 4.9$).

1.5.1 LAr Calorimeter

The electromagnetic (EM) calorimeter is required to reconstruct electrons and photons in the energy range of 2 GeV to 5 TeV. The principal benchmark channels for the electromagnetic calorimeter are $H \rightarrow ZZ^* \rightarrow 4e$ and $H \rightarrow gg$. These channels place the most stringent requirements on the electromagnetic calorimeter in terms of energy resolution, energy range, and particle identification. The channel $H \rightarrow ZZ^* \rightarrow 4e$ requires electron identification down to 5 GeV.

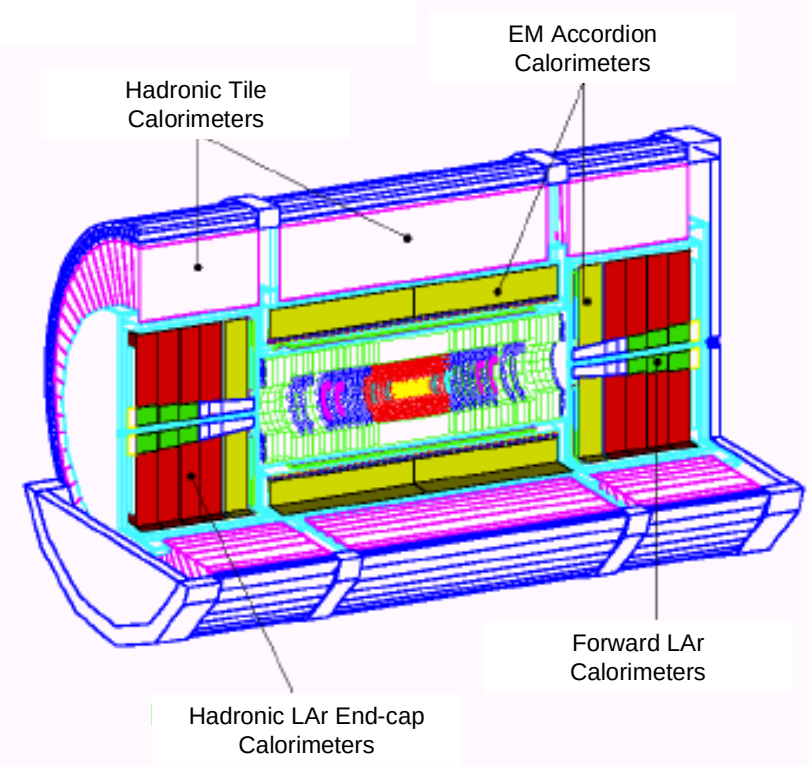

Figure 1.6: *ATLAS Calorimetry System*

Searches for rare processes require an excellent coverage in pseudorapidity, as well as the measurement of the missing transverse energy of the event, and the reconstruction of jets. In the mass range of interest, an energy resolution of 1% is needed.

Backgrounds to electrons and photons come predominantly from hadronic jets. A high jet rejection factor is needed in the range 25 GeV < p_T < 100 GeV to suppress *g*-jet and jet-jet backgrounds to the $H \rightarrow gg$ channel. The calorimeter must also reject isolated high-p_T π^0 particles from jet fragmentation. Electron-jet separation is necessary for the efficient identification of isolated electrons from *W*, *Z* and heavy flavour decays.

The EM calorimeter is a lead-Liquid Argon (LAr) detector [7] with accordion shaped kapton electrodes and lead absorber plates, shown in figure 1.7, over its full coverage. The barrel of the electromagnetic calorimeter covers $|\eta| < 1.475$ and the two identical end-caps cover $1.375 < |\eta| < 3.2$. The thickness of the lead absorbers varies as a function of pseudorapidity to optimize the energy resolution of the calorimeter.

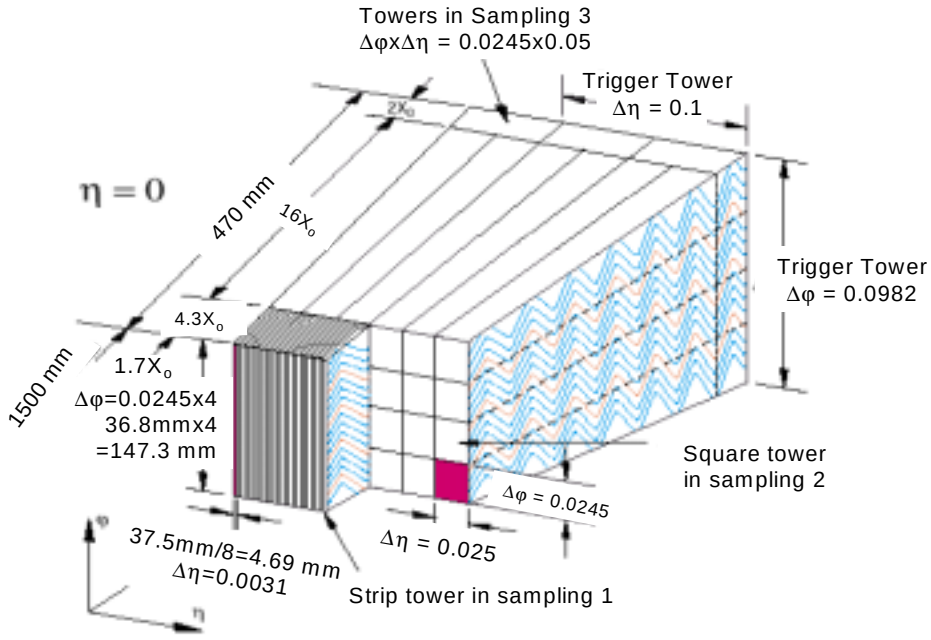

Figure 1.7: *Accordion structure of the LiAr calorimeter.*

Over the pseudorapidity range $|\eta|<1.8$, the LAr calorimeter is preceded by a pre-sampler detector, installed immediately behind the cryostat cold wall, and used to correct for the energy lost in the material (ID, cryostats, coil) upstream of the calorimeter (~2 X_0 at $\eta=0$). In the transition region between the barrel and end-caps, the amount of material reaches 7 X_0. This region is not used for high precision physics measurements.

The Liquid Argon technology is radiation resistant and provides long-term stability of the detector response, excellent hermeticity, good energy resolutions, and relatively easy detector calibration. The total thickness of the electromagnetic calorimeter is >24 X_0 in the barrel and >26 X_0 in the end-caps. The approximate number of channels is 200 000.

The segmentation of the calorimeter is $\Delta\eta\times\Delta\phi \sim 0.025\times0.025$, aiming for the energy resolution given by the following expression.

$$\frac{\sigma}{E} = \frac{10\%}{\sqrt{E}} \oplus 1\% \qquad (E \text{ in GeV}) \tag{1.5}$$

where $\oplus$ is the quadratic sum operator, i.e. the square of the energy resolution is equal to the sum of the square of the two terms.

1.5.2 Hadronic Calorimeters

The main function of the hadronic calorimeter is the identification, measurement and reconstruction of jets, and the measurement of the missing p_T in an event.

The discovery of a high mass Higgs decaying into a high-p_T $W \rightarrow jet\text{-}jet$ requires *jet-jet* mass reconstruction and forward *jet* tagging. For low mass Higgs searches, mass reconstruction via the channel $H \rightarrow bb$ and *jet* spectroscopy are important. The decay of $H^0 \rightarrow tt$ according to the Minimal Supersymmetric Standard Model requires good resolution and energy reconstruction. Studies of quark compositeness require good measurement of p_T jets.

The ATLAS hadronic calorimeters cover the range of $|\eta| < 4.9$ using different techniques best suited for the widely varying requirements and radiation environment over the large η-range.

The calorimeter provides good resolution for high energy jets. The large η-coverage will also guarantee a good E_{Tmiss} measurement, which is important for many physics signatures and in particular for SUper SYmmetry (SUSY) particle searches.

The hadronic barrel calorimeter is a cylinder divided in three sections: central barrel and two identical extended barrels. They have an inner radius of 2.28 m and an outer radius of 4.23 m and are sampling calorimeters with iron as absorber material and scintillating tiles (3 mm thick) as active material, called Tile Calorimeter [8]. The signals produced at one both sides of the scintillating tiles are read out by wavelengths-shifting (WLS) fibers into two separate photomultipliers (PMT). The total number of channels is 10000. The resulting segmentation of the hadronic calorimeter is $\Delta\eta \times \Delta\phi \sim 0.1 \times 0.1$. The total thickness is 11 interaction lengths (λ_0) at $\eta=0$, including 1.5λ of the outer support. The barrel and extended barrels of the tile calorimeters support the LiAr cryostats and also acts as the main solenoid flux return.

At larger pseudo-rapidities, where higher radiation resistance is needed, the intrinsically radiation-hard LAr technology was chosen: the hadronic end-cap calorimeters (HCAL) and the forward calorimeter (FCAL) with the front face 4.7 m from the interaction point. HCAL is a copper LAr detector with parallel-plate geometry while FCAL is a dense LAr calorimeter with rod-shaped electrodes in a tungsten matrix. The number of channels is about 3584 for the total of both sides.

The expected energy resolution for the hadronic calorimeter is $\frac{\Delta E}{E} = \frac{50\%}{\sqrt{E}} \oplus 3\%$ for $|\eta| < 3$

and $\frac{\Delta E}{E} = \frac{100\%}{\sqrt{E}} \oplus 10\%$ for $3 < |\eta| < 4.9$.

Part of the work done in this thesis has led to the implementation of the control system of the setup used for the final calibration of the Tilecal modules using particle beams in summer 2001. For this reason a more detailed description of the detector and its control system is given in other chapters of this thesis.

1.6 The Muon Spectrometer

Principal benchmark processes for the performance of the muon spectrometer [9] include both Standard Model and Minimum Supersimmetric Standard Model Higgs decays with muons in the final state, as well as new vector boson decays and B-physics. The design and performance of the Muon Spectrometer must satisfy the following requirements:

- identify, reconstruct and measure the momenta of muon tracks, as well as provide an association with measurements in the inner detector. Good transverse momentum resolution must be maintained down to 5 GeV as well as a coverage in pseudorapidity of up to $|\eta| = 3$ and good hermeticity,
- Trigger selectivity: transverse momentum thresholds of 10-20 GeV/c are adequate for high-mass states, which will be in the focus of LHC physics at nominal luminosity.
- Trigger coverage of about $|\eta| < 2.4$ is found to be sufficient.
- Bunch-crossing identification: the LHC bunch-crossing interval of 25 ns sets the scale for the required time resolution of the first level trigger system.

A wide pseudorapidity coverage is essential for track reconstruction in rare processes. Momentum and mass resolutions of the order of 1% are essential for the reconstruction of narrow final states with two or four muons, for background rejection and charge identification. The muon spectrometer must also measure a second coordinate in the non-bending plane for muon tracks, with a spatial resolution of 5-10 mm to ensure good track reconstruction and momentum measurement.

For the muon trigger system, transverse mass thresholds in the range 10-20 GeV are used for large mass particles, whereas the more stringent requirements come from B-physics, where a p_T threshold of down to 5 GeV is required. A trigger coverage of $|\eta| < 2.4$ is currently deemed to be adequate.

The Muon Spectrometer dominates the size of the ATLAS experiment with its outer diameter of ~22 m. Figure 1.8 shows a cut of the Muon Spectrometer.

The ATLAS Muon Spectrometer is based on deflection of muon tracks in a magnetic field provided by a system of three large super-conducting air-core toroid magnets instrumented with separate function trigger, the Resistive Plate Chambers (RPC)

and the Thin Gas Chambers (TGC), and high-precision tracking chambers, the Monitor Drift Tubes (MDT) and the Cathode Strip Chambers (CSC).

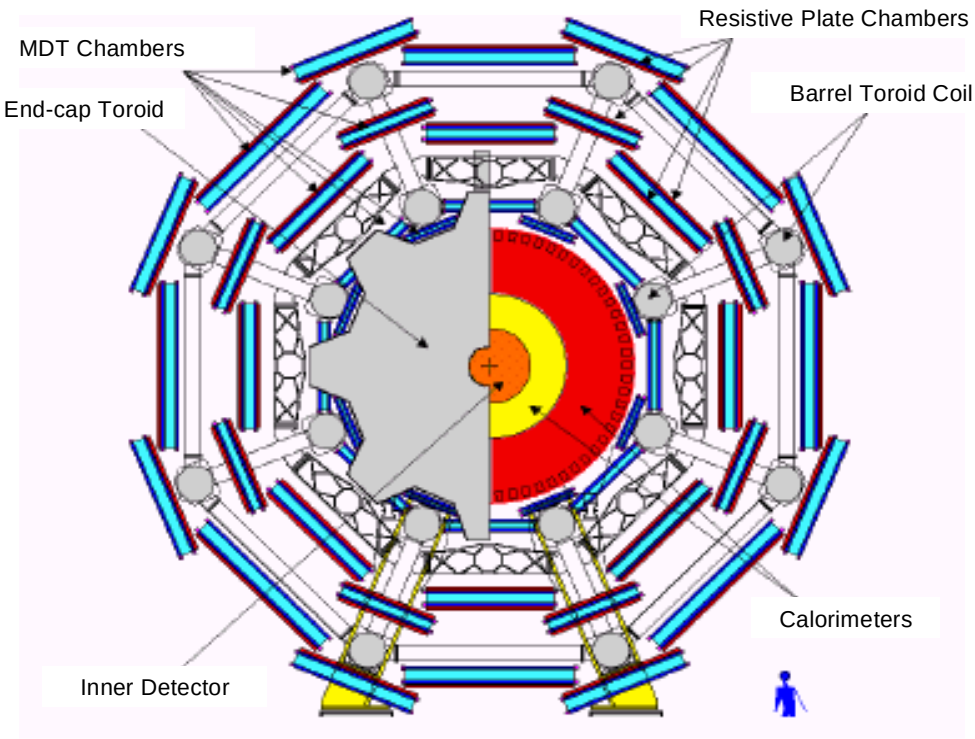

Figure 1.8: *Layout of the muon spectrometer*

The magnet system is designed to provide a large volume magnetic field covering the pseudorapidity range $|\eta| < 2.7$.

The trigger chambers must identify bunch crossings, trigger with well-defined p_T thresholds and measure a second coordinate orthogonal to that measured in the muon chambers.

In the barrel, the chambers are arranged on three concentric cylinders whereas in the end-caps they are arranged in four disks. This arrangement is such that particles from the interaction point traverse three chambers.

1.6.1 Magnet system

The magnet system [10] consists of three air-core super-conducting toroids with an open structure to minimize the contribution of multiple scattering to the momentum resolution. Over the range $|\eta| \leq 1$, magnetic bending is provided by the large barrel toroid. The barrel toroid extends over a length of 25 m, with an inner bore of 9.4 m and an outer diameter of 20.1 m. For $1.4 < \eta < 2.7$, muon tracks are

bent by two end-cap magnets inserted into both ends of the barrel toroid. They have a length of 5 m, an inner bore of 1.64 m and an outer diameter of 10.7 m. Over $1 < \eta < 1.4$, usually referred to as the transition region, magnetic deflection is provided by a combination of barrel and end-cap.

Each toroid consists of eight flat coils assembled radially and symmetrically around the beam axis. The barrel-toroid coils are contained in individual cryostats, whereas the eight end-cap toroid coils are assembled in a single, large cryostat. This magnet configuration provides a 2 T field that is mostly ortogonal to the muon trajectories. The average toroidal magnetic field will be ~0.5 T. The toroidal design of the magnet system made it possible to provide a high resolution, large acceptance and robust stand-alone Muon Spectrometer.

1.6.2 Tracking system

The chambers are arranged such that particles from the interaction point cross three stations of chambers. The positions of these stations are optimized for full coverage and momentum resolution. The barrel chambers form three cylinders concentric with the beam axis, at radii of about 5, 7.5 and 10 m. They cover the pseudorapidity range $|\eta| < 1$. The end-cap chambers cover the range $1 < |\eta| < 2.7$ and are arranged in four disks at distances 7, 10 and 14 and 21 m from the interaction point, concentric with the beam axis.

The precision measurement of the muon tracks is made in the *R*-*z* projection, in a direction parallel to the bending direction of the magnetic filed; the axial coordinate (*z*) is measured in the barrel and the radial coordinate (*R*) in the transition and end-cap regions.

Over most of the η-range, a precision measurement of the track coordinates in the principal bending direction of the magnetic filed is provided by Monitored Drift Tubes (MDT). At large pseudo-rapidities and close to the interaction point, Cathode Strip Chambers (CSC) with higher granularity are used in the innermost plane over $2 < |\eta| < 2.7$, to withstand the demanding rate and background conditions. These two tracking detectors are shown in figure 1.9. Optical alignment systems have been designed to meet the stringent requirements on the mechanical accuracy and the survey of the precision chamber.

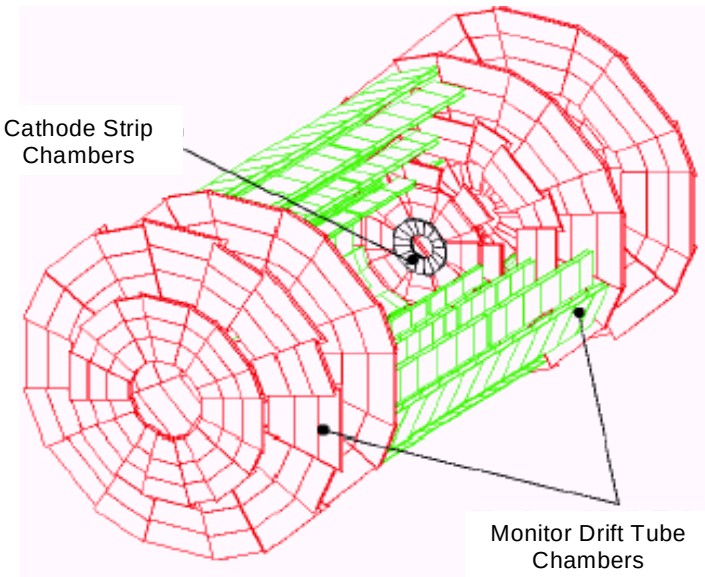

Figure 1.9: *Tracking detectors of the muon spectrometer.*

1.6.2.1 Monitored Drift-Tubes chambers

The MDT chamber are proportional detectors made of aluminium tubes of 30 mm diameter and lengths varying from 70 cm to 630 cm. To measure the coordinate in the bending plane of the magnet the tubes are placed orthogonal to the beam axis. The single wire resolution is ~80 μm which results in a momentum resolution

$$\frac{\sigma}{p_T} < 10^{-4} GeV^{-1} \cdot p \tag{1.6}$$

To improve the resolution of a chamber beyond the single-wire limit, and to achieve adequate redundancy for pattern recognition, the MDT chambers are constructed form 2×4 mono-layers of drift tubes for the inner station and 2×3 mono-layers for the middle and outer stations. The current induced in each tube is readout independently.

1.6.2.2 Cathode strip chambers

The MDT are not used in the forward regions since due to their length a too high rate is induced. In this region the CSC chamber are used. The CSC are multi-wire proportional chambers with cathode strip readout and a wire spacing of 2.5 mm. The precision coordinate is obtained by measuring the charge induced on the segmented cathode by the avalanche formed on the anode wire. A measurement of the transverse coordinate is obtained from orthogonal strips, i.e. originated parallel to the anode wire, which form the second cathode of the chamber.

The CSC chambers are arranged in 2×4 layers. Good spatial resolution, better than 60 μm, is achieved by segmentation of the readout cathode and by the charge interpolation between neighboring strips.

1.6.3 Trigger system

The trigger system covers the pseudorapidity range $|\eta| < 2.4$. Resistive Plate Chambers (RPC) are used in the barrel and Thin Gap Chambers (TGC) in the end-cap regions as shown in figure 1.10. The trigger chamber for the ATLAS spectrometer serve a threefold purpose:

- bunch crossing identification, requiring a time resolution better than the LHC bunch spacing of 25 ns;
- a trigger with well-defined p_T cut-offs in moderated magnetic fields, requiring a granularity of the order of 1 cm;
- measurement of the second coordinate in a direction orthogonal to that measured by the precision chambers, with a typical resolution of 5-10 mm.

1.6.3.1 Resistive plate chambers

The RPC is a gaseosus detector providing a typical space-time resolution of 1 cm *x* 1 ns with digital readout. The basic RPC unit is a narrow gas gap formed by two parallel resistive bakelite plates, separated by insulating spacers. The primary ionization electrons are multiplied into avalanches by a high, uniform electric field of typically 4.5 kV/mm. Amplification in avalanche mode produces pulses of typically 0.5 pC. The signal is read out via capacitive coupling by metal strips of two types on both sides of the detector. The η–strips are parallel to the MDT wires and provide the bending view of the trigger detector; the ϕ-strips, orthogonal to the MDT wires, provide the second-coordinate measurement which is also required for the offline pattern recognition.

1.6.3.2 Thin gas chambers

The TGC are similar in design to multi-wire proportional chambers, with the difference that the anode wire pitch is larger than the cathode-anode distance. Signals from the anode wires, arranged parallel to the MDT wires, provide the trigger information together with readout strips arranged orthogonal to the wires. These readout strips are also used to measure the second coordinate.

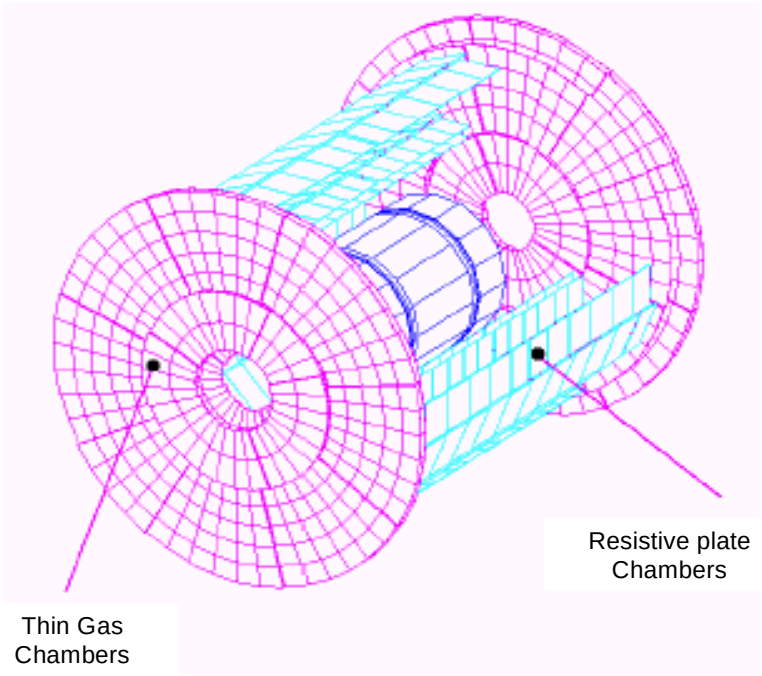

Figure 1.10: *Trigger chambers of the muon spectrometer.*

The TGC are constructed in doubles and triplets of chambers. The inner station consists of one doublet and is only used to measure the second coordinate. The seven chamber layers in the middle station are arranged in one triplet and two doublets which provide the trigger signal and the second coordinate measurements.

To form a trigger signal, several anode wires are grouped and fed to a common readout channel. The number of wires per group varies between 4 and 20, depending on the desired granularity as a function of pseudorapidity.

1.6.4 Alignment

The requirements on the momentum resolution of the spectrometer call for an accuracy of the relative positioning of chambers traversed by a muon track of the order of the intrinsic resolution and the mechanical tolerances of the precision chambers. Over the large global dimensions of the spectrometer, however, it is not possible to stabilize the dimensions and positions of the chambers at the 30 μm level. Therefore, chamber deformations and positions are constantly monitored by means of optical alignment systems and displacements up to ~1 cm can be corrected for the offline analysis.

1.7 Trigger and Data Acquisition System

There are three major systems that enable the coherent operation of the different subdetectors as a single entity, namely the Trigger, Data Acquisition (DAQ) and the Detector Control Systems (DCS). These three system are addressed in the common framework of the TDAQ/DCS project [11, 12]. The Trigger and Data Acquisition Systems are presented firstly. This thesis work is centred on the design and study of the DCS, which will be explained in more detail in the following chapters. The communication between the DCS and the DAQ is described in chapter 2.

1.7.1 Trigger System

The trigger system selects bunch crossings containing interesting interactions. The bunch crossing rate at LHC will be of 40 MHz, and at design luminosity, there will be about 23 interaction per bunch crossing leading to an interaction rate of ~10^9 Hz. The online triggering system will be capable of selecting interesting physic signatures to approximately 100 Hz. Therefore, within seconds the data flow from the detector has to be reduced by a factor ~10^7 while retaining an excellent efficiency for the rate for new physics, such as Higgs boson decays. This is achieved by defining different trigger levels (LVL1, LVL2 and LVL3 also called Event Filter) as shown in picture 1.11.

The LVL1 trigger uses reduced-granularity data from a subset of detectors (muon trigger chambers and calorimeters). The LVL1 trigger accepts data from these detectors at the full LHC bunch-crossing rate of 40 MHz (every 25 ns). At this stage, the subdetectors are treated individually. The latency, which is the time to form and distribute the LVL1 trigger decision, is 2 μs and the maximum output rate is limited to 100 kHz by the capabilities of the subdetector readout systems and the LVL2 trigger.

During the LVL1 processing, the data from all parts of the ATLAS detector are held in pipeline memories of the front-end electronics. The LVL1 trigger must identify unambiguously the bunch crossing containing the interaction of interest and introduce negligible dead-time. The LVL1 trigger decision is based on combination of objects required in coincidence.

Events selected by LVL1 are read out from the front-end electronics systems of the detectors into Read Out Drivers (RODs) and from there forwarded to Read Out Buffers (ROBs). At this states, full granularity and full precision data from most of the detectors is available. To minimize the latency, only data from regions of interest, defined by LVL1, are transferred to the trigger processors. The LVL2 trigger reduces the rate from about 100 kHz after LVL1 to 1 kHz with a latency ranging from 1 to 10 ms depending on the event.

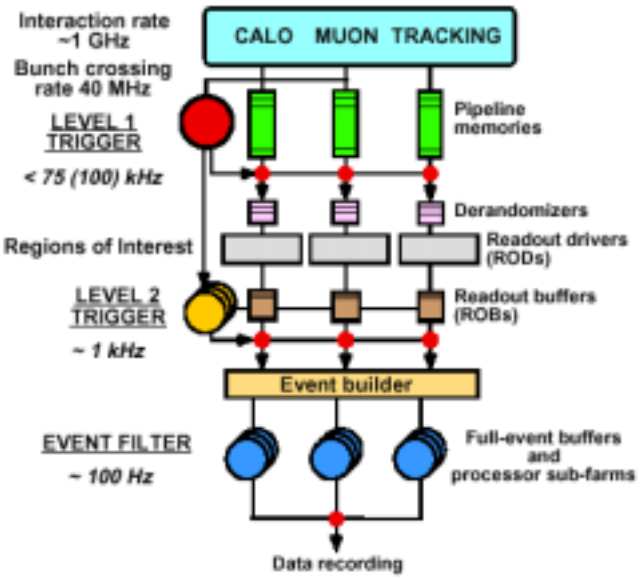

Figure 1.11: *Trigger architecture of the ATLAS experiment.*

All data for the selected bunch crossing from all the detectors are held in the ROBs until the LVL2 trigger takes the decision to either discard the evert or to accept it.

After an event is accepted, the full data are sent to the Event Filter processors via the event builder. The Event Filter trigger uses the full event data together with the latest available calibration and alignment to make the final selection of events for the off-line analysis. At LVL3 a complete reconstruction is possible with decision times up to about 1 s. The Event Filter must achieve a data storage of 10-100 MB/s by reducing the event rate and the event size.

1.7.2 The DAQ System

The DAQ system handles the distribution of data from the ROD to mass storage and the overall monitoring and control of the data taking. For this reason, the system has been factorized in two major components: DataFlow and Online Software.

The DataFlow provides the functionality of receiving and buffering detector data from the ROD, distributing events to the High Level Triggers (HTL) and forwarding selected events to mass storage. These functions are handled by the 4 components of the DataFlow subsystem, namely the ReadOut, the LVL2 DataFlow, the Event Builder and the EF I/O. The ReadOut subsystem receives and buffers data coming from the ROD. The LVL2 DataFlow subsystem manages flow of events and control messages within the second level event selection system. The Event Builder collects all data fragments corresponding to the same bunch crossing from the ROD and

builds a complete and formatted event. The EF I/O passes the events assembled by the Event Builder to the Event Filter and sends the selected events to mass storage.

The online software system controls the overall experiment: it provides run control, configuration of the HLT and DAQ system and manages data taking partitions. This component constitutes the interface point between the DAQ system and the DCS and will be described in more detail in chapter 3.

Chapter 2

The ATLAS Detector Control System

A Detector Control System must ensure the safe and coherent operation of the whole experiment. The ATLAS control system is being developed in the common frame of the HLT/DAQ/DCS project, which also comprises the Data Acquisition and the High Level Trigger systems. The system is based on the experience gained during the design and maintenance of the DCS of the OPAL experiment at LEP, which is described in the first part of this chapter. In the following, the main requirements of the system are presented. The architecture of the ATLAS DCS is described. The internal organization of the different subdetectors is briefly presented and finally, the communication between DCS and external systems and the DAQ system is discussed.

2.1 Introduction

The necessity of an overall Detector Control System (DCS) has arisen with the complexity of the LEP experiments in the late 1980s. Controls are not longer stand-alone systems but part of the experiment which ties physic and technology. Although the experience gained at LEP is an important input to the design of the detector controls, the generation of detectors for the LHC experiments bring further requirements onto the DCS due to the size of the experiments and the hostile environment due radiation and magnetic field.

The DCS must ensure the coherent and safe operation of the equipment and serve as a homogenous interface to all subdetectors and to the technical infrastructure of the experiment. The DCS has to continuously monitor all operational parameters, signal any abnormal behavior to the operator and allow automatic or manual corrective actions to be taken. The system has to provide online status information to the level of detail required for global operation. It is mandatory that, concerning the hardware of the detector, all actions initiated by the operator and all errors, warnings and alarms are handled by the DCS. Also, the interaction of equipment experts with their subdetector should go via the DCS, in order to verified internally,

that the operations requested are safe for the equipment. In safety-critical areas a special interlock system, which is also monitored by the DCS, has to be implemented in parallel. In some cases the usage of uninterruptable power supplies or electricity generators is also foreseen.

Besides the obvious supervision of the subdetectors and the common technical infrastructure of the experiment, DCS must enable a homogeneous way of communication with the DAQ and the external systems, like CERN services and the LHC accelerator.

The DAQ system and the DCS act like the *glue* of the experiment, making all the different integrating systems to work coherently like a whole. Both systems are complementary in, as far as, the first treats all aspects of the physics event-data, which are identified by an *event number*, and the second deals in general with the other data, which is normally categorized with a time stamp. All data of the second type, which are needed for understanding the behavior if the detector and for the subsequent physics analysis, have to be acquired, analyzed and stored by the DCS.

The safety of the personnel is beyond the scope of the DCS and for this, a dedicated system, which the DCS must not influence, will exist.

The ATLAS DCS is influenced by the DCS of the LEP experiment OPAL. The author of this thesis has been collaborating in the maintenance of the OPAL DCS during the last two year of operation of the experiment, which has served him as background on detector controls.

2.2 OPAL

The Omni Purpose Apparatus at LEP (OPAL) [13] has been, together with ALEPH, DELPHI and L3, one of the four particle physics experiments dedicated to the study of the electron-positron interaction at CERN. OPAL has been taking data during the two phases of Large Electron Positron (LEP) operation:

- In LEP1 (1989-1995) the LEP energy was set to the mass of the Z boson, 91 GeV, responsible of the neutral currents of the Electroweak Theory according to the Standard Model (SM). The main purpose of this phase was to measure precisely the production of the Z and its main decay channels (muon, Bhabha, photon pair, tau, neutrino, hadronic, b-quarks, etc.). OPAL was the first of the four LEP experiments in observing the Z boson in 1989.
- In LEP2 (1996-2000) the LEP energy was increased beyond 172 GeV. This is the threshold for production of pairs of W bosons, the charged gauge boson in the electroweak theory. The mass of the W boson is precisely predicted using the SM and LEP1 data, so a direct measurement of the W mass was a powerful check of the theory.

During the last two years of LEP operation, a number of improvements were made for data taking, which increased the Higgs discovery potential, extending the sensitivity of the Higgs boson search to approximately 115 GeV if the data from all four LEP experiments are combined. Approximately 426 pb^{-1} of e^+e^- annihilation data were collected by OPAL in the years 1999 and 2000 at centre-of-mass energies in the range 192-209 GeV. Searches were performed for the "Higgs-strahlung" [14] process,

$$e^+e^- \to HZ \to Hf\bar{f} ,$$

where H is the Higgs boson and $f\bar{f}$ is a fermion-antifermion pair from the Z^0 decay. Only the decays of the Higgs boson into $b\bar{b}$ and $\tau^+\tau^-$ are considered in the analysis: $HZ \to b\bar{b}\, q\bar{q}$ (four-jet channels), $HZ^0 \to b\bar{b}\nu\bar{\nu}$ (missing energy channel), $HZ^0 \to b\bar{b}\tau^+\tau^-$ and $\tau^+\tau^- q\bar{q}$ (tau channels), $HZ^0 \to b\bar{b}e^+e^-$ and $b\bar{b}\mu^+\mu^-$ (electron and muon channels). The results of this search yielded a lower bound of 109.7 GeV on the Higgs boson mass at the 95% confidence level. These results are compatible with those obtained by ALEPH [15] and L3 [16] collaboration. LEP finished in November 2000.

2.2.1 The Detector

OPAL has been a multi-purpose particle physics detector designed to efficiently reconstruct and identify all types of e^+e^- events. The basic features of the detector were the following:

- Tracking of charged particles in the central region of a solenoid coil with measurements of their direction and momentum, particle identification by *dE/dx* and reconstruction of primary and secondary vertices at and near the interaction region.
- Identification of photons and electrons and measurement of their energy.
- Measurement of hadronic energy by total absorption using the magnet yoke instrumented as a calorimeter.
- Identification of muons by measurement of their position and direction within and behind the hadron absorber.
- Measurement of absolute machine luminosity using Bhabha scattering events in the very forward direction with respect to the beam line.

The detector is described in detail in [13]. Its overall layout is shown in figure 2.1.

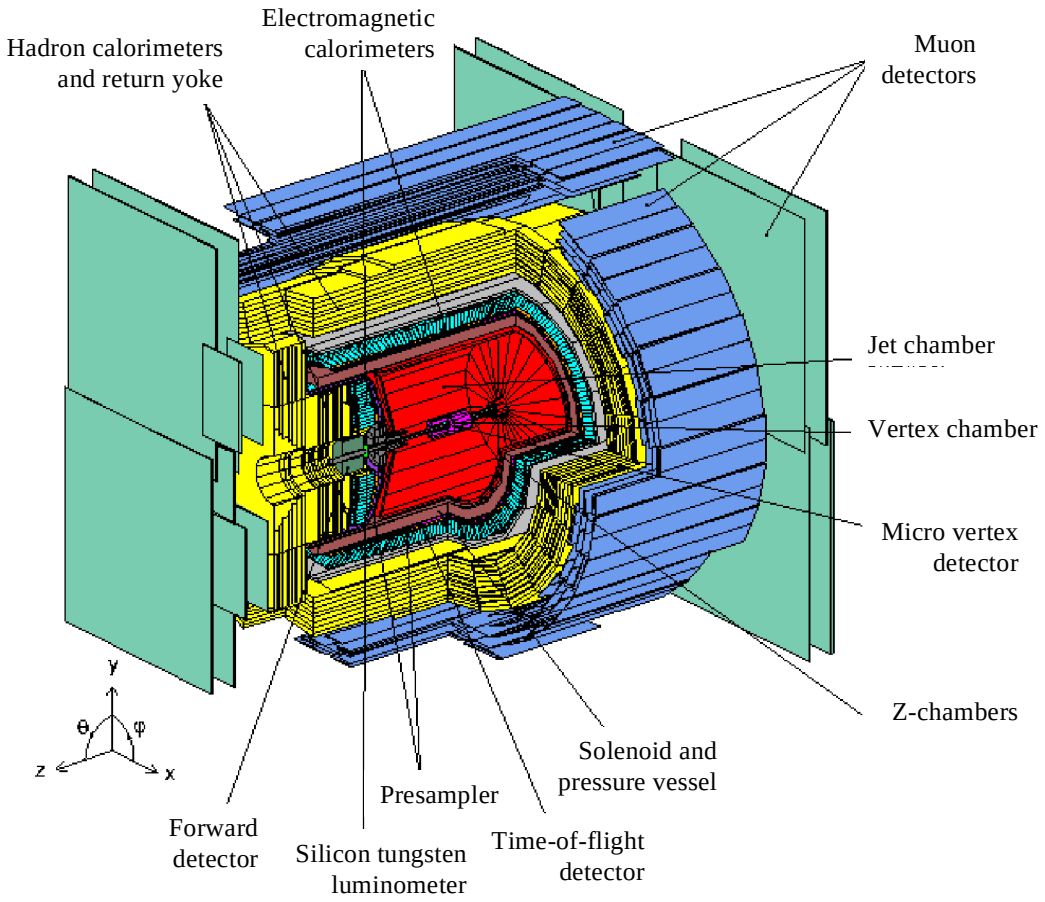

Figure 2.1: *The OPAL detector at LEP.*

The components of the detector are arranged outside the beam pipe, in a layered structure. Particle tracking is performed in the Central Detector. This is a system of three drift chamber devices: the Vertex Detector, Jet Chamber and surrounding z-Chambers, all situated inside a pressure vessel at 4 bar. A solenoid, mounted around this vessel supplies a uniform axial magnetic field for the Central Detector of 0.435 T. Outside of the solenoid, in successive layers is a Time-Of-Flight scintillating counter array. The Electromagnetic Calorimeter consists of a cylindrical array of lead glass blocks. In front of this calorimeter and surrounding the pressure vessel, thin gas detectors (pre-samplers) provide measurement of the position and energies of the electromagnetic showers which start in front of the lead glass.The yoke of the magnet is instrumented with streamer tubes and form the main Hadron Calorimeter. The entire structure is surrounded by several layers of Muon Chambers. The luminosity of the colliding beams was determined by observing the small angle Bhabha scattering processes with the forward calorimeter.

2.2.2 OPAL DCS

Due to the complexity and size of the OPAL experiment, a dedicated control system [17] was implemented to enable a coherent and safe operator of the detector. As the spectrometer was situated 90 m underground, it required continuous monitoring of all operational parameters with the possibility of taking automatic corrective actions in case of failure.

As it was shown above, the detector consisted of several subdetectors arranged hierarchically. The DCS followed the natural partition of OPAL in dedicated partitions plus one additional partition which handled the monitoring and control of the general infrastructure such as power distribution, cooling and gas distribution, called *common controls.* All partitions of the system were built up from standard hardware and software building blocks.

The implementation of the subdetectors local control system was handled by the different members of the OPAL collaboration, following the main requirements defined by the central DCS team. The *common controls* partition also performed the communication with the external system, in particular the LEP accelerator and CERN services, as well as the communication with the Data Acquisition System. In order to facilitate the communication with the DAQ system, the *common controls* partition was included in the DAQ readout stream, making possible to include information of general interest like temperatures, voltages or pressures, directly into physics event record. However, the DCS had a dedicated local database to store, retrieve and view all the variables of the system.

2.2.2.1 Hardware architecture

Each of the 14 subdetectors was controlled and readout by its local system crate (LSC), placed in electronics huts distributed all around the installation. Each control station consisted of VME-based common controls system crate (CCSC) and auxiliary crate (CCAC), interface boxes, a hard disk (60 Mbyte), an Apple Macintosh SE personal computer, which displayed the overall status of the subdetectors, and a line printer. All LSC and CCSC are connected to an Ethernet network.

The CCSC were based on Motorola MC68020 microprocessors, running under the operating system OS-9. This family of processors was adopted from the DAQ system to facilitate the communication between both systems. It had also an Ethernet interface module, a multiplexed ADC (1024 12-bit channels) and two general purpose input/output modules (24-bit bidirectional).

The CCAC was used to connect to the CCSC by means of I/O registers. The signal from all sensors was either an analogue voltage (0-10 V) or the activation of an electrical opto-isolated switch (open/close).

The supervision of the general infrastructure partition was performed by seven VME-based control stations. One of them was placed in the gas building at the surface of the installation, whereas the others were installed in each of the six underground electronics huts. A control station had typically 1000 analogue and 300 digital channels to read.

These LCS allowed to run each partition both locally from the VME station or integrated in the detector hierarchy, via the computer network from a dedicated station installed in the underground control room.

2.2.2.2 Software architecture

The software to control the different subdetectors usually run in the corresponding LSC, although it was also possible to distributed it over different stations interconnected via a LAN. The software was organized in three layers as shown in figure 2.2:

- Human interface: it implemented the top layer and it handled the communication of the control system with the operator. It consisted of a variety of programs providing different functionality:
  - SC_MENU was a menu-driven interface which run on a terminal.
  - Run control was a dedicated data acquisition program, which managed the different partitions of the system and prepare the detector for data-taking according with the configuration chosen by the operator from a predefined list.
  - SC_ALARM displayed warnings and alarms for the whole system.
- The bottom layer was formed by the applications acting directly on the front-end equipment, for instance, performing control loops or reading the ADC channels of the CCSC and comparing these with the nominal values for later triggering of warning or alarms in case of discrepancy.
- The middle-ware comprised the following 4 main C programs needed for the communication of the layers described above:
  - **SC_PROC**, which started and supervised all programs in this layer.
  - **SC_FILTER**, which accepted commands from the human interface layer, checked their validity an triggered an appropriate application of the bottom layer.
  - **SC_ROUTER,** which informed to the relevant application about the state of the command issued.

- **SC_ERROR**, which logged and transferred unsolicited output of the application programs like errors.

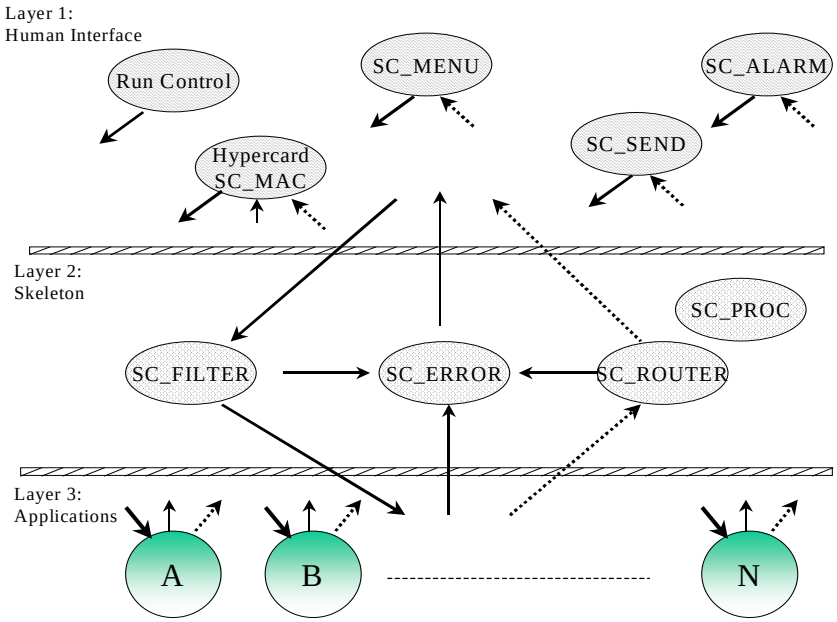

Figure 2.2: *Software architecture of the OPAL DCS.*

2.2.3 Conclusions

The OPAL control system design had a layered architecture to achieve modularity. This made possible to run the same software in many places and to enable a very easy implementation of user-written application programs. The system was easily extendable.

The architecture chosen made possible the control in a coherent way of all the subdetectors as a Finite State Machine (FSM), despite their diverse nature, of the common infrastructure and of the safety parameters.

The system was ready on time and proved to be both user-friendly and robust. It was successfully operated in a reliable manner for 12 years. A key element in this successful implementation, was the right selection of the building blocks since the beginning of the implementation. Contrarily to the other LEP DCS systems, the OPAL system had not to undergo a major upgrade. Only the microprocessors were replaced by a more powerful model of same family.

However some drawbacks of the system were identified. The main issue was the lack of a proper database, which was not available under the operating system OS-9. Another problem was the lack of standardization in many areas (e.g. different programming languages were employed) and the use of custom hardware or

protocols, the maintenance during the lifetime of the experiment was, in same cases, difficult. Another problem faced was the update to make the system *y2k* compliant.

For these reasons, OPAL constitutes a precious background in the implementation of detector controls. Many of the design, architectural and operational concepts will guide the ATLAS DCS as it is shown in the following.

2.3 The ATLAS DCS Architecture

The Detector Control System is addressed in the frame of the HLT/DAQ/DCS project, which also comprises the Data Acquisition and the High Level Trigger systems. A detailed description of the project architecture can be found in [12].

The ATLAS DCS is a collaboration between CERN, NIKHEF (Amsterdam, Holland), and the PNPI (San Petersburg, Russia) groups. The system is being developed in the frame of the Joint COntrols Project (JCOP) [18] at CERN, which aims at providing common solutions for the implementation of the DCS of the four LHC experiments.

2.3.1 General requirements

The ATLAS Detector Control System [19] provides complete control over all subdetectors, all infrastructure and services, and all interactions with the LHC machine. All operator actions on the detector will be through DCS. Similarly, the presentation of all error messages, warnings and alarms to the operator will be notified by the DCS. The protection of the apparatus is the responsibility of each subsystem. The status of such protection must, of course be monitored, by the system. A set of generic requirements of the DCS has been defined and described in the User Requirements Document [20]. The DCS performs the following tasks:

- parameter monitoring, loading, logging and setting
- online status display
- issuing of commands for certain actions (mostly operational)
- correlating parameters from different parts of the detector.
- collaborating with the DAQ system via the Run Control layer.
- control calibration and alignment processes
- supervising the safety of the detector in collaboration with the Detector Safety System (DSS)
- triggering alarms, emergency procedures, etc.
- Handling of error messages.

As a general rule, based on experience at LEP and other collider detectors, a monitoring cycle of about one or two seconds for a particular parameter is normally sufficient. Two successive readings of a bad status or values are required to trigger an alarm.

The essential features of the ATLAS DCS are reliability, robustness, scalability and modularity since the system will have to operate continuously regardless the status of the DAQ system and its configuration will undergo modifications and extensions throughout the lifetime of the experiment.

The ATLAS spectrometer presented in the previous chapter, consists of three major subdetectors, built in a number of institutions in different countries, resulting in a wide range of hardware types. Given the diversity of equipment and the large number of people from different groups that are responsible for its operation, a basic goal is to design a homogeneous system with an uniform architecture. Therefore the DCS promotes standardization across subsystem boundaries.

Due to the decomposition of the ATLAS experiment into subsystems, the DCS will also follow this partitioning into independent control and monitoring applications in charge of single subdetectors or subsystems. These systems need to be operational well before the installation of the subsystems to aid in the checkout and the subsequent commissioning of the subsystems. The DCS is structured to allow the evolution from small stand alone systems to fully integrated operation of the whole detector. Each of these subdetector control applications will also use common system components such as a global database, an error reporting and logging system, and the DCS software to control and monitoring actions on the physical devices.

It is also necessary to provide control applications which are one level higher in the control hierarchy to allow the operation of the experiment as a whole. It should also be easy to adapt the system to reflect changes in the control hardware and accommodate new functions corresponding to operations of new types of devices. For these reasons, the DCS should be modular and be composed out of well defined building blocks, both of hardware and software. Modularity and standardization of components will satisfy the individual requirements for each subdetector, while assuring the coherency and homogeneity of the system.

2.3.2 Organization

The DCS of the ATLAS experiment will allow a hierarchical consolidation of the participating systems to obtain a fully integrated and coherent detector operation. This will be achieved by the definition of system layers and clear interfaces between them. At the same time, the implemented DCS architecture has to be flexible to satisfy the real-time requirements of individual subdetectors. Subdetectors will

continue to be able to access their equipment independently from other subdetectors for maintenance, upgrading and debugging. From the point of view of controls, the detector is composed of largely independent units, organized in a tree-like structure of many levels as shown in figure 2.3.

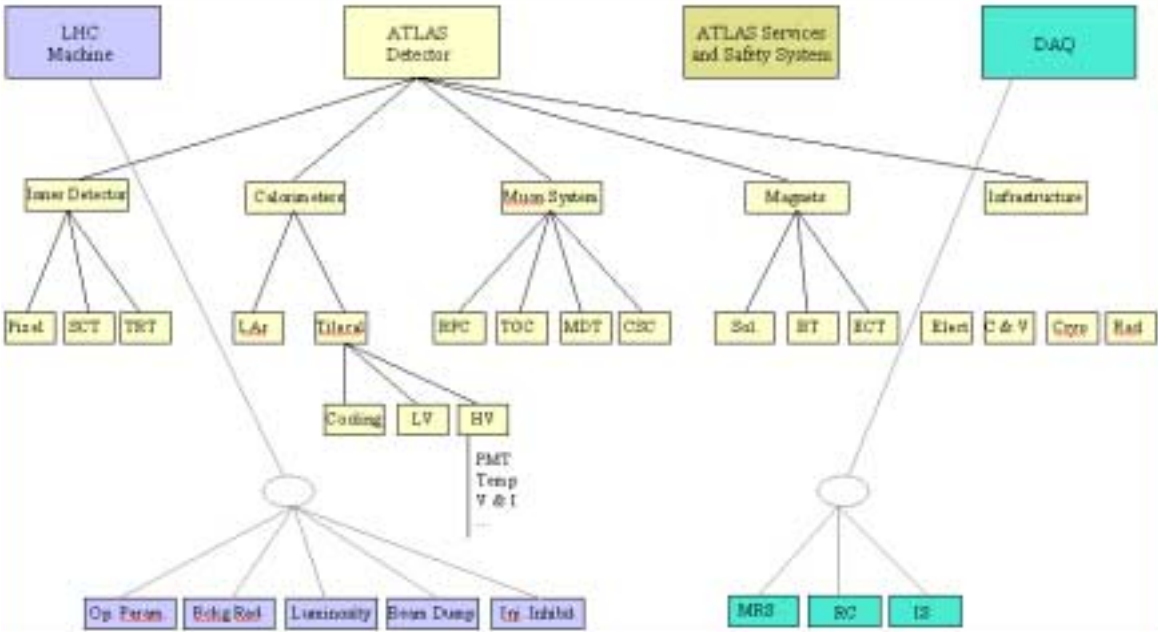

Figure 2.3: *Hierarchical organization of the ATLAS DCS.*

The highest level of this structure consists of the 3 subdetectors described in the previous chapter. The control of the magnets and of the common infrastructure of the experiment like electronics crates, racks and cooling is also placed at this level. Each subdetector is subdivided in further units. This subdivision varies depending on the subdetector and it is suggested by either functional (e.g. gas system, high voltage system), topological (e.g. end cap, barrel), or organizational reasons (e.g. groups from different countries). As these units will be constructed at different places around the world, they need to be controlled in a stand-alone manner first.

The architecture will, therefore, be based on partitioning into self-contained subsystems, which can be separately developed, maintained and operated. It is important for design of the control system, that the main information flow, both data and commands, is normally only vertically. Horizontal communication between subsystems will consequently be minimized.

The clear vertical separation and hierarchical structure of the system should also allow implementing of a single user interface to the experiment. The operation has to comprise the full range from global operator interaction to detailed expert interactions.

2.3.3 Structure of the DCS

The architecture of the DCS and the technologies used for its implementation are strongly constrained by environmental and functional reasons. The DCS consists of a distributed Supervisory Control And Data Acquisition system (SCADA) running on PCs and called Back-End (BE), and of the Front-End (FE) systems.

The name SCADA indicates that the functionality is two-fold: It acquires the data from the front-end equipment and it offers supervisory control functions, such as data processing, presenting, storing and archiving. This enables the handling of commands, messages and alarms.

The DCS instrumentation consists of a wide variety of equipment, from simple front-end elements like sensors and actuators, up to complex computer systems that are connected to the SCADA stations by means of standard fieldbuses. A SCADA Real-Time (RT) database contains records of all equipment where the data values are stored.

The DCS architecture will have to model the organization of the experiment described in the previous section. It will be distributed with computing power divided into three logical layers: *supervisory*, *control* and *process* layers. The SCADA component will be distributed on the two first layers while the front-end equipment will be in the process layer. This layered structure follows the geographical distribution of the equipment in three different areas as shown in figure 2.4. The actions on the operator timescale are performed at the upper level, while the RT operations are performed at the lower layers.

- **Process Layer:** The Front-End (FE) electronics in UX15 (see figure 1.3) is exposed to radiation and to strong magnetic field. The instrumentation in the cavern must be radiation-hard or tolerant to levels of 1–10^5 Gy per year in the muon subdetector and inner tracker, respectively. In addition, depending on the location, a magnetic field of up 1.5 T has to be tolerated.

  The equipment at this level consists of controllers, which connect to the hardware, either as separate modules or as microprocessors incorporated in the front-end electronics. Field instrumentation like sensors and actuators will be of various types and it will be tributary to the requirements for the detector hardware. In all cases, the interfaces to the control equipment will follow well-established electrical standards like 0-10 V for voltage interfaces or 4-20 mA for current loop interfaces. Where this is not possible for technical reasons, signal conditioning interfaces will have to be added for the connection to the control stations.

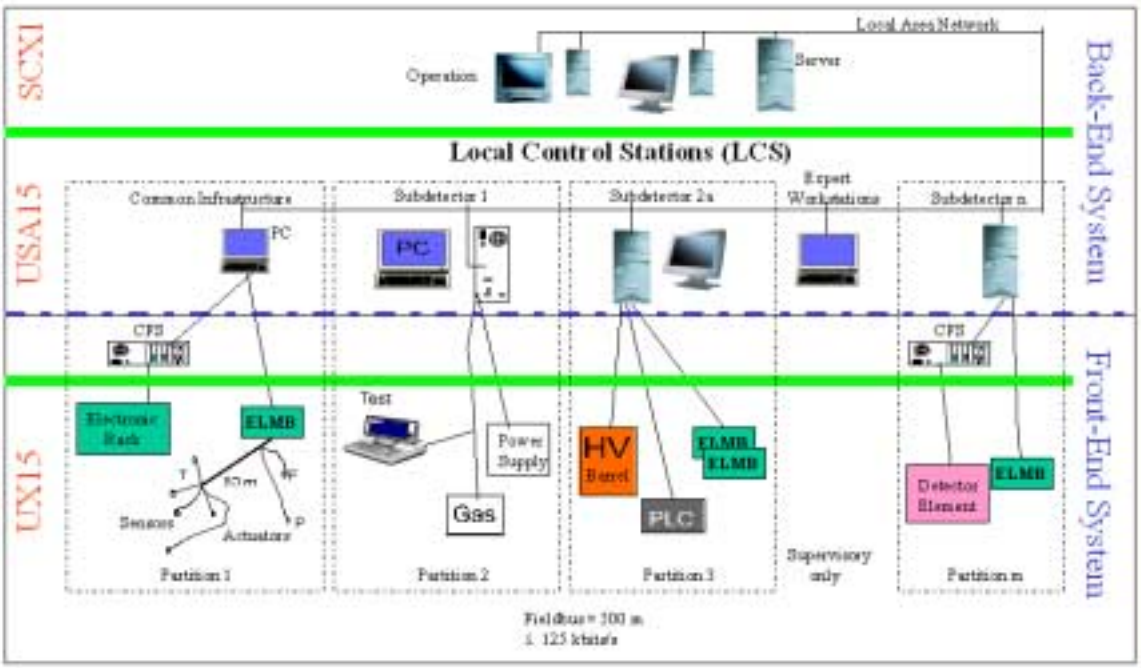

Figure 2.4: *ATLAS DCS architecture.*

This equipment is distributed over the whole volume of the detector with cable distances up to 200 m. The distribution underground is governed by two conflicting constraints. Because of the radiation level, the magnetic field and the inaccessibility at UX15 during beam time, the equipment should be located in USA15. However, complexity, cost and technical difficulties of cabling suggest condensing the data in UX15 and transferring only the results to USA15.

Hardware interlocks of components will be implemented wherever needed. This is the case, for example, for automatic switch off of the front-end electronics of the pixel detector in case of problems of its cooling system, or for automatic ramp-down of high voltages in presence of over-currents. The operation of interlocks must be ensured even in the case of power failure and therefore most of the interlock systems have to be fed by Uninterruptable Power Supplies. Remote sensing and actuator equipment at the detector level and in the electronics crates and ancillary equipment, such as safety and general electricity, will be connected directly to one of the proposed standard buses or via suitable interface modules. The field buses will be interfaced to the dedicated controller stations of the layer above.

- **The control layer:** The process equipment will be interfaced, via fieldbuses, to multipurpose front-end computer equipment and Programmable Logic Controllers (PLC) compliant with the relevant recommendation given in [21]. The equipment of this layer will be installed in the underground electronics room USA15, which is accessible, and it will consist of:

- Workstations, foreseen for subdetector experts for the supervision of individual partitions, mainly during commissioning and maintenance periods.
- Dedicated stations that control the equipment running real-time operating systems, usually distributed around the installation. It is foreseen to use a dedicated control computer for each detector. In this context, a controller station is not necessarily a single computer but can be clustered if a high channel count or the heterogeneity of the equipment leads to this requirement. These systems are called Local Control Stations (LCS) in figure 2.4 and they will run the SCADA software collecting data from the front-end devices in their partition. The LCS allows to run a partition either independently in standalone mode or integrated as part of the whole detector.
- Depending on the complexity of the subdetectors, it is envisaged to introduce a further grouping at the level of the controller stations. Whenever convenient, like in case of large number of field instrumentation channels to be controlled, VME-based controllers may be used. This non-SCADA Complex Front-end Systems (CFS) are dedicated to a specific task. An example is the alignment system of the muon subdetector, where a dedicated processor reads the images of CCD cameras and calculates the alignment constants of the individual chambers. The CFS are normally connected to LCS over a dedicated Local Area Network (LAN). CFS can also be placed in UX15 if they support the hostile environment.

• **Supervisory layer:** The equipment of this layer will be installed in the main control room in building SCX1 at the surface of the installations. This area will always be accessible to the personnel. The equipment will consists of general-purpose workstations, which will be linked to the control layer through a LAN providing TCP/IP communication.

  The workstations will retrieve information from the LCS of the different partitions and can be used to interact with them by means of commands or messages. The system will only provide a limited set of macroscopic actions to generate the sequence of operations necessary to bring the experiment to a giving working mode. In addition the system will monitor the operation of the sub-systems, generate alarms and provide the interlock logic where necessary.

  This layer is also responsible for the dynamic splitting of the experiment into independent partitions and the possibility of concurrent data taking from the partitions. Nevertheless, the direct access to each sub-system in order to gain detailed information and control will always be possible through the dedicated MMI. However, the detailed actions will be executed by the sub-systems.

  This layer represents the interface point with the DAQ, magnet and safety system and the LHC accelerator. Information for these subsystems will be used to build the overall status of the experiment.

Access from remote locations will also be provided subject to that proper access authorization.

2.3.4 Subdetectors organization

All the subdetectors in ATLAS will have their own local DCS with a minimum of one Local Control Station per subdetector. The detailed architecture of these systems strongly depends on the structure of the general DCS system of the ATLAS experiment and on electrical architecture and mechanical issues of the subdetectors.

Each local DCS controls and monitors the operation of a subdetector and related equipment. These systems are needed to monitor both fast and very slow variations in important detector parameters, and to take appropriate corrective actions to maintain the required level of detector parameter stability important for reliable performance. Additionally, they must provide all the functionality needed for stand-alone operation during the construction, testing, commissioning and calibration of the subdetectors. The plan is to have ready all subdetectors DCS by early 2004, when installation starts.

Although each subdetector is responsible for the implementation and for the internal organization of the subsystems, they must fully conform to the requirement defined in the ATLAS DCS User Requirements Document [19]. The DCS of the subdetectors must follow the general ATLAS DCS system architecture as much as possible unless there are special reasons where the subdetectors need tailored solutions. By conforming to the general DCS structure the system of the subdetector will be easy to maintain in the future by any DCS expert.

The communication between the general DCS and the subdetectors must be bi-directional. Information regarding to the status of the different subsystems must be transferred to the general DCS and then be used to present to the user the overall status of the experiment. On the other hand, the DCS system will perform common tasks to all subdetectors, like the monitoring of the environment. The overall system has connections to centrally provided services: the Global DCS, the Central Safety System, the DAQ system and the LHC machine control system. This information must be known to the subdetectors for their operation, e.g. environmental parameter like the barometric pressure, room temperature or humidity, must be known to the subdetectors for reason of mechanical stability.

The central DCS team defines the standards to be followed and provides the tools needed for its implementation like the high level SCADA software, LCS interface boards for connection with a fieldbus or general-purpose front-end equipment, which will be common to all subdetectors. The DCS of the subdetectors can meet the main stream of the overall DCS at different points of the hierarchy described in the previous section. The general DCS also aims at providing common solutions for

histogramming, trending, error reporting and alarm handling. This guarantees a unique data and command flow with the overall DCS and provides standardization amongst the ATLAS subdetectors leading to a homogeneous and coherent system.

A detailed description of the implementation of the different systems can be found in the respective Technical Design Report of the subdetectors. In the following the main requirements and the internal organization are listed.

2.3.4.1 Inner Detector

The ATLAS Inner Detector (ID) incorporates three subdetectors as described in section 1.4. From the point of view of controls these subdetectors are very different and have specific requirements. The pixel detector has a very high power density across the active area which needs a sophisticated fast interlock system between power supplies and the cooling system. The Semi-Conductor Tracker (SCT) covers a large area with silicon detectors which have to be very stable and well aligned. The Transition Radiation Tracker (TRT) is a gaseous detector with the controls of the gas system closely coupled to the high voltage system.

These subdetectors have to be operated in a high radiation environment inaccessible for servicing during long periods. Most monitoring can be done in a more friendly environment outside the SCT detector where the services are generated. For monitoring in the high radiation environment inside the ID, the aim is to have as few complex active elements as possible but the choice of technique also has to take into account the amount of material which will be introduced into the tracker.

Pixel detector

The pixel detector consists of 1750 individual detector modules (the sensor itself which is further equipped with 16 readout chips and a module controller chip). Each module has an optical link for the data transfer. From the DCS point of view a detector module is the smallest unit the DCS can act on. This modularity is determined by the different levels of radiation in the detector which rises the need of different voltages and currents to be applied to the different parts of the detector and by the amount and thickness of the cables needed.

From the controls point of view, the main components of the pixel detector are the cooling system and the power supplies which feed all units of the detector [6]. Additionally the boards, where active components will be located (like opto board and patch panel 2), require monitoring of their related quantities (like voltage and current of the regulators), loading of parameters through single serial links and a connection to this interlock system via the logic unit.

The control system of the pixel detector will map the hierarchical organization of the detector, described in the previous chapter, using a geographical approach. This organization is shown in figure 2.5.

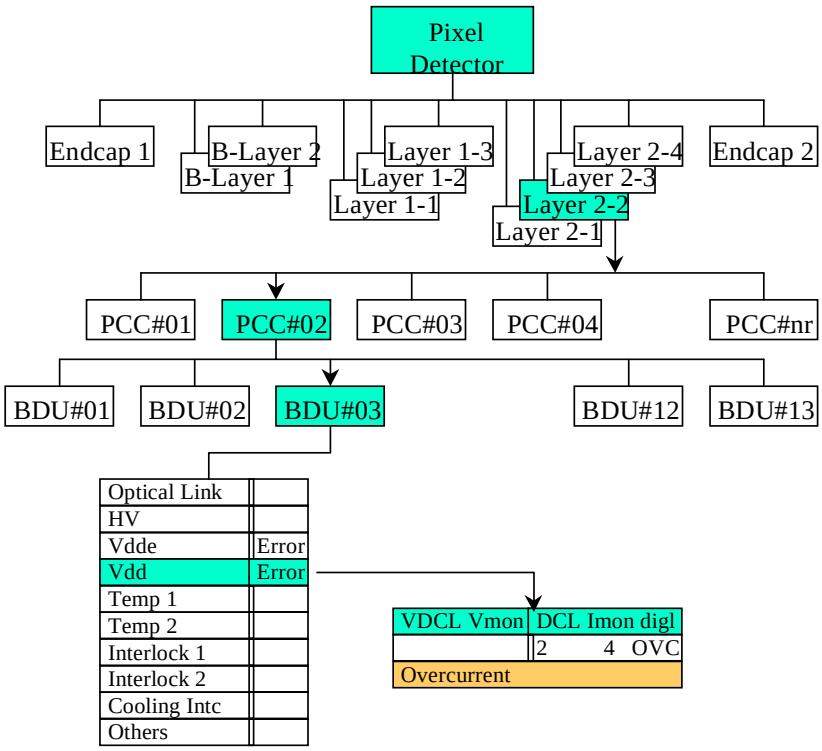

Figure 2.5: *DCS organization of the Pixel detector.*

The top level of the pixel DCS hierarchy consists of the pixel detector itself and it handles the communication with the overall DCS main data stream and possibly with other pixel-specific applications. It accepts commands from the ATLAS DCS passing them to the lower levels in the hierarchy. Level 1 and 2 consist of the barrel 1 and 2 and the B-layer of the pixel detector. The lowest level is given by the base detector unit (BDU) built by one or two detector modules. Such an hierarchical structure helps the operator in tracing of problems, as all relevant for a detector unit can be seen in one glance.

cooling

As the pixel detector is very sensitive to heat ups, each module is equipped with an on-board NTC resistor for temperature monitoring and read out independently of the data acquisition system. The cooling systems is shared with the SCT detector and is being designed to evacuate 0.7 W/cm^2. This system is controlled and supervised by a dedicated LCS running SCADA.

Power

It is planned to use commercial power supplies. The system will be able to take decisions autonomously, not relying on the functionality of a network and reducing the field-bus traffic in order to improve the safety of the detector.

Interlocks

A dedicated thermal interlock acting on the power supplies will be implemented to avoid damage to the detector in case of temperature increase due to the harsh radiation environment to which the pixel sensors are exposed. The interlock box acts in case of failure of the DCS software. This is a pure hardware solution capable to operate in stand-alone mode or integrated within I/O modules. The signals from the NTC sensors is compared to some given thresholds and sets, in case of large discrepancies, a 2-bit logical signal. It can disable the power to either all or to a single module.

SCT detector

Although contrarily to the geographical approach followed by the pixel detector, the subsystems are organized attending to a functional criteria, a logical hierarchical structure is built on the top of the functional blocks to be presented to the user. The system split into three partitions: cooling, power and environment and alignment. This allows the parts to be run autonomously in the commissioning phase. The alignment and cooling systems are run in stand-alone mode with no direct electrical contact to the detector modules whereas the power is directly linked to silicon detector modules. The organization of the local DCS [5] is shown in figure 2.6. Information from these partitions is presented to the user in a logical tree-like structure built in SCADA. This arrangement models the detector organization:

- SCT detector
- section: a cylinder in the barrel or a disk in the forward detector, which can be operated as a unit.
- sector: a stave of the barrel layer or a part of the disk which can be operated autonomously
- module: silicon sensors with hybrids and readout electronics, which constitutes the smallest part of the detector.

The DCS of the SCT has one main Local Control Station (LCS) although it can be split on several LCS if this improves flexibility in the commissioning phase, and several Satellite Control Stations (SCS). The communication between the LCS and the different SCC will be handled internally by the SCADA software. The SCS connect to other components of DCS via interface cards. The LCS is the interface

module between the general DCS running the SCADA software and I/O modules or PLC.

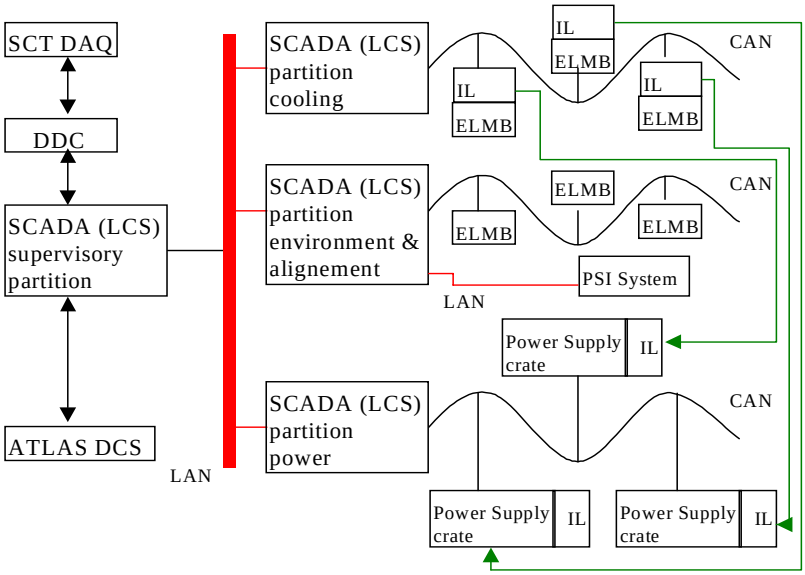

Figure 2.6: *DCS organization of the SCT detector.*

Environment

The environment partition will handle the monitoring of temperatures, humidity, barometric pressure and radiation levels inside the thermal isolation of the SCT subdetector. These data are needed for the alignment system. Since grounding and shielding are very complicated, temperature sensors (NTC) located close to the readout electronics have their own current source. This partition also contains a highly autonomous subsystem monitoring the alignment of the SCT.

cooling

The cooling system will control everything from compressors to regulation of mass flow in cooling pipes. The SCT will interface to the cooling system by monitoring temperatures on cooling pipes and by reading status bits of the cooling plant. Platinum thermal resistor sensors will be used giving a relative precision better than 0.2 °C and the corresponding absolute precision will be better than 0.5 °C.

Power

Like the pixel tracker, the power system will control and monitor the High Voltage and Low Voltage supplies. Each of the 4088 silicon detector modules in the SCT will have independent supplies. The monitoring of voltages and currents is done at the power supplies and a precision of about 2.5% of the nominal value is expected. As

for the case of the pixel detector, the power cables have leads for bringing the signals of the probes to the readout boards outside the high radiation environment.

Interlocks

As in the case of the pixel detector, an interlock at the level of software and hardware between the cooling system and the power supplies is also needed. The interlock will operate on all voltage supplies of the SCT subdetector simultaneously. The interlock system will have its own monitoring sensors connected to a hardware logic for fast response. Monitoring sensors for both hardware and software interlocks are separated. The algorithm for the software interlock can be more complex than for the hardware interlock but the reaction time is slower. The software interlock can switch off a limited number of power supplies being a section of the SCT the smallest part it will be operated on. There will be a second interlock system between the optical readout of the DAQ system and the power supplies.

TRT

The TRT detector is a gaseosus detector implying very specific features from the point of view of controls with respect to the silicon trackers. The local DCS [5] will be split according to the geographic positions of the different components of the detector to be controlled. The DCS subsystem of the TRT subdetector are the following:

- Temperature measurement system
- Gas system
- Power system
- cooling system
- Electronic racks control system
- Interlock system

The overall view of the system is presented in figure 2.7. Two Local Control Station Crates will handle the entire system. One will be installed on the surface, while the other will be placed in the service cavern USA15. They contain interfaces to the controllers of the TRT subsystem electronics, I/O registers for less complicated tasks and the CPU which holds the operating system and runs the monitor and control software. The LCS are connected together via a LAN on which Global DCS communications also take place.

Temperature measurements

The temperature has influence on the stability of the mechanical structures of the detector, on the stabilization of the response of the detecting elements, on the electronics lifetime and safety, and on the cooling system for an efficient cooling and control of gradients.

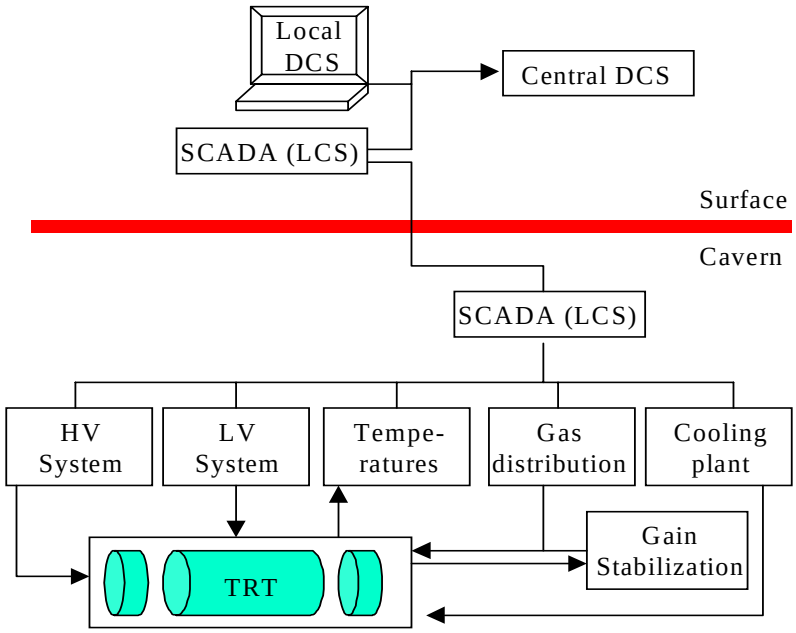

Figure 2.7: *DCS organization of the TRT detector.*

The temperature of the gas will be monitored to ±0.5 ^{o}C and that of the front-end electronics to ±2.0 ^{o}C. Standard resistive temperature sensors (PT-100; PT-1000) with two-wire readout (due to the limited number of lines) will be used. Some temperature sensors will supervise the cooling system inside the detector while others will monitor services outside the volume, including electronics racks, power supplies, the cooling system and gas systems.

Gas system

Fully stand-alone operability of the of the gas system is necessitated for the correct performance of the detector. The role of the TRT DCS is to serve both, as a supervisor and as a platform where information is collected and correlations are performed. The system will monitor and control the quality of the gas mixture and its distribution as well as the operating conditions (flow, pressure and status of the hardware) at different points of the system.

Power Systems

As for the rest of the applications, the usage of commercial HV power supplies is envisaged in the TRT detector. The system is also needed for calibration purposes of the subdetector. The gas system controls are interfaced via software to the high voltage system where the gas gain stabilizing function takes place. The system tunes the values of the high voltage applied to the straws to maintain constant gas amplification in a changing environment.

Cooling system

The entire volume of the TRT detector has to be kept at a constant temperature of about 25 ^{0}C. To fulfil this requirement, heat produced inside the detector due to the front-end electronics and the ionization avalanche current in the straws of the detector, has to be efficiently removed.

The cooling system uses two cooling fluids; gaseous CO_2 for cooling and ventilation of the TRT end-cap detectors, and water which removes heat from the gas and cools both front-end electronics and barrel detectors.

Interlocks

The interlock system plays a very important role in safety of detector operations. Many different failure modes require urgent intervention. The following hardware interlocks will be implemented and monitored by the local DCS of the subdetector:

- General Safety System (GSS) interlock to the power and gas systems: The status of the gas system should be tied to the detector safety interlock, which, in case of unpredictable behavior, uncontrollable parameter drift or any predefined emergency condition would activate detector shutdown (high voltage, low voltage etc.)
- HV power supply system to Gas System and Detector cooling systems: the HV has to be interlocked with the gas system to ensure safety of the detector. Most likely this has to be ensured by hard-wired means to allow the detector to be safely shut down.
- LV power supply system to Electronics cooling system

The HV and LV systems will also be interlocked to the temperature measuring system, although this interlock might be executed via software only.

2.3.4.2 Calorimeters

LiAr Calorimeter

The detector control subsystem for the liquid argon calorimeters [7] is mainly concerned with the following tasks:

- monitoring of the detector mechanics in both position and stress
- monitoring of subdetector conditions like temperature, pressure or purity of the argon liquid
- monitoring and control of electronics and functional parameters like high and low voltages, status signals
- monitoring of safety relevant parameters.

Figure 2.8 shows the different DCS subsystems of the LiAr calorimeter.

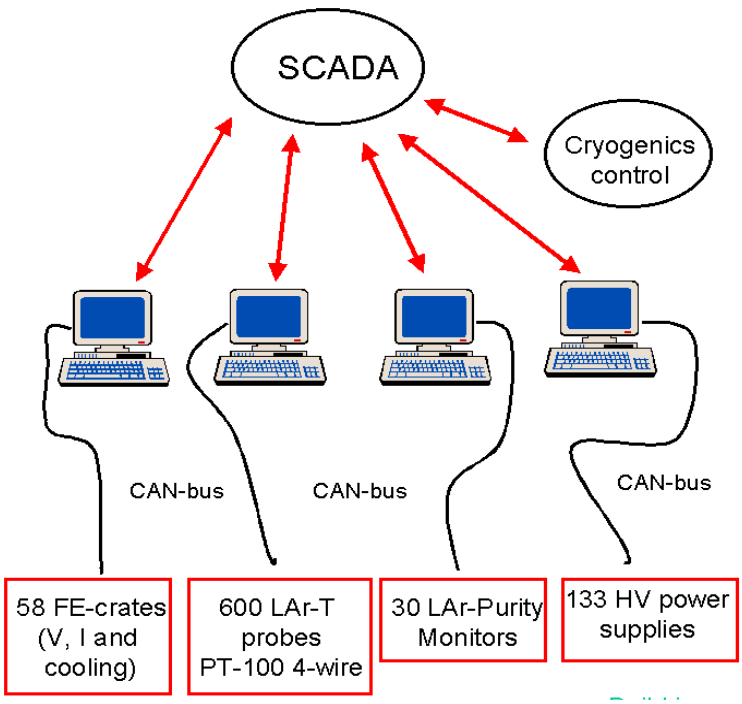

Figure 2.8: *DCS organization of the LiAr calorimeter.*

The monitoring of the proximity cryogenics (gas levels, gauge valves, pressures, temperatures) and cryostat conditions (temperature and vacuum level of the feedthroughs) will be performed with a standalone PLC-based system. This part is essential to the good functioning of the LiAr calorimeter and implies many different elements to be monitored and regulated like gas levels, pumps, valves, pressures, temperatures (both cryostat and feedthroughs). In particular, the temperature

information is essential and must provide good resolution to allow for a precise regulation. The monitoring and regulation have to be performed constantly. Information exchange via software needed between the local DCS and this system is needed for the safe operation and performance of the calorimeter.

Strain and Position

Monitoring of the position and stress on the cryostat during cool-down, warm-up, filling and emptying, are of crucial importance for the safety of the experiment.

The monitoring of the stress of the components of the calorimeter will be done with probes consisting of standard Ni/Cr resistors laid on kapton foils, whose resistance varies with the applied stress.

Position measurements are required to control the calorimeter centricity with respect to the cryostat inner vessel, and the position of the front face. They will be performed using a Low Voltage Differential Transformer, which delivers a current proportional to the displacement. The range of distances to be measured is of the order of 10 mm, with an accuracy of measurement better than 0.2 mm at room temperature and at liquid argon temperature of -186 °C.

High Precision Temperature Probes

The main requirement on the temperature measurement comes from the physics performance of the calorimeter. The response of the liquid argon calorimeters depends on the temperature and varies roughly by 2% per Kelvin. In general there are several heat sources in the cryostat: the cryostat walls, the suspension clips of the internal cryostat parts, the electrical cables and the ionizing radiation of the beam. The heat produced by these sources is taken away using liquid nitrogen heat exchangers. In addition, the temperature monitoring allows to prevent large deformations of the cryostat due to temperature gradients during cool-down and warm-up in different parts of the calorimeter.

The temperature sensors will be distributed inside the cryostat in such a way that their distance is small enough to guarantee a sufficiently precise temperature map of the calorimeter. The temperature gradients inside of the cryostats will be monitored by 600 PT-100 probes, which are connected by a 4-wire readout. The accuracy needed to preserve the energy resolution of the calorimeter is around +-50 mK.

LiAr Purity Monitor

The control and monitoring of the purity of the liquid argon is essential to understand the response of the detector and to identify accidental pollution of the liquid. The signal of drifting electrons in liquid argon decreases by recombination and by the attachment of electrons to electronegative molecules like O_2, called *impurities*. While the mean recombination rate is constant for a fixed electric field

and geometry, the electron lifetime has to be monitored since a possible change affects the resolution of the calorimeter.

Two different types of purity measuring devices will be implemented in ATLAS: the so-called α- and β-chambers. In the α-chamber, strongly ionizing α-particles from an ^{241}Am source produce electron ion pairs in the liquid argon within approximately 200 µm in front of the cathode. The electron charge drifting in the electric field induces a signal on the anode which is converted into a voltage signal by a charge sensitive preamplifier. The β-chamber exploits the fixed energy of the conversion electrons from a ^{207}Bi source mounted on the cathode to produce an approximately 3 mm long track of electron ion pairs. A laser chamber, which is able to measure directly and simultaneously the electron lifetime and the drift velocity, serves for an initial calibration of the source based monitors. There will be a total of 30 monitors distributed over the 3 cryostats and one laser chamber per cryostat.

The monitoring has to be performed every few minutes. The read-out of these monitors is done via special digitizing boards, where the amplitude is histogrammed as well. These histograms and the control of the system is done via a CAN-SLIO (Serial-Link-IO) interface. This readout will use dedicated CAN-Bus cables.

HV Modules

The voltages and currents of the low- and high- voltage power supplies have to be monitored constantly. The equipment chosen by the LiAr calorimeter group, has a built-in CAN-interface, which is used to control and monitor the voltage/current of each of the individual channels. About 130 HV modules with 32 channels each, are needed to operate the LiAr calorimeter.

Front-End-Crate Monitoring

The LiAr calorimeter has a total number of 58 FE-crates. A total of 6 voltages and currents, 6 temperature probes measuring the temperatures of the cooling water and a number of flowmeters will have to be monitored for each front-end crate. The front-end crates need to be interlocked to the cooling system in order to shut-down the electronics if a possible failure of the cooling system occurs, and to the power system to detect possible over-voltages or over-currents.

Tile Calorimeter

The detector control system of the Tile Hadron Calorimeter is described in detail in chapter 4. A first attempt to integrate the different DCS subsystem of this detector has been performed in the last testbeam period in summer 2001, where part of the calorimeter modules have undergone the calibration with particle beam.

2.3.4.3 Muon Spectrometer

The muon DCS equipment [9] comprises the services for the four integrating detectors and the alignment systems, namely RASNIK and MPA–ALMY, which supply the precision alignment and position monitoring.

Contrarily to the Inner Detector where the three integrating subdetectors have different DCS requirements, the subdetectors forming the muon spectrometer present common needs and can be arranged in the same manner from the point of view of controls. Figure 2.9 shows the overall organization of the DCS systems of the muon spectrometer, which comprises the following elements:

- Gas system
- Temperature monitoring
- Power system of the detector and front-end electronics
- cooling
- Alignment

Environment monitoring in terms of radiation level in the vicinity of the detector, magnetic field using Hall probes, humidity and commonly provided services is also required.

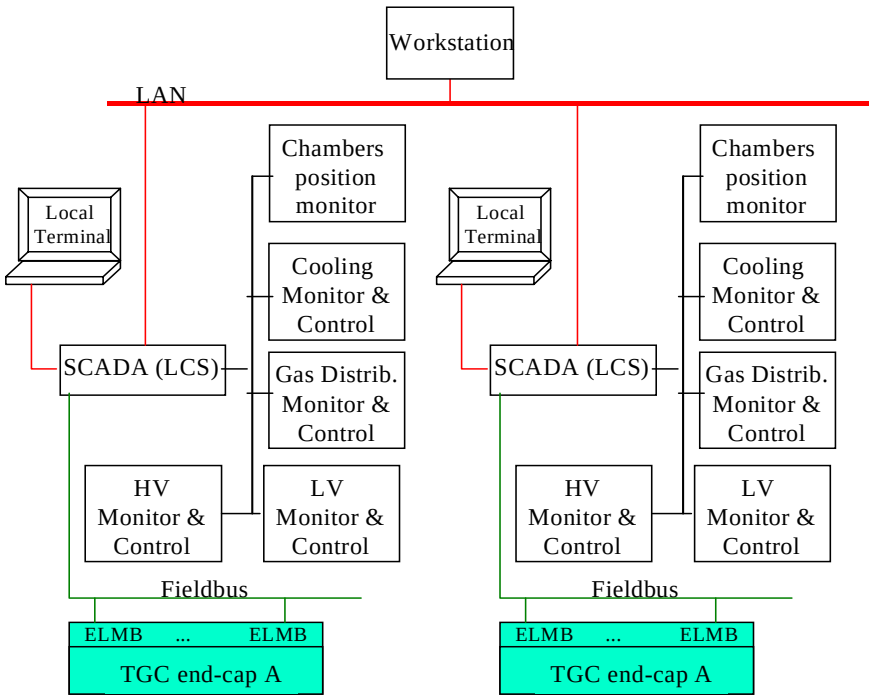

Figure 2.9: *DCS organization of the TGC detector. This arrangement is also followed by the other systems of the Muon Spectrometer.*

Gas systems

The gas system provides the needed gas mixtures for the operation of the four subdetectors of the muon spectrometer. The gas mixture must be supervised and then analyzed to provide feedback on the mixing to the system. The same analysis station also monitors the return gas. The mixed gas is delivered to gas racks residing in the detector hall. Each of these racks supplies a number of chamber cluster of the different detectors. Each cluster gas supply is monitored and controlled by the DCS. Additionally the DCS has to monitor the pressure and flow at different points of the installation and monitor the oxygen and water contamination of the mixture.

Electrical systems

Each layer of tubes in an MDT chamber is operated by a separate high voltage supply. One high voltage supply is also needed per chamber of the other muon subdetectors. These supplies reside in racks on the periphery of the detector. The high voltage will be controlled and the current and voltage monitored by the DCS. Similarly the low voltage needed for the logic electronics of the subdetectors will also be controlled and monitored for level and current. In addition discrimination levels and test pulses are required by the FE electronics boards.

The electronics readout for these subdetectors is controlled through VME crates. Each crate is connected to the DCS for control, monitoring and calibration. The calibration signals are carried through the DCS.

Alignment systems

The alignment of the CSC, RPC and TGC chambers will be performed using resistive proximity sensor. For the MDT modules optical alignment systems, namely RASNIK and MPA-ALMY. The alignment systems, consist of different arrangement of CCD, lens and masks providing a precision in the order of tens of μm. These systems are controlled and read out from VME crates. The data is processed in the VME crate and only the results sent over the LAN or fieldbus to the LCS.

Environment

The temperature of the tracking chamber of the muon spectrometer must be continuously monitored. Although it does not seem necessary to monitor the temperature on the RPC and TGC chambers, monitoring of the temperature of experimental hall at the gas distribution manifolds and of the front-end electronics will be performed. All the temperatures are monitored with a resolution of 0.5°C by NTC thermistors with conditioning circuitry and ADC.

Most MDT and CSC need a precise measurement of the magnetic field. For this purpose, these chambers are equipped with Hall mounted on three surfaces of a plastic cube to provide three orthogonal components of the field.

The readout of those temperature and magnetic sensors is carried out by a fieldbus node embedded on each chamber.

2.3.5 External Systems

The term *External Systems* designates systems having their own control system with which the DCS has to interact. We can distinguish two main external systems: the CERN technical infrastructure and the LHC accelerator. The former consists of a number of subsystems like cooling and ventilation, electricity distribution, radiation monitoring, etc. The Detector Safety System (DSS) and the Magnet Control System are also considered part of the technical infrastructure. All these external systems must be concurrent into the general DCS. Although these systems are designed to react in case of problems, early indications of their status must be notified to the DCS since they may have consequences onto the detector and automatic corrective actions, driven by the DCS, may be required. The DCS will reflect also the states of all these systems and, in many cases, will act as their user interface.

The connection will support bidirectional information exchange and, in some cases, also the sending and receiving of commands. This interface will be unique for the 4 LHC experiments and it will be developed in the framework of the JCOP.

2.3.5.1 Technical Services

The technical services around the ATLAS detector include cryogenics and conventional cooling, ventilation, gas system, electricity, radiation monitoring, low and high voltage power supplies. The DCS will also have access to the control and status of infrastructure including AC mains, air conditioning etc. These services will monitor the environment to guarantee the safety of the personnel and equipment and will enable the different subdetectors of the experiment to function within their required operating conditions. Some of the systems will need feedback from the subdetector to operate. This is the case for the gas system and cooling, where part of their equipment consist of external stand-alone PLC or commercial I/O modules, whereas some information come from the detectors themselves. Therefore, slow closed-loops maybe needed between the DCS and this type of systems.

2.3.5.2 Environmental Infrastructure

Environmental parameters including humidity and atmospheric pressure in the cavern and at surface, the composition of the air in cavern (O_2 levels etc.) will be monitored by the overall DCS and made available to the detectors. The temperature, for example, ranges from 4.5 K for the super-conducting magnets, to 88 K for the liquid argon calorimeters, to 253 K for the pixel and silicon parts of the inner detector to 293 K for the TRT, tile calorimeter and muon chambers. The state of these systems and early indications of problems must be presented to the operator. The DCS will handle, present and log this data. Automatic corrective actions must be taken by the DCS if required. Moreover, after the temporary stop of one of these systems, the DCS has to prepare the detector for the restart.

Radiation monitoring is an area where information from many sources will be used. The subdetectors themselves are sensitive radiation probes, but also dedicated sensors and information from the monitoring of the environment will be used.

2.3.5.3 Detector Safety System

As previously mentioned, the DCS is not responsible for the security of the personal nor for the ultimate safety of the equipment. The former is responsibility of the LHC-wide hazard detection systems, which will alert the fire brigade in case of severe problems such as gas leaks or fire, whereas the latter has to be guaranteed by hardware interlocks and stand-alone PLC and it is responsibility of the Detector Safety System. Although the information exchange between the DCS and the DSS must be bi-directional, actions must go only in one direction. The DCS must not disturb the operation of the safety system. However, warnings about problems detected by the safety system must be notified to the DCS in order to take corrective actions or to shut down the problematic part of the detector. Control access will also be handled by the CERN services and it will be needed at the DCS side.

2.3.5.4 Magnet system

The magnet system, described in the first chapter, represents one third of the total budget of the ATLAS detector. Although due to its critical requirements [10] and complication, a dedicated PLC-based control system will be implemented and the operator will not need direct control, a detailed online status and knowledge of all important parameters of the magnets, is essential for the operation of the detector and for the subsequent physics analysis. This dedicated system will supervise and control the cryogenics, the cooling system, the power supplies and the instrumentation of the magnet.

The toroid coil system has a 21 kA power supply and is equipped with control systems for fast and slow energy dumps. The central solenoid is energized by an 8

kA power supply. An adequate and proven quench protection system has been designed to safely dissipate the stored energies without overheating the coil windings.

The central solenoid is cooled by a refrigerator. In addition, the barrel toroid and the end-cap toroid, have cold helium pumps to guarantee appropriate cooling by a forced helium flow at 4.5 K. The cooling power is supplied by a central refrigeration plant located in the side cavern and the services are distributed among the four magnets.

A fieldbus will connect all instrumentation to the main control centre in the USA15 cavern. The magnet supervisory control system could be implemented using some standard tools of the general DCS, thus SCADA and general-purpose I/O modules. This would facilitate the integration of this subsystem within the overall DCS.

2.3.5.5 LHC

An robust interface between the experiment and the accelerator must be provided. Instantaneous beam parameters like the different types of background, beam position, individual bunch luminosities, observed in the detector must be transferred from the experiment to the accelerator for consequent tuning of the beam.

The experiment will also give all information on its status such as status of its magnets, in particular, the solenoid which acts directly on the beams, status of sensitive equipment like high voltage on the sub-detectors and other status signals as well as global status signals such as the operation state of the detector, setting up, etc. The DCS has to make sure that the detector is in an appropriate state (e.*g.* voltage settings) before LHC is allowed to inject particles.

ATLAS may need the possibility to request actions like a fast beam dump should the backgrounds become dangerous for the subdetectors or injection inhibit. This important feature has to be implemented by a fast interlock system.

On the other hand, machine parameters like status signals for setting up, shut-down, controlled access, stable beams, beam cleaning must be transferred from the accelerator to the experiment. The machine should also provide information on the beam like emittance, focusing parameters, energy, number of particles per bunch, a horizontal and vertical profile, needed for offline physics analysis. Information on the vacuum conditions in the vicinity of and in the experimental straight section and position of the collimator are also of interest to the experiment.

The LHC has dedicated instrumentation for the comprehensive measurement of all these parameters. The subset of operational parameters of the accelerator, relevant

to the operation of the detector or to the subsequent physics analyses have to be delivered to the DCS and must be logged.

Although the exchange of many of these parameters is only needed during data-taking, a subset of this information, like the integrated radiation doses in the different parts of the detector measured by the DCS, has to be known to the LHC at all times. Therefore, this communication is required regardless the state of ATLAS. This is one main reason why this communication will be handled by the DCS on the ATLAS side and not by the DAQ system.

Similar functionality is currently required to interface the CERN Super Proton Synchrotron (SPS) during testbeam activities and commissioning of the LHC experiments. The solution currently adopted is presented in chapter 5.

More work is required concerning the interaction of accelerator and the experiment during operation which will have to be addressed in the coming years. All information exchange should be done with the same mechanism as used for the communication with the other external systems.

2.3.5.6 DAQ

Requirements

The DAQ system and the DCS are complementary in, as far as, the first treats all aspects of the physics event-data, which are identified by an event number, and the second deals in general with the other data, which is normally categorized with a time stamp.

The ATLAS collaboration has chosen to split the DAQ and DCS functionality into two independent systems. This approach is also followed by other LHC experiments namely, ALICE and CMS whereas the LHCb collaboration has adopted a solution which combines all functionality into a common experiment control system. There are two main reasons for this factorization in ATLAS:

- The DAQ system is only needed for data-taking whereas the DCS needs to be operational continuously in order to ensure the safety of the experiment. Moreover, periods with no beam might be used for the upgrade of the DAQ system.
- The DCS system is needed well ahead the final DAQ system is set up for the start of overall integration of the detector in 2004, and some of its subsystem are needed for quality assurance and calibration during commissioning.

For these reasons it was decided to keep separated data and control paths for both system. However, in order to ensure the performance of the experiment bi-directional communication between both systems will be provided. All DCS data and status of the equipment relevant to the data-taking and physics analysis must

be transferred to the online DAQ system for later storage. Similarly, information flow from DAQ to DCS is also needed. For instance, the DAQ must notify the start of run to the DCS. Issuing of commands from DAQ to DCS is also required, e.g. the DAQ system must request to regulate the high voltage as result of a calibration procedure. The main requirements of the interconnection between the DAQ system and the DCS can be found in reference [22].

The interaction between both system takes places at the SCADA level on the DCS side and through the online software components on the DAQ system. No direct connection between the DAQ system and the DCS front-end is foreseen. This communication will be performed by the DAQ-DCS Communication (DDC) software package which connects the two systems. This component is one of the DCS building blocks and a detailed description can be found in the next chapter.

Interaction during operation

Intense information exchange between both system must be provided in different situations:

- Transition to a different state of the detector, e.g. start of run once the operator has selected a configuration from a predefined list. This will take place through the following steps on the DAQ side:
  - Load; initializes any software packages required for operation
  - Config; reads required parameters from the database, connects to other modules (e.g. establishes network connections), starts any other services or request any resource required.
  - Start of data taking.

  All these phases must be synchronized with the status of the LHC accelerator, as well as, the states of the detector equipment and partitions handled by DCS, by means of messages and command transfer.
- Calibration of the detector, where three main types can be distinguished:
  - Only the DAQ system is involved like the case where subdetector adjusts the pedestals for zero suppression during run-time by analyzing the signals of physics event data.
  - Pure DCS calibration like in the TileCal subdetector where a radioactive source wanders through the detector, the currents of the photomultipliers are measured and the high voltages are adjusted.
  - Both system are required. Although in this case, the DAQ system usually drives the procedure like calibration during a cosmic run, the possibility where the DCS may be the master of the process must be considered. In the latter, results from the DAQ system, calculated from physics event-like data,

may be needed to find the optimal set of parameters.

Some calibration procedure may be performed during a physics run, e.g. the calibration with the laser system of the Tilecal where a special trigger signal is injected. In other cases a dedicated DAQ run is required, e.g. the calibration of the Tilecal modules with a Cs source. In all cases the calibration constants determined, will be stored in the experiment-wide calibration DB.

Partitioning

Partitioning constitutes another point where strong collaboration between the DCS and the DAQ system is required. During operation, commissioning and debugging of the ATLAS experiment it will be necessary to run a subset of detector elements independently from and concurrently with another set. A partition is defined as a logical and / or physical subset of elements which can be operated as an entity, such as an ATLAS system, subsystem or a part of a subsystem. A partition includes both, hardware and software components.

Although the DAQ does not apply the same boundaries for the definition of the partitioning than the DCS, both must be matched and synchronized to ensure the coherence of the run and an unambiguous data flow. It is foreseen to have for each partition a controller tree. In this structure one controller will be responsible for synchronization with the DCS. The management of DAQ partitions is performed by the Online Software component and their description will be handled in the configuration database, whereas on the DCS side is handled by the SCADA software. This imposes strong requirements on the openness of SCADA package to be chosen.

Recently, the first steps for the coordination of partitioning have been given with discussion between responsible of both working groups.

Chapter 3

The ATLAS DCS Building Blocks

The ATLAS Detector Control System consists of two main components: a distributed supervisor system called Back-End system, and the different Front-End systems. In this chapter the different technologies selected to implement the DCS are described. In the first part the general requirements which must be satisfied by these components are outlined. In the following sections, the different building blocks of the ATLAS DCS are presented. The supervisory layer of the DCS will be implemented by the commercial SCADA product PVSS-II. A brief description of the product is given in the chapter and its main characteristics relevant for detector controls are mentioned. Special emphasis is given to the Embedded Local Monitor Board (ELMB), which has been designed as a general-purpose plug-on module for the monitoring and control of the front-end of the ATLAS subdetectors. In the so called ATLAS DCS Vertical Slice, the ELMB is interfaced to PVSS-II via a CANopen OPC server. An intensive bi-directional communication between the DAQ system and the DCS will be provided by the DAQ-DCS Communication software, which constitutes a major component of the ATLAS DCS. This package is presented in the last part of the chapter.

3.1 Requirements

As it was shown in the previous chapter, the DCS equipment will be geographically distributed over three regions. Most of the front-end equipment will be installed in the experimental cavern being exposed to harsh environmental conditions imposing strong requirements on the components used. These requirements are outlined below:

- ***Radiation tolerance:*** The radiation levels vary by many orders of magnitude, from up to 100 kGy/year close to the interaction point and in the forward region, down to 1 Gy/year in areas shielded by the calorimeters, which absorbs fully electrons and photons. The radiation left consists of mainly neutrons, about 10^{11}

particles / cm^2 (equiv. 1 MeV Si) over 10 years of operation. The ATLAS simulated radiation map is shown in figure 3.1.

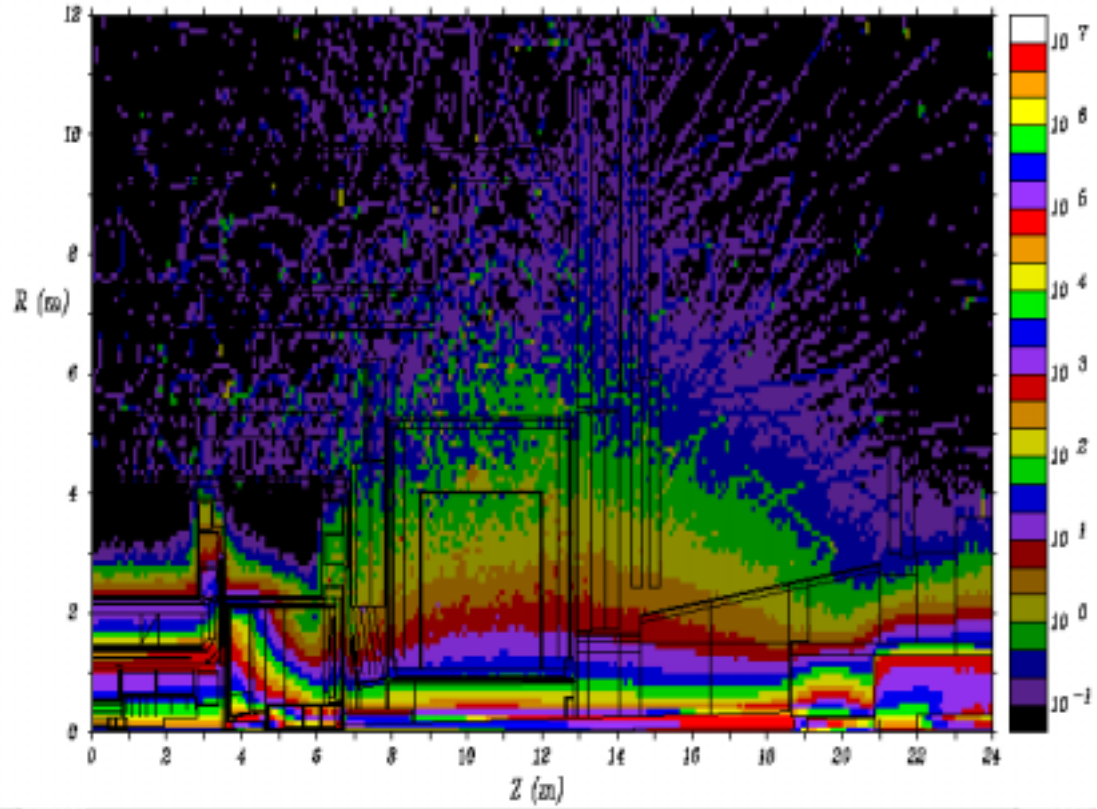

Figure 3.1: *Simulated map of total ionization dose (Gy/year) in ATLAS (July 2001).*

All equipment located inside the calorimeters must be radiation-hard and will be designed using special technologies. In many cases only sensors will be installed here and the signal will be brought to I / O modules, placed outside the calorimeters, by means of wires.

In the shielded region, tolerant electronics will be sufficient. For these electronics, which will be installed at accessible places, one should be able to use standard commercial Components-Of-The-Self (COTS). However some special care in the design has to be taken and only selected components, with samples verified in radiation tests will be used.

In some cases, the possibility to replace the electronics during the lifetime of the experiment is foreseen.

- ***Operation in a magnetic field:*** The magnetic field in the cavern will vary in direction and magnitude from place to place and reaching values of a few hundred Gauss. Therefore electronics components like coils, chokes, transformers and some types of DC / DC converters can not be used. As power supplies may be sensitive to magnetic field, it is foreseen to feed the power

remotely via cables requiring low-power consumption front-end electronics.

- ***Inaccessibility to the ATLAS cavern*** due to the hostile environment during data taking. Access will only be allowed during periods without beam in the LHC machine and therefore remote operation, configuration and monitoring must be provided.
- ***Experiment size***, which requires a very large number of I/O points. For this reason high density I/O concentrators must be employed in order to keep a reasonable cost. On the other hand, the DCS will undergo different software upgrades during the lifetime of the experiment and therefore in-system re-programming capability must be provided due to the large number of devices.
- ***Highly distributed I/O points*** over the whole volume of the detector. Cable lengths up to 200 m is required in order to connect the I/O devices to the LCS placed in the underground electronics cavern. The geographical location of the equipment also imposes strong requirements on the software, which must map this distribution.
- ***Large lifetime of the experiment***. In order to reduce the maintenance effort, the DCS must be implemented out of well-defined and common building blocks. To promote ease of repair or replacement of hardware, and to provide superior technical documentation, the use of commercial hardware, where possible, is strongly encouraged. Custom protocols and modules must be subsequently avoided and whenever possible industrial standards must be used.

3.2 DCS building blocks

The ATLAS Detector Control System consists of two main parts: a distributed supervisor system, running on PCs, called Back-End (BE) system, and the different Front-End (FE) systems. On the SCADA side, homogeneity is guaranteed by using the same commercial software system throughout.

FE systems are the responsibility of the subdetectors groups. The standard approach adopted by ATLAS is to place in the cavern I/O concentrators, with limited local processing capabilities, transferring the data to the LCS for further processing. According to the complexity of the task and the nature of the equipment, different solutions will be employed. Standardization and homogeneity at this level will be achieved by the utilization of well-defined industrial standards wherever possible and common DCS building blocks.

Interfacing SCADA to the FE systems will be done by a limited number of standard protocols such as fieldbuses and software standards.

3.3 Front-End systems

3.3.1 Fieldbuses

A fieldbus is a simple cable bus, connecting intelligent nodes by means of a well-defined protocol. The nodes usually contain a microprocessor and can execute simple tasks like data conversion and reduction, error detection, etc.

Industry fieldbuses differ in their technical characteristics like bandwidth, network topology, length, determinism, robustness, error handling, openness, redundancy, etc. They can be divided in three main categories:

- Sensor buses, used to connect intelligent sensors to PLC or front-end equipment.
- Device buses, which connect I/O modules to PLCs or front-end.
- A full-size bus, which are similar to LANs and are used to handle data at higher levels between the PLCs or front-end equipment and the supervisory stations.

In the two first types, the communication usually is periodic and deterministic whereas in full-size buses transmission is frequently on-request. Both sensor and device buses will be used in ATLAS and will constitute the standard approach to connect front-end equipment to the LCS.

Fieldbuses are well supported by industry both in hardware (chip-sets, ready made general-purpose modules, measurement instruments) and in software (drivers, diagnostic tools and supervisor software). In order to limit types of fieldbuses used at CERN, a major evaluation effort was performed and concluded with the recommendation [21] of three fieldbuses to be used in the LHC era: CAN, WorldFip and Profibus. These three fieldbuses are complementary in their technical aspects and domain of application and therefore, should suffice to meet all requirements for applications at CERN in both, accelerator and experiment fields.

Profibus is specially recommended in applications where a large data volume must be handled, whereas WorldFip is appropriate for systems with critical time requirements. CAN is specially suited for applications where high flexibility and reliability of data transmission are needed. From these three fieldbuses, CAN is the most appropriated for control and sensor readout of simple devices and for this reason has been selected by the ATLAS community.

3.3.2 CAN

The CAN (Controller Area Network) specification was introduced in the late 80s by the german company Bosch. It was originally designed for automotive control but

meanwhile it is widely used for industrial applications. CAN is standardized by the International Standardization Organization in the document ISO/OSI 11989. It defines a serial communication protocol which covers only the two first layers of the OSI communication layer model, thus the physical and data link layers. The commonly used bus media is a shielded twisted pair cable. A detailed description of the protocol is given in [23, 24, 25]. The main reasons why CAN is especially suited for the implementation of the detector controls are given in the following:

- ***Reliability;*** the CAN error checking mechanism is of particular interest in the LHC environment where bit errors due to radiation effects will occur. For error detection the CAN protocol implements three mechanisms at the message level (Cyclic Redundancy Check, Message frame check and Acknowledgement errors) and two at the bit level (Bit Monitoring and Bit stuffing).

  When an error is detected, the current transmission is aborted and an error message is sent, preventing other stations to accept the faulty message and ensuring the consistency of data throughout the network. When the transmission of an erroneous message has been aborted, the sender automatically re-attempts transmission. The error confinement procedure allows to distinguish between temporary errors due, for instance, to environmental conditions, and permanent failure of the nodes. CAN chips with permanent failures are automatically taken off the bus.

- ***Determinism;*** The priority of the CAN frames is implicitly determined by the message identifier. CAN uses an arbitration method called *Carrier Sense Multiple Access with Collisions Advoidance (CSMD/CA)*. If an identifier collision is detected by the CAN controllers of the modules, the lower priority device immediately ceases transmission and waits for the higher-priority message to complete before is automatically sent to the bus. This mechanism leads to a non-destructive priority-based bus arbitration. It is guaranteed that the higher-priority message always gains access to the bus.

  In addition, unlike other bus systems, the CAN protocol does not use acknowledgement messages but instead signals any error that occurs. This improves performance and ensures real-time behavior of the network.

- ***Coverage;*** CAN is conceived for distributed monitoring and control. The effective speed of data transfer depends on the bus length and the values are given in the table 3.1. Bus speeds of 125 or 250 kbits/s fit the required distance to cover the experimental cavern of ATLAS.
- ***Robustness;*** CAN is designed for operation in a harsh environment like automation and it provides high noise immunity.
- ***Galvanic isolation***; which is essential for high data quality transmission over distances above 100 m.
- ***Operation in magnetic field;*** CAN devices do not employ magnetic sensitive components like DC/DC converters, transformers or coils.
- ***Radiation tolerance;*** Although it is not possible to find radiation-hard

components, it is possible to qualify pre-selected COTS for operation in radiation environment up to the levels expected in some regions of the ATLAS cavern.

Table 3.1 *Bus speeds for different cable length*

Bus Speed	Cable length
10 kbits / s	6.7 km
20 kbits / s	3.3 km
50 kbits / s	1.3 km
125 kbits / s	530 m
250 kbits / s	270 m
500 kbits / s	130 m
1 Mbit / s	40 m

- ***Low power dissipation;*** also essential for remote powering via the CANbus.
- ***Openness;*** CAN is not a proprietary system and therefore has no license fee.

In addition, CAN commercial hardware, down to the chip level, is well-supported by industry. CAN chips are inexpensive and are produced by many manufacturers. Moreover, owing to the requirements of the automotive market, the availability of products is guaranteed at least during the lifetime of the experiment.

3.3.3 CANopen

It is highly desirable to have a homogenous implementation of the CAN fieldbus in the ATLAS experiment, not only for reasons concerning design and production, but also for the subsequent maintenance. Although the usage of direct CAN for low level applications may be adequate, the ATLAS DCS requires a higher-level communication protocol on top of CAN. From the different higher-level communication protocols available, CERN has selected CANopen on the basis of flexibility and market acceptance. CANopen is defined by the CAN in Automation (CiA) organization and a detailed description of the protocol is provided in [26]. This standard implements layer seven of the OSI communication model, the application layer. It also defines how the data-bytes of the CAN frames are used among the different nodes on the bus. The protocol must also guarantee the inter-operability of devices from different manufacturers standardizing:

- The application layer, which defines common services and protocols for all devices.
- The communication profile, which defines the communication between devices

on the bus. The CANopen communication model implements both master-slave and slave-slave communications modules. In a CANopen network there must be at least one master application performing the boot-up process and maintaining the network in an operational state.

- The so-called Device Profile Specifications (DSP), which specify the specific behavior for types of devices such that the inter-operability of devices from different producers and basic network operation are ensured.

In the following, the basic elements of the protocol are summarized and their relevance for detector controls is outlined:

- Standardized description of the node functionality by means of the so-called Object Dictionary (OD). The OD is a standardized database, which holds an ordered collection of objects containing the description of the device and network behavior i.e. the device specification profile. The object dictionary is not stored in the CANopen node itself but defined in an Electronic Data Sheet (EDS). The OD is subdivided in three main areas: the *Communication* area, the *Manufacturer Specific* area and the *Device Profile* area.
- Standardized communication objects; two main types of mechanisms are implemented.
  - Process Data Objects (PDO), which are broadcasted and unconfirmed messages containing up to 8 data bytes. This mechanism is used for real-time transfers.
  - Service data objects (SDO), which are confirmed transfers of any length. Peer-to-peer communication is established between two nodes of the network by this mechanism. This type of objects are used for configuration of the nodes by direct accessing to their object dictionaries.

  PDOs are higher-priority messages than SDOs. This differentiation among real-time and configuration transfers and the arbitration collision mechanism of CAN, make this protocol specially suited for detector control since I/O operation affecting the status of the system are performed in real-time while lower-priority functions are always performed at low levels of bus occupancy.
- Standardized Network Management (NMT) including system boot-up, node supervision and node identifier distribution. The CANopen master handles the transition of the slave between the possible states: initialization, pre-operational, operational, stopped. After the boot up sequence the device enters in pre-operational state. NMT messages are used to bring a slave node to operational or stopped states.

  Of particular relevance for LHC applications is the network supervision where the master node guards all remote slaves on the bus. There are two main mechanisms:
  - Node guarding, where the master produces guard messages that must be acknowledged by the slaves.

- Heart-beat, where the slaves send messages to the bus at regular time interval that are consumed by the master.

If the master does not receive a reply from a node within a certain time period the node is regarded as not functional and an error flag may be set.

- Standardized systems services for synchronous operation of the network and handling of error messages from the nodes. Synchronous mode of operation is particularly interesting for detector control. The network master can query current values of the input channels by issuing a SYNC command to the bus. If the input PDO of the slave nodes have been configured to be operated synchronously, they are transmitted are response to a SYNC to the bus. This permits to obtain a *snap-shot* of the detector at regular time intervals.

3.3.4 The ATLAS Embedded Local Monitor Board

3.3.4.1 Introduction

CAN nodes can either be embedded in commercial equipment (e.g. electronics crates or power supplies) or be purpose-built for ATLAS. The latter ones can either be designed for a specific application (*e.g.* the CAN modules used for the HV control of the Tile Calorimeter) or a general-purpose module can be used, which needs only to be configured via software depending on the application.

Although it is strongly recommended to use commercial components for the implementation of the DCS at both software and hardware levels, in some cases, operation in magnetic field, radiation tolerance and the very large number of channels to measure and control, make very difficult the utilization of commercial components keeping a reasonable cost. The ATLAS DCS team has pushed for the development of a multi-purpose front-end module, the Embedded Local Monitor Board (ELMB), providing uniformity throughout the ATLAS subdetectors and fulfilling the environmental requirements mentioned. The usage of the ELMB by the ATLAS subdetectors provides the following benefits:

- Same hardware and software interfaces to the SCADA system.
- Same software for driving the I/O lines.
- Qualification of components for operation in the ATLAS environment.
- Reduction of design effort.
- Massive production leading to lower cost.
- Spares and maintenance.

The development is based on a previous development started in mid 1990s at Nikhef, Amsterdam, called CANDIDE [27]. It aimed at producing a CAN node which could be embedded in the FE electronics to readout all operational

parameters of the MDT chambers. A few years later, this development was taken on board by the ATLAS DCS team at CERN, leading to the production of a first prototype, the Local Monitor Box (LMB) [28, 29] in 1998. This node was a stand-alone modular system, which was satisfactorily used and tested in many applications with the subdetectors. Recently, a collaboration with the DCS group from NIKHEF has been established and a new version of the module, the Embedded Local Monitor Box (ELMB) has been released, where feedback from the subdetector groups was also considered. This development aims at fulfilling the requirements from all subdetectors, presented in chapter 2.

The ELMB [30] is a general-purpose, low-cost I/O concentrator for the supervision and control of front-end equipment. It can either be directly plugged onto the front-end electronics of the subdetectors, or onto a multi-purpose motherboard which handles the signal conditioning. The ELMB fully conforms to the industry standard CANbus and CANopen is used as high level communication protocol. The module has been designed using COTS previously selected to meet the environmental requirements. The general specifications of the design of the ELMB are the following:

- Radiation Tolerance to about 5 Gy and 3×10^{10} neutrons/cm^2.
- Operation in magnetic field up to 2 T.
- Low power consumption, allowing for remote powering of the module via the CANbus
- Low cost per I/O channel, due to the large number of nodes needed for the whole of the experiment (~5000)

The two first requirements are imposed by the location of the ELMB as it is intended to use the module in the USA15 cavern, in the MDT layer 3 region after the shielding of the calorimeters. In addition, specific requirements were differential inputs and opto-isolation in order to eliminate ground loops.

The work done by the author of this thesis with the ELMB has consisted in testing of the module, participation in the definition of the node and network behaviors, implementation of a number of applications with the subdetectors, interfacing to SCADA and study of performance and scalability of ELMB networks.

3.3.4.2 Previous work with the LMB

In a first step, the LMB prototype was intensively tested in different applications with the subdetectors. The input from this previous experience was considered and led to the current design of the ELMB. In the following, these applications are presented and their relevant results are outlined. In all cases the number of channels was of a few tens and the acquisition software was developed using Bridge View,

which was considered as an interim solution, while the selection of a final SCADA product was made.

High precision temperature measurements

The test was performed at the LAr electromagnetic calorimeter end-cap cryostat in the experimental line H6 of the CERN SPS in 1998. A detail description of the test is given in reference [31]. Nine low-cost Pt-100 temperature sensors were read-out using one LMB module with 4-wire connection and compared with the values given by a high precision temperature sensor calibrated to an absolute accuracy of 1.5 mK. An effective resolution of the LMB equal to 0.8 mK per channel and an absolute accuracy of 3.1 mK were found. The study of the long-term stability of the LMB performed over 1 month showed a drift of about 2 mK. This was found to be sufficient for the monitoring of the temperature of the LiAr calorimeter.

ATLAS Pixel and SCT cooling tests

In these tests [32], three ELMB nodes were accommodated on the same bus shared with WAGO commercial modules. This has proven the compliance of the ELMB to the CAN and CANopen standards. The ELMB was found to be very well suited for this type of application where a high number of I/O channels is needed.

Magnetic field test

The test [33] was performed at CERN and aimed at determining the influence of a magnetic field up to 1 T on the performance of the LMB node. Results for the three orthogonal field directions X, Y and Z, showed that no relevant effects due to the magnetic field were induced on the ELMB.

Radiation test

Preliminary radiation test of the LMB were preformed over a period of 11 weeks at the TCC2 facilities at CERN [34, 35]. Although the results of these tests did no allow for radiation qualification of the LMB due to the undefined beam composition and imprecise radiating dose, they served to identify components vulnerable to radiation effects like certain types of opto-couplers and multiplexers.

3.3.4.3 ELMB Hardware

Contrarily to the modular LMB, the ELMB is a single board of credit card-size (50×67 mm^2) that constitutes the final design of the hardware. The printed circuit board (PCB) is populated with components insensitive to magnetic field. The block diagram of the ELMB is shown in figure 3.2.

Three different power regions identified: the CAN controller part, the digital part having two microprocessors and the ADC (Analogue to Digital converter) region. This independence between the CAN part and the processors gives the flexibility to chose the best suitable components for the implementation.

These three parts are separated with opto-couplers to prevent current loops. These devices are sensitive to radiation effects. For this reason, two different types are used in the ELMB. The CAN part is isolated by means of fast optocouplers whereas slow optocouplers are used to separate the ADC and digital regions. The fast optocouplers employed in the ELMB (HCPL-0601) are more vulnerable to radiation, however, possible radiation effects at this point, are automatically corrected by the CAN controller, which ensures the proper transmission of the messages. The slow optocouplers employed in the ELMB (HCPL-0731) were carefully selected for operation in radiation environment.

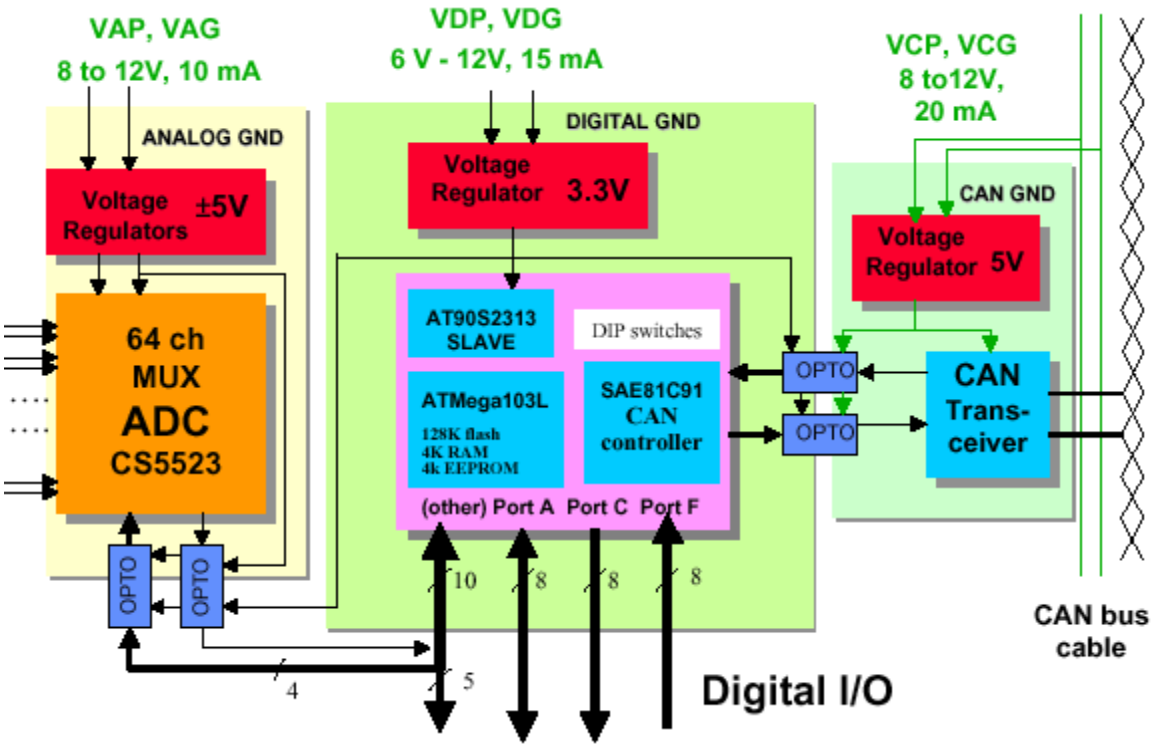

Figure 3.2: *Block diagram of the ELMB*

Every part is equipped with a Low Dropout (LDO) 80 mA voltage regulator manufactured by Micrel (MIC5203). These elements also provide current limitation and thermal protection to prevent against damaging effects due to radiation. The analog circuits need ±5V, which is generated by a separate CMOS switched-capacitor circuit. The power supply of the digital and CAN parts of the ELMB provide 3.3 V, 15 mA and 20 mA at 5.5 V respectively.

CAN module

The CAN module is mounted on the front of the PCB as shown in figure 3.3. This side of the PCB is also populated with the digital microprocessors and all circuitry needed for operation.

The CAN part consists of the low cost SAE81C91 Full-CAN controller from Siemens, which handle the bus protocol, and the PCA82C250 bus transceiver from Phillips, which translates the logic levels to CAN levels. A galvanic isolation is made with fast opto-couplers between the CAN bus transceiver and the protocol chip. The main features of the CAN controller are shown in table 3.2

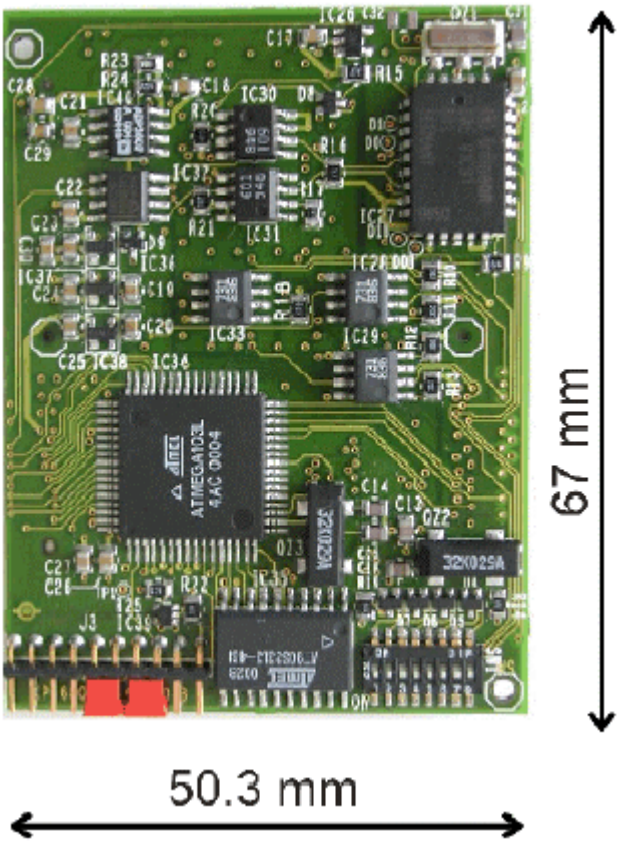

Figure 3.3: *Front side of the ELMB with the master and slave microcontrollers, CAN chip and DIP switches for node identification and setting of the baud rate.*

Table 3.2 *Main features of the CAN controller*

Full CAN controller interface with PCA82C250
Physical layer ISO 1189
Real Time Counter with a separate 32 kHz crystal
4 baud-rates supported
Node ID selectable via DIP switches (Up to 64 nodes per bus)

Microprocessors

The local intelligence of the ELMB is provided by 2 microcontrollers of the AVR family (8-bit processors), manufactured by ATMEL. The main processor of the ELMB is the ATmega103L running at 4 MHz. This CMOS integrated circuit contains on-chip 128 kbytes of flash memory, 4 kbytes of SRAM, 4 kbytes of EEPROM and a range of peripherals including timers/counters and general-purpose I/O pins. The I/O lines of this microcontroller are shown in table 3.3.

Table 3.3 *I/O lines available*

6 external interrupt inputs
Port A 8 digital bi-directional I/O lines[1]
Port C 8 digital output lines[1]
Port D 5 digital bi-directional I/O lines
Port E 5 digital bi-directional I/O lines
Port F 8 digital input lines or 8 analog inputs for the ADC

1. can alternatively be used for external SRAM

The main monitoring and control applications and the CANopen stack run on this processor. The second on-board microcontroller is a much smaller member of the same type, the AT90S2313 with 2 Kbytes flash-memory, 128 bytes of SRAM and 128 bytes of EEPROM. The slave processor works in parallel with the master and performs two main functions:

- Provides remote in-system programmability of the processors via the bus.
- Monitors the operation and performs recovery actions like reset or reprogramming of the master processor, to prevent effects due to radiation.

The different parts of the module are connected to the CAN controller via the serial bus Serial Peripheral Interface (SPI)[a] bus.

All components used in the ELMB have been selected to ensure low power consumption of the module. The total current consumption is less than 30 mA making possible to feed the modules from a remote power supply via the bus.

The baud rate and the node identifier are set by means of on-board DIP switches. The maximum number of ELMB per bus is limited by the hardware addressing scheme of the node to 64 since only six bits are used.

ADC

The back-side of the PCB is populated by an ADC, 16 analog multiplexers and different power supplies as shown in figure 3.4. The CS5523 16-bit ADC, manufactured by Crystal Semiconductors, was chosen for reasons of performance, linearity, stability and cost. Its main features are shown in table 3.4.

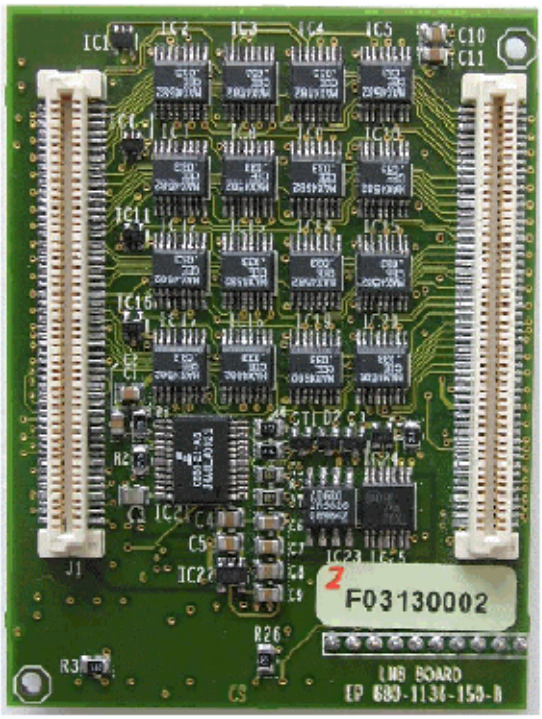

Figure 3.4: *Back side of the ELMB with the ADC, multiplexers and 100-pins SMD connectors.*

A total of 16 analogue multiplexers are to provide a multi-channel solution. An ADC can handle up to 64 high-impedance input channels. In order to minimize the pickup noise and ground loops, differential inputs are used.

a Serial Peripheral Interface bus is a widely used serial bus for synchronous data transfer between microcontroller and peripheral devices.

Table 3.4 *Characteristics of the optional delta-sigma ADC CRYSTAL CS5523 with 64 channel multiplexer*

6 bipolar or unipolar input ranges from 25mV to 4.5V
8 conversion rates from 2 Hz to 100Hz
Resolution: 16 bit
Linearity Error: ±0.0015% of Full Scale
Offset drift: 20 nV/°C or < 1 ppm /°C
Common Mode Rejection[1]: 120 db
Isolation from CANbus with opto-couplers

1. at DC, 50 and 60Hz.

The ADC has a programmable gain (7 bits) amplifier, accepting input signals ranging from 25 mV to 5 V; conversion rate ranges from 1.88 Hz to 202 Hz, although the upper limit is set by software to 32.5 Hz, in order to operate the opto-couplers efficiently. The readout time for 64 channels varies from 2.58 to 35.57 s. The overhead is due to the time invested by the multiplexer when changing channels.

The resolution depends on the conversion rate. 16 effective bits are used provided that the conversion rate is kept below 60 Hz. The ADC is optimized for DC measurements below 100 mV and, for the other input ranges, the absolute precision can deteriorate up to ±15%. The calibration of the ADC is always performed via software before starting a conversion. The ADC also has a chopper stabilized instrumentation amplifier to ensure signal stability (drift of 5 nV/ºC). The ADC includes digital filters to reject noise at 50 Hz and 60 Hz simultaneously. The AD680JR power supply from ANALOG DEVICES provides a very stable reference voltage of 2.5 V. The common mode range is -0.15 V to 0.95V on the three lowest voltage ranges and -2 V to 5 V in the other ranges.

The ADC is connected via the SPI bus and opto-isolated from the processor. Therefore the supply voltage must either be fed from the front-end electronics or using an external power supply. The total analog current consumption is 10 mA per 64 channels.

3.3.4.4 ELMB Software

CANopen has been adopted as high-level communication protocol to implement the application layer in the ELMB. The ELMB provides the minimal functionality of a slave node according to the specification of this protocol.

The ELMB software [36] is written in C and is divided into two main applications:

- The ELMBio, running on the master processor and handling the CANopen protocol, as well as the monitoring and control of the I/O channels. This package offers the flexibility required to support a wide range of applications. The program conforms to the Device Specification Profile (DSP) 301, where multiplexed PDO are used for the transmission of analogue input channels.
- The ELMBmon, which runs in the slave processor and provides the functionality needed for remote in-system re-programmability via the bus and a mechanism to prevent and correct against radiation effects.

The structure of the software allows for the operation of the ELMB as a finite state machine with four possible states:

- Initialization
- Stopped.
- Pre-operational, which is typically used to configure the node via the SDO protocol.
- Operational.

Transitions between these states are triggered by the appropriate NMT message. The monitoring of the I/O channels and the handling of PDO starts when the node enters in operational state.

Since both the flash technology and EEPROM memories have been proven to be particularly robust to radiation effects, all constants are locally stored in these two types of memories. These parameters are reloaded after resetting of the node. All configuration parameters are stored in the Object Dictionary (OD) of the ELMB and can be accessed via SDO. The ELMB OD is listed in [36]. In particular, the ADC is modelled, via software, by an object in the OD to allow for its configuration, in terms of type of measurement, gain, offsets, conversion rate, number of channels.

The real-time data, thus the digital I/O signals and the analogue inputs are communicated via the PDO protocol. Digital ouputs are transmitted asynchronously using the first Received PDO (RPDO1), whereas for the Digital Inputs both transmission types, synchronous and asynchronous are used. In this latter case, the first Transmitted PDO (TPDO1) containing two data bytes (PORTF and PORTA respectively), is used. The minimum time interval between two successive updates of the input channels, called debounce time, can also be set via software.

Due to the large number of analogue input channels, a multiplexed PDO is used to communicated their values. This is the so-called second Transmitted PDO (TPDO2). This PDO is sent to the bus as many times (up to 64) as defined in the OD. It accepts different transmission types and contains 4 data bytes with the following syntax.

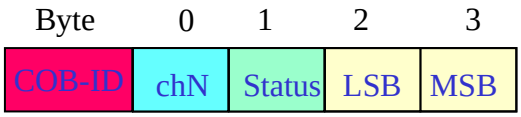

Figure 3.5: *Syntax of TPDO2 as used in the ELMB.*

where the first data byte contains the channel number that is being transmitted and its value is communicated using the third and fourth data bytes. The second byte contains information on the ADC configuration and the status of the reading. TPDO2 does not fully conform to the definition of multiplexed PDOs in CANopen. According to the specification 4 data bytes are used for addressing of the PDO as follows:

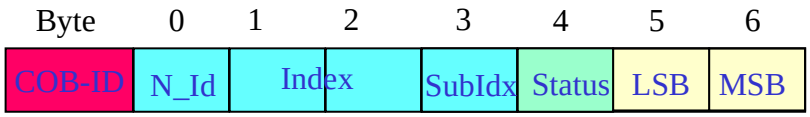

Figure 3.6: *Multiplexed PDO with source addressing*

where *N_Id* stands for the identifier of the source node, *Index* gives the index of the object in the OD where the PDO is mapped and SubIdx indicates the corresponding entry in this object, i.e. the channel number being transmitted. The three data bytes used for the object index and the node identifier[a] are redundant and result in an overhead on the bus.

Multiplexing is a very delicate topic. In fact, as it will be shown, it represents one of the major issues when looking for a commercial solution to interface the ELMB and SCADA. Commercial interfaces implement only a subset of the protocol specifications which fulfils the industry requirements. In particular multiplexing is not often supported. The main reason is that commercial CANopen nodes provide a limited number of I/Os and a unique PDO is defined for each of them. In the ELMB it was decided to limit the number of PDO in order to conform to the CANopen Pre-defined Configuration set [26], which defines as default 4 PDO per module. The maximum number of PDO in one direction on the bus, i.e. either transmitted of received PDO, is 127 and therefore an increase of the number of PDO per ELMB would lead to a reduction of the number of nodes per bus. In addition, as the

a The node identifier is implicitly contained in the PDO COB-ID (Communication Object Identifier).

COB-ID is formed from the PDO type and the node identifier, problems can arise when using a high number of PDO per node, due to addressing conflicts.

However, migration from the custom approach followed to the addressing scheme defined in the standard for multiplexed PDO would be straightforward, and it would be implemented, provided that a commercial interface is identified

For standard applications, the software library released provides all functionality required in a wide range of applications. The ELMB can be used as a conventional I/O module and no programming knowledge is required. In addition, since the software described so far only occupies 12 kbytes of the 128 available in the master processor, and it is possible to write user specific applications to extend the functionality of the ELMB. This is the case of the TGC and RPC subdetector groups, which modify the ELMBio code in order to drive front-end readout chips via I2C and JTAG, and perform high level functions like averaging and histogramming directly at the ELMB level. Another example where the functionality was extended in order to drive off-board analogue output modules will be shown in section 6.3.2. In all cases, the ELMBio program must be used as skeleton for these new programs in order to conform to the CANopen protocol and the ELMBmon application must not be modified.

3.3.4.5 Motherboard and signal adapters

Although the ELMB can be directly embedded onto the front-end electronics of the subdetectors, it can also be used as an stand-alone I/O module by plugging it onto a multi-purpose motherboard. In the former case, the signals must be conditioned to the proper levels of the ADC by means of dedicated circuitry. In the latter, this adaptation can be done by using generic adapters, which are plugged onto the sockets of the motherboard. Figure 3.7 shows the ELMB mounted onto the back-side of the motherboard and the 18-pin sockets for the adapters.

Figure 3.7: *Back side of the mother board with the ELMB and 16 signal adapters for analogue inputs.*

On the front-side of the motherboard, shown in figure 3.8, the connectors for the ADC inputs, digital ports, SPI interface and power and bus connectors are located. The motherboard can be mounted on a DIN rail housing of size 80×180 mm^2.

Each adapter serves groups of four channels. The ADC reference voltage (+2.5 V) and ground are also available on them. The following types of adapters are provided:

Figure 3.8: *Front side of the ELMB mother board with 4 connectors for analogue inputs, digital ports A, C and F, SPI bus, power connector and CAN bus connector.*

- ***Resistive Sensors with 4-wire connection:*** This types of adapter is used in applications where high precision measurement are required. The method eliminates the voltage drop in the wiring. The layout and the measurement principle of this adapter is shown in figure 3.9.

  Two differential channels are used to determine the resistance of the sensor. One measures the current flowing through it, whereas the second channels measures the voltage drop in the sensor. The resistance is therefore proportional to the ratio of both channels, according to the following expression:

$$R_{sensor} = R_s \cdot \frac{ch_1}{ch_0} - R_{offset} \tag{3.7}$$

  where R_s is defined in figure 3.9 and its precision determines the performance of the method. The value of this resistor is typically found by calibration where the sensor is substituted by a high precision resistor of known value. R_{offset} is also determined by calibration and takes into account the resistance of the wires.

  The resistor R_c in the figure, is used to feed the current from the reference voltage and must be selected in order to use the full-scale of the ADC.

- ***Resistive Sensors with 2-wire connection:*** The principle of this method is shown in figure 3.10. Unlike to the procedure described above, only one channel of the ELMB is used per sensor. Up to a 10 mA current can be fed to the sensor using the voltage reference of the ELMB, The voltage across the sensor is directly measured by the ADC. The calibration is done with a high precision resistor of a known value. An absolute precision of 0.1 K can be easily achieved. This adapter is typically used with resistive platinum or Negative Temperature Coefficient (NTC) thermistors although other sensors like strain gauges and position sensors where the resistance changes as function of the parameter can also be employed.
- ***Differential attenuator:*** The ADC used in the ELMB can measure voltages in the range of ±4.5 V. In order to measure voltage out of this interval, a voltage divider can be used to match the signal to the input range of the ADC. The principle of this adapter and its design are shown in figure 3.11.

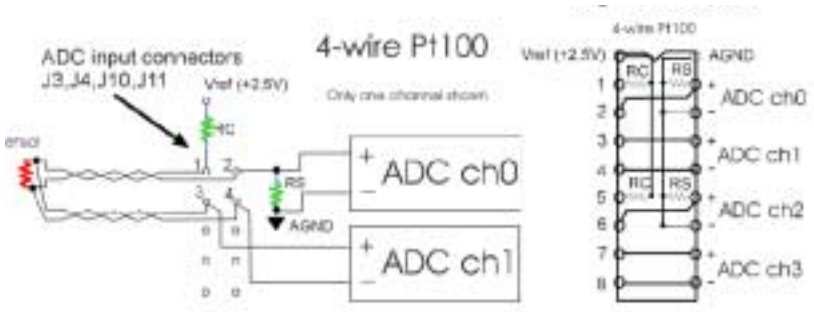

Figure 3.9: *Measuring principle of the 4-wire adapter for resistive sensors.*

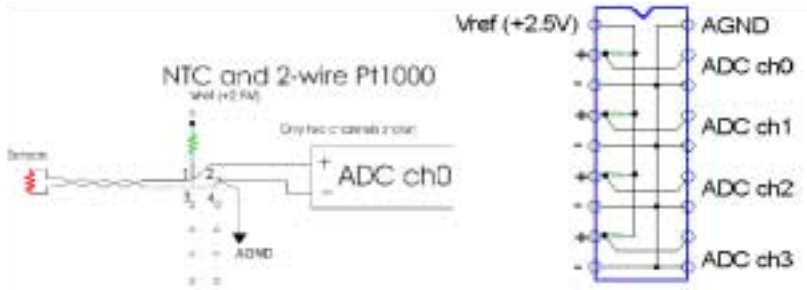

Figure 3.10: *Measuring principle of the 2-wire adapter for resistive sensors.*

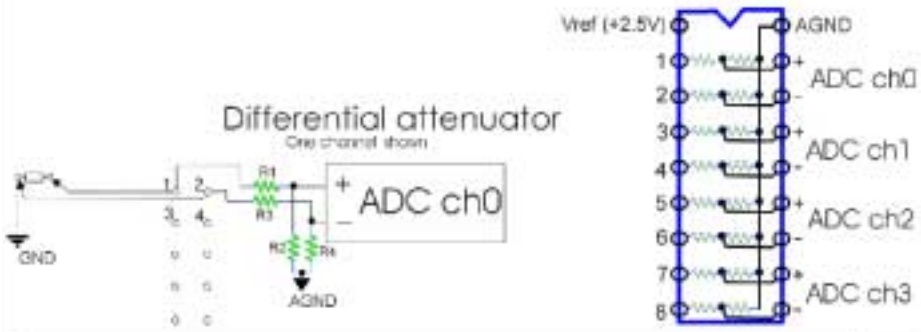

Figure 3.11: *Measuring principle of the differential attenuator.*

- ***Resistor Network:*** If the voltage is within the input range of the ADC, a standard 16-pin dual-in-line resistor network, can be used to connect the signal directly to the multiplexers of the ADC.

3.3.4.6 Add-ons for the ELMB

DAC

Although the ELMB module does not currently provide analogue output channels, these will be required in large quantities in ATLAS. Moreover, some subdetectors, like the Pixel, intend to perform close-loop control using the ELMB analogously to a PLC. Valves and regulators will be adjusted by the ELMB in response to changes of temperature. For this reason, an off-board prototype with up to 64 analogue output channels is currently being designed. The DAC chips will have a resolution of 12-bits, producing a voltage output ranging from 0 to 20 V. The offset of this signal will be adjusted via software. It will also be possible to produce a current output from the modules by using standard adapters. Two main types of applications can be distinguished:

- Low current consumption, where the power will be directly fed from the ELMB

power supplies.

- High current applications, where the utilization of external power supplies will be required.

The ELMB software is already prepared to operate analogue output channels. The second received PDO (RPDO2) will be used for this purpose. Each output is buffered and can be ramped up or down

Interlock box

As it was described in chapter 2, some applications in ATLAS, like the cooling and high voltage systems of the Pixel subdetector, will require a fast interlock system. Although this system will be hardware-based solutions operated in stand-alone mode, in same cases an integrated operation with the ELMB is required. For this reason an interlock box compatible with the ELMB has been developed and is reported in [32].

3.3.4.7 Production and Cost

One of the main design requirement of the ELMB was to provide an economical solution due to the large number of modules required in ATLAS. The present estimated cost of the ELMB nodes, motherboard and adapters is shown in table 3.5.

Table 3.5 *ELMB cost. Prices are given in CHF*

ELMB with only digital part	150
ELMB with ADC	250
Motherboard	150
4-wire resistive sensor adapter[1]	12
2-wire resistive sensor adapter[1]	10
Voltage Attenuator[1]	10
Resistor Network[1]	7

1. Components of 1% accuracy.

These prices represent at least a factor 10 less than those of commercial modules offering I/O similar functionality[a].

a This does not consider radiation-hard devices capable to operate in strong magnetic field.

A first production of 20 units was done in 2000 by the ATLAS DCS team. These units were used for testing of the functionality of the modules. A second production of 200 pieces was done in 2001 in collaboration with the CERN electronics pool. These modules were rapidly distributed among the ATLAS subdetectors although some units were purchased by other experiments like CMS and COMPASS and other groups at CERN like the gas and magnet systems. The central DCS team is now preparing a tendering for the final production of 5000 units, which will be produced by an external company. The ELMB knowledge will be given to this company with the compromise of obtaining the modules at the production cost.

3.4 SCADA

3.4.1 Introduction

SCADA systems [37] are commercial software packages normally used for the supervision of industrial installations. They gather information from the hardware, process the data and present them to the operator. Even though SCADA products are not tailored to LHC experiment applications, many of them have a flexible and distributed architecture and, because of their openness, are able to fulfil the demanding requirements of the ATLAS DCS.

Besides basic functionality like Human Machine Interface (HMI), alarm handling, archiving, trending or access control, SCADA products also provide a set of interfaces to hardware, *e.g.* CERN recommended fieldbuses and PLCs, and software, *e.g.* Application Program Interface (API) to communicate with external applications, or connectivity to external databases via the Open or Java DataBase Connectivity (OBDC and JDBC respectively) protocols.

SCADA products constitute a standard framework to develop the applications leading to a homogeneous DCS. Its usage saves development effort reducing the work for the subdetector teams. In addition, they follow the evolution of the market, protecting against changes of technology like operating system or processor platforms.

3.4.2 Evaluation of SCADA products at CERN

For the reasons outlined above, a major evaluation exercise of SCADA products [38] was performed at CERN in the frame of the JCOP. The author of this thesis forms part of the JCOP project and has been heavily involved in the SCADA evaluation.

The selection process was performed in two phases over two years. In the first phase more than 150 products were identified and their basic functionality and usability, both in development and run-time were studied. This first phase concluded with the selection of a short list of candidates. The selected products were intensively evaluated in the second phase according to the following criteria defined within JCOP:

- ***Openness****;* in terms of both connectivity to external databases or systems, like the DAQ system or LHC accelerator, and capability to extend the functionality of the product to interface custom applications or equipment (e.g. availability of driver development toolkit). This criteria is derived from the very demanding requirements outlined in chapter 2 that differ from those of the industry.
- ***Distribution****;* this refers to the capability to split the supervisory software into small application communicating over the network and it is imposed by the distribution of the DCS equipment in different locations in ATLAS. This characteristic is also determined by the scalability of the product.
- ***Internal Architecture;*** owing to the very large number of I/O channels in ATLAS, it is preferred that the internal communication mechanism of the product is entirely event-driven. Values and alarms must be notified on change with the possibility to define a *deadband* or *window* range. Systems which poll data values and status at fixed intervals present too big an overhead and have too long reaction times resulting in lack of performance.
- ***System modelling;*** In conventional SCADA systems every single process variable is represented by one data-point called *tag*, with no logical organization. Complex items are split into many separated data-points difficult to group and a considerable maintenance effort is required. This type of products are *tag-oriented*. In the so-called *device-oriented* products, process variables that logically belong together are combined in hierarchically structured data-points. They define and use different levels of abstraction which allow to model an item. *Device-oriented* products adopt many properties from object-oriented programming languages like inheritance and instantiation. These features facilitate the partitioning and scalability of the application. For these reasons, this kind of products is more appropriate to model the natural partitioning and hierarchy of the detectors described in chapter 2.
- ***Multi-user/multi-location;*** this requirement arises due because the control system of the LHC experiments will be developed by many teams distributed all around the world. The SCADA product must allow for conveniently integrate these applications into a coherent system. This features is also tied to the partitioning aspects of the ATLAS DCS.
- ***Performance;*** in terms of configuration of large number of variables, alarms, archiving, and of run-time behavior, e.g. number of variable changes per second, avalanche of alarms, script performance, trending and archiving, multiple data servers.
- ***Others;*** like remote access, scripting, exporting of configuration to external databases.

3.4.3 PVSS-II

The evaluation concluded with the selection of the PVSS-II from the austrian company ETM that fulfils all requirements outlined above. Its main characteristics are shown in table 3.6. A detailed description of the product can be found in [39]. It is a device-oriented product where the properties and functions of each data point can be parametrized by means of several attributes, e.g. alarm handling, periphery address, etc. PVSS-II is conceived as distributed systems. The single tasks are performed by special program modules called *managers*. The communication among them takes place according to the client-server principle, using the TCP/IP protocol. Its architecture is centralized around the *RT Event Manager* which handles the communication with all other modules. The different components can be arranged in functional layers as shown in figure 3.12.

Table 3.6 *PVSS-II system data*

Client-server architecture
Multi-platform: Windows NT/2000, Linux
Device-oriented data-point model
Unlimited number of data-points
High speed database
Unlimited archiving size
SQL-based interface
Application Program Interface (API) developed in C++
User Interface Builder
C-like interpreter
Multi-tasking and multi-threading capabilities
Time or event controlled triggering of scripts
Web interface
Software interfaces: DDE[1], DLL[2], ODBC, JDBC, etc.
Hardware interfaces: OPC, Profibus and others.

1. Dynamic Data Exchange (only under Windows).
2. Dynamic Link Library.

The Front-end Interface layer provides the communication with the hardware by means of dedicated drivers or communication standards such as OLE[a] for Process Control (OPC). It also provides drivers for standard fieldbuses, like Profibus and PLC. Neither CANbus nor VME are supported. The front-end layer also performs

data processing to reduce the data volume from the equipment. In addition to handling of bi-directional transmission of the messages between the different managers, the management layer is also responsible for managing RT data, archiving, alarm handling and administration of the user privileges.

The Processing layer contains control applications which are written within the SCADA system using its own programming language. They can be of two types: the first implements procedures dedicated to monitoring and controlling the detector; the second consists of specialized programs which extend the SCADA functionality, such as Finite State Machine (FSM) or additional reporting features.

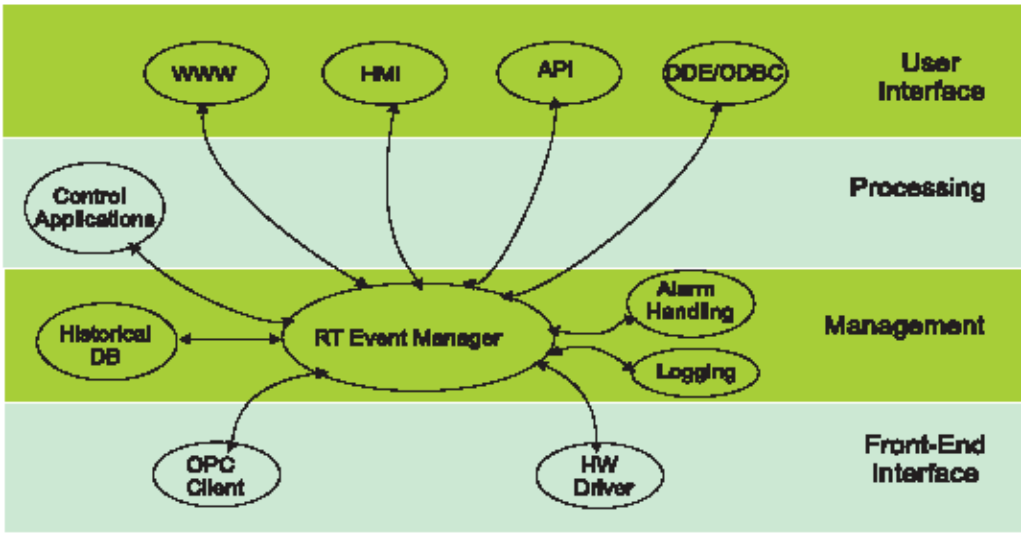

Figure 3.12: *PVSS-II System Architecture*

The user interface layer takes care of external interactions. PVSS-II provides a powerful Human–Machine Interface (HMI) easily customizable by means of graphical objects that can be linked to the different process variables in the application. It includes a WWW server for remote access to the application. External programs communicate with the Management layer via the API, allowing external applications to subscribe to any RT and historical data and alarms.

PVSS-II is multi-platform, running under several varieties of Windows, Linux and Unix flavours. The managers can be distributed over different platforms, and the communication between them is internally handled by PVSS-II. This has been one of the crucial points in the selection of this product since the DAQ system of the ATLAS experiment is been developed entirely under Linux.

a OLE stands for Object Linking and Embedding and it is a Microsoft standard based on the Distributed Compound Object Model (DCOM).

Although PVSS-II will be used as the basis of the LHC experiment controls, this has been found not to be sufficient to develop an homogeneous and coherent system. An engineering framework on top of PVSS-II is being developed. It is composed of a set of guidelines, tools and components which will be provided to developers of sub-systems in order to:

- Reduce to a minimum the work to be performed by subdetectors teams by re-using standard components rather than duplication.
- Design the system architecture in terms of distribution of functionality and network distribution.
- Define guidelines for development, alarm handling, control access and partitioning, to facilitate the development of specific components coherently in view of its integration in the final, complete system.
- Improve performance reliability and robustness.
- Cover the lack of functionality of PVSS-II like interface to CANbus or VME, integration of FSM.

3.5 Integration FE - SCADA

The ELMB will be widely used in the implementation of the subdetector front-end systems. On the other hand, the PVSS-II product will be used as SCADA system for the implementation of the supervisory layer of the ATLAS DCS. There are two main approaches to interface the ELMB, thus CANopen networks, within back-end control software like PVSS-II:

- Dedicated CANopen driver for PVSS-II
- Use a middle-ware like OLE for Process Control (OPC). This commercial specification implements a multi-client/multi-server architecture and is becoming the industrial standard to interface hardware and software. OPC defines a middle-ware, which provides a mechanism to access data from a source and communicate the data to any client application in a standard way. The OPC principle is shown in figure 3.13. No specific drivers are needed for each client. A detailed description of the OPC specification and its basic concepts is given in [40, 41].

The first solution rises problems in terms of portability and maintenance, whereas the second method was chosen since most SCADA systems implement OPC client functionality.

3.5.1 CANopen OPC servers

Figure 3.14 show the basic principle of operation of a CANopen OPC server. The I/O device network is interfaced via the server to a SCADA system, which acts as an OPC client. Using a commercial CAN network card, the data is passed from the

CANopen nodes into the PC. The OPC server works as the CANopen master of the bus handling network management tasks, system configuration and connecting to the individual object dictionaries of the devices. The OPC server usually scans the network for attached CANopen devices or these are added to the configuration individually. The device capabilities are specified in the EDS, which is imported by the OPC server. In the next step, the configuration of the CANopen network is performed as follows:

- Mapping of OD entries in the device profile area onto PDO.
- Assignment of COB-ID to PDO.
- Configuration of OD entries for OPC access via SDO

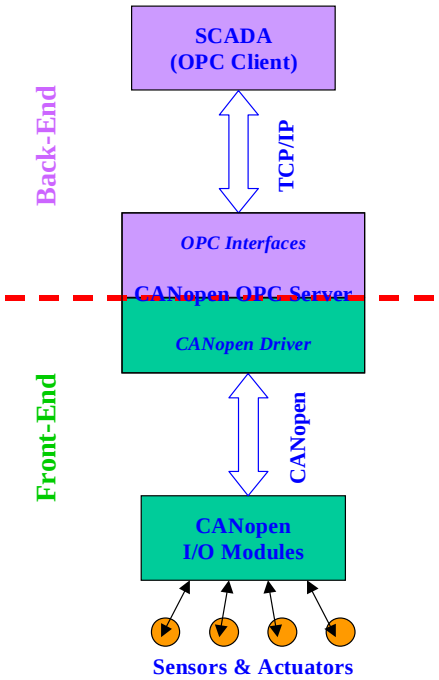

Figure 3.13: *OPC defines a middle-ware as interface middle-ware between hardware and software.*

On startup of the OPC communication, a CANopen manager integrated into the OPC server configures the CANopen devices and brings them to the operational state. The OPC standard hides the CANopen protocol from the user. No knowledge of the protocol is required at SCADA level.

Several firms offer CANopen OPC servers but those investigated present three major problems:

- They are tailored to their specific hardware interface cards.
- Lack of openness of the product; this rises problems when trying to handle the

configuration of the system from an external source as in ATLAS where the knowledge of the system configuration will reside in the SCADA database.

- Lack of functionality; the products evaluated were found to implement limited subsets of the CANopen protocol. Although they fulfil most of industrial requirements, these subsets do not provide all functionality required by the DCS of the LHC experiments. In particular, multiplexed-PDO, used in the ELMB, are not supported by any of the products studied although in some packages, this limitation can be bypassed using an additional software layer, like a softPLC. In this case, the softPLC serves as a bridge between the I/O network and OPC and handles the de-multiplexing of the CAN frames. However this solution has to be investigated further as problems of configuration from SCADA can arise.

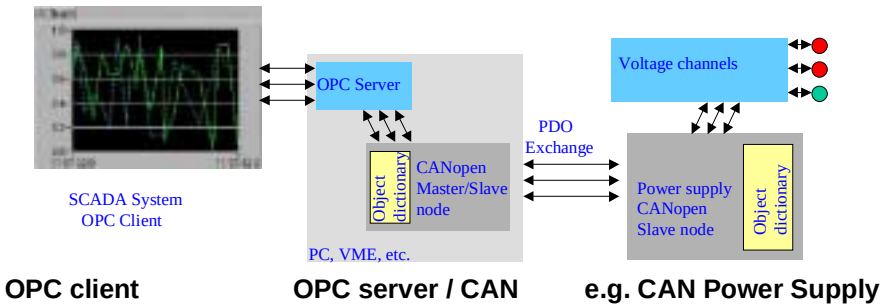

Figure 3.14: *Operation principle of a CANopen OPC server.*

For these reasons, the ATLAS DCS team has developed a custom CANopen OPC server [42], which provides all the required functionality. The server was developed according to the OPC Data Access specification 2.0 and the revision 3.0 of the CANopen specification. The server supports the CANopen DSP-301, which defines the common functionality of the I/O modules, and DSP-402, which defines multiplexing of PDO. The main features of the OPC server are shown in table 3.7 The work done by the author of this thesis consisted in testing of the product and definition of the functionality and enhancements to be added to the server.

The package is organized in two main blocks:

- Hardware dependent part, which is tailored to the specific CAN interface card from National Instruments (NI-CAN[a] with two bus ports) used. This block of the OPC server acts like a CANopen driver.
- Non hardware-dependent part, which implements all OPC interfaces and main loops to handle the communication with external applications.

a The OPC server has been tested with both PCI and PCMCIA versions of the interface card.

This factorization of the code of the OPC server facilitates the portability to a new CAN interface card, if required for reasons of performance or cost.

Several buses, with up to 127 nodes[a], each can be operated by the OPC server. The system topology in terms of networks and nodes per bus is modelled dynamically in the address space of the OPC server from a configuration file.

The server also provides a very flexible mapping of data bytes in a PDO into OPC items. It is possible to map a segment of any length and starting at any position of the PDO data bytes into a single OPC item.

Table 3.7 *Main features of the CANopen OPC server*

CANopen v. 3.0 and OPC DA 2.0
Node guarding
Access to node guarding states
SYNC generator
SYNC interval[1]
SDO[a]
Sync and Async PDOs.
Variable mapping of PDOs
Remote Transmission Request (RTR)
Direct access to NMT
NMT reaction on boot-up and emergency msg.
Up to 127 nodes per bus
Access to many CANopen networks

1. also during run-time

3.6 ELMB SCADA Framework

An ELMB software package has been developed using SCADA tools, as a framework to facilitate the usability of the ELMB node to the ATLAS users but also to achieve homogeneity of the SCADA software in ATLAS. This package will be released as a component of the general PVSS-II framework described in section 3.4.3. The product is distributed as a self-installing application, which creates all

a This limit is imposed by the addressing scheme in CANopen.

infrastructure needed to work with the ELMB. The package has been entirely developed by the author of this thesis in collaboration with J. Cook from the ATLAS DCS team. A detailed description of the application can be found in reference [43].

Once the application is started, the OPC configuration file is imported into SCADA. This information is used to model the system topology in terms of CANbus, ELMB and sensors in the PVSS-II database using data-points. There are three main data point types, which cover the minimum functionality of ELMB networks. One instance of these types is created per sensor, device or bus per each of the items on the bus:

- The ElmbBus data point type is used for network management and to identify the nodes on a particular bus.
- The Elmb data point type reproduces the modules on the different buses and their behavior in terms of I/O functionality.
- The ElmbSensor data point type is used to describe each sensor attached to the bus via an ELMB.

These data-points are connected to the items in the CANopen OPC server address space. Figure 3.15 shows the parametrization panel for the peripheral address configuration of a given analogue input channel of the ELMB data point.

Setting a data-point in PVSS-II will trigger the OPC server to send the appropriate CANopen message to the bus. In turn, when an ELMB sends a CANopen message to the bus, the OPC server will decode it, set the respective item in its address space and hence transmit the information to a data-point in PVSS-II. The SCADA application will carry out the predefined calculations to convert the raw data coming from the ELMB to physical units and trend and archive the values. The framework also provides panels for configuration and run time of the project.

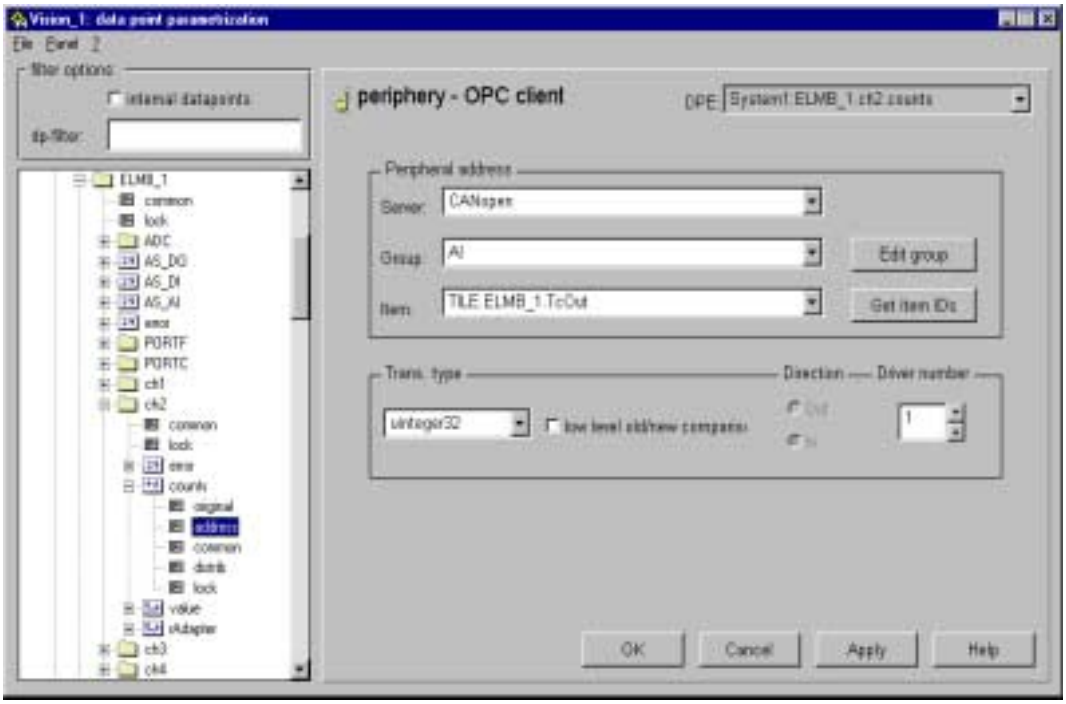

Figure 3.15: *Addressing of the ELMB data-point elements to OPC items.*

3.7 The ATLAS DCS Vertical Slice

The ATLAS DCS *Vertical Slice* [44] is defined as the full readout chain, which ranges from the I/O point (sensor or actuator) up to the operator interface comprising all the elements described above: ELMB, CANopen OPC Server and PVSS-II. The vertical slice also comprises PVSS-II panels to manage the configuration and the settings and the status of the bus.

The vertical slice has been the basis for several control applications of ATLAS subdetectors like the alignment systems of the Muon Spectrometer, the cooling system of the Pixel subdetector, the temperature monitoring system of the Liquid Argon subdetector and the calibration of the Tile Calorimeter at a test beam. The latter application is treated in detail in chapter 5 and the influence of the DCS parameter on the response of the Tilecal modules in chapter 6. In the next chapter the performance of the vertical slice are presented.

3.8 DAQ-DCS Communication

The DAQ-DCS Communication software (DDC) [45, 46] serves as interface between DAQ and DCS. This package is regarded as a DCS building block as it was

developed within the DCS activity as a collaboration between NIKHEF (Holland), PNPI (Russia) and CERN.

The work done by the author of this thesis consisted in the participation of the definition of the URD (User Requirements Document) [47] and testing of the functionality of the product in a testbeam as it will be shown in section 6.3.4.3. This was the first application of the DDC package.

A major requirement in the implementation of the DDC component has been to keep the independence between the DCS and the DAQ system while fulfilling all needs of run-time information exchange between both systems described in chapter 2, thus:

- Bi-directional data exchange like parameters and status values;
- Asynchronous transmission of messages, e.g. alarms from DCS to DAQ;
- Issuing of DAQ commands on DCS.

As these functions are independent and in order to increase the robustness of the DDC, the product was factorized into three independent subsystems: the Data Transfer *(ddc_dt*), the Message Transfer (*ddc_mt*) and the command transfer (*ddc_ct*) components.

The DDC uses the SCADA API as interface on the DCS side. This API provides full access to its run-time database, which is sufficient to implement the three subsystems of the DDC software. Handling of historical DCS and physics data is beyond the scope of the DDC.

On the DAQ side the Online Software [12] is used as interface for each of the components mentioned above. The Online Software system implements a set of tools and services for supervision and control of the components of the DAQ, including run control, configuration of the HLT/DAQ system and management of data-taking partitions, and coherent operation of the DAQ components. This system can be regarded as an equivalent to the SCADA system on the DCS side. The Online system consists of several components: run control, database or information service, message reporting system, monitoring and anciliary. The DDC connects to three different subsystems to perform each of the functions mentioned previously:

- ***ddc_dt*** interfaces the Information Service (IS) component. This DAQ subsystem handles the instantaneous values of parameters and status information similarly to the Event Manager at the SCADA level. The *collaboration-diagrams* of the ddc_dt component use cases, are shown in figure 3.16.

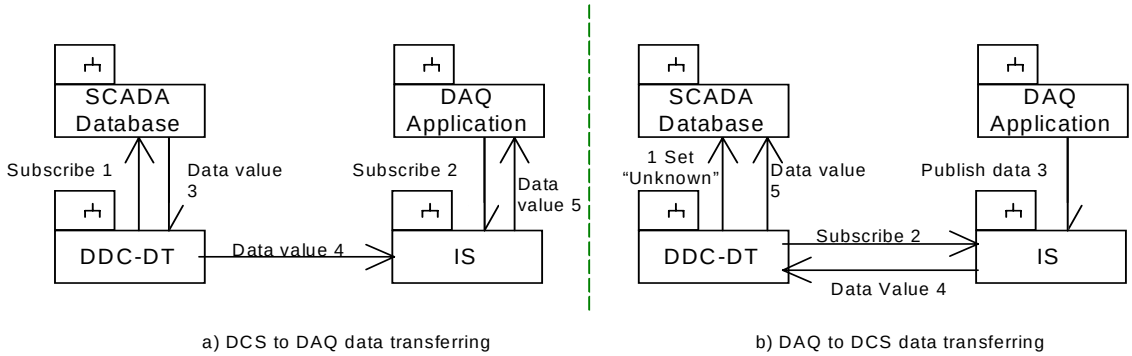

Figure 3.16: *Collaboration-diagrams of the ddc_dt component.*

- ***ddc_m***t uses the Message Reporting System (MRS) of the DAQ system as interface point. This system acts as a common distributor of asynchronous events such as error messages, making them available for any application. The *collaboration-diagram* of the ddc_mt component is shown in figure 3.17.

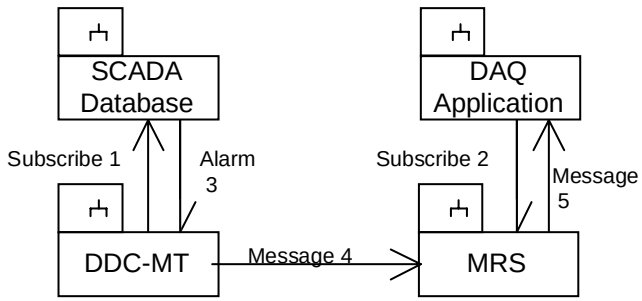

Figure 3.17: *Collaboration-diagram of the ddc_mt component.*

- ***ddc_ct*** interfaces the Run Control component of the Online Software. The RC component controls the data-taking activities by coordinating the operations of the HLT/DAQ/DCS systems, other online-software components and external systems. It is implemented as a hierarchy of interconnected controllers, which operate as FSM and are responsible for a well-defined set of devices. For these reason, the ddc_ct component is implemented as both a PVSS-II API manager, similarly to ddc_dt and ddc_mt, but also as a controller, which can be integrated in the DAQ hierarchy. The *collaboration-diagram* of the ddc_ct components is shown in figure 3.18.

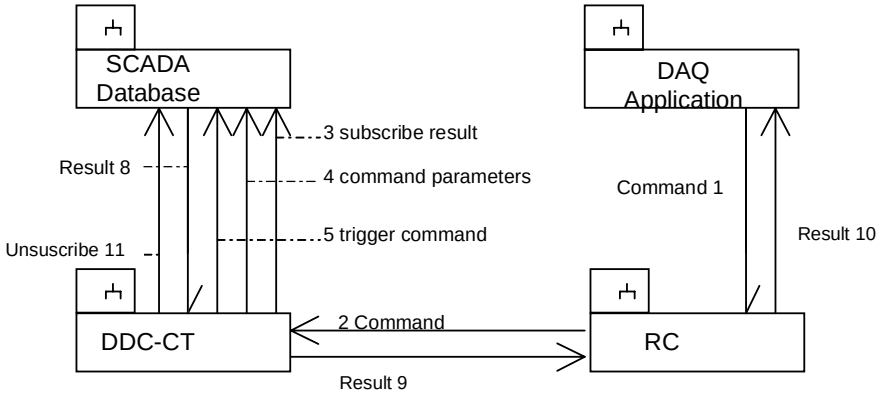

Figure 3.18: *Collaboration-diagram of the ddc_ct component.*

Although the Online Software components run on different platforms, Windows is not supported. For this reason, the multi-platform and the possibility of merging different operating systems within the same applications capabilities of PVSS-II has facilitated the integration of both systems.

Chapter 4

ELMB radiation qualification and system tests

The number of ELMB nodes in ATLAS will be of the order of 5000. The ELMB has recently been qualified for operation in presence of radiation and the different tests performed and the results we obtained are discussed in this chapter. A second set of measurements were realized to study the scalability of the *ATLAS DCS Vertical Slice*. A system with 16 nodes has been successfully operated from PVSS-II using the CANopen OPC Server as interface. The results of this tests are presented in the last part of the chapter.

4.1 Radiation Qualification of the ELMB

The radiation qualification of the ELMB has been performed in accordance to the *ATLAS Policy on Radiation Tolerant Electronics* [48]. This procedure defines essentially five steps for qualification of electronics using COTS:

- Listing of all radiation components used.
- Calculation of the so-called *Radiation Tolerant Criteria (RTC)* at a given location in ATLAS. The RTC defines the minimum dose rate that the electronics must withstand. It is calculated for the three main types of effects of the radiation on electronics:
  - **Total Ionization Dose (TID)**, which estimates the effects of the accumulated ionizing dose deposited in the oxides of the electronic components. The TID test methods are performed with gamma or X-ray irradiation.
  - **Non Ionizing Energy Loss (NIEL)**, which considers the effects caused by neutral particles, like neutrons, on the lattice of the components resulting on a degradation of the electrical parameters of the electronics components. The test procedure is therefore, done using high energy neutrons.
  - **Single Event Effects (SEE)**, this is a generic term, which encloses different

effects depending on the damage produced on the electronics:

- Soft SEE or Single Effect Upsets (SEU), which are non-permanent effects induced by radiation like bit flips that corrupt data or system configurations.

- Hard SEE or hard SEU, where effects are permanent and lead to corrupted data or system configurations.

- Destructive SEE like latch-up, burnout, gate rupture, which produce permanent short-circuits and may require protections against thermal destruction of the components. Components susceptible to this type of effects are forbidden for safety reason since they can originate fire.

The SEE test is essentially based on irradiation with high energy protons or neutrons.

The RTC for a given radiation effect is calculated from the *Simulated Radiation Levels* (SRL_{effect}) for this effect multiplied by three safety factors according to the following expressions:

$$RTC_{effect} = SRL_{effect} \times SF_{sim} \times SF_{ldr} \times SF_{lot} \tag{4.8}$$

where SF_{sim} represents the inaccuracies of the radiation, SF_{ldr} of the low dose rate effects and SF_{lot} is the correction factor due to the variation of radiation tolerant of components belonging to non-homogeneous lots. These safety factors depend on the type of effect and of the situation of the equipment in the experiment.

Under some conditions these safety factor can be reduced or event neglected ($SF=1$). This is the case of the SF_{ldr} for TID effects should an accelerated ageing test at elevated temperature is performed (SF_{ldr}=1), and of the SF_{lot} for all types of effects should components from homogeneous lots are employed (SF_{lot}=2).

The probability of soft SEU production is almost identical for all hadron above 20 MeV, whereas the contribution of lower energy hadron can be neglected [49]. Therefore, it is possible to determine the rate of SEU at a given location by extrapolation of the results obtained with 60-200 MeV protons, as follows:

$$Soft\ SEU = \frac{Soft\ SEU_m \times SRL_{see}}{ARL \times 10^8 s} \times SF_{sim} \tag{4.1}$$

where,

- Soft SEU_m is the total number of soft SEU measured during the total duration of proton beam tests;

- *ARL* is the Applied Radiation Level (total fluence of 60 – 200 MeV proton applied during SEE measurement, in hadron / cm2);

- SRL_{see} is given in hadron/cm^2 and represented the simulated fluence of high energy hadrons in 10 years;

- $10^8 s$ where s is given in seconds, represents the integrated beam time expected in 10 years.

Recovery procedures from SEE can differ depending on the type of effect. Some errors due to SEU can be automatically corrected by means of procedures built in software after a new reading. Some others require a software reset or even power cycle of the node or branch. Hard SEE usually require the replacement of the module.

- Pre-selection[a] of components to be tested.
- Qualification of batches of components according to the test procedures described in [48].
- Purchase of the qualified batches.

4.1.1 Requirements

The aim of these tests was the radiation qualification of the ELMB to be used in barrel 3 of the MDT subdetector, after the shielding of the calorimeters. The expected doses in 10 years, taken from [48] are:

- Total Ionizing Dose: 1.2 Gy.
- Non-Ionizing Energy Loss: 5.7×10^{10} neutrons/cm 2 (equivalent to 1 MeV Si).
- Single Event Effect: 9.5×10^{9} hadrons/cm 2 (>20 MeV).

Thus, applying the safety factors for each process and considering that components from homogeneous lots will be used in the mass production of the ELMB ($SF_{lot}=2$), and the TID tests are completed with an accelerated ageing test at high temperature was ($SF_{ldr}=1$), the following RTCs are obtained:

- Total Ionizing Dose: 1.2 Gy $\times$ 3.5 $\times$ 1 $\times$ 2 = 8.4 Gy.
- Non-Ionizing Energy Loss: $5.7\times10^{10} \times 5 \times 1 \times 2 = 5.7\times10^{11}$ neutrons/cm^2 (equivalent to 1 MeV Si).
- Single Event Effect: $9.5x10^{9}$ hadrons/cm^2 $\times$ 3.5 $\times$ 1 $\times$ 2 = 9.5×10^{10} hadrons/cm^2 (>20 MeV).

where the first safety factor considers uncertainties of the calculation of the SRL for each effect, and the safety factors due to low dose rate effects and components from non-homogeneous lots are 1 and 2 respectively, *i.e.* accelerated ageing test at high

a In the case of the ELMB this step is slightly different since a specific set of COTs, those used in the module, had to be tested.

temperature will be performed and components from homogeneous lots will be employed.

4.1.2 TID

The qualification of the ELMB for TID effects was carried out in several campaigns, and a total of 5 nodes were exposed to radiation. The nodes were irradiated using gamma sources with different dose rates to evaluate a possible dependence of the results on this parameter.

The setup employed was similar in all cases. The nodes were connected to a PC running a SCADA application for data acquisition via a 30 m long CANbus. A CAN bus analyzer was used as bus monitor while the tests were performed.

Constant DC bias voltages were applied to each channel of the ADC by a resistor network and the values were displayed and stored by the SCADA application. 17 digital outputs and inputs were interconnected. A dedicated test program, running in the ELMB, was used to set the output port while the input port was directly read into the SCADA application. The readout interval was 1 minute in all cases. In addition, the current flowing in each of the three power regions of the nodes, CAN, digital and analogue parts, were also monitored using another node. The values obtained were compared to those measured before and after the test.

4.1.2.1 PAGURE Test

In this first test [50, 51] two ELMB modules (ELMB1[a] and ELMB2) were exposed to gamma radiation from a ^{60}Co source at the PAGURE facility of CIS-bio International, Saclay, France. The energy of the gamma radiation was 1 MeV. The ELMB were placed 1.4 m perpendicularly to the source, where the expected dose rate was 77 Gy / h.

ELMB2 was irradiated up to a total dose of 80 Gy. At this value the ELMB stopped working.

Two main problems were identified in this test:

- High current consumption by the CMOS components of the ELMB, the two microprocessors and the CAN controller, was found. This caused the on-board current protections to reduce the power by decreasing the voltage on this

a An special magnetic coupler was tested in this node although it was not intended to be used in the design of ELMB. This resulted to be a weak component causing the ELMB1 to block the bus after 55 Gy. For this reason, it is considered that results obtained for this node are not significative.

component beyond the operating threshold. After the test, the protection circuit was bypassed and the node could be operated again. Figure 4.1 shows the sum of digital and analogue currents measured during the test. A significative increase of current is found after a total dose of 35 Gy. No problems were found for the CAN and analogue currents. The values of the overall current consumption of the node, before, during and after the test, are shown in table 4.1.

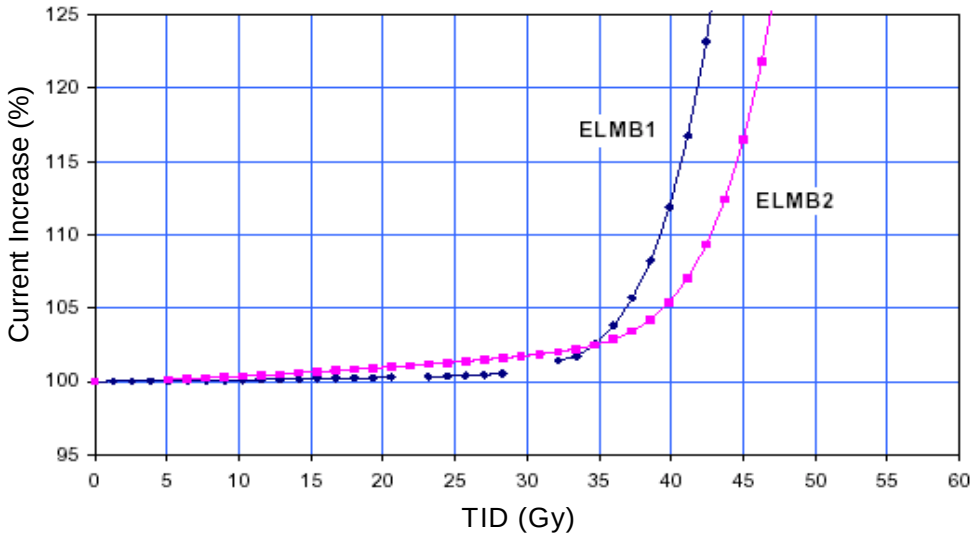

Figure 4.1: *Increase of the digital and analogue currents of ELMB1 and ELMB2 as a function of the TID. Dose rate 77 Gy/h ±6%.*

Table 4.1 *Current consumption of the different power regions of the ELMB (TID ~80 Gy).*

Power Supply	Before Test	After Test	After 48 h
CAN	19 mA	19 mA	19 mA
Digital	35 mA	130 mA	118 mA
Analogue	9-10 mA	10 mA	9 mA

- Studies of the microprocessor after the test (~80 Gy), showed that although the flash and EEPROM memories were still functional, the in-system re-programming capability of the microprocessors was lost.

4.1.2.2 First test at GIF and the annealing test

A second test was performed at the Gamma Irradiation Facility (GIF) at CERN [50, 52], where a third module (ELMB3) was irradiated by a ^{137}Cs gamma source of

0.662 MeV. This ELMB was mounted at 25 cm of the source where the measured dose rate was 0.48 Gy / h.

Contrarily to the test performed at PAGURE, digital and analogue currents were measured independently. A total dose rate of 43 Gy was accumulated. The data obtained confirmed the results found in the previous test. The digital current starts increasing after an integrated dose around 30 Gy and the re-programming function stopped operating after the test. Figure 4.2 shows the analogue, digital and CAN currents of ELMB3 during the test.

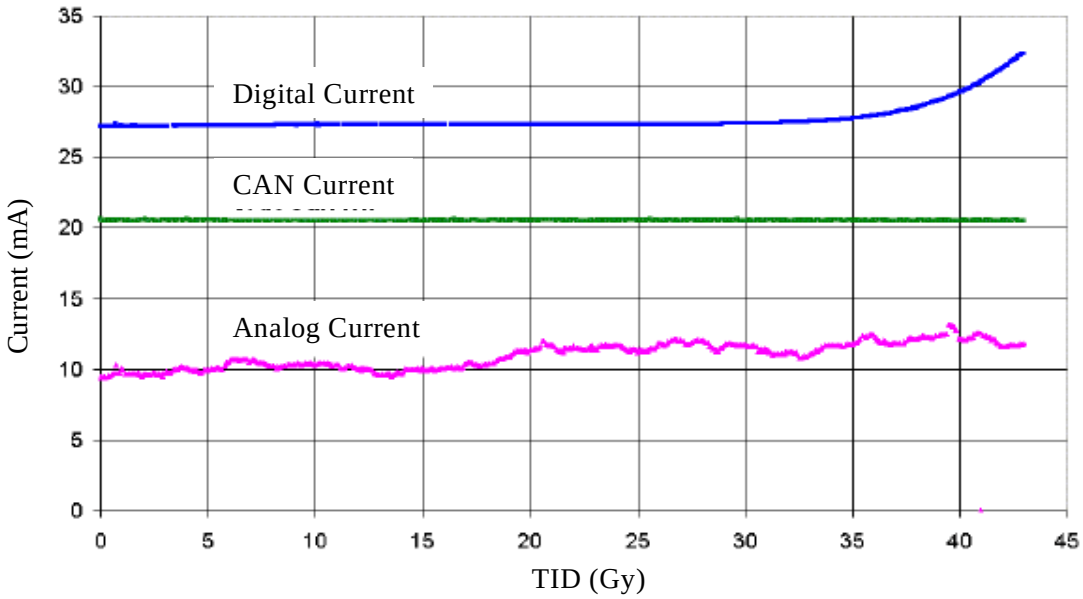

Figure 4.2: *ELMB3 currents as function of the TID in GIF (Dose rate ~0.48 Gy/h).*

The TID measurements were completed with an annealing test at high temperature in a climate chamber. The temperature of ELMB3, together with a non-irradiated node, referred as ELMB4, was varied from the room temperature, to 50, 75, 85 and 100 ^{o}C, *i.e.* beyond the maximum operating temperature of some of the components used. The equivalent total number of hours of operation of the device (*device hours*) reached was 40000 at 25^{o} C or one week at 100^{o} C according to [53].

The results showed in table 4.2, indicate that the three currents of ELMB3 returned to the original values after this test. CA subsequent check of the processors showed that the re-programming functionality of the flash and EEPROM memories was recovered and the processors were fully operational with all parameters well within the specifications.

Table 4.2 *Current consumption for the three power regions of the ELMB.*

	$I_{Digital}$ (mA)	$I_{Analogue}$ (mA)	I_{CAN} (mA)
Before Test	27.2	9.6	20.5
After ~43 Gy	32.4	11.8	20.5
After ageing Test	26.8	9.5	20.4

4.1.2.3 Second Test at GIF

A new version of the ELMB module was released after the previous tests. The only difference with respect to the modules previously tested was its operating voltage which was decreased from 5 to 3.3 V. This third test was also performed at the GIF installations at CERN for the same dose rate [54].

Contrarily to the previous tests where all modules were irradiated continuously, the module under testing, ELMB5, was irradiated during periods of about 10 h per day. Periods with no beam were used to test the in-system re-programming capability of the ELMB by loading a new version of the ELMB code. The test was also motivated by the study of the evolution of the currents measured after these periods of irradiation.

The total accumulated dose in this test was 80 Gy and the results reproduce those obtained in the previous tests. Figure 4.3 shows a comparison of the digital current measured during this test with those from previous studies. Additionally, it was found that the reprogramming capability of the microprocessors stopped working after receiving a total dose between 35 and 40 Gy.

4.1.2.4 Conclusion after the TID campaigns

The three TID tests performed showed reproducible results. The digital part of the ELMB works satisfactorily up to an accumulated dose of about 35 Gy. At this point the in-system re-programming capability is lost and it is observed that the current consumption of the digital part of the node starts increasing. These two effects seem to be independent on the dose rate in the range from 0.48 to 77 Gy/h. No effect is observed on the ADC performance. These results suggest the possibility to use some ADC channels of the ELMB to monitor its own currents in order to detect a current increase and replace the module well before the reprogramming functionality is lost. On the other hand, although small changes of the analogue and CAN currents are observed, they are not relevant for the operation of the ELMB. After annealing the ELMB is fully operation and all parameters are within the specifications.

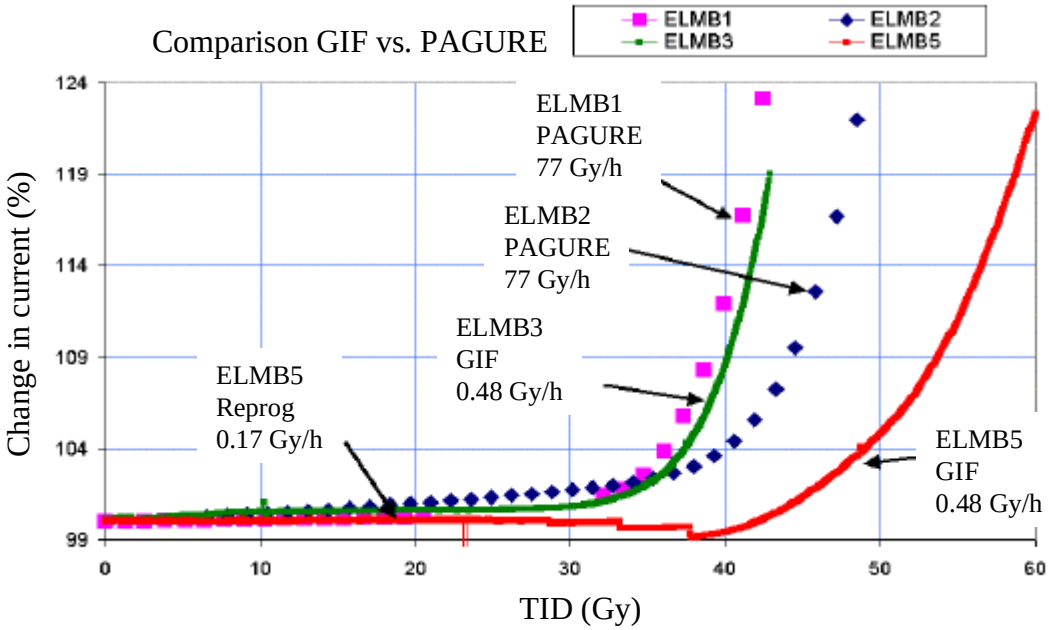

Figure 4.3: *Comparison of the digital current from all TID tests.*

4.1.3 NIEL Test

The test was performed at the installations of the PROSPERO reactor of CEA, Valduc, France [50, 55]. A total of 10 ELMB were exposed to a neutron beam of energy 0.7 MeV and a maximum fluence of 6×10^{12} neutrons/cm^2. The test setup was similar to that used in the TID tests although contrarily to this test, no power is applied to the modules. In addition to the test for digital, analogue inputs of the ELMB and the monitoring of the current consumption before and after the test, the bipolar components used in the ELMB, thus the voltage reference AD680 and the two low drop voltage regulators MIC5203-5V and MIC5203-3.3V were examined in detail. The results show that the ELMB were fully operational after the test and no changes were found in the ADC response. The digital part current, shown in figure 4.4, presents a small increase of about 10%, although it is not significative. The output voltage of the bipolar components under study was found to be well within the specifications given by the manufacturer (±3%). The re-programing capability of both microprocessors was found to be working normally after the test.

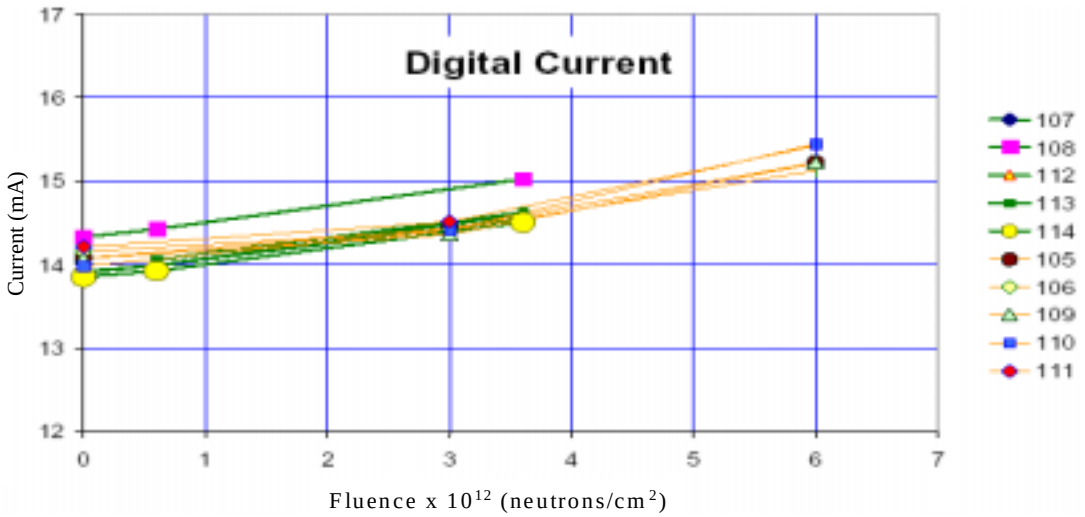

Figure 4.4: Digital current of for 10 ELMB nodes as a function of the neutron fluence during the NIEL test at PROPERO.

4.1.4 SEE Test

The SEE test was performed at the facilities of the CYclotron of LOuvain-la-NEuve (CYCLONE) of the Universite Catholique de Louvain, in Belgium [56]. The irradiation was performed with a 60 MeV proton beam. As this type of particles also induces TID effects on the electronics, the fluence of the beam was selected such that the total accumulated dose was kept of the same order as the maximum dose tolerated by the ELMB (~35 Gy) found in the tests described above. This allowed to isolated pure SEE effects on the electronics. A fluence of 3×10^{10} protons/cm^2, corresponding to 39 Gy was chosen. In order to achieve the minimum required fluence, 3×10^{11} protons/cm^2 in this test, a total of 11 ELMB nodes were irradiated, thus a total fluence of 3.3×10^{11} protons/cm^2. The flux of the beam was fixed to a value of 2.5×10^{7} protons$\times$cm$^{-2}\times$s^{-1} in order to ensure a low SEE rate and therefore being capable of record all them.

Input signals and all currents were monitored as explained for the TID tests. The most susceptible components to SEE effects are memories and registers like CMOS devices. For this reason, a systematic study of the memories of the microprocessor and static registers of ADC and CAN controllers was performed. A dedicated software application running on the master processor of the ELMB was used to detect SEE events on these devices. A bit pattern was written into the memories and registers and after a few seconds, the pattern was read back and compared to the original. This allowed to identify possible bit changes in the pattern.

A total of 29 incidents affecting to the normal operation of the nodes under study caused by SEE effects were logged. These are shown in table 4.3, as well as the beam fluence at the time they occurred and the recovery procedure followed.

Table 4.3 *Errors observed during the SEE test and recovery procedure followed.*

Recovery	Number of SEEs detected for $3.3x10^{11}$ protons/cm^2	Fluence for 1 error
Power cycling[a]	1 (Single Event Latch-up)	3.3×10^{11}
Power cycling[b]	3	1.1×10^{11}
Software reset	5	6.6×10^{10}
Automatic recovery	20	1.6×10^{10}
All types of recovery	29	1.1×10^{10}

a. The digital current increased abruptly and simultaneously, the program running the tests in the ELMB stopped working.
b. Power cycling was performed three times for the following reasons:
   - Digital inputs of one ELMB were sent every ms blocking the bus.
   - The test loop time increased for one module.
   - One of the nodes stopped sending data.

Most of SEE effects are recovered automatically and, even more important, two successive errors in the same ADC channel were never observed. This is particularly remarkable because, as mention in chapter 2, two consecutive wrong readings will be required to trigger an alarm in ATLAS.

One Single Event Latch-up was observed, which was manifested as a high increase of the current consumption in the digital part of the ELMB although it was not possible to identify in which of the 3 CMOS components of the module. A power cycle of the node was required in order to recover the operation of the node. No permanent damages of the ELMB were induced due to the over-current protection circuit implemented in the ELMB. This incident suggests to monitor the current consumption of the node and the implementation of procedures for automatic on/off power cycle of the bus.

As the fluence achieved in this test differs from that expected in barrel 3 of the MDT detector, 9.5×10^{10} protons/cm^2, the results obtained must be scaled accordingly.

Table 4.4 gives an example of the maximum allowed rates for the different types of SEE and the error recovery procedure to be followed, based on the LEP experience

Table 4.4 *Example of maximum allowed rates for the different categories of SEEs.*

SEE Category / Symptoms	Error recovery	Maximum allowed rate
Soft SEE / Data readout errors	Automatic digital filter	6 per 1h per CAN branch
Soft SEE / CAN node hangs	Automatic software reset	1 per 24 h per CAN node
Soft SEE / CAN branch hangs	Automatic power cycling	1 per 24 h per CAN branch
Hard SEE / Permanent error	Manual replace ELMB	1 per year for 1200 ELMBs
Destructive SEE / Damage	Not allowed	Not allowed

The values shown in this table can be used to determine the maximum allowed number of SEE of each type per node and in 10 years of operation of the detector, *i.e.* 10^8 s of ATLAS integrated beam time, according to [48]. These values, together with the results obtained in this test, are shown in table 4.5 where a total of 32 ELMB nodes per branch has been assumed.

Table 4.5 *Result of the SEE test compared to the maximum allowed rates of the example case given in table 4.4*

Recovery	Requirements for 9.5×10^{10} h/cm^2	Measured for 3.3×10^{11} p/cm^2	Result for 9.5×10^{10} h/cm^2
Soft SEE			
Automatic	6250	21	6
Software reset	1429	5	1.4
Power cycling	45	4	1.2
Hard SEE			
Replacement	0.0083	0	0

All the expected rates are well below the requirements although, due to the lack of statistics, the hard and destructive SEE effects can not be estimated.

The examination of the memories and registers during the test, showed a similar behavior for all ELMB nodes. Figure 4.5 shows the map of the SRAM addresses where SEE were found. The results obtained are summarized in table 4.6. In this table the cross section of a process is given as the total number of events of this type divided by the total fluence of the beam and the size of the memory under study. The cross section represents the probability of having a SEE effect of a particular type per bit of memory.

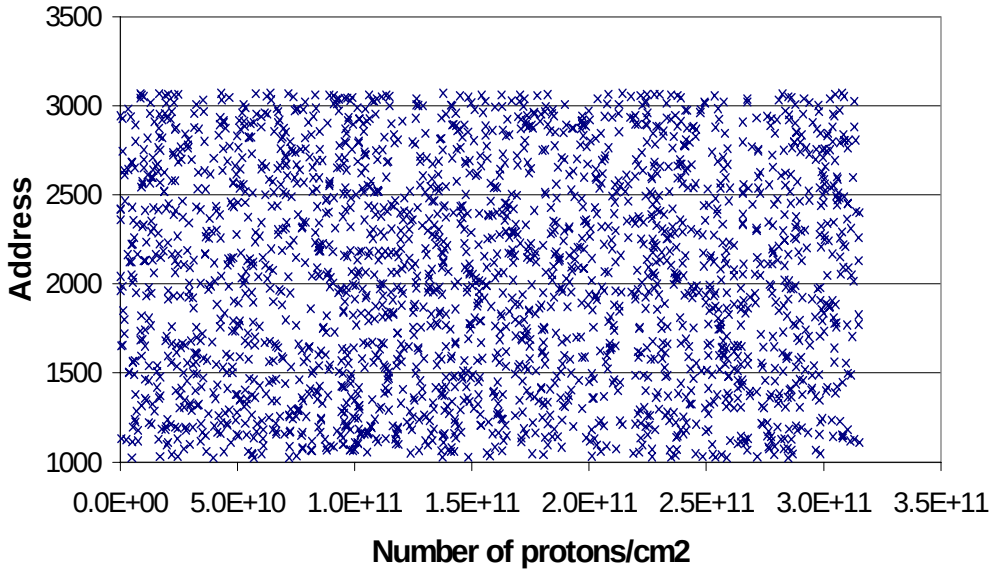

Figure 4.5: SRAM addresses where SEE were detected.

Table 4.6 *Total number of errors due to SEEs in the different memories and registers of the ELMB.*

Type of Memory	No. of bits tested	No. of errors	Cross-section (cm^2/bit)
SRAM	16384	2320	4.3×10^{-13}
EEPROM	28672	<1	$<1.1\times10^{-16}$
FLASH	1048576	<1	$<2.9\times10^{-18}$
CAN registers	320	23	2.2×10^{-13}
ADC registers	264	22	2.5×10^{-13}

These results indicate that both EEPROM and FLASH technologies are more robust than SRAM to SEE events. Therefore, it is possible to decrease the sensitivity of the ELMB to this type of events by structuring the software such that it makes an intensive usage of the EEPROM and FLASH while the values residing in SRAM are regularly updated from the other memories.

The TID data analysis showed that no relevant changes were induced on the electronics after an accumulated dose of 39 Gy, confirming the results obtained in previous measurements.

4.1.5 Conclusion from the radiation qualification

Table 4.7 shows the final results of the radiation qualification tests of the ELMB for each of the different effects. The results in this table are compared to the requirements, defined according to the ATLAS policy on radiation tolerant electronics for components placed outside the calorimeters in ATLAS, *i.e.* the MDT barrel region.

Table 4.7 *Summary results of the radiation qualification of the ELMB compared to the requirements for the MDT barrel region.*

Radiation Effect	Requirement	Qualification
TID	8.4 Gy in 10 years	~40 Gy in 10 years
NIEL	5.7×10^{11} neutrons/cm^2 (1 MeV eq.) in 10 years	$>5.0\times10^{12}$ neutrons/cm^2 (1 MeV eq.) in 10 years
SEE	9.5×10^{10} hadrons/cm^2 (>20 MeV) in 10 years	$>>9.5\times10^{10}$ hadrons/cm^2 (>20 MeV) in 10 years

For all types of effects, the results achieved during the different campaigns have qualified the EMLB to be used in the barrel region outside of the calorimeters of ATLAS,.

4.2 ELMB full branch

All applications previously mentioned in chapter 2, have used a reduced number of ELMB modules. However, the present estimate for the number of ELMB used for the whole of the ATLAS experiment is around 5000. The maximum number of ELMB per bus is limited by the hardware addressing scheme of the node to 64, since only six bits are used. However, in an ATLAS application, this number will be determined by the following conflicting constrains:

- Cost; a higher number of ELMB modules per bus would imply a lower number of CAN networks and, therefore, less interface cards and PC would be required.
- Affordable number of channels to be lost in case of a branch failure.
- Performance and reliability of the readout system.
- Powering of the CAN network; the ELMB node is designed for low power consumption to allow for remote powering of several nodes on a bus. The power will be provided to the ELMB nodes via the CANbus from remote power supplies. These are placed in the underground electronics room USA15 because of the harsh environmental conditions in UX15. An excessive number of ELMB nodes per bus can cause a voltage drop on the cable beyond acceptable limits.

To investigate the scalability of the *ATLAS DCS Vertical Slice* to the size required, a full vertical slice (or full branch) with 16 ELMB, was assembled [57]. The aim of this test was to observe the behavior of the system under these conditions in order to discover the limits and settings required to achieve the optimal results. In particular, the following was to be inspected and investigated:

- Powering
- Bus loading
- Number of nodes per bus (and its effect on bus loading)
- Load distribution amongst the different (processing) elements in the read-out chain
- Bus software settings such as update rates for OPC and SYNC interval
- Determination of bottle necks in the chain

The data traffic on the bus has to be distributed in order to keep the bus load low under normal operation. However, in the worst case (major failure in the system), all ELMBs will attempt to send data to the bus at the same time. This will cause an avalanche of channel information which must be handled by the system, and therefore simulated for this test.

Results from this test together with radiation tests of the ELMB will define the evolution of the ELMB bus behavior as well as the load distribution.

4.2.1 Test setup

Figure 4.6 shows the setup as used for the test. The front-end consists of a 200m CAN bus with up to 16 ELMB connected to this end, with a spacing of 0.5m between each one. The characteristic impedance of the bus cable was matched using 120 Ω terminators at each end of the bus. The back-end consists of two PC interconnected via a TCP-IP network. The communication between these PC is handled internally by PVSS. Both PCs were running PVSS-II v2.11.1. The Local Control Station (LCS) PC also contained the OPC Server and a National Instruments (NI) CAN interface card for connection to the bus. The supervisory station PC ran the user interface for starting, stopping and analyzing the tests.

4.2.1.1 Hardware Setup

A single Power Supply (PS) was used giving power to the CAN and digital parts of the ELMB. A link was made between the digital and analogues parts of each ELMB so that the latter also powered from this source. Connectors were used to be able to decouple the power lines of the NI interface card and of the CAN bus. This allowed each part to be given a hard reset independently of the other. Under normal

circumstances, the PS would be set to supply 12 V. This was found to be insufficient and more details about this can be found in section 4.2.3.

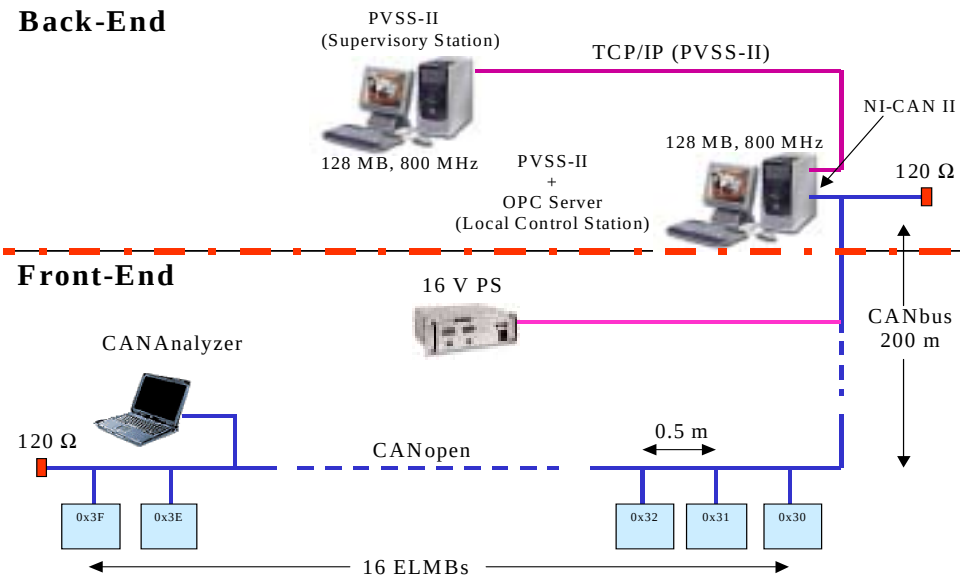

Figure 4.6: *ELMB Full Branch Test Setup*

Figure 4.7 shows the setup as it was for the test. The laptop PC was used to run software called CANalyzer, from Vector Informatik GmbH, that can listen to the bus traffic at the CANopen level. The other two PC shown in the figure are the LCS and the supervisory station. The long white coil is the 200 m CAN bus. Several multi-meters and an oscilloscope were used for monitoring the power at various points along the bus.

For 16 ELMB nodes the total number of channels read is 1024. For the shake of simplicity, deue to this large number of channels, no sensor devices were connected to the inputs, and as the OPC standard ensures that data is only updated on change, a way to force values to vary had to be found. To do this, the ELMB software was modified so that a *count* value was added on to each ADC reading.

4.2.1.2 SCADA Software

For this test, PVSS II was configured as a distributed network application running on two PC. This gave the flexibility to swap PVSS II managers from one PC to the other in order to try different software configurations allowing the load distribution to be investigated. The software organization as used in this test is shown in figure 4.8.

Figure 4.7: *Vertical Slice physical setup*

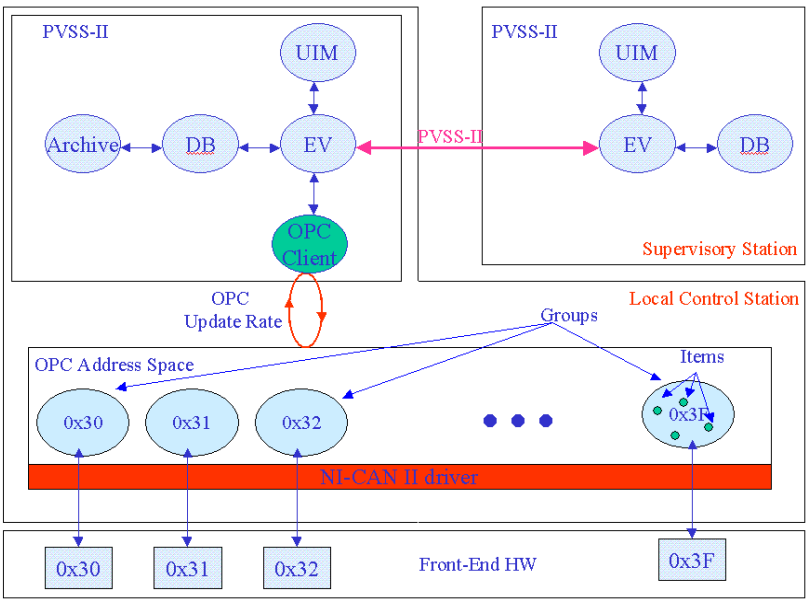

Figure 4.8: *Software Architecture*

Figure 4.9 shows the main user interface panel for the run control part of the SCADA software. This panel was used from the supervisory station PC for starting and stopping each test run.

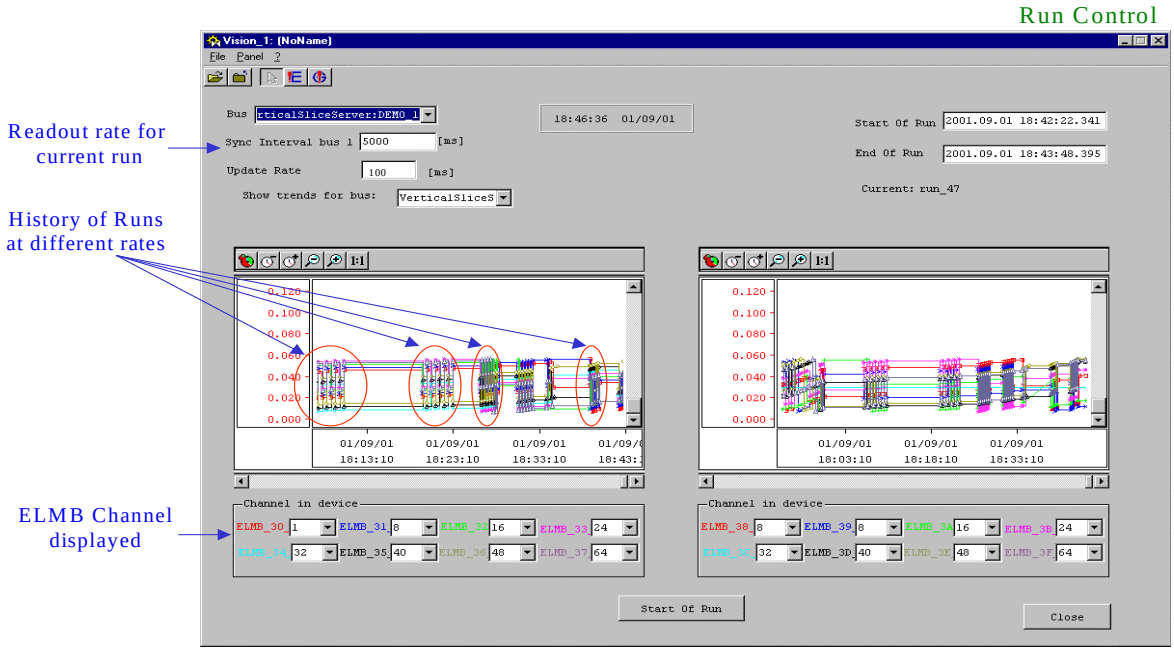

Figure 4.9: *: Run Control user interface for Vertical Slice test*

While the tests were running, the values being read from the ELMBs were displayed on a plot, giving an indication of how much information was being accepted into PVSS. For each ELMB, one channel, which could be selected at run time, was displayed. Every time a run was started, a new data point would be created which was given a unique name corresponding to a run number. This data point holds information such as start and stop times and the synchronization interval set for the run. This information was then used to calculate other parameters for the analysis and to aid in the extraction of data from the archive to check for missing data.

Figure 4.10 shows the panels used for the offline analysis. The most important part of the main panel was a display of the number of data elements received from each ELMB. If the expected number of data elements were accepted, then the ELMB shown would be displayed with a green background. If an unexpected number of elements were received, then the ELMB would have a red background. This gave a quick and informative overview of the general performance of the run. For any of the ELMB, more information may be requested by double-clicking the desired node. This displays the number of data elements received for each channel of that ELMB, again displayed with a green background for “OK” and a red one for “Bad”. The information could also be displayed as a histogram.

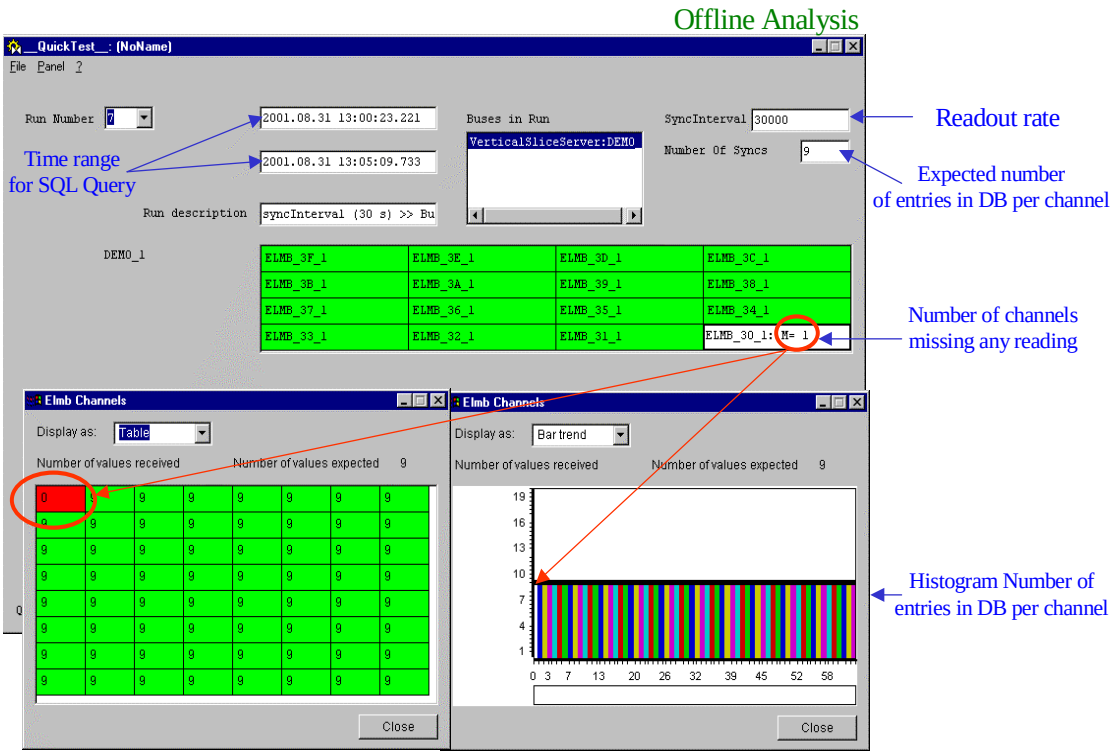

Figure 4.10: *Off-line Analysis panels*

4.2.2 Test Procedure

Using the panels described above a run would be started which would set the sync interval for the OPC Server, the update rate for the OPC Groups and log the start time of the run. Just before the run was started, the CANalyzer would be set to log all messages to a log file for comparison later on in the analysis phase. After a number of syncs had been transmitted, the run would be stopped, setting the sync interval to zero (no more syncs sent), logging the end time which allowed for the expected number of syncs within that time interval to be calculated. Various runs were performed for different ADC conversion rates, OPC update rates and synchronization intervals, to ascertain what effect these have on performance.

In order to check for the performance characteristics, two monitoring points were used. Firstly, the CANalyzer, which logs all messages entered onto the bus. This is mainly used to check that all ELMB were responding correctly at the time of the run. Secondly, the PVSS archiving facility that was used to store all the information entered into PVSS. The two sets of information were then compared to check for inconsistencies. Any data that is missing from the archive, but that is found in the CANalyzer, could then be attributed to a breakdown in the chain. However, to find out where the data went missing is a different problem. From the monitoring point of the CANalyzer to the archive, there are three possible locations where data could

have been missed, namely the OPC Server, the PVSS OPC Client / PVSS Online Database or the PVSS Archiving. No tools were available for monitoring these points and so no extra investigation was possible.

4.2.3 Measurements

Following the procedure described in the previous section, a preliminary test was performed with the aim of checking the system operation, where only the LCS shown in figure 4.11, was used. The PVSS-II archiving manager was running on this PC together with all other processes previously mentioned. The performances of the system were measured in terms of transmission of CAN frames from the ELMB to the bus and then to the PVSS-II database. These measurements were done for the four ADC conversion rates considered here, 1.88, 7.51, 15.1 and 32.5 Hz. The results at 32.5 Hz are shown in figure 4.11, showing the poor performance of the system. Two major problems were identified: powering of the bus and the large CPU usage by the PVSS-II archiving manager.

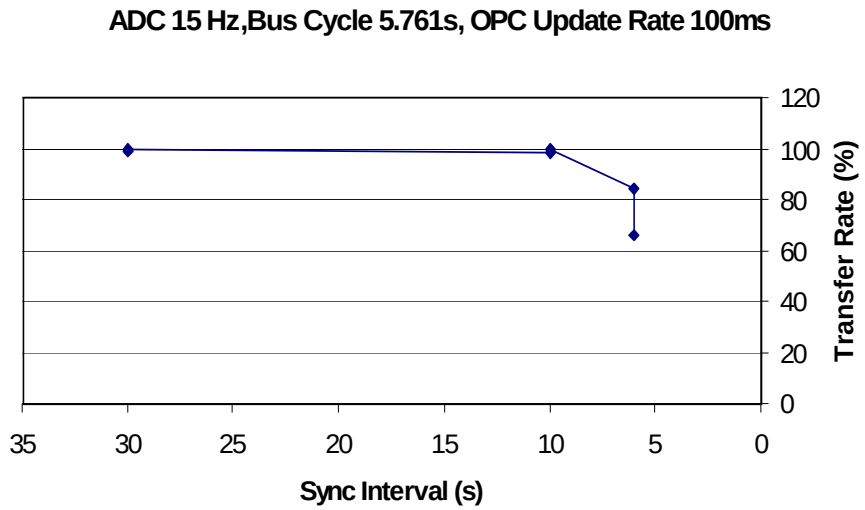

Figure 4.11: *Preliminary performance without powering optimization. All SCADA software running on the LCS.*

4.2.3.1 Powering

Checking of the CAN analyzer files allowed to find that some ELMB were not replying to a SYNC but transmitting an emergency message instead. Then the power of the ADC during its activity was monitored with a scope, and a voltage drop of about 1.4 V was observed during the transmission of frames to the bus, as a consequence of the current consumption by the opto-coupler of the ELMB. Figure 4.12 shows the voltage at the input of the ADC for several SYNC messages.

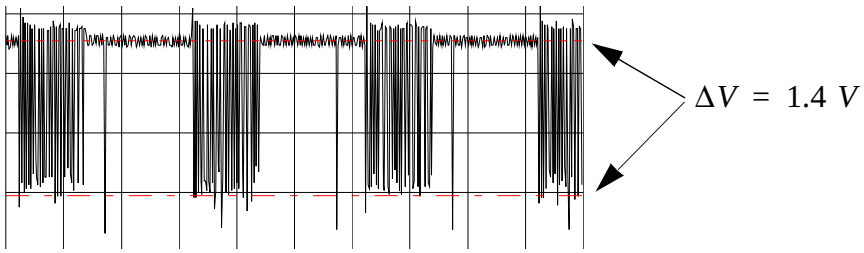

Figure 4.12: *Voltage drop at the input of the ADC for several SYNC as consequence of the current consumption by the ELMB opto-couplers.*

This current consumption caused the voltage on the analogue part of the ELMB to drop below the operating threshold of the ADC (4.5 V) in some cases, and therefore explained the absence of CAN messages for a given ELMB on the bus. The powering configuration was optimized and the final conditions were as shown in table 4.8. The voltage supplied was raised from 12 to 16 V. This value guarantees a voltage above the threshold of the ADC while the opto-couplers are operating. The voltage drop due to the resistance of the bus (ϕ = 0.5 mm^2, 37.5 Ω/km) is 3.9 V for the digital and analogue parts of the ELMB and 2.3 V for the CAN part. A voltage difference of 0.3 V was found between the positive and ground signals on the CAN part of the bus, which was caused by the NI-CAN interface card.

Table 4.8 *Summary of the powering of a 200 m long ELMB bus with 16 nodes.*

Cable resistance	37.5 Ω/km	7.5 Ω in 200m		
Currents (mA)			**Voltages**	
CAN	16×20	320	V_{PS_CAN}	16 V
ADC	16×10	160	$V_{ELMB\_16\_CAN}$	11.05 V
Digital	16×15	240	$V_{PS\_Dig+Ana}$	16 V
			$V_{ELMB\_16\_Dig+Ana}$	8.26 V
Grounding				
Drop G_CAN	2.63		Drop DP+AP	3.88 V
Drop P_CAN	2.31		Drop DG+AG	3.88 V
Difference	0.32		Difference	0
Digital + Analogue voltage drop during ADC activity				1.44 V

4.2.3.2 Software process distribution

The second problem identified was the high CPU load caused by the PVSS-II managers, which under some conditions like a fast ADC conversion, SYNC or OPC update rates, reached 100%. The major consumer of CPU was the PVSS-II archiving manager. The load distribution in terms of processes was therefore optimized. Archiving and the user interface were moved to the supervisory PC as shown in figure 4.8. With this new work load distribution, the CPU usage of the LCS never exceeds 75% while it was found that in some cases the usage raises up to 85% on the supervisory station depending on the run settings. It is clear that this problem will be minimized as PC become more performant.

4.2.4 Results

4.2.4.1 Bus Behavior

According to the CANopen standard, PDO can have different transmission modes like synchronous, asynchronous, etc. In the setup described here, the PDO used for the transmission of analogue and digital input channels were configured for synchronous transmission, i.e. they are sent to the bus as reply to a SYNC command. Additionally, the digital input signals are also communicated on change, *i.e.* asynchronously. PDO used for digital output are purely asynchronous.

Figure 4.13 shows the bus activity after a CANopen SYNC command is sent to the bus. All ELMB try to reply to this message at the same time causing collisions of the frames on the bus. The CAN mechanism of arbitration of collisions handles this situation according to the priority of the messages. Messages with lower priority are retransmitted once the end-of-frame signal corresponding to the message being transmitted (higher priority) is sent to the bus. In this figure, the bus period is defined as the time taken for all synchronous messages to be sent by all nodes on the bus after the SYNC command has been sent. δ defines the time between consecutive CAN frames on the bus and it is a function of the bus speed (typically 0.7 ms at 125 kbits/s), which also defines the maximum CANbus length. The time between successive analogue channels from a single ELMB, which is dependent upon the ADC conversion rate, is given by Δ. The SYNC command is generated by the CANopen OPC server at regular time intervals thus defining the readout rate of the bus.

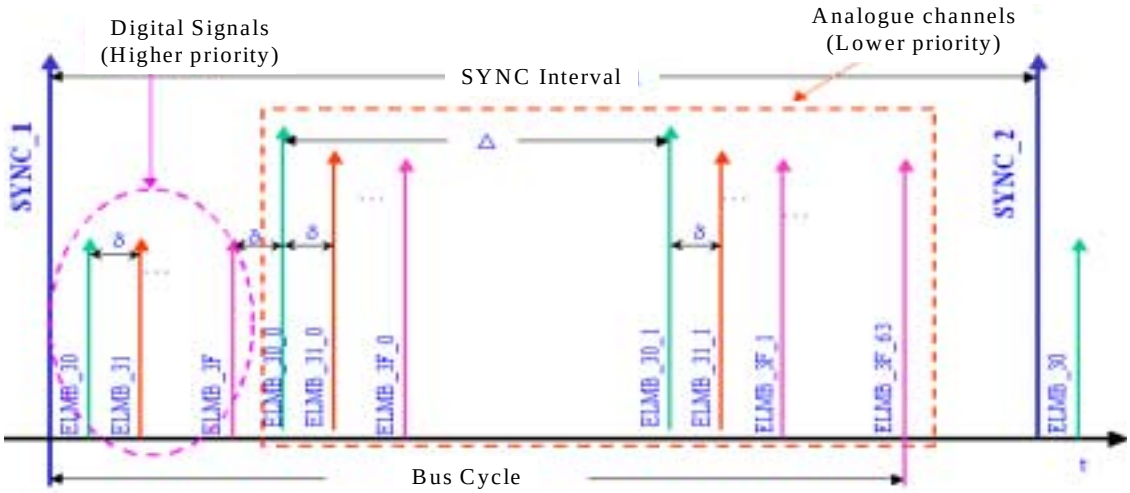

Figure 4.13: *Bus behaviour after a SYNC.*

Figure 4.14 shows the peak of the bus load as a function of the number of ELMB nodes on the bus for different ADC conversion rates. In all cases, the OPC update rate was set to 1 s. As previously mentioned, the traffic on the bus is purely due to PDO from the ELMB carrying information of the analogue and digital input channels and node guarding, performed by the CANopen OPC server in order to check the aliveness of the nodes on the bus. The peak of the bus load is reached when the avalanche of analogue channels coincides with the node guarding messages. The value of this peak at ν_{ADC} = 32.5 Hz and 16 ELMB modules on the bus is about 27%. This plot indicates that the expected level of occupancy for a bus having 32 ELMB nodes at 32.5 Hz, would be above the recommended level of 50% for pure traffic of PDO and node guarding.

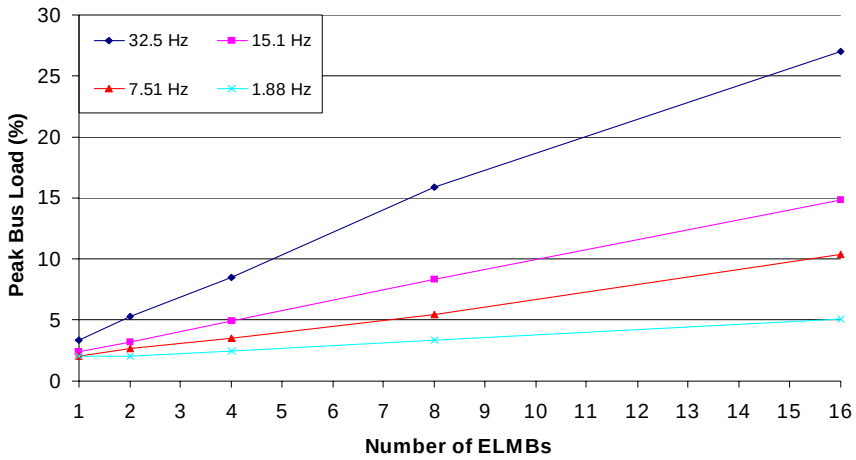

Figure 4.14: *Bus load peak as function of the number of ELMbs on a bus for different ADC conversion rates.*

Figure 4.15 shows the bus load in terms of the CAN data frames per second as a function of the number of ELMB nodes on a bus for different ν_{ADC}. This gives the number of CAN messages arriving to the interface card. These frames are buffered at this level and successively decoded by the CANopen OPC server, setting the corresponding items in its address space. These values are then transferred to the OPC client of PVSS-II at regular intervals, defined by the OPC update rate. For the values of the ADC conversion rate considered in this test, the number of data frames per second on the bus is a function of the number of ELMB modules and the ADC conversion rate. Neither the bus speed nor the SYNC interval have any influence on the rate of messages. For small buses having less than 5 ELMB nodes, the number of frames per second is dominated by the node guarding process, while for bigger buses, this rate is determined by the avalanche of analogue input channels after a SYNC.

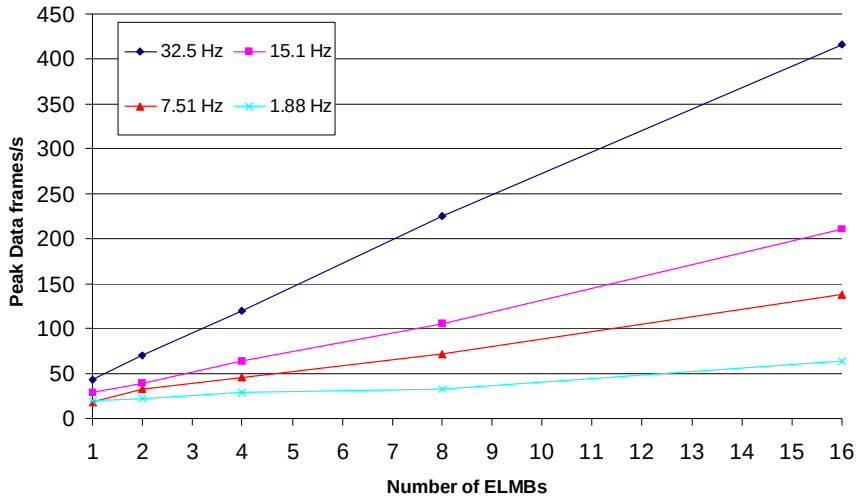

Figure 4.15: *Peak of Data frames/s as function of the number of nodes on the bus for different ADC conversion rates.*

4.2.4.2 Transfer rate

The data transfer rate from the bus to the PVSS-II database was measured as described in section 4.2.2. The measurements were performed for a bus with 16 ELMBs and different settings of the bus parameters, *e.g.* ADC conversion rate, SYNC Interval. During the test, the OPC update rate was set to 1 s and the SYNC interval was modified from greater values than the bus period down to values tending to it. A readout rate close to the bus period implies continuos buffering of messages arriving at the interface and therefore a continuos activity of the OPC server and PVSS-II managers.

The CPU usage for a conversion rate of 32.5 Hz and different SYNC intervals is shown in figure 4.16 for the LCS and supervisory PC respectively. The CPU activity

drops at a SYNC interval of 3.5 s as a consequence of overflows in the read buffer of the interface card. This observation is confirmed by the data shown in table 4.9, which shows the performance of the system at an ADC conversion rate of 32.5 Hz. The transfer rate is calculated as the rate between the number of entries found in the PVSS-II and the number of messages sent to the bus. Runs performed at different conversion rates show excellent performance achieving a transfer rate of 100% in all cases.

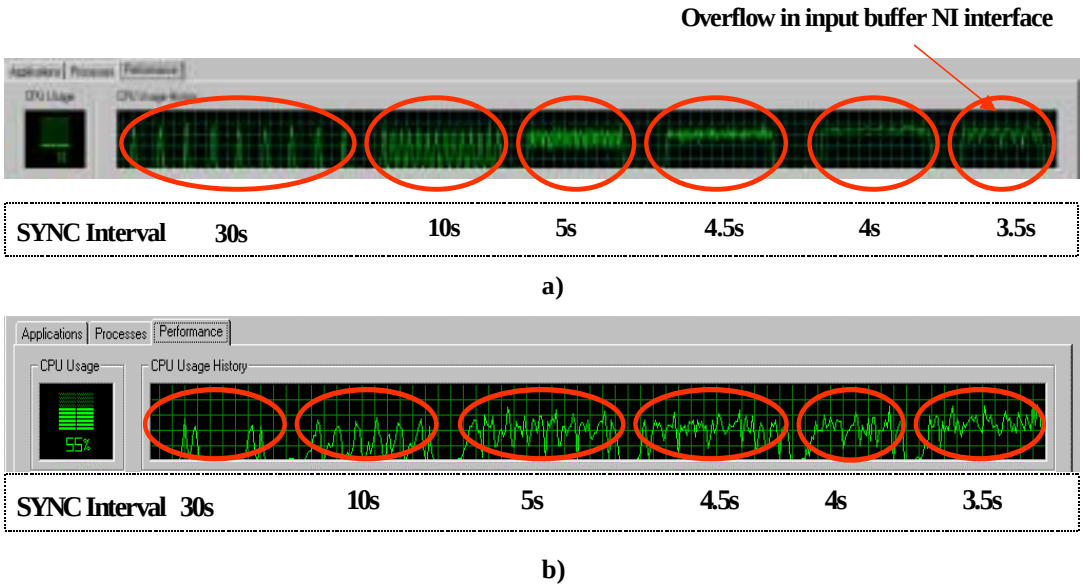

Figure 4.16: *CPU usage at ν_{ADC} = 32.5 Hz for different SYNC intervals. a) LCS, consumption due to the CANopen OPC server and PVSS-II event, database and OPC client managers. b) Supervisory station, consumption due to exclusively PVSS-II archiving manager.*

Table 4.9 *Transfer rate at 32.5 Hz and 1 s OPC update rate for different SYNC intervals*

SYNC Interval (s)	No. of SYNCs	Expected DB entries	PVSS-II DB entries	Transfer rate (%)
30	14	14336	14336	100
15	18	18432	18432	100
10	15	15360	15360	100
5	25	25600	25600	100
4	45	46080	46080	100
3.5	6	6142	5513	89.76
3	19	19456	13271	68.19

Figure 4.17 shows the measured bus period as a function of the ADC conversion rate for a bus with 16 ELMB nodes. The fastest readout rate and its difference with respect to the bus period are also shown in the figure.

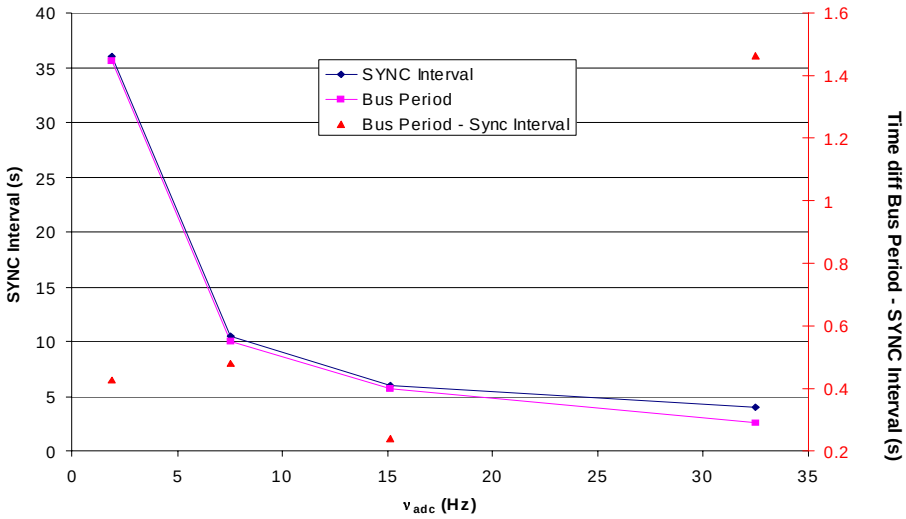

Figure 4.17: *Best possible read-out parameters as a function of the conversion rate for a transfer rate bus - PVSS-II database for different conversion rates.*

Figure 4.18 shows the transfer rate as a function of the SYNC interval for a bus with 16 ELMB nodes working at an ADC conversion rate of 32.5 Hz. The transfer rate gracefully degrades when the SYNC interval tends to the bus cycle. The fastest achievable SYNC period keeping 100% of transfer rate was 4 s.

Under these conditions, *i.e.* ν_{ADC} = 32.5 Hz and SYNC interval = 4 s, the dependence of the transfer rate with the OPC update rate was studied. The result is shown in figure 4.19. Changes of the OPC update rate imply changes in the load distribution of the different PVSS-II managers as a result of the frequency of data exchange between the OPC server and PVSS-II. The shorter the update rate is, the more often OPC communication takes place. This means that the PVSS-II managers handle smaller bunches of OPC items but continuously. Under these circumstances, the CPU usage of the PVSS-II database manager increases from 28% at a OPC update rate of 1 s to 36% at 100 ms while the CPU usage by the event manager drops from 30% at 1 s down to 4% at 100 ms, resulting in a degradation of the transfer rate. This result must be followed up together with ETM. On the other hand, the performance was worse when the OPC update rate is set too high, *i.e.* of the order of the bus period, as expected.

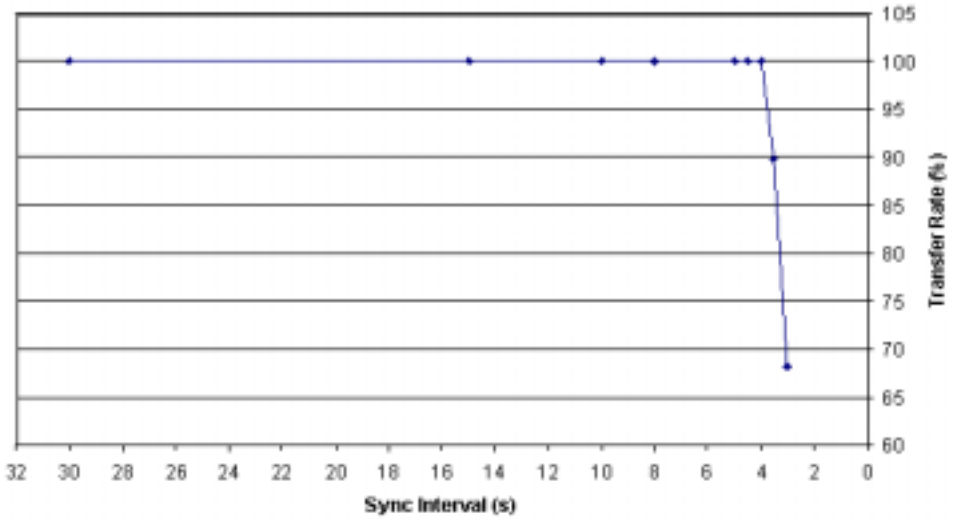

Figure 4.18: *Bus - PVSS-II transfer rate as a function of the SYNC interval for an ADC conversion rate of 32.5 Hz, OPC update rate 1 s and bus speed 125 kbits/s*

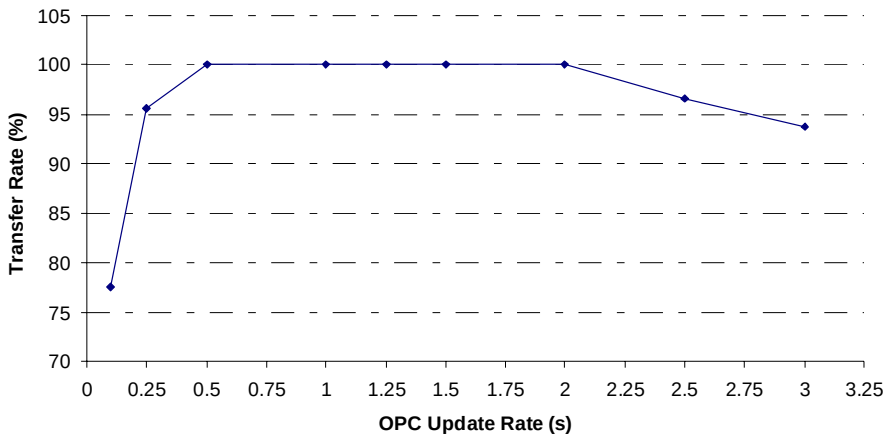

Figure 4.19: *Transfer rate at SYNC interval of 4s as a function of the OPC update rate. Bus having 16 ELMBs, ADC conversion rate of 32.5 Hz and bus speed 125 kbits/s*

4.2.4.3 Comparison at different bus speeds

Complementary measurements were performed at a bus speed of 250 kbits/s in order to estimate the influence of this parameter on the performances of the system. As previously seen 4.2.4.1, the expected bus load peak at 125 kbits/s would exceed the recommended 50% for a bus with 32 ELMB nodes. Figure 4.20 shows a comparison of the evolution of the bus load with the ADC conversion rate for a bus with 16 ELMB modules for the two bus speeds considered here. The picture shows a

much better behavior of the bus load for a bus speed of 250 kbits/s. At this speed the expected bus load peak for a bus with 32 ELMBs would be around 35%.

An increase of the bus speed leads to a shorter time interval between successive messages on the bus, i.e. δ in figure 4.13, and therefore frames arrive at a higher frequency at the interface. Figure 4.21 shows the measured transfer rate for the two cases under study, for a bus with 16 ELMB nodes working at an ADC conversion rate of 32.5 Hz, as a function of the SYNC interval. The results show very good performance of the readout chain at this bus speed. The minimum SYNC interval achieved was also 4 s. Although the fastest readout rate having a transfer rate of 100% can not be improved at 250 kbits/s, one observes slightly better performance of the system at shorter rates.

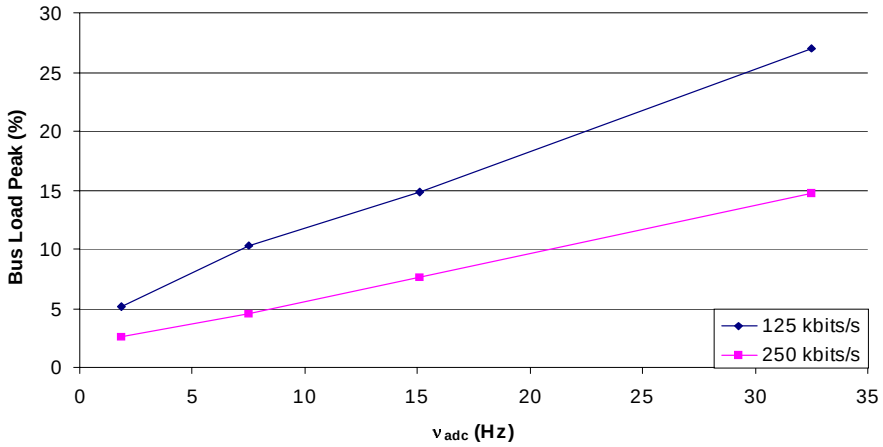

Figure 4.20: *Bus load peak as function of the ADC conversion rate for different bus speeds. The number of ELMBs on the buses is 16.*

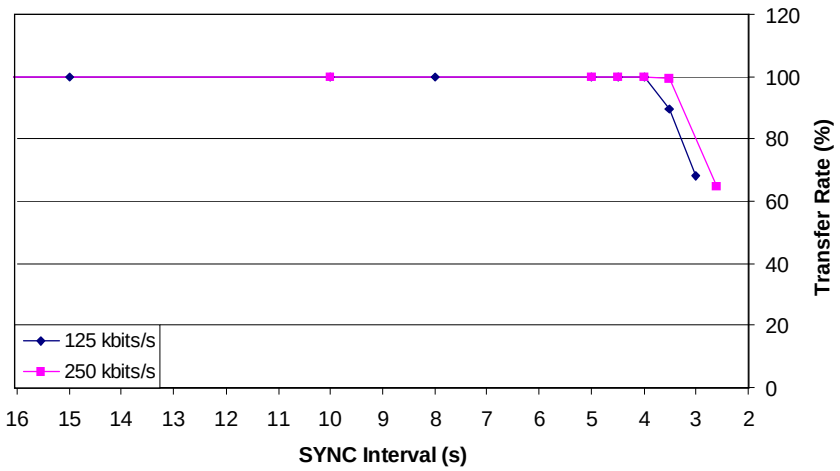

Figure 4.21: *Transfer rate as function of the SYNC interval for bus speeds of 125 and 250 kbits/s. Other bus parameters: Number of ELMBs = 16, ADC conversion rate = 32.5 Hz, OPC update rate = 1s.*

4.2.5 Conclusions and outlook

A 200 m long CANbus using up to 16 ELMB nodes has been setup. This is the expected length of a bus going from the underground electronics room (USA15) to the experiment's cavern (UX15) in ATLAS. Because of the number of input (1024 analogue and 256 digital) and outputs (126 digital), the system is comparable to some subdetectors. The test performed was aimed at reproducing the worst possible case in which all ELMB modules on the bus send data at the same time. The setup was successfully operated from a PVSS-II distributed application using a CANopen OPC server as interface. When long buses are used, the powering must be closely examined to ensure that the losses along the bus do not have an adverse effect on any ELMB. A voltage drop on the analogue part of the ELMB was found as a consequence of operation of the opto-coupler. Due to the demands made on the CPU by the archiving process, it is better to move this to a separate PC. However, this has an inconvenience as any problems on the network results in a loss of data being stored. The powering configuration and the work load distribution between the software elements in the readout chain were optimized. Performance of the system in terms of bus load and transfer rate from the ELMB nodes to the PVSS database have been measured. Results show an excellent behavior of the system with 4 s being the fastest readout rate for a bus with 16 nodes working at an ADC conversion rate of 32.5 Hz. This value corresponds to the theoretical limit of the bus readout rate, which is given by the addition of the bus period and the OPC update rate. Using a bus speed set to 250 kbits / s, which allows for a bus length of up to 270 m, keeps bus load lower (as expected) and no noticeable effect was observed on CPU usage for the attached PC. Therefore, a higher bus speed is recommended.

This test must be extended in both number of ELMB nodes per bus and number of buses per PC. The current maximum number of ELMB modules per bus planned in the ALTAS detector is 64. This has not been thought realistic for some time, however, 32 nodes in a bus should be possible. Different physical distributions of ELMB nodes on the bus must be investigated, *e.g.* eight at far end and eight at PC end, to investigate any powering problems. As half of the ELMBs would be very close to the power supply, these would be likely to have an over voltage if the supply is set such that the far ELMB modules have enough power. All tests so far have been with only one bus. The NI-CAN card allows for two buses to be connected to the same PC. Also the utilization of more than one card per PC, and the CPU loading in this case, need to be investigated. Due to the high CPU usage, some of the processing may be moved to other parts of the readout chain. As PVSS is interpreted, it is relatively slow, therefore moving processing down to the ELMB or the OPC server would increase speed as these calculations would then be pre-compiled. However, this depends upon radiation tests (in the case of the ELMB functionality) and configuration issues in either the ELMB or the OPC server. It is probable that in the future the ELMB will perform alarm handling, sending data asynchronously in case of problem. Additionally the ELMB would also send data at

regular interval for archiving and trending of the different channels. This would reduce the traffic on the bus considerably. However, the results presented here would still be valid, as the situation reproduced here could still occur in case of major problems in the system.

Chapter 5

The DCS of the ATLAS Tile Calorimeter

The application part of this work has been performed in collaboration with the ATLAS Tile Hadron Calorimeter. In the first part, some principles on hadronic calorimeter are summarized. The calorimeter construction and the different subsystems are described in detail. The main results on the calorimeter performance obtained in previous tests are outlined. Finally, the local DCS of the Tile Calorimeter and its internal organization are presented.

5.1 Notions on hadronic calorimetry

5.1.1 Calorimeters in HEP

A calorimeter is a device which measures the total or part of the energy of incident particle [58]. The energy deposition of the particles traveling across a calorimeter is produced through the development of a shower or cascade of particles with increasingly lower energy. Showers can be either electromagnetic or hadronic. The interaction processes depend on the energy and nature of the incident particle, as well as on the absorber. A small fraction of the deposited energy is used to produced a detectable signal which can be measured. The quality of the measurement is given by the intrinsic energy resolution and linearity of the calorimeter signal with respect to the energy of the incident particle.

Calorimeters play an essential role in the HEP experiments for the following reasons:

- Calorimeters are sensible to charged and neutral particles
- The energy deposition by shower development is an statistical process [59]. The number of secondary particles produced $\langle n \rangle$ is proportional to the energy of the

primary particle. The energy resolution $\sigma / \sqrt{\langle E \rangle}$ of the calorimeters behaves as $1 / \sqrt{\langle n \rangle}$, *i.e.* it improves with the energy of the incident particle as $1 / \sqrt{\langle E \rangle}$.

- The calorimeter dimensions increase with the logarithm of the energy of the incident particle, which allows to build relatively compact devices.
- The shower development is different depending on the nature of the primary particle. This characteristics is used for particle identification in the calorimeters.
- Unlike the tracking detectors, no magnetic field is required to determine the energy of the particles.
- Calorimeters are the unique devices which can measure energy of jets.
- The full geometric coverage of the calorimeters allows for measurements of missing transverse energy E_{Tmiss}.
- A proper segmentation of the calorimeters allow to measure the direction of the particles.
- The fast response of the calorimeters allow the operation at high particle rates. This characteristic makes also possible the usage of the calorimeters for selective trigger of events.

Attending to their construction, the calorimeters can be divided in two main types:

- **homogeneous**, in which the passive energy absorption and the active signal generation is produced in a unique medium permitting the full volume of the calorimeter;
- **sampling calorimeters**, in which these two functions are separated in alternating layers of different materials.

Sampling calorimeters allow to choose the passive medium according to the requirements of the experiment, *e.g.* compact dimensions, high granularity which leads to a better particle identification and better signal uniformity. However, the major part of the energy of the incident particle is released in the passive medium and only a tiny part of the energy of the incident particle is deposited in the active medium. This leads to a deterioration of the resolution of the response as compare to that of homogeneous calorimeters.

As mentioned in chapter 1, the Tile Calorimeter is a hadronic sampling calorimeter. In the following, a brief description of the main characteristics of this type of detectors is given.

5.1.2 Hadronic showers

Unlike electromagnetic cascades, in which the evolution of the shower undergoes a few well-understood processes, hadronic showers are rather complicate. The shower development in a hadronic cascade is governed by interactions between

hadrons and nuclei of the absorber medium. Two main types of hadronic processes, with different timescales, can be distinguished during evolution of the cascade:

- Fast development of the cascade by multiplication of particles with a timescale of the order of 10^{-22} s. In the interaction of hadrons with the absorber nuclei, fast protons, neutrons and heavy nuclear fragments like α-particles are produced. These can hit other nuclei bringing them to an excited state.

  Some of these particles, like γ, η and mainly π^0, produced during the shower propagate the cascade without any further nuclear interaction originating an electromagnetic component of the shower. The electromagnetic fraction of the shower may fluctuate significantly from event to event since production of these particles is random. These particles loose energy mainly by ionization and pair anhiquilation.

  The shower ceases when the energy carried by the secondary particles is no longer sufficient to continue the multiplication process. The rest of the energy is released by ionization, Comptom scattering and photoelectric effect.

- The second phase is characterized by a slow and low energetic deexcitation of nuclei produced in the previous phase within a timescale of about 10^{-18} s. This takes place in successive evaporation of nucleons (slow neutrons, protons, α-particles) and emission of γ during nuclear transitions. Nuclear fission may also occur for very heavy elements like Uranium.

Part of the energy of the incident particle is absorbed by the passive medium of the calorimeter, namely the energy required to release nucleons from the nuclei due to the binding energy or nuclear breakup. This energy may represent a 40% of the energy of the incident particle and it is lost for calorimetric purpose since it does not contribute to the calorimeter signal [60].

5.1.2.1 Profile of hadronic showers

The shape of the shower in a calorimeter depends on the nature of the incident particle among other factors. This property allows to perform particle identification using calorimeter and fast trigger event selection. The average longitudinal distribution of the shower is measured in units of nuclear interaction length, λ_{int} defined by the following expression:

$$\lambda_{int} = \frac{A}{N_A \rho \sigma} \tag{5.1}$$

where A is the mass number of the absorber, N_A is the Avogadro's number, ρ the density of the absorber material and σ the total cross section of the process. λ_{int} represents the mean distance traveled by a high energy hadron until its energy has been reduced to a fraction $1/e$ of the initial energy.

Hadronic showers are broad due to multiple scattering of particles, mainly of neutrons, of the cascade before disappearing. A detailed description of the hadronic shower profiles can be found in [58, 60, 61].

5.1.3 The e/h ratio and calorimeter compensation

As mentioned above, the interaction between hadrons and nuclei of the absorber originate an electromagnetic component of the cascade of particles. The calorimeter response to the full shower can be expressed as follows:

$$R = \varepsilon_h E_h + \varepsilon_e e \tag{5.2}$$

where ε_h and ε_e represent the detection efficiency of the calorimeter for the hadronic and electromagnetic components of the cascade, and E_h and E_e the respective energies of both components of the shower.

The ratio E_e/E_h depends on the event and its fluctuations determined by the variation of the production of π^0 from event to event.

Due to the large fraction of energy lost in nuclear breakup reactions, ε_h is usually smaller than ε_e. Therefore, the average signal produced by monoenergetic hadrons in general is smaller than the average signal produced by electrons of the same energy.

The ratio between the response of the calorimeter to electrons and pions of the same energy is referred to as e/π and it is defined according to the following expressions:

$$\frac{e}{\pi}(E) = \frac{\varepsilon_e E}{\varepsilon_e E_e + \varepsilon_h E_h} = \frac{\varepsilon_e}{\varepsilon_e \langle f_{\pi^o}(E)\rangle + \varepsilon_h (1 - \langle f_{\pi^o}(E)\rangle)} = \frac{e/h}{1 + \langle f_{\pi^o}(E)\rangle (e/h - 1)} \tag{5.3}$$

where $\langle f_{\pi^o}(E)\rangle$ is the average electromagnetic fraction in a hadronic shower and *e/h* is a shorthand for $\varepsilon_e/\varepsilon_h$.

The so-called compensated calorimeters verify that *e/h* = 1. A ratio $e/h \neq 1$ has the following implications on the calorimeter response:

- The resolution of the calorimeter is influenced by the fluctuations of the production of π^0.
- Non-gaussian energy deposition for monoenergetic hadrons in the calorimeter.
- The calorimeter signal is not proportional to the energy of the incident particle.
- The calorimeter resolution does not improves with the energy according to $1/\sqrt{E}$.

Sampling calorimeters are the most natural choice if a ratio $e/h \rightarrow 1$ is desired since it is possible to combine several factor, like nature and thicknesses of the absorber and active materials, in order to achieve this value.

5.1.4 Energy resolution of sampling calorimeters

The energy resolution of calorimeters is governed by three main factors. As described above, the development of the hadronic shower is an stochastical process where the number of particles increases with the energy causing, the accuracy of the measurement to improve as $1/\sqrt{E}$. In addition, the non-gaussian deposition of energy by hadrons, *i.e.* the non-compensation nature of some calorimeters, influences their resolution. On the other hand, the energy resolution of the sampling calorimeters is also determined by fluctuations due to the inhomogeneity of the medium. The readout electronics may contribute to the accuracy of the measurement due to the photo-electron statistics (assuming PMT readout), noise due digitalization, and miscalibrations. For these reasons, the energy resolution of the calorimeters is given by the following expression:

$$\frac{\sigma}{E} = \frac{a}{\sqrt{E}} \oplus \frac{b}{E} \oplus c \tag{5.4}$$

where $\oplus$ is the quadratic sum operator. The first term includes contribution from sampling fluctuations due to the statistical nature of showering and photostatictics (assuming PMT readout).The second factor is called noise term and considers the noise induced by the readout electronics and background processes also called *pileup*. This term can usually be neglected for high energy events. The last term is due to non-compensation and calibration errors of the calorimeters.

5.2 The ATLAS Tile Calorimeter

5.2.1 Design requirements

The design of the Tile Calorimeter is strongly determined by the required physics performance. The major tasks of the Tile Calorimeter will consist in identifying jets and measuring their energy and direction. The calorimeter will have to cope with events in a wide energy range per detector cell. This extends from a 0.5 GeV, deposited by muons traversing the calorimeter, up to a few TeV per cell due to jets according to simulations. An intrinsic energy resolution, given by expression 5.5, is needed to achieve this goal.

$$\frac{\sigma}{E} = \frac{50}{\sqrt{E}}\% \oplus \frac{3.06}{E} \tag{5.5}$$

The calorimeter will also play an essential role in the determination of the total missing energy and low-p_T muon identification. For this purpose, a large acceptance and hermeticity of the calorimeter is required.

The detector will improve the particle identification of the electromagnetic calorimeter. This requirement calls for a fine granularity of the calorimeter in order to define hadronic leakage cuts needed for electron and photon identification. This required segmentation of the calorimeter is $\Delta\eta\times\Delta\phi = 0.1\times0.1$. The high granularity of the detector will also allow to minimize the effects due to non-compensation below 2% and to restore the linearity of the calorimeter by weighting techniques.

In addition the detector must absorb all radiation but muons in front of the Muon Spectrometer, thus requiring a thickness about 11λ (including also all elements placed before the Tile Calorimeter).

Finally, the calorimeter will form part of the LVL1 trigger system. Therefore, a fast readout system is required. Moreover, the precision of the read-out system must not result in a limitation of the energy resolution of the calorimeter given above. A precision of at least 10-bits will be used to meet this requirement.

Finally, the materials used for the construction of the calorimeter and associated front-end electronics must be radiation-tolerant to the expected dose [48] to ensure operation during the lifetime of the experiment.

5.2.2 Mechanics

The Tilecal [8, 62] is a non-compensated sampling calorimeter, which uses laminated steel as passive absorber and scintillating tiles as active material in a ratio 4 to 1. It is placed behind the electromagnetic LAr accordion calorimeter at approximately 2λ from the interaction point. The calorimeter has a cylindrical shape of outer radius 8.5 m and is 12.2 m long. The total weight is about 2900 tons and the total thickness is 11 interaction lengths (λ) at η=0 (including 1.5 λ of the outer support). The calorimeter body and the massive iron outer support act as magnetic flux return for internal solenoid. The general layout of the calorimeter is shown in figure 5.1.

The detector is built in three sections:

- 1 central barrel covering $|\eta| < 1$
- 2 extended barrels enlarge the rapidity coverage to $1.6 < |\eta|$

The central and extended barrels are separated by gaps of 70 cm. These are the so-called crack regions and are required to route the cables of the inner detector and electromagnetic calorimeter, as well as the cryogenics for the central solenoid.

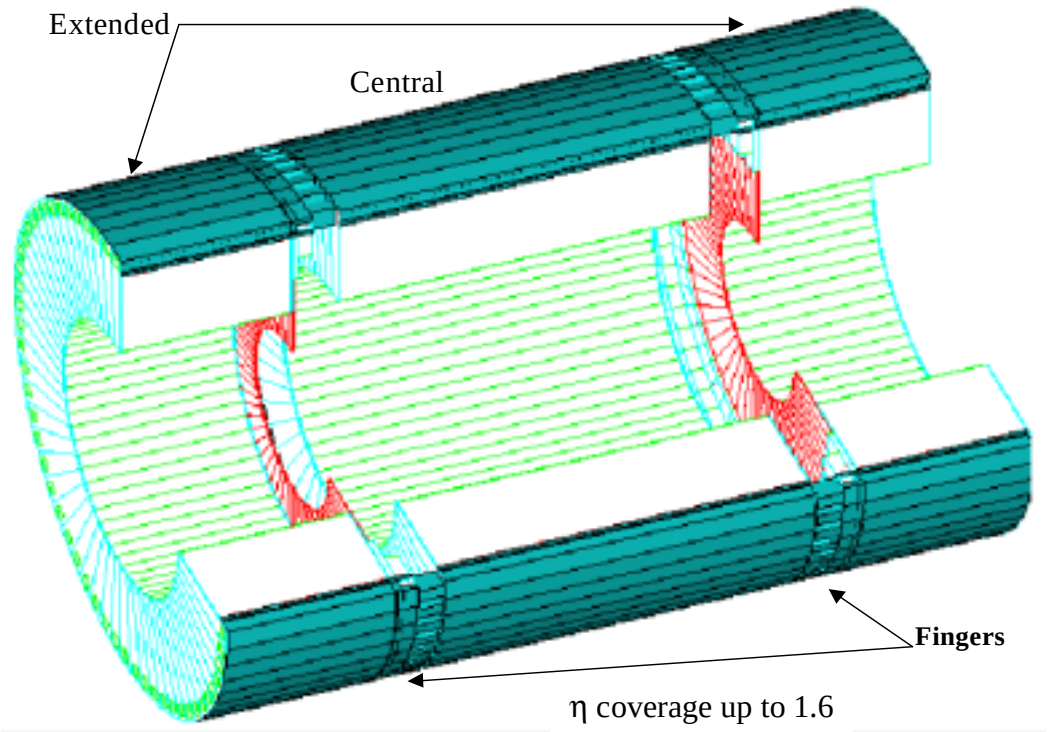

Figure 5.1: *Layout of the Tile Calorimeter.*

These sections are azimuthally divided in 64 wedges called modules. Each of these modules is built out of repeating elements called periods or sub-modules. A module of the central barrel comprises 19 sub-modules whereas those of the extended barrels only 10. A sub-module is a stack of laminated precut steel plates with a tolerance of 250 μm consisting of:

- large trapezoidal plates, 5 mm thick called master plates
- small trapezoidal plates, 4 mm thick called spaces.

The spacers are glued to the masters with epoxy. Each module is segmented in three sampling layers of thicknesses of 1.9, 4.2 and 1.5 λ going radially outwards. There are two holes penetrating each of the plates in order to accommodate the guide tubes for the Cs calibration system, which is explained in section 5.2.4.1.

After the mechanical steel assembly, 3 mm thick scintillating tiles are inserted into the module. The tiles are wrapped to improve the response uniformity over one Tile. The light produced by particles or jets in the scintillating tiles is read out using WaveLength Shifting (WLS) optical fibers into two separate photomultipliers

(PMT). These fibers are placed on each side of the scintillating tiles as shown in figure 5.2.

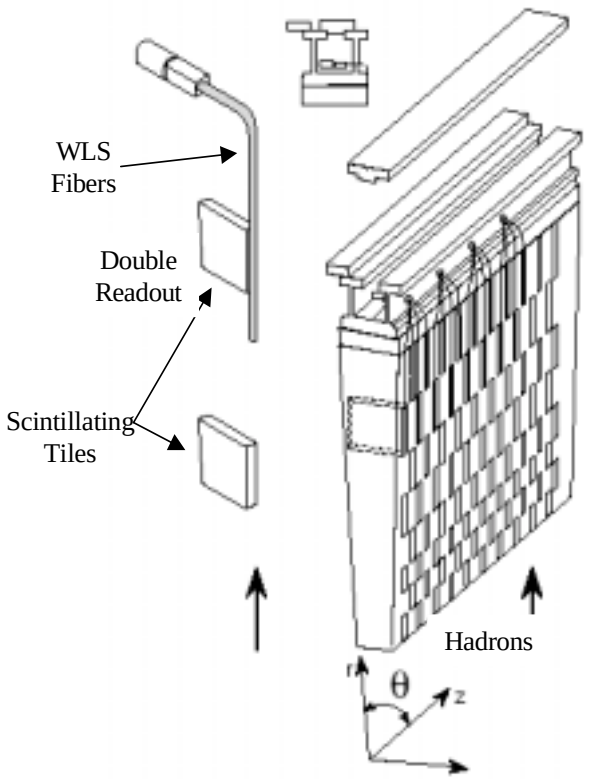

Figure 5.2: *Principle of the Tile Calorimeter design.*

The fiber to fiber response fluctuations is less than 5%. The fibers run along sides of the modules. The use of scintillating tiles as active material in sampling calorimetry provide speed performance, easy readout and low noise level.

In all calorimeters of this type constructed up to now, the tiles are placed normal to the particles trajectories, which makes it non-trivial to read out the light while maintaining detector hermeticity. In this case the scintillating tiles are placed in the plane perpendicular to the beams solving these problems.

The fibers are grouped in a projective way into bundles at the outer end of the detector. This grouping defines the segmentation of the modules into cells and towers as shown in figure 5.3. The resulting granularity of the hadronic calorimeter is $\Delta\eta\times\Delta\phi\sim 0.1\times0.1$. The instrumentation of a module of the central section of the calorimeter is shown in figure 5.4

The bundles are then routed through rubber feed-throughs to a light mixer which spreads the light uniformly over the surface of a PMT tube.

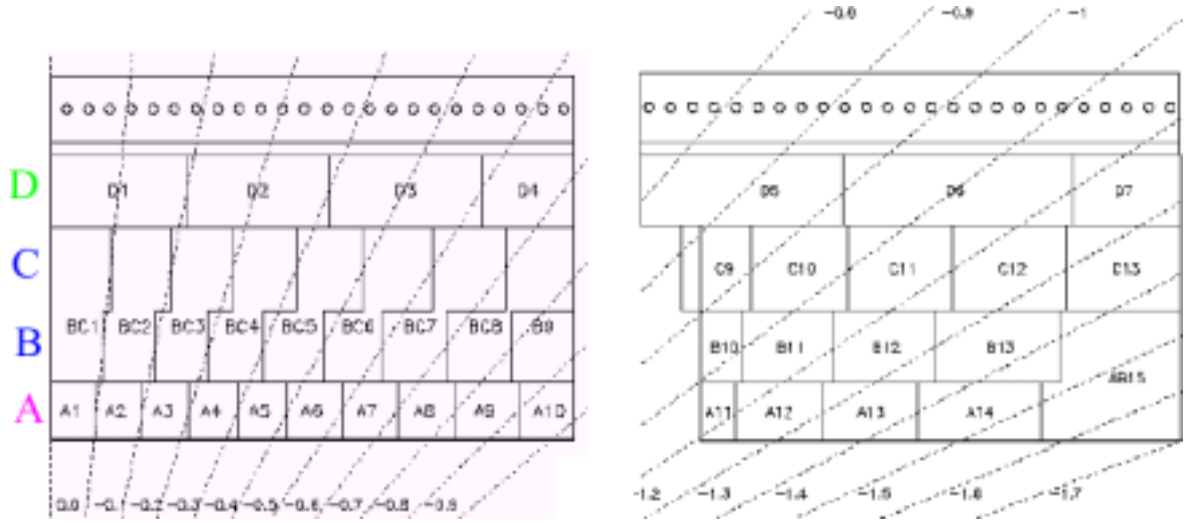

Figure 5.3: *Cell layout of half central barrel and extended modules showing the 4 sample layers and projectivity in* η.

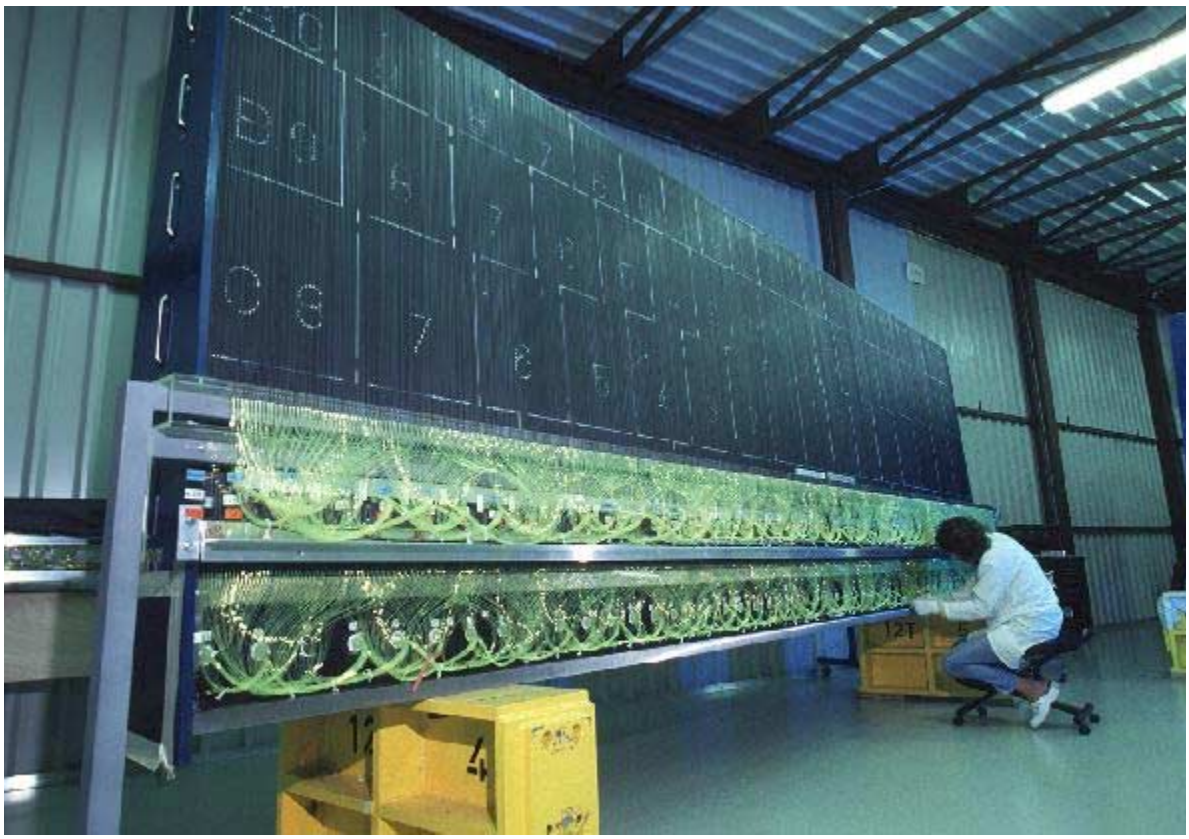

Figure 5.4: *Instrumentation of a module of the central barrel. The routing of the WLS optical fibres to the PMT defines the cell granularity of the module.*

5.2.3 Read-out

The fast read-out electronics must process the signals from all PMT at the LHC bunch crossing frequency. Signals corresponding to the energy in 2000 trigger towers must be composed and sent to the electronics of the LVL1 system every 25 ns. All these signals must be locally buffered during the 2.5 μs of latency of the LVL1 system. During this time, the trigger decision is taken and data accepted by the LVL1 system are passed to the read-out drivers of the DAQ.

All front-end electronics and photomultipliers are located in a movable drawer system of 1.5 m. These drawers are inserted in a support girder located at the outer radius of the modules. A system comprising two drawers is called super-drawer and has a total length of 3 m. One super-drawer, is needed to readout each module of the extended barrels, whereas two super-drawers are required to cover the full length of the modules of the central barrel (~6 m).

Each drawer houses up to 24 PMT blocks and contains electronics boards to provide the HV levels required for the operation of the elements of the PMT block and to process the signals induced by physics or calibration events. The total number of PMT is 10140. The electronics boards are connected to the drawer by means of motherboards arranged in the top and bottom sides of the drawer as shown in figure 5.5.

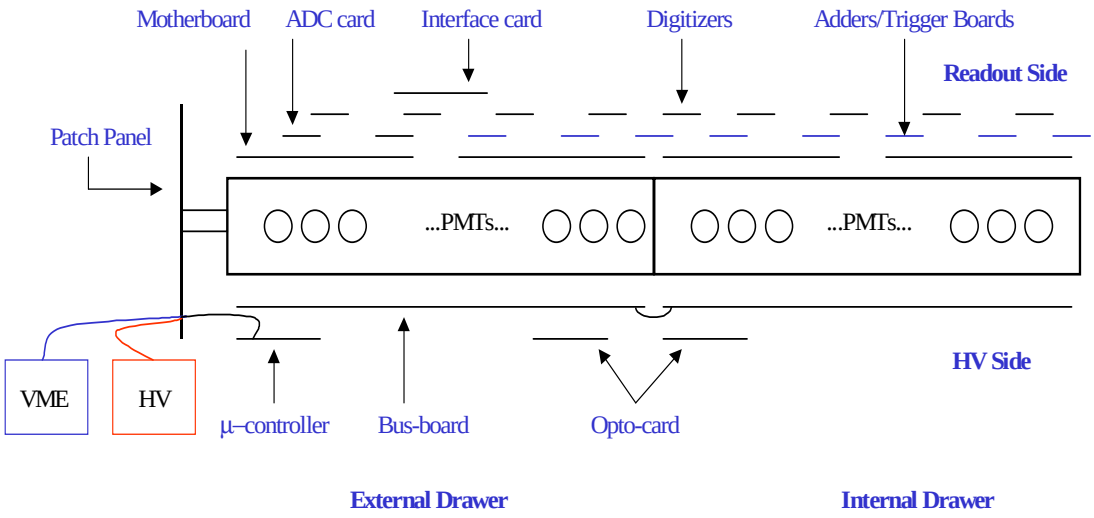

Figure 5.5: *Organization of the superdrawer electronics.*

The PM tubes are placed inside the PMT blocks, which also comprises a several optical elements, a voltage divider, front-end electronics required for its readout and magnetic shielding up to 200 Gauss in any direction. A schematics view of the PMT blocks is shown in figure 5.6.

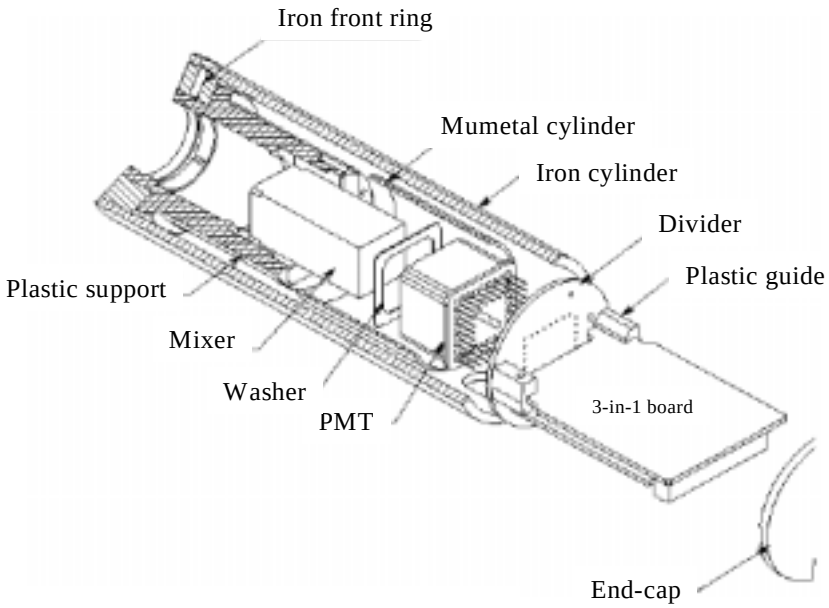

Figure 5.6: *Different elements of a PMT block.*

An intensive evaluation of PMT series has been performed by the Tilecal group and the results are reported in [63]. The PMT model chosen is the R7877 from Hamamatshu and its main characteristics are shown in table 5.1.

Table 5.1 *Main feature of the PMT model R7877 from Hamamatshu*

metal channel dynodes
8-stages or dynodes
gain 10^5 at 650 V
useful area 324 mm^2
dark current < 100 pA
quant. eff. at 480 nm 17%

The utilization of a light mixer improves the uniformity of the collection of light in the PMT. Light from different fibers is mixed in the light guide and then is spread uniformly over the central region of the photocathode window. This compensates the variations of the quantum efficiency of the photocathode window as a function of the position of incidence.

In the following, the main elements of the readout electronics are described and their main functions are outlined.

The micro-card is used for the HV regulation. It contains all settings required for the operation of the PMT and handles the communication with a VME crate used for the control of the HV.

The opto-boards regulate and distribute the adequate HV value on the PMT.

The ADC integrator card reads out signals from the Cs source. A special ADC is used to measure continuos currents due to background events also called Minimum Bias (MB) events.

The interface card brings in the clock signal, 40 MHz, via an optical fiber. This signal is needed for the control logic. This card also handles the external communication with a VME used for control and sends digitizer signals.

The so-called 3-in-1 card in picture 5.6 is directly connected to the PMT via the voltage divider, which works as a socket and provides the adequate HV levels at the different dynodes of the PMT. The 3-in-1 card contains three major components performing different tasks:

- A fast shaper electronics interface, between the PMT and the pipeline dedicated to the pulse analysis.
- A slow integrator circuit, for measuring the current from the Cs calibration system and minimum bias events.
- Control logic.

The current pulses from the PMT are shaped and converted to a voltage signal at the 3-in-1 card. The signal is then split in two: one signal is passed on to the trigger boards. The other signal is sent to the fast digitizers placed on the external end of the drawers and then is injected into the DAQ readout chain.

The trigger boards, also called adders, provide two output signals:

- Groups of five PMT are arranged in a trigger tower, which corresponds to the path of the passing particle. All PMT in a tower are connected to one adder, which performs the sum of energy deposited in the corresponding cells. This gives a fast information about the energy of the particle.
- Secondly, they give the sum over all PMT in sample D of the module providing therefore, a fast trigger for muons.

Trigger signals are treated by the LVL1 trigger system. Meanwhile the LVL1 decision is taken, the signals are stored on the digitizers.

5.2.4 Calibration Systems

Calorimeters are characterized by a *conversion factor* that is applied to determine the energy released in the calorimeter by a particle or jet (typically given in GeV), from

the digitized signal at the end of the readout chain (usually a charge in pC). This calibration factor must be determined for each channel of the readout system in order to minimize channel-to-channel variations of the overall calorimeter. This factor may change over a long period of time as a consequence of the ageing of the components used in both the construction of the calorimeter and of the readout electronics. Therefore, the capability to monitor the variation in time of the response of the different elements of the calorimeter over the life-time of the experiment is provided.

From the particle interactions in the calorimeter to the digitized output of the physics signal read-out chain, the signal path can be separated in three stages where several effects can lead to variations of the response of the calorimeter:

- Production of a light pulse on the scintillating tiles by interaction of particles or jets that is driven to the PMT using WLS fibers. Ageing of the tiles can may lead to variations of the light-yield and therefore of the response of the cells. These effects can be monitored by inducing light with certain known characteristics on the tiles using a radioactive source for comparison between the different cells and in time.
- Conversion from the light pulse to a current pulse at the PMT. Drifts of the gain or of the quantum efficiency of the PMT may result in variation in this conversion. Changes at this stage can be monitored by injecting a light pulse of known characteristics directly into the PMT.
- Processing and read-out of the physical signal. Variations at this stage can be mainly due to the non-linear response of the electronics as a result of the ageing of the components. The monitoring system at this stage can be based in injecting a known current on the readout chain.

For these reasons, the Tile Calorimeter comprises a set of calibration and monitoring systems to evaluate the operational parameters and their behavior with time, at these three stages:

- The ^{137}Cs calibration system
- The laser system
- The Charge Injection system
- The Minimum Bias Events monitoring system

Figure 5.7, shows the signal path and the availability of the calibration system in each stage.

Signals induced by the calibration systems are read out through the same electronics as physics events. In the following, a brief description of the operation principle of the systems is given.

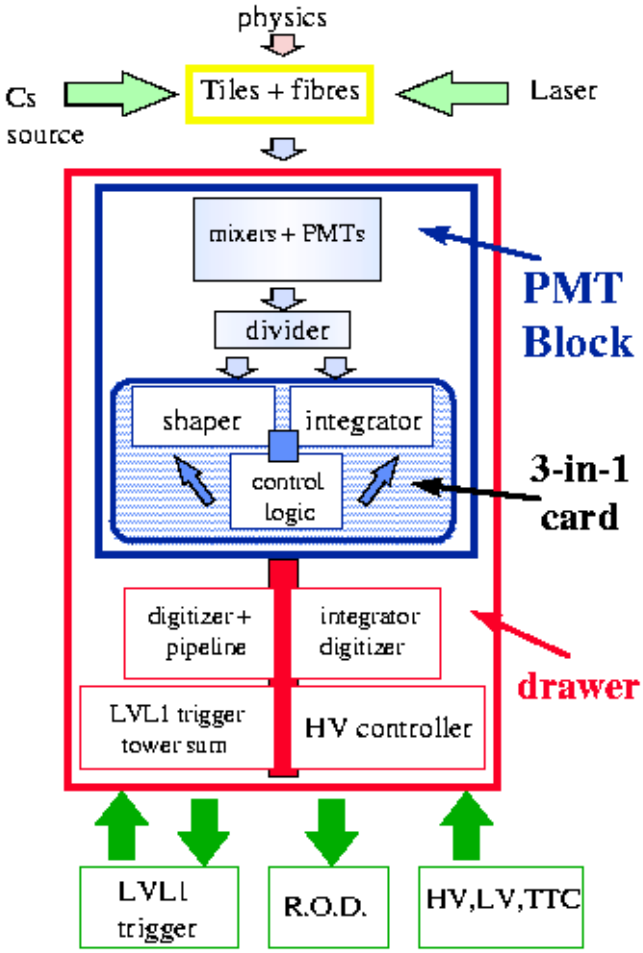

Figure 5.7: *Readout path of each of the physics and calibration events in the Tile Calorimeter.*

5.2.4.1 The Cs calibration system

This calibration system of the Tile Calorimeter uses a radioactive sample of 5 mCi ^{137}Cs to scan the modules. The source induces light in each individual scintillating tile of the modules. The capability to check individual tiles is determined by the mean free path of the ^{137}Cs γ, that is chosen of the order of the separation between tiles, 18 mm. The source is inserted in a guide tube and driven along the symmetry axis of the modules by an hydraulic pump as shown in figure 5.8. The current induced by the source on the PMT is shown in figure 5.9 as a function of the position of the radioactive sample.

The system allows for checking of the quality and uniformity of the optics (scintillating tiles, readout optical fibers and PMT). The characteristic multi-peak histogram observed is due to the passage of the source through five consecutive

cells having several tiles each. Any anomaly in the system is clearly traced by the system as shown in the picture.

The system also allows to compensate the response variations from cell to cell, to obtain the same average current from all readout cells, by adjusting the HV of the corresponding PMT. The current from the PMT is of 50 nA at the nominal gain. This current is averaged over a long time scale to suppress the ripple from individual pulse and fluctuations in the amplitude and rate of energy.

A third feature of the system is the monitoring of the long-term drift[a] of the signal from the optics by running the source periodically. This allows to maintain the overall energy calibration of the cells.

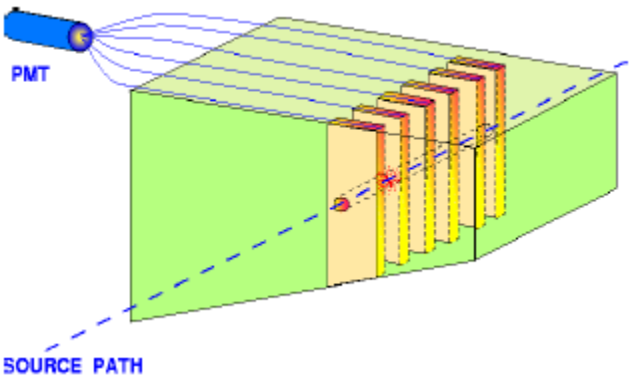

Figure 5.8: *Operating principle of the ^{137}Cs calibration system.*

Unlike other calibration systems used by the Tile calorimeter, the Cs system provides an absolute calibration of the modules, since the signal is produced and processed similarly to that induced by particles.

The calibration with the Cs source is performed during periods with no data-taking. All modules of the calorimeter will undergo this calibration process during the commissioning phase, in order to determine the so-called *Cs calibration constants*. These constants will be used to obtain the overall calibration of the modules. In the final system, the whole calorimeter will be calibrated using a limited number of sources.

a In this case, the decay rate of the ^{137}Cs sources must be known precisely.

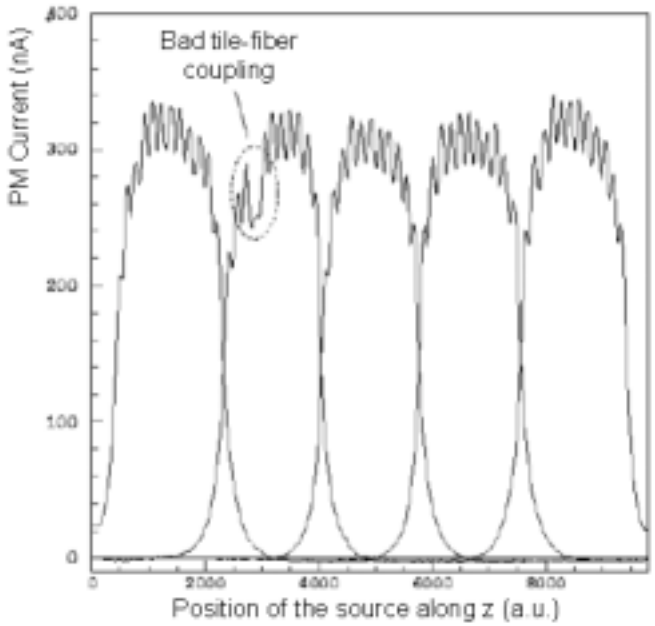

Figure 5.9: *Current induced in the PMT as a function of the position from a Cs scan along five readout cells.*

5.2.4.2 Laser System

This system employes a YLF solid-state laser to calibrated the PMT gain of the modules with a precision of 0.5%. The system bypasses both scintillating tiles and optical fibers of the readout system. It allows to isolate effects purely due to PMT, like gain drifts, or to the electronics of the data acquisition system. The characteristic of the laser light are similar to those of the light induced by particles on the scintillating tiles, with a wavelength of 480 mm and a pulse width of 15 ns. Part of the laser light is sent onto two photo-diodes which allow for a precise measurement of the laser light intensity on pulse-to-pulse basis. The response of the photo-diodes is monitored using a ^{241}Am source, which provides a stable reference signal. After traversing several attenuator filters (non-attenuated, 10-time attenuated and 100-times attenuated), the rest of the light is sent onto the PMT using special clear fibers. The usage of different laser intensities incident onto the PMT allows to simulate a variety of events with different energies in the cells of the calorimeter. This permits to explore part of the dynamic range of the calorimeter.

Contrarily to the Cs monitoring system, the calibration with the laser system is performed during data-taking. A number of laser runs at different intensities are alternated with physics events. This allows for online monitoring of the performance of the system and diagnose of possible anomalies due to the PMT.

5.2.4.3 Charge Injection

The charge injection system complements the calibration systems described above in measuring the linearity of the signals. This system allows to isolate effects of the electronics, like read-out faults and cross-talk. Additionally, it allows to test and calibrate the behavior of each readout channel over its full dynamic range with realistic patterns of energy deposition. It bypasses all optical elements in the readout chain and evaluates the effects purely due to the readout electronics. Different charges of know values, measured with a precision of 1%, are injected at the input of the pulse shaper of the 3-in-1 cards and then measured by the DAQ system.

5.2.4.4 Monitoring of the minimum bias events

A fourth diagnostic tool is being developed to complement the previous systems on a large time scale. Its principle consist of measuring the noise induced on the detector, by the background of inelastic proton-proton collision at small momentum transfers. In fact, this type of events, called *Minimum Bias event*s (MB), are manifested in the Tile calorimeter because they induce a quasi-DC component between 5 and 500 nA of the PMT anode signal. MB event signals depend on the LHC luminosity, pseudorapidity and cell location. Its monitoring permits to signal possible anomalies of the response of two PMT in a given cell and may be particularly interesting to determine possible damage due to sudden beam losses.

5.3 Calorimeter Performance

In this section the main results obtained in previous test of the modules of the Tile Calorimeter are summarized. Detector performance have been measured in both stand-alone operation and combined with the LiAr Calorimeter [64, 65]. Stand-alone tests of the Tile Calorimeter comprised two major sets of measurements using 1 m prototypes and a real size prototype called *Module0* from 1993 to 1995. In all cases the response of the calorimeter to π, *e* and μ was measured.

The combined test beam run performed with a 300 GeV π beam showed the following energy resolution (see figure 5.10):

$$\frac{\sigma}{E} = \left(\frac{(38.3 \pm 4.6)}{\sqrt{E}}\% + (1.62 \pm 0.29)\%\right) \oplus \frac{(3.06 \pm 0.18)}{E} \qquad (5.6)$$

whereas studies with *Module0* determined an energy resolution of the Tile Calorimeter of compatible with:

$$\frac{\sigma}{E} = \frac{50}{\sqrt{E}}\% \oplus \frac{3.06}{E} \tag{5.7}$$

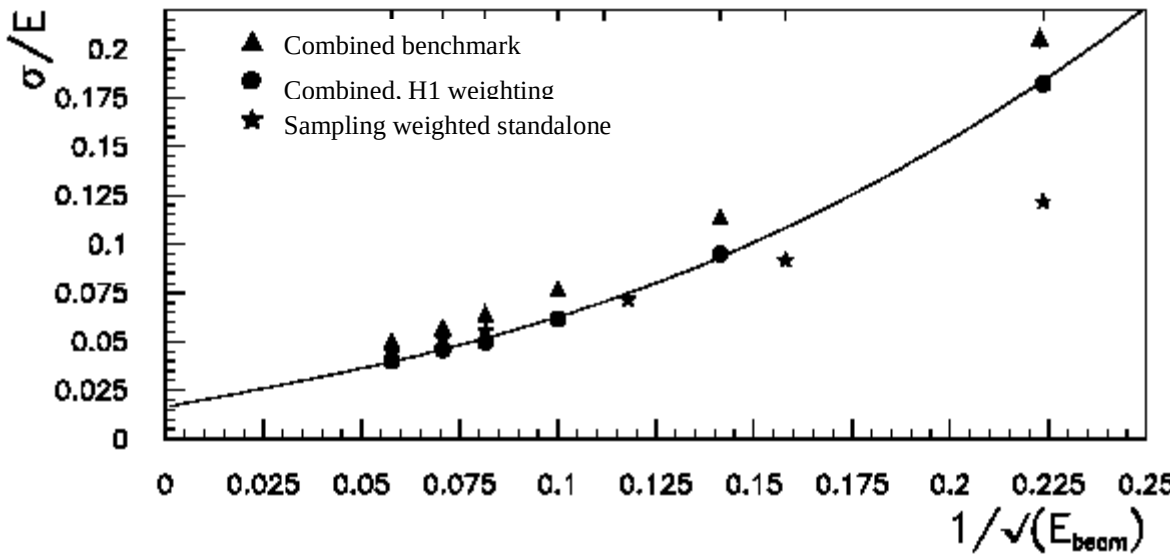

Figure 5.10: *Combined energy resolution of the ATLAS calorimetry system.*

Comparison of the results obtained for electrons and pions allowed to determine the value of the ratio between calorimeter response to the electromagnetic and hadronic components of the shower, e/h=1.36±0.1 from the ratio e/π.

The development of the hadronic shower Tile calorimetry has been measured in [66]. The response linearity of the modules at different energies of the incident π beam was measured [67]. As a consequence of non-compensation (e/h>1) of the calorimeter, non-linearity as a function of energy in the pion response is observed, although this can be corrected offline by software. The results showed a response linearity in the energy range from 20 to 300 GeV better than 1%.

The response uniformity of the modules as a function of η and ϕ was also measured. As example, the uniformity in η is shown in figure 5.11. The results indicated a response uniformity within 2%.

The high photostatistics, *i.e.* the number of photoelectrons generated in the photocathode of the PMT, was also investigated. A photoelectron yield of 64 p.e./GeV was measured. The high photostatistics of the calorimeter makes possible to resolve muons from noise.

The response to muons and its uniformity were studied in systematic η and ϕ scans [68]. The results provided a good understanding of the muon loss serving as a good basis for the Monte Carlo simulations (MC).

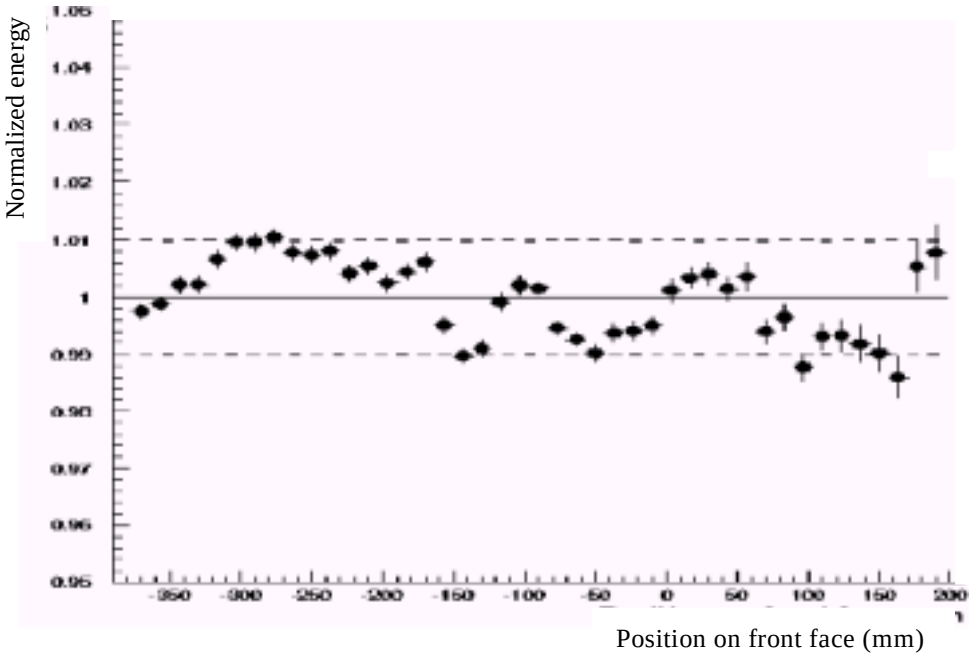

Figure 5.11: *Uniformity of the modules for η scan over 1 m measured with 100 GeV pions.*

5.4 Tilecal Detector Control System

Similarly to other subdetectors described in chapter 2, the DCS of the Tile Calorimeter is subdivided attending to functional criteria into different subsystem, which run autonomously during the commissioning phase. The system comprises the following functional blocks:

- HV system, required for the operation of the PMT
- LV system, needed for the HV regulation and readout electronics
- cooling system, which handles the monitoring and control of the temperature inside the drawers.
- Stand-alone systems like the different calibration systems. These will have their own control system although they will have to be interfaced by the main DCS. This is needed to guarantee data exchange and issuing of commands from the DCS in order to ensure the safe and coherent operation of the detector.

In addition, the Tile Calorimeter DCS group foresees the implementation of special procedures dedicated to perform diagnose and to detect faulty electronics components.

In all cases the utilization of VME crates is foreseen for the implementation of the different partitions. The crates will interface the front-end equipment via CAN bus.

There will also be one LCS per subsystem, which will interface the VME crates via TCP/IP. The so-called *Tilecal Communication Interface (TCI)* based on CORBA could also be used for this purpose.

At the supervisory level, a logical hierarchical structure will be built on the top of the functional blocks to offer to the user, information in a tree-like structure which models the geographical detector arrangement. In the following the subsystems of the Tilecal DCS are described.

5.4.1 High Voltage System

The HV system of the Tile calorimeter [69] is used to feed the PMT with a voltage ranging from 400 to 1000 V and a current of 20 mA per channel. Each of the 256 modules (or super-drawers) of the calorimeter is equivalent from the HV point of view. The HV system comprises a number of sources and distributors. Each source consists of two racks with 16 crates with two HV channels, a communication and a control units each.

Each HV source provides power to the super-drawers. The crates comprise over-current and under-current protection mechanisms. All functions and parameters of the crates can be controlled either manually or remotely by means of the communication and control units, using a serial interface line.

Only three voltage levels are provided to each channel: -700, -900 and -1100 V. These levels are then locally regulated by the HV board (based on a single INTEL 8051 chip) to the proper values. There is one HV board per drawer capable to regulate up to 24 channels.

The so-called CPU board, based on a 32-bit microcontroller, supervises the voltages applied to each PMT and serves as interface to a VME crate. Finally, the bus boards are used to carry the common high and low voltages and commands to the two distributor boards and to deliver the HV to each PMT. The HV distributors can operate up to 350 V below the supplied level. The stability of the response of the PMT is strongly determined by precision of the supplied voltage (~0.2 V).

5.4.1.1 DCS of the HV system

The overall operation of the system will be controlled and supervised by VME crates located in the underground electronics cavern USA15. These crates will be connected to the drawer via a 100 m long CAN bus handling the transfer of data and commands. The VME crate will perform the monitoring of the voltages and currents in the modules. Each drawer will also be equipped with 7 temperature probes placed at different positions. These sensor will be directly read out by the HV system in order to shut down the electronics in case of thermal hazard.

The VME crate can be interfaced to a PC, running the high level SCADA software via TCP / IP. It is envisaged to employ a CORBA-based solution to interface the VME crate to PVSS-II. This interface is currently under development by the Tilecal DCS group.

5.4.2 Low Voltage System

The LV system of the Tilecal detector feeds two main components of the drawers: the HV distributor electronics and the readout front-end. Both parts are completely separated from the LV point of view in order to suppress cross-talk effects. The analogue readout electronics, *i.e.* motherboards, are very sensitive and the peak-to peak noise level must be kept below 2 mV. In addition, the digitizers and the interface card of each drawer must be powered independently from the analogue readout electronics in order to avoid ground-loops. Table 5.2 shows the LV specifications of each of the components mentioned above.

Due to the limited space inside the detector, the power must be supplied remotely and then adjusted to the appropriate levels locally. The local LV power supplies and all logic necessary for their operation will be installed in the Tilecal fingers, rising the following environmental constrains:

- Radiation dose[a] up to 20 Gy / year and 4×10^{11} 1 MeV n / cm^2. The finger region is specially delicate in terms of radiation. The space between the central barrel and extended modules, where the fingers are located, is used to pass the cable for the services of the inner detector. Therefore, no shielding by the mass of iron of the calorimeter cells is provided in this region.
- Magnetic field up to 30 Gauss
- Restricted space available.

The power supply distribution is organized in modules that feed eight super-drawers. These modules are subdivided into eight identical sections of DC / DC converters.

Each line requires its own voltage sensing return line over a twisted pair cable. These return lines will be isolated from the others, specially from those of different super-drawers, in order to avoid ground loops. The return lines corresponding to different voltage level in a module will be interconnected inside the drawer. In order to reach the low ripple levels required for the analogue lines, additional passive filters will be added.

A first prototype based on industrial DC / DC converter bricks was tested in June 2000. A big ripple of about 2 V peak-to-peak was observed although it was

a No safety factor applied

considerable reduced down to 80 mV peak-to-peak with the addition of filters. Based on this experience a new and flexible LV system is being designed, which fulfils all the requirements outlined above. The new development started in February 2001. The system was conceived as a two stage converter. In the first phase, the voltage from a 300 V DC input is converted to 28 V. In the second stage, the voltage is converted to a few output voltage levels in the range from +3.3 to ±15 V.

Table 5.2 *LV power requirements of the Tilecal Drawers*

Mother Board	
	+5 V Analogue
	-5 V Analogue
	+15 V Analogue
Interface Board	
	+3.3 V
Digitizer Board	
	+5 V analogue
	+3.3 V
High Voltage	
	+15 V
	-15 V
	+5 V

5.4.2.1 DCS of the LV system

The LV system must be interfaced to the general DCS in order to ensure a reliable and safe operation. Apart from the obvious tasks of supervision and control of the equipment, the DCS of the LV system must provide the functionality needed to take automatic corrective action in case of over-voltage, over-current or over-heating problems. In addition an interlock between the LV and cooling systems must be implemented at the level of software in order to stop operation in case of failure of the latter system.

Due to its reduced dimensions, high density of channels and the possibility of being embedded directly in the electronics of the power supplies, the idea of using the ELMB for the supervision and control of the LV system is being considered. However, the expected radiation dose in the finger regions is still uncertain. Recent calculations [70], indicate that this value could be well-below the radiation dose

given in the previous section, making possible the utilization of the ELMB in this region.

On the other hand, the control of the low voltage power supplies requires remote steering. This functionality is not currently provided by the ELMB although it will be available in early 2002. As it was described in section 3.3.4.4, the ELMB software already supports analogue output functionality and the addition of off-board DAC chips to be driven by the ELMB is straightforward. Actually, this functionality was required for the last testbeam period in summer 2001 where two external DAC chips were integrated in the ELMB. This work is reported in section 6.3.2.1.

The utilization of the ELMB in the implementation of the finger LV power supplies would also facilitate the integration of the LV system within the SCADA and therefore, within the overall Tilecal DCS.

5.4.3 cooling System

The cooling system of the Tile calorimeter [71] must ensure a stable and uniform temperature of the readout electronics modules. The response of some active element of the calorimeter like the PMT, changes significantly with the temperature. ATLAS has recently set up a common cooling project for both electromagnetic and hadronic calorimeters aiming at providing a common framework for the cooling of the front-end electronics of both detectors.

The power dissipated for each of the calorimeters is:

- Tile 52 kW in 4 partitions of 13 kW each for 4×64 drawers and;
- LiAr 255 kW

The general requirements of the designed the cooling system of the calorimeters are:

- Efficiency; heat produced by the electronics must be efficiently removed from the calorimeters in order to ensure constant temperature of the electronics components within 0.5 ^{0}C over a long period. There are two main sources of heat in the drawers: the HV system, which dissipate a power of about 200 W and the low voltage system, with a power dissipation of 100 W per module. The low voltage power supplies located in the fingers will be cooled by the same line. Therefore, each cooling channel will have to dissipate of the order of 300 W.
- Uniformity of the temperatures along the drawers.
- Equal temperature of the aluminium of the drawer and the iron of the girder. The iron is at ambient temperature (18-20 ^{o}C) and also contributes to the cooling.
- Safety; leaks of cooling system would have fatal effects on the electronics.
- Low cost.

Figure 5.12 and 5.13 show the layout of the cooling system of half Tile barrel and that of the Tile end-cap respectively.

It is important to notice that due to the large dimensions of the calorimeter, gradients of temperature up to 4 ^{0}C can be met depending on the height.

The same thermal conditions in ATLAS must be respected when the TileCal will be assembled and calibrated, in order to use the calibration data for the correspondence charge-energy. The same cooling system is needed during the calibration of the modules, currently ongoing, well-ahead the overall installation in ATLAS. The so-called Leakless cooling System, which works with water at sub-atmospheric pressure, will be used. The system has already been developed and operated in the calibration periods of the modules in summer 2001. A detailed description of the system is given in [72].

Although this system is already running in many experiments at CERN, the huge dimension of ATLAS and severe environment (inaccessible, high radiation, magnetic field) call for a full-scale demonstrator in order to estimate the performance of the system, to test the selected components and to develop the control system [72]. Different tests have been done to estimate the performance of the system and the influence of the temperature on the calorimeter response. The performance of the cooling system are given in the next chapter. In chapter 7, the influence of the cooling temperature on the calorimeter response is shown.

5.4.3.1 DCS of the cooling system

The cooling system and its controls will be developed by the CERN EST division. It will be based on the usage of PLC from the Schneider group running largely independent. The automats will perform close-loop controls for the regulation of the temperature and pressure of the cooling liquid. However, the allocation of the PLC in ATLAS is unclear due to the high vulnerability of these systems to radiation effects. This control system will be interface to the general DCS using the OPC standard described in chapter 3.

An additional system will be implemented on top, which will perform passive monitoring of the status of the devices of the cooling unit, e.g. valves and pumps, and the operational parameters like temperatures and pressures at different locations. This secondary monitoring system will be fully integrated in DCS and will be implemented using the standard DCS tools, *i.e.* the components of the *ATLAS DCS vertical slice* described in section 3.7. The first steps of its implementation have already been given in summer 2001, where a monitoring system was develop to supervise the parameters of the cooling system and to determine its performance during the calibration of the Tilecal modules with beam particles. The system is described in section 6.3.3.

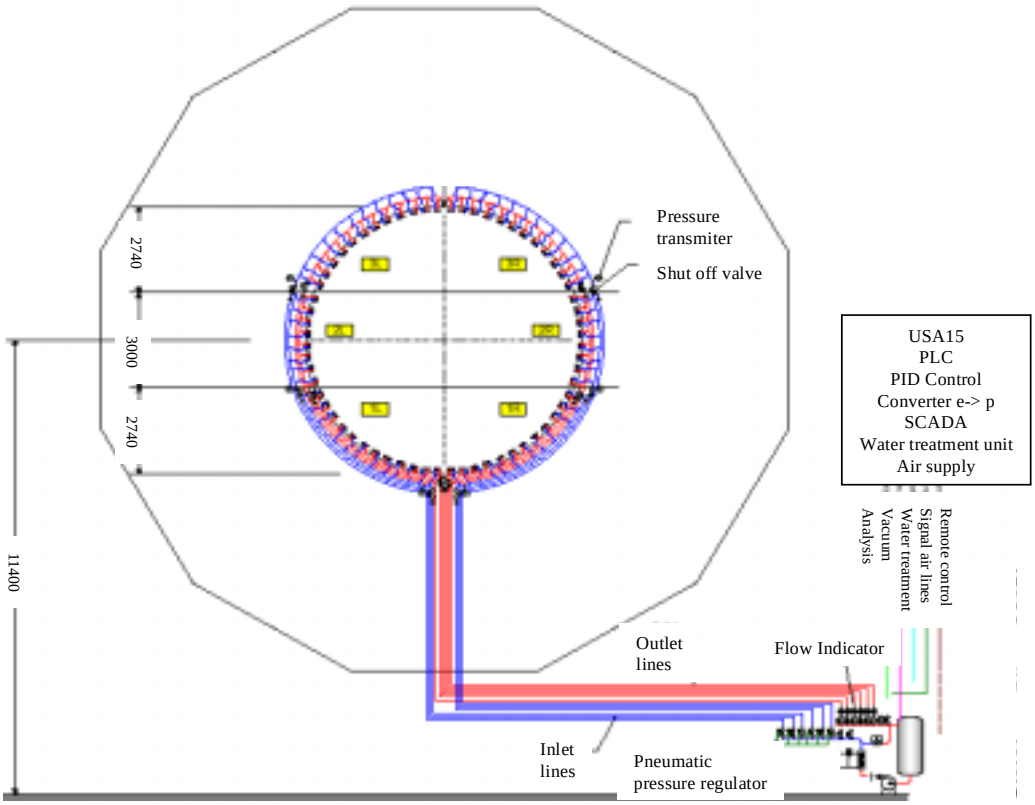

Figure 5.12: *Layout of the cooling system of half Tile barrel.*

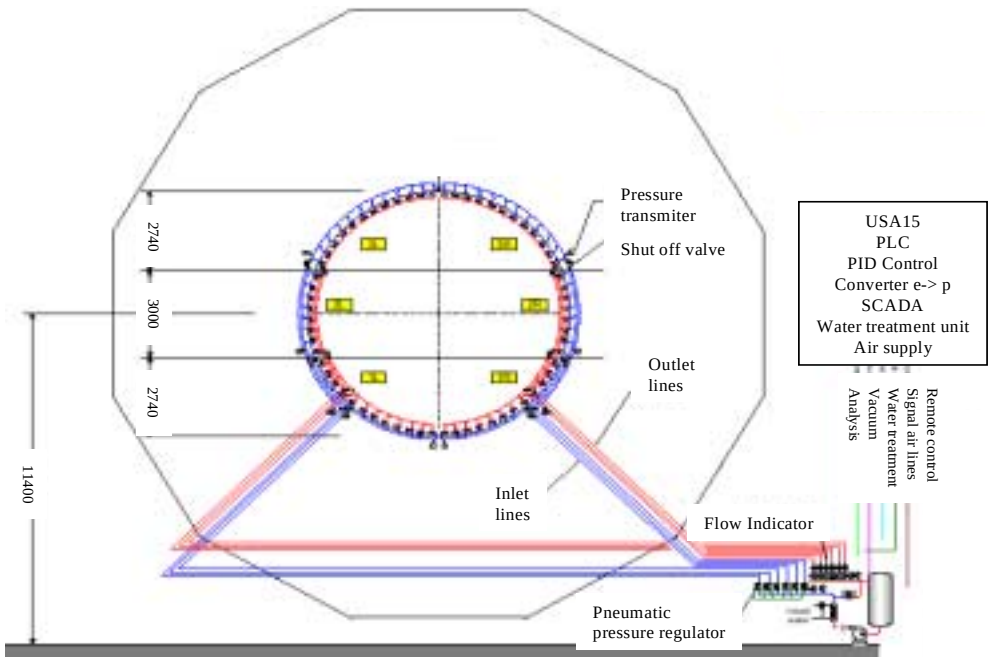

Figure 5.13: *Layout of the cooling system of half Tile end-cap.*

5.4.4 Stand-alone systems

All calibration systems described in section 5.2.4, must be remotely controlled and monitored. In all cases a dedicated control systems will be implemented for this purposes. They will be based on VME crates placed on the underground electronics cavern running dedicated C programs. These crates will interface the front-end equipment via the CAN field bus. The control system will drive the specific equipment but also monitor all operational and environmental parameters of the systems. A first implementation of these control system have been done by different groups of the Tilecal collaboration.

From the point of view of the general DCS, these control systems are regarded as stand-alone systems that the DCS will have to interact with. Information exchange with general DCS is foreseen at the supervisory level. The DCS must also be capable to issue commands on these systems to ensure the safe operation of the detector. The first steps in this direction have recently been given by the responsible of the calibration systems and the Tilecal DCS co-ordination group.

Chapter 6

Calibration of the Tile Calorimeter

Part of the modules of the Tile Calorimeter have undergone the final calibration with particle beam during summer 2001. The general calibration procedure is presented in the first part of this chapter. A DCS was implemented for these testbeams using the standard ATLAS DCS building blocks previously presented. The development allowed the integration of the different DCS subsystems of the calorimeter, namely the cooling, HV and LV systems, and provided communication with the DAQ system. A detailed description of the DCS is given. The chapter concludes with the description of the different tests realized to study the performance of the cooling system of the calorimeter.

6.1 Calibration with the Cs source

A first calibration using the Cs source is performed to all modules of the calorimeter. This allows to check the quality of the response of the different components of the module and equalize the response of all cells of the calorimeter. After instrumentation of the modules, the HV applied to the PMT is set to the nominal value (G_{PMT}=10^5). However, this does not ensure the uniformity of the response of all cells of the module. The light intensity arriving to the PMT depends the characteristics of the scintillating tiles and on the different attenuation of the signal due to the different lengths of the optical fiber used for the readout. The Cs system allows to adjust the HV applied to each individual cell to obtain an homogeneous response of the module. This procedure allows to adjust the current integrals for the PMT to better than 2%. Typically this is achieved in 2-3 iterations. The Cs calibration source provides and absolute calibration and allows to determine the so-called *Cs calibration constants* for each individual cell, which will be applied for offline corrections.

6.2 Scope of the testbeam

The main scope of the beam was the final calibration of the modules of the Tile Calorimeter with beam particles. Only a 12% of the modules, thus one module per octant of each of the three sections of the calorimeter, will be calibrated using particles. In the calibration runs performed in the H8 beam line of the Super Proton Synchrotron (SPS) at CERN during three beam periods in summer 2001, 4 extended and 1 central barrel modules were calibrated.

From the point of view of controls, the testbeam represented a good opportunity to integrate the different DCS subsystems of the Tile Calorimeter and also to introduce the standard building blocks, described in chapter 3, to the collaboration.

6.2.1 Experimental setup

The calorimeter modules were installed on a scanning table, which allows for different positions and orientations of the modules with respect to the beam. The set up, as used for the calibration, is shown in figure 6.1.

It consisted of two central barrel modules and two extended modules although only one central barrel and one extended modules could be instrumented with the electronics drawers at the same time. The extended barrel modules of Tilecal are smaller than the barrel ones. The sizes of the tiles of the barrel and extended barrel are the same, but a different fiber configuration allows a different radial segmentation to adapt the modules to the higher values of η where they will be located. The cell structure of the modules is shown in figure 6.2 for the central barrel and in figure 6.3 for the extended barrels. The numbers in each cell indicate the two corresponding PMT numbers used for the readout.

The calibration of the modules was performed essentially with electrons since the shower originated by this type of particles is almost contained in a cell of the module, giving therefore, an absolute calibration of individual cells. Moreover, the hadronic shower originated by particles like pions is not fully contained in the setup here described. However, as it is shown in the following, studies for different types of particles were carried out during the calibration periods.

Upstream of the calorimeter modules, scintillating detectors are placed making a trigger counter telescope, which define a beam spot of about 2 cm diameter. Two multi-wire chambers, each with *x* and *y* readout, allow to reconstruct the impact point of beam particles on the calorimeter face. Cherenkov detectors in the beam line assist in the identification of the particles.

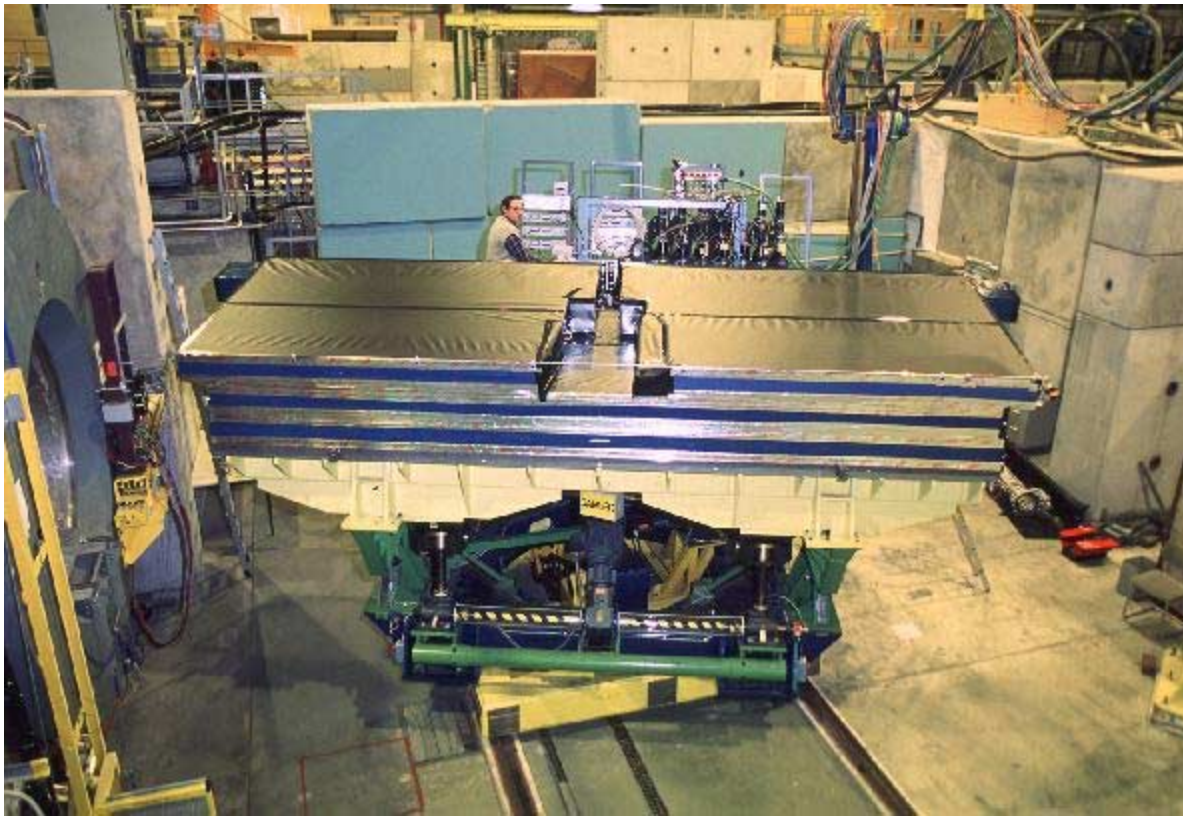

Figure 6.1: *Setup as used during the beam calibration periods. On the scanning table, from bottom to top, a barrel prototype (module 0) is installed, then a production barrel module and two production extended barrel modules.*

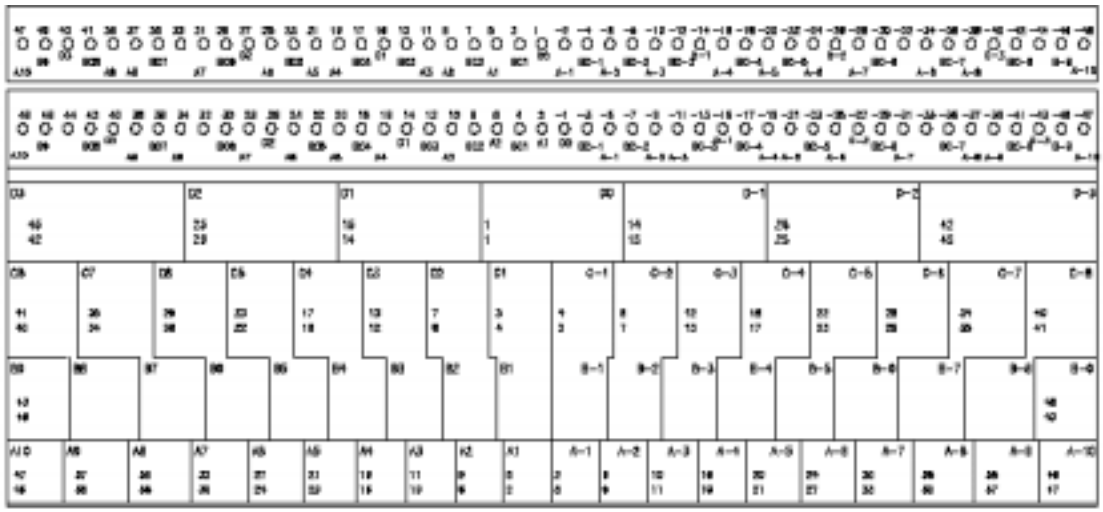

Figure 6.2: *Cell layout of the central barrel module.*

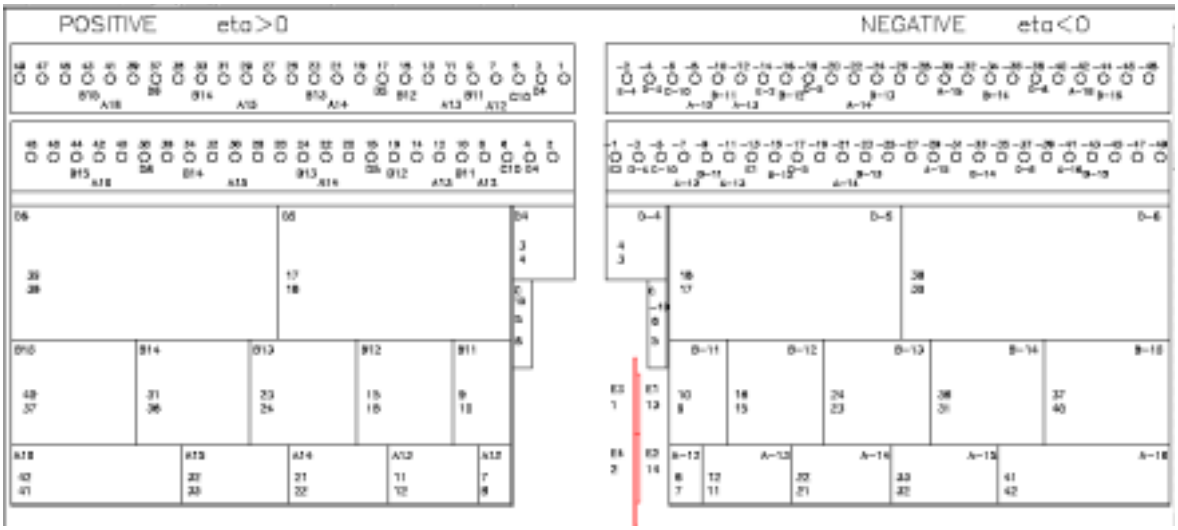

Figure 6.3: *Cell layout of the extended barrel modules.*

Two layers of 2 cm thick scintillating (*muon walls*) installed on the table, one behind the modules and the other laterally, allow the possibility to classify events as either *longitudinal* and / or *lateral leakage* or *no leakage* and assist in the identification of muons.

The stability of the PMT gain was supervised with the laser monitoring system. The charge injection system was employed to determine the linearity of the read-out electronics.

Data were taken for *e*, μ and π beams of different energies and at different orientations with respect to the modules. The DAQ -1 prototype [73] of the data acquisition system was used for the read-out of the calorimeter cells. All physics events as well as the data from the calibration systems and different detectors of the beam line corresponding to each run were stored in *ntuples* for offline analysis.

6.2.2 Calibration physics programme

The calibration of the Tilecal modules covered a wide physics programme including the following aspects:

- Calibration with *e* and π
  - check of the Cs calibration
  - θ angular scan at different beam energies
  - uniformity scans over wide ranges of *z* and *y*
- Calibration with μ

  - Comparison of Cs and muon signals
  - energy dependence of the muon response
  - measurement of the e/μ ratio
  - response uniformity
- Study of fluctuation of the calorimeter response due to tile and fibres
- Dependence of the calorimeter response on the DCS controlled parameters, which constitutes the application work of this thesis and will be described in the following sections.

6.3 The DCS of the calibration testbeam

A flexible Detector Control System (DCS) was developed for the calibration periods of the Tilecal modules in summer 2001. The application aimed at the integration of the different DCS subsystems within Tilecal, namely the Low- and High-Voltage (LV and HV), the cooling system and the scanning table. Currently, the different calibration system are operated fully stand-alone.

The DCS provided the needed tools to monitor and control the running parameters and operational conditions of the Tilecal modules. DCS also enabled the communication with external systems like the SPS accelerator, to retrieve the information of the beam line H8, and to interface the Data Acquisition system (DAQ) by means of the ATLAS DDC package. All relevant DCS parameters were transfer to DAQ for offline analysis. The organization of the different subsystems during the testbeam periods is shown in figure 6.4.

The system developed uses the standard tools chosen to implement the final DCS of the ATLAS experiment. An integrated monitoring application for the LV and cooling system was developed using the components of the ATLAS DCS *Vertical Slice*. For the LV system the standard functionality of the ELMB was extended to drive analogue output channels by means of off-board DAC chips. For the monitoring and control of the HV system, an existing Labview application was used. This application was developed by the Tilecal DCS group. It interfaces a VME crate, which directly controls the FE equipment via the CAN fieldbus.

In the following, a detailed description of the monitoring and control of the different subsystems used in these tests is given.

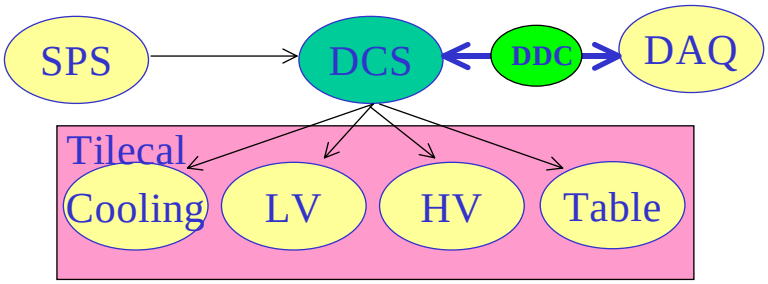

Figure 6.4: *Testbeam system organization*

6.3.1 The DCS of the HV system

Unlike the cooling and LV systems, the DCS of the HV systems was already implemented and had been intensively used in the test-bench of the electronics drawers. A detail description of the system and its performance can be found in [69]. The system is based on a VME crate which runs dedicated C programs for the supervision and control of the HV applied to the PMT. The system handles up to six drawers with the following parameters each:

- Monitoring and control of 48 PMT HV values.
- Reads 7 temperature sensors located in the drawers.
- Monitors 6 more parameters like the HV current consumption and low voltage levels.

The location of the seven probes in a super-drawer is shown in figure 6.5. They measure the temperature of the following elements:

- T1_1 and T2_1: Internal and external HV opto board temperatures respectively.
- T1_2 and T2_2: Internal and external drawer temperatures.
- T1_3: Temperature of the PMT block 22.
- T1_1: Interface card temperature.
- T3: Temperature of the HV micro card.

The VME crate is connected via CAN bus to the front-end equipment. The supervisory software has been developed using LabView. This was considered to be an intermediate solution and the application is currently being ported to SCADA. All signals are read into the VME module and then transferred, via TCP/IP, to a Labview control application running on a PC. Due to the lack of a database at the LabView level, data were stored in simple ASCII files. The integration of this Tilecal subsystem within the PVSS-II framework allowed to transfer all these parameters online for proper archiving in the SCADA database. This integration also permitted

trending of historical data of the HV system using the PVSS-II tools and the presentation to the user the overall status of the experiment in a single Graphical User Interface (GUI) and allowed for offline correlations with the temperatures monitored by the cooling system.

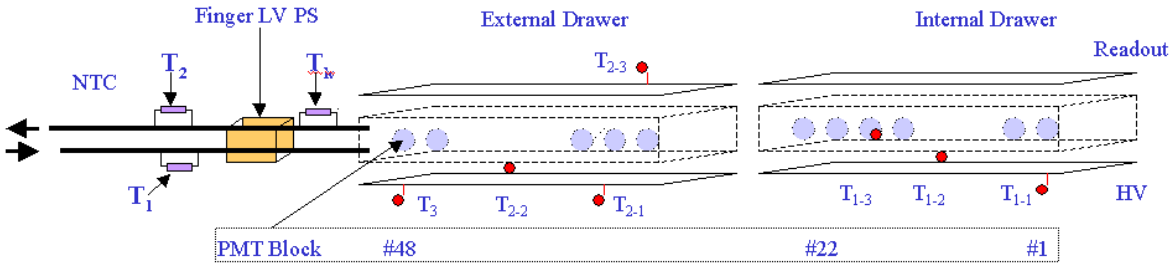

Figure 6.5: *Location of the temperature probes in the drawers and cooling pipes.*

The integration of this Tilecal subsystem within the PVSS-II framework was done via the DLL[a] written in C++, which called subroutines of the API of PVSS-II to access to the real-time database. This interface was developed by the author of this thesis in collaboration Tilecal DCS group. The source code of the library can be found in Appendix A. It basically contains two main functions:

- int *pmt_put(unsigned short int* drawer, unsigned long int* timestamp, signed short int* pmt*), which is called from the LabView application with the drawer number and the corresponding HV values, temperatures and other parameters in an array as arguments. This function stores the values of these parameters with the timestamp in a certain location of the shared memory of the Windows NT system and returns an error code for the operation.
- int *pmt_get(unsigned short int* drawer, unsigned long int* timestamp, signed short int* pmt)*. This second function is called from a PVSS script for a certain drawer number. It was used to poll the shared memory of the operating system at regular time intervals. The readout rate was selectable from the main PVSS-II panel of the application. The function reads the timestamp and array values from the memory location accessed by the first function. If the timestamp read, differs from that stored in the PVSS-II database, the arrays value are set to the proper PVSS-II data points. This values are then archived and displayed on a GUI.

a DLL stands for Dynamic Link Library

6.3.2 The DCS of the LV system

As it was described in the previous chapter, the LV power is provided from a remote 300 V power supply and then it is adjusted to the adequate levels by local power supplies installed in the fingers of the Tilecal modules. A new prototype of these latter power supplies was developed by the Tilecal group for these testbeams. These power supplies provided the 5 voltage levels required for the operation of the readout electronics and HV regulators. The development was based on commercial 300 V DC / DC converters.

Unlike the HV system, the DCS of the LV system was developed completely. The system was implemented using the components of the ATLAS DCS *Vertical Slice*. The monitoring and control of the finger power supplies was performed with the ELMB. The ELMB was embedded on the front-end of the power supplies as shown in picture 6.6 saving space considerably.

In this application it was required to extend the functionality of the ELMB in order to steer two off-board DAC chips needed for the operation of the logic of the supplies. A total of five DAC channels were steered. This work was done by the author of this thesis in collaboration with the Tile Calorimeter group.

Figure 6.6: *ELMB embedded in the electronics of the finger LV power supply.*

6.3.2.1 Extension of the ELMB functionality: DAC

Two Max 255 DAC modules were connected to the PORTE of the ELMB. The schematics of the motherboard design for this purpose is shown Appendix B. Pins PE3 and PE4 were working as chip selects for the two chips whereas PE5 was used for DACCLK and PE6 for DACDATA. The power supplies also provided different

protection mechanisms to avoid damage in case of over-current, over-voltage or over-heating.

The structure of the ELMB software code greatly simplified the integration of the DAC chips. Only the hardware dependent-part had to be modified to call the routines needed to drive the DAC chips. The object dictionary of the ELMB already provides an object, 0*x*2100, to accommodate up to 64 DAC channels. Due to lack of time before the testbeam, the mapping of the entries of this object onto the second received RPDO2 was not implement. The DAC values, stored in the first five entries of this object, were directly accessed via SDO protocol issued by the CANopen OPC server.

All current and voltages, as well as the temperature of the finger power supply were monitored by the ELMB. The list of parameters of the LV system is given in table 6.1. In this case the standard functionality of the ELMB was sufficient. The configuration of the ADC of the ELMB is shown in table 6.2.

Table 6.1 *LV channels of the 300 to 28 V converter and LV switcher boards.*

300 V to 28 V Converter Board		
Reference	**Description**	**ELMB IO Pin**
DISABLE1	Set status of the converter	PORTC bit#1
STATUS1	Read status of the converter	PORTF bit#1
VMON1	Output voltage monitor	ADC channel#1
IMON1	Output Current monitor	ADC channel#2
LV Switcher Board[a]		
Reference	**Description**	**ELMB IO Pin**
DISABLE[2,3,4,5,6]	Set status of switcher	PORTC bits#2,3,4,5,6
VMON[2,3,4,5,6]	Output voltage monitor	ADC channel#3,4,5,6,7
IMON[2,3,4,5,6]	28 V Input current monitor	ADC channel#8,9,10,11,12
IMON[7,8,9,10,11]	LV Output current monitor	ADC channel#13,14,15,16,17
TEMPERATURE	Temperature of the board	ADC channel#18
OTEMP[2,3,4,5,6]	Over temperature indicator	PORTF bits#2,3,4,5,6
OVOLT[2,3,4,5,6]	Over voltage indicator	PORTF bits#7,8,9,10,11
OCURR[2,3,4,5,6]	Over current indicator	PORTF bits#12,13,14,15,16

a. One LV switcher board was used per drawer.

Table 6.2 *ADC Settings*

Mode	Unipolar
Conversion rate	32.5 Hz
Gain	5 V

A total of six finger power supplies having one ELMB each were developed for the testbeam. All ELMB nodes were accommodated on a single CAN bus shared with one more ELMB module used for the monitoring of the cooling system. An additional ELMB node was employed to control and monitor the current output of the 300 V power supply needed to feed the system, which was placed in the main control room. The 80 m long CAN bus was connected to a NI-CAN II interface card, housed in a WNT PC situated in the control room. The layout of the CANbus is shown in figure 6.7. The bus speed was set to 125 kbaud. The ELMB were powered remotely from the control room via the bus with a 9 V DC power supply. The ELMB nodes were readout into SCADA via the CANopen OPC server every 5 seconds. The utilization of the ELMB in the implementation of the front-end of the power supplies has also facilitated the integration of the LV system within the SCADA framework.

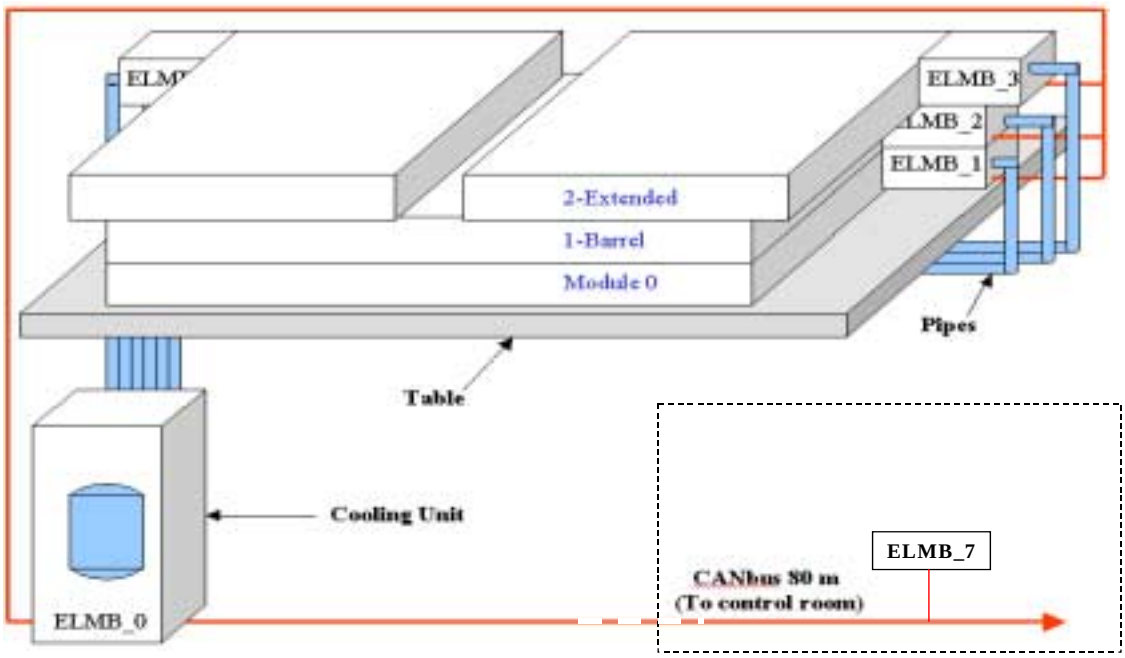

Figure 6.7: *CANbus layout as used for the beam calibrations in the H8 zone. The cooling unit is fixed to the frame of the scanning table.*

Unfortunately only one finger power supply could be tested the last day and several grounding problems were observed. These problem impeded the read-out

of the drawers and they require the redesign of the power supplies. However, the steering and monitoring of the power supplies was satisfactorily tested and all experience gained with this prototype will facilitate new developments. In fact, it is highly desirable that the control of the finger power supplies in ATLAS will be performed with the ELMB.

6.3.3 The DCS of the cooling system

6.3.3.1 cooling system

A new cooling system has been installed and operated in the H8 zone for the summer 2001 beam calibrations. This cooling system is identical to the one that will be used for the Cesium calibrations of all modules of the calorimeter.

The cooling system provided six cooling lines and it was designed to evacuate 2 kW. The required temperatures are 18 ^{o}C for the modules inlet water and up to 20 ^{o}C for the outlet water. The unit is a closed liquid circuit working according to the Leakless cooling System principle [72].

During the summer 2001 calibrations, the finger LV power supplies were not installed. During the normal operating conditions, the cooling water temperature was 18 ^{o}C and the water flow was 60 l/h.

6.3.3.2 Monitoring

The monitoring of the cooling system of the Tilecal modules can be split into three main applications:

- Monitoring of the temperatures of the cooling liquid along the pipes (outside the drawers).
- Interface to the HV system to retrieve the temperatures inside the drawers.
- Monitoring of states and alarms of the different devices integrating the cooling unit.

As previously mentioned, the transfer lines of the cooling system and the modules were instrumented with probes to determine the temperature of the cooling liquid and the different elements integrated in the drawers.

Similarly to the LV system, the DCS used for the monitoring of the cooling system was implemented with the elements of the *ATLAS DCS vertical slice*.

Temperature monitoring outside the drawers

Outside the drawers, three 10 kΩ NTC sensors per module were employed. They were in contact with the cooling water and therefore measuring the temperature of the liquid at the entrance and exit of the drawers, as well as, the temperature of the liquid after the LV power supplies. Additionally, the temperature of the cooling liquid leaving and returning to the unit and the ambient temperature were also monitored. The NTC probes were calibrated with a external reference temperature with a relative accuracy of about 0.1 ^{o}C. The formula used to determine the temperature as function of the resistance of the sensor is given in equation 6.1:

$$T = \frac{1}{a + b \cdot \ln((R_{NTC}) + c(\ln(R_{NTC}))^3)} - T_{offset} \quad (6.1)$$

where $a = 9.577x10^{-4}$, $b = 2.404x10^{-4}$, $c = 2.341x10^{-7}$ and T_{offset} is a calibration constant.

Monitoring of the cooling unit

As the cooling unit is locally controlled by a Programmable Logical Controller only passive monitoring was performed. The status and alarms of the devices composing the cooling unit were also monitored. Their states were transmitted as relay contacts between the pins of the 8- and 12-pins burndy connectors of the module. As the outputs of the unit are isolated, these contacts were measured feeding a small current through the pins.

The following parameters were read:

- Status ON / OFF of the vacuum pump and circulator
- Two levels of alarms from the temperature controller.
- General alarm of the cooling unit.

All cooling parameters were read out by means of one single ELMB (ELMB_0 in figure 6.7) placed onto the cooling unit as shown in figure 6.8. This ELMB node was connected to the same CAN bus used for the LV system.

As these signals were of different types and ranges, it was necessary to adapt them to the ELMB ADC range. Contrarily to the LV system, signal conditioning was done by means of signals adapters plugged onto the ELMB motherboard as described in section 3.3.4.5.

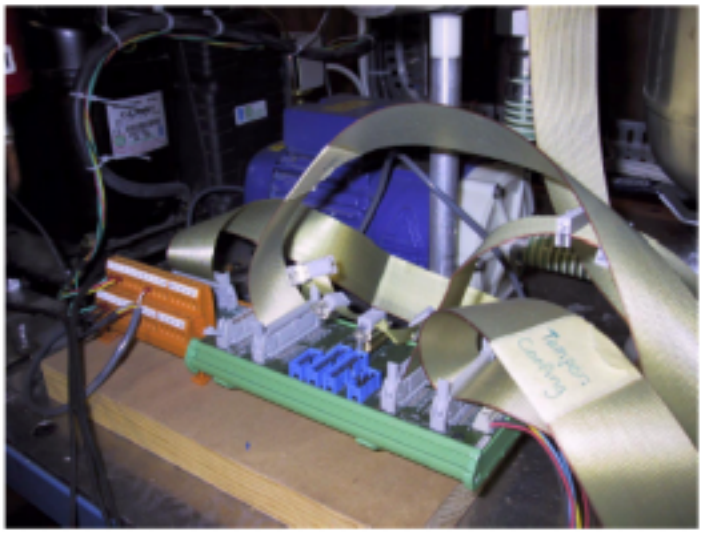

Figure 6.8: *Elmb located onto the cooling unit*

6.3.4 SCADA Application:

All the data coming from the Tile Calorimeter DCS subsystems, as well as the beam information from the SPS and the table coordinates, were stored to the PVSS-II historical database. A subset of the data was transferred online to the DAQ system using the DDC software and then archived for offline analysis. The readout rate for the subsystems was set independently, three seconds being the shortest possible interval. The organization of the software employed in the testbeams is shown in figure 6.9.

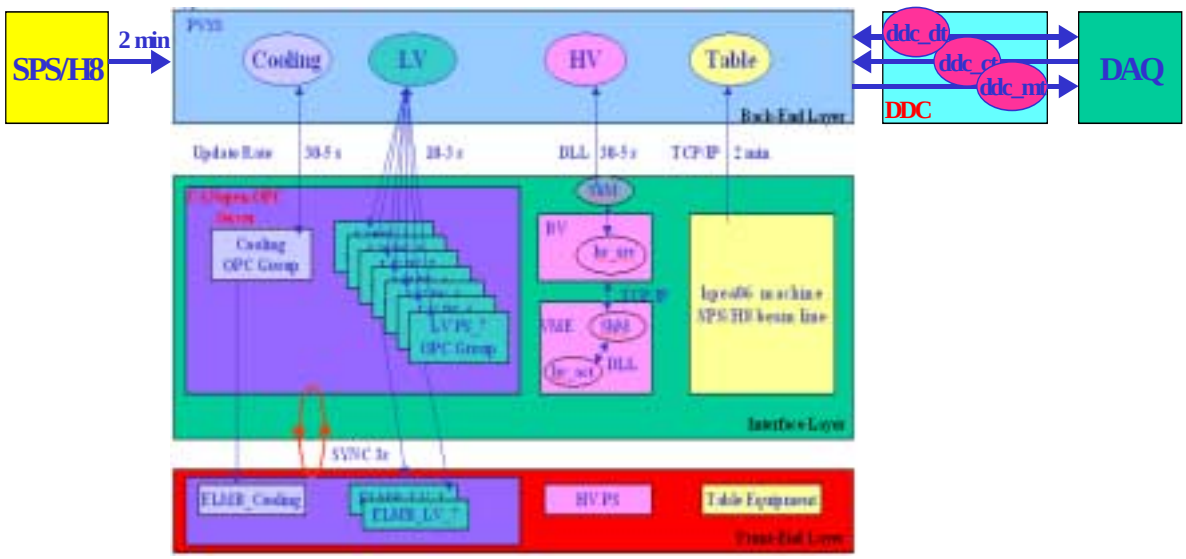

Figure 6.9: *Software organization as used for the calibration periods*

The device-oriented nature of PVSS-II permits to model each Tilecal module as a structure or data point in the database as shown in figure 6.10. Similar data points were created to model other devices in the setup, like the cooling unit or the ELMB nodes. This structure holds a hierarchical and logical representation of the different DCS subsystems of each module. The bottom-most leafs in these structures are called *dp-elements* and represent the actual variables of the systems, which can be addressed to hardware channels.

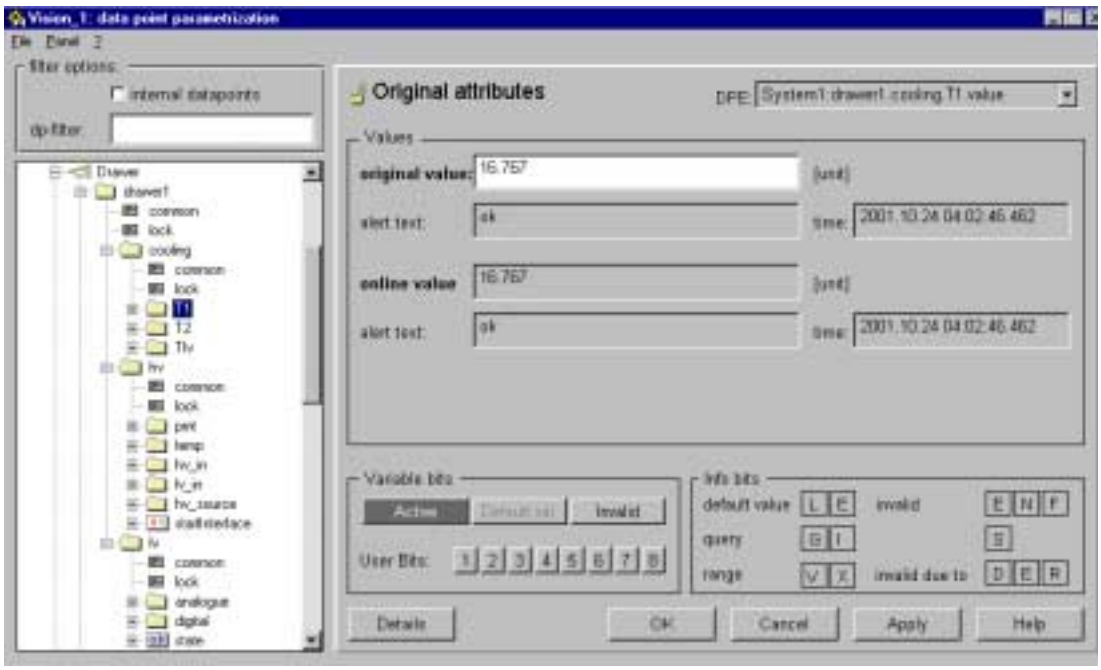

Figure 6.10: *Drawer data-point.*

6.3.4.1 Operator Panels

Figure 6.11 shows the main panel of the PVSS-II application. Three main areas can be distinguished corresponding to the three DCS subsystems. The general states of the different data sources are color-coded and the current readings of the operational parameters are also shown in the panel. Dedicated panels for each subsystem and a graphical interface to the historical database for trending and exporting of data, as well as alert handling are also provided.

Figure 6.12 shows the trends of the cooling parameters for drawer 1 over several days. Ambient temperature and the output and return temperatures of the cooling liquid from / to the unit, are also shown in the panel. As during this period, the LV system was switched off and with no cooling, the trend of the temperature of the LV system follows the ambient temperature.

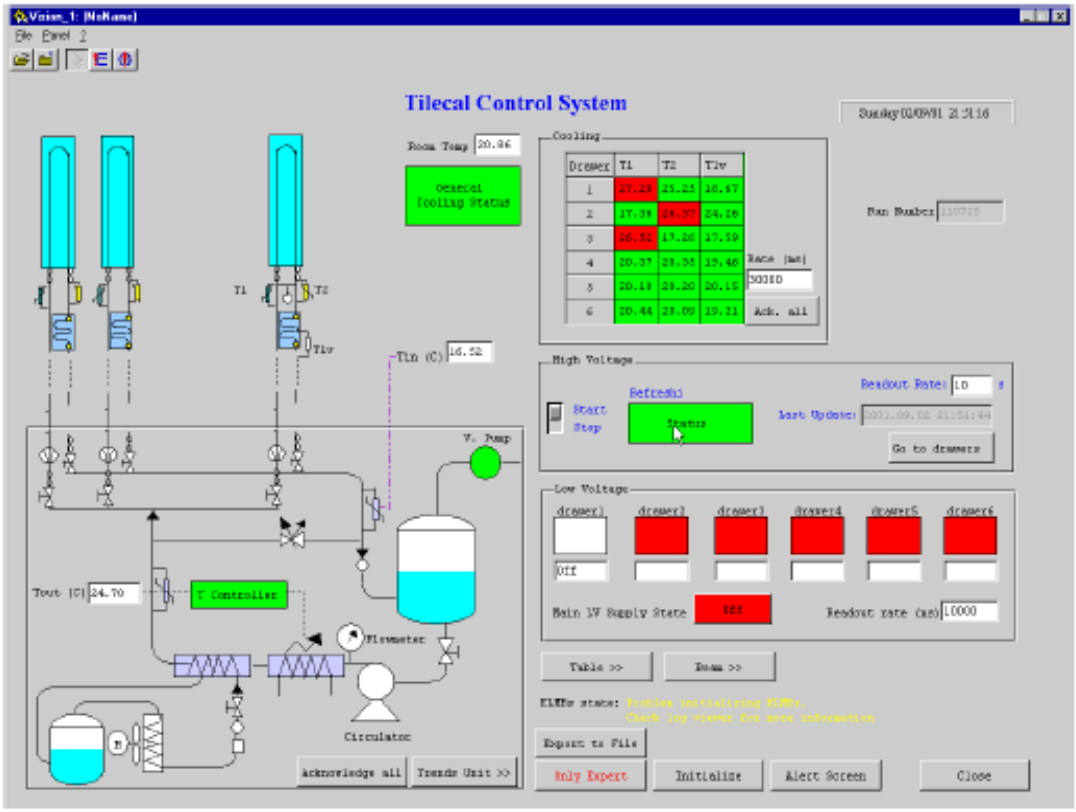

Figure 6.11: *PVSS-II operator main panel*

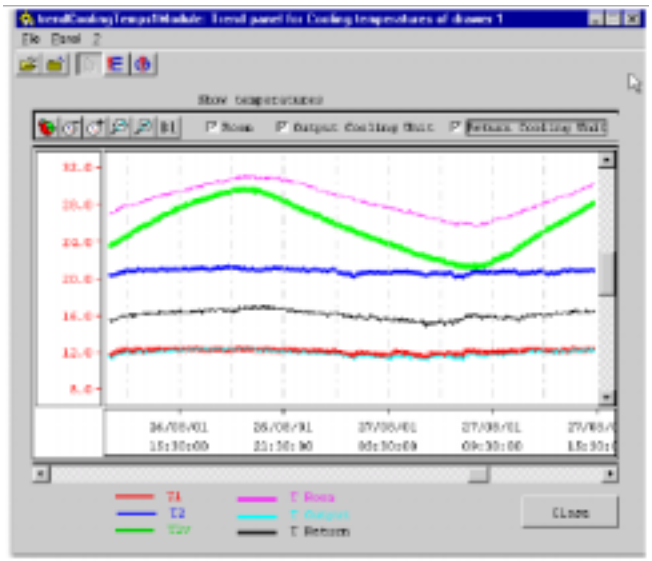

Figure 6.12: *Trend panel of the cooling system.*

Figure 6.13 shows the dedicated PVSS-II HV panel for a certain drawer, which can be accessed from the main panel of the application. The tables in this panel show the current values of the HV parameters. Historical data can be accessed by means of the specific trend panels.

Figure 6.13: *HV panel for drawer 1.*

A similar panel for the finger LV power supplies is shown in figure 6.14.

Figure 6.14: *PVSS-II panel for the finger LV power supply placed on drawer 1.*

Due to the need of accessing to the DCS data remotely, a dedicated web interface[a] to the application was developed. This interface allows for SQL queries to the PVSS-II

database from any web browser. Figure 6.15 shows the online values of the cooling parameters accessed with a web browser. Historical data can also be exported to a downloadable ASCII file. In this case, the SQL query can be performed for a particular run number or a defined time interval.

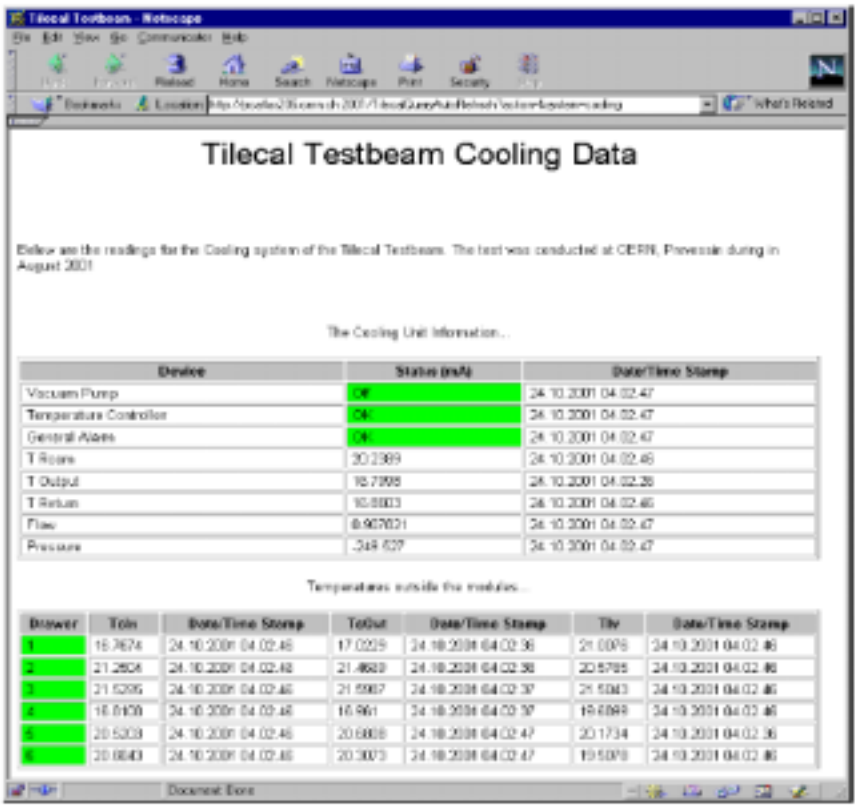

Figure 6.15: *PVSS-II Web Interface showing the on-line values of the cooling system.*

6.3.4.2 Interface to the SPS and scanning table controls

As we have seen in chapter 2, one of the tasks of the DCS is to provide an efficient interface to the accelerator. This functionality was also implemented in the control system described here. The beam information for a certain beam line is published by the SPS in the so-called Non Standard Block (NSB) every two minutes. The NSB contains a list with 256 integer parameters which describe the beam composition and its characteristics, as well as the states of the different optical elements in the beam line H8, like collimators or bending and focusing magnets. A remote shell was opened from the PVSS-II application in order to access to the SPS NSB. This file was directly imported in the application. The relevant beam parameters were

a URL: http:/ / pcatlas206.cern.ch:2001

decoded and compared to those read from the PVSS-II database. The changed values were updated to the corresponding data points in the SCADA database. Figure 6.16 shows the PVSS-II panel used to display the beam information.

The scanning table is also controlled remotely and independently from the DCS. However, these information is essential for the offline analysis. For these reason, a interface similar to that used for the beam information, was developed to access to the co-ordinates of the table. The table panel of the application is shown in figure 6.17.

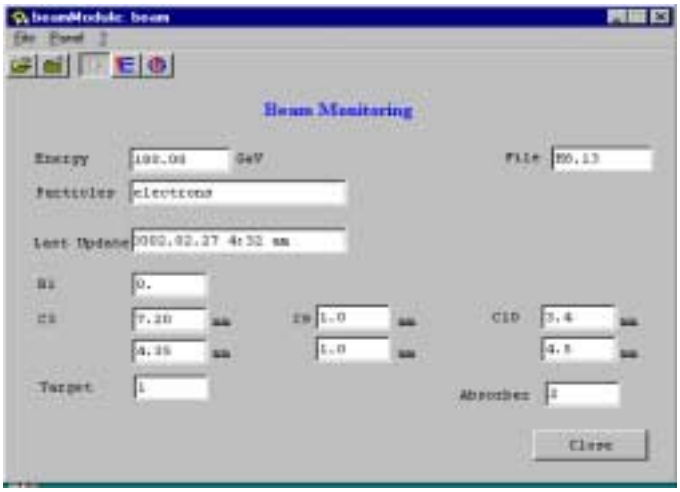

Figure 6.16: *Dedicated PVSS-II panel for the beam.*

Figure 6.17: *Dedicated PVSS-II for the scanning table*

6.3.4.3 Experience with the DDC software

A first implementation of the DDC package was released in 2001. It provided the functionality described in chapter 3. The utilization in this testbeam periods constituted the first experience with the product and served as test-bench for the product. Although the three managers comprising the DDC package were satisfactorily tested, several issues and limitations of the version of the product evaluated, were identified. The feedback provided to the developers allowed to re-design some features of the product according to the User Requirements Document [47]. In addition, the testbeam permitted to identify some new features which would enhance the functionality of the package during data taking. In the testbeams, all DCS data relevant for the offline analysis are transferred from the PVSS-II application to the DAQ system using the DDC package. In the following the experience with the DDC product is described.

The usage of the components of the DDC package required the utilization of a special version of the DAQ libraries. It was found that PVSS-II and the DAQ software employ different compiler options, in particular, the so-called Real Time Type Information (RTTI) used on the DAQ side. This impeded the DDC software to be started. This has already been discuss with ETM and an special version of the PVSS-II API has been released for its utilization in ATLAS.

The *ddc_dt* component, which provided bi-directional data exchange between DAQ and DCS, was employed during the three beam periods. The version of the ddc_dt used, supported only basic data types. Other types, like arrays, will be added in next releases of the product. Table 6.3 gives the total number of parameters per DCS subsystem handled by this component.

Table 6.3 *Total number of IO channel per subsystem during the testbeam and number of variables handled by the ddc_dt manager from DCS to DAQ.*

Subsystem	Total Channels	Handled by DDC
cooling	26	22
LV	216	186
HV	366	330
Beam	256	256
Scanning Table	18	18
Total	**882**	**812**

The size of the database after the three calibration periods was about 100 MB belonging to ~500 runs collected. This data volume does not represent a problem neither for the DDC nor on the DAQ side. The data traffic was mainly from DCS to

DAQ. Only the run number was transferred from DAQ to DCS. This parameter is very useful on the DCS side since it allows for correlations between operational parameters and calorimeter performance for a particular run. Besides, it allows to define certain time intervals, which correspond to the duration of a particular run, in the DCS database. These intervals can be used for offline retrieval of a set of parameters using the SQL and web interfaces of the PVSS-II application, for a given run. Transfer of data from DAQ to DCS was rather complicate using this first version of the DDC software. DAQ parameters are published in the Information Service as structures, which are unknown to the DDC. In order to access the run number in this testbeam, the so-called *Run_Params* structure of the DAQ system, containing the parameter, was coded in the DDC source. This limitation of the *ddc_dt* will be corrected in future versions of the component in which the data type of the different elements will be interrogated and the structure will be dynamically modelled by *ddc_dt*.

The transfer of data from DCS to DAQ is straightforward since it only requires the definition in a list of the DCS parameters, i.e. of the PVSS-II data-points, to be handled by the DDC. This list is imported by the ddc_dt component at start and the corresponding SCADA data-points are published in the DAQ Information Service on change. The current value of the DCS parameters is therefore, available to any DAQ application, in particular to the so-called Online Bookkerper of the DAQ system, which handles the archiving of data to the database. Another issue was met at this point since the data update by both the DDC and the Online Bookkepper only takes place on change. This can arise problems at start of run as the current values of the DCS parameters are required in the DAQ side but these are only update on change. Although this is seen as a limitation in the DAQ side due to lack of functionality of the Online Bookkeeper, during the testbeam periods it could be overridden by forcing the update of the relevant SCADA data-points by means of a script. However, this was rather slow (~3 s) and a proper mechanism for data update on request must be implemented either in the DDC software or on the DAQ side. This procedure would also reduce the data traffic significantly since some data are only required at start of run.

The issuing of commands from DAQ to DCS by means of ddc_ct was also tested during first beam period to trigger actions, like update of DCS data at start and end of DAQ runs. The commands are defined in the DAQ database and are transferred at certain transitions of the finite state machine of the DAQ system. As result of the command, a data-point having the same name as the command is set in PVSS-II triggering an associated script which performs a particular task. Several problems, which broke the independence between DAQ and DCS, were identified. The limitation reside in the fact that the DDC assumes that the DCS is available running as specified in the User Requirements Document. However, this is not always the case during commissioning and testbeam periods where the development of the system may be required in parallel to data-taking. As explained in section 3.8 the ddc_ct component is implemented as a controller in the DAQ hierarchy. This

controller can not be started should the connection to the PVSS-II event manager fails, causing a general failure of the DAQ system. This limitation is currently being solved and in future releases of the software the ddc_ct component will implement a wait-loop to retry the communication with PVSS-II ensuring the independence between the DCS and the DAQ system.

In the last beam period, the third component of the DDC package, the ddc_mt was satisfactorily tested. As request from the DAQ side, trips of the HV system were asynchronously notified to the Message Reporting System. The implementation of this functionality was done in a short period of time (~10 min.), due to the experience gained with the other components in previous campaigns and the quality of the documentation.

The feedback from the testbeam periods has been taken into account by the developers. All limitations mentioned above are suppressed in the DDC version 3.2 that will be released for the test beam periods in summer 2002.

6.4 Performance of the cooling system

The control system described above has been used to determine the performance of the cooling system as well as, the influence of the DCS controlled parameters, like cooling and HV settings, on the response of the calorimeter. This section describes the different tests performed in order to determine the performance of the cooling system and its repercussion on the front-end electronics. The physics analysis and results on the dependence of the calorimeter response on the DCS parameters can be found in the next chapter.

6.4.1 Stability of the cooling system

The final values of the operating cooling parameters (temperature and flow) depend on the stability requirements of the Tile calorimeter and power dissipation with all the components installed, including the finger low voltage power supplies. At the end of the September period, some dedicated cooling tests were done in order to check and to measure the performance of the cooling system and the response of the calorimeter as function of the cooling settings. One of the tests consisted in varying the water flow and looking at the evolution of the temperatures in the system. Another test consisted in varying the water cooling temperature and in measuring the effect on the temperatures inside the drawers and on the gain of photomultipliers.

The stability of the cooling system has been monitored using temperatures probes located inside and outside the drawers. During the September period, only two

super-drawers were installed (in the extended barrel modules EBC-15 and EBC-24). In the following, drawer 2 refers to the super-drawer installed in module EB-C-15 and drawer 5 to module EBC-24.

Figure 6.18 shows the whole history of the cooling outside the drawers during the calibration period in September 2001.

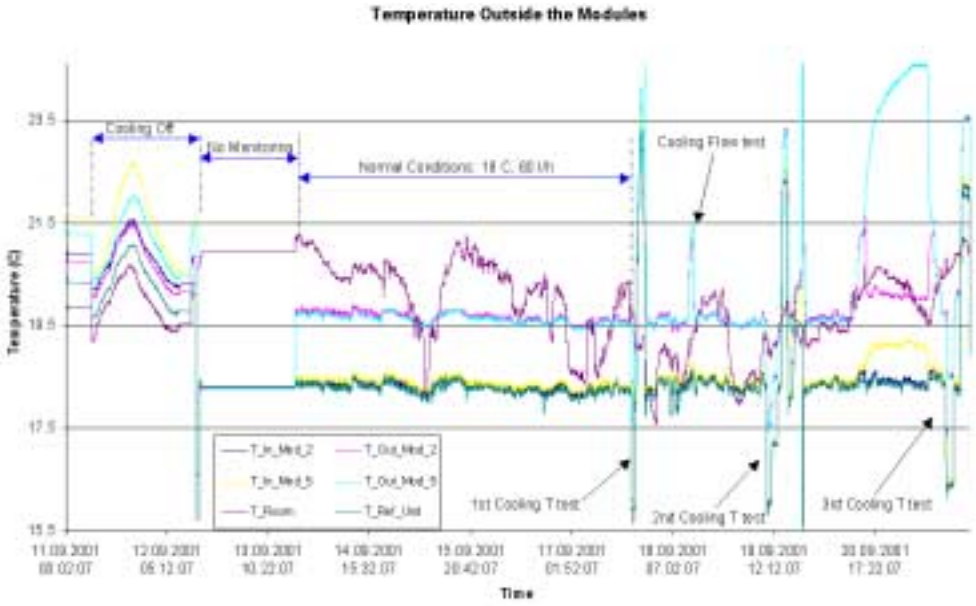

Figure 6.18: *History of the cooling outside the drawers during the calibration period in September 2001.*

Figure 6.19, represents, as a function of time and for a period of 5 days, the value of the inlet and outlet water temperature of the two super-drawers and of the water temperature at the output of the cooling unit. The values of the inlet temperatures and at the level of the cooling unit are very similar since isolated pipes of 10 meters long were used between the cooling unit and the super-drawers. One can see that the behavior of the five temperature probes as a function of time is the same. The small instabilities are due to the regulation cycles of the cooling system.

The average value as well as its error, for the five temperatures, is given in table 6.4. Therefore, we see that the cooling unit shows a very good stability, as well as the temperatures at the output of the unit, they are stable within 0.1 ^{o}C. Over the same period, the temperature difference between the inlet and outlet water is $\Delta T = 1.35\ ^{o}C \pm 0.05\ ^{o}C$ for drawer 2 and $\Delta T = 1.25\ ^{o}C \pm 0.05\ ^{o}C$ for drawer 5. If the final finger low voltage power supplies would be installed, the expected ΔT would be approximately 2 ^{o}C. This will be confirmed during next year calibrations.

.

Table 6.4 *Mean value of the temperature of the water at the input and output of the two drawers and at the output of the cooling unit. These values area averaged over the five days of the September calibration period.*

Temperature	Average value (^{o}C)
Inlet drawer 2	18.3 ± 0.1
Inlet drawer 5	18.4 ± 0.1
cooling output	18.3 ± 0.1
Outlet drawer 2	19.7 ± 0.1
Outlet drawer 5	19.6 ± 0.1

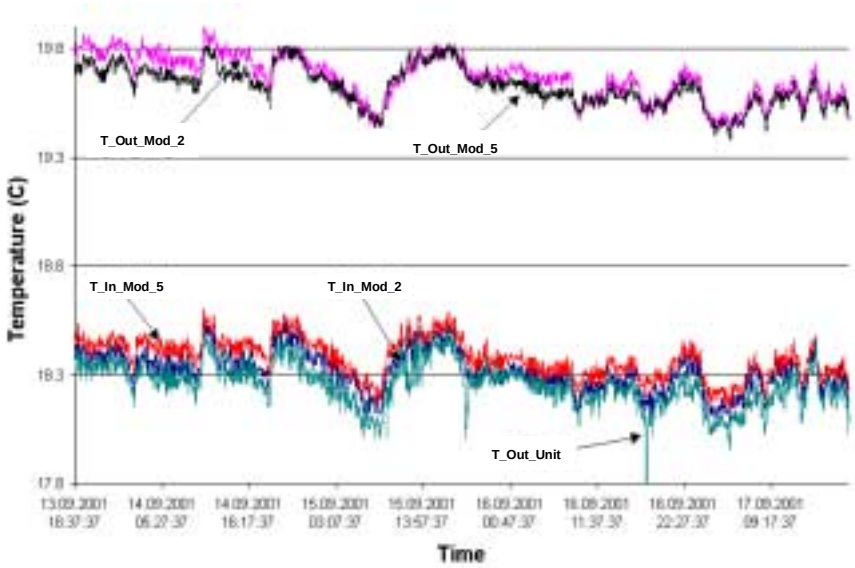

Figure 6.19: *Variation of the temperature of the water at the input and output of the two drawers and at the output of the cooling unit, as a function of time during the September calibration period.*

The stability of the temperature inside the drawers has also been measured by the use of the temperature probes readout by the HV system (see section 2). Figure 6.20 represents the variation of the seven temperature probes inside drawer 2 during the September period. One can see that all the seven temperatures are very stable. The probe located near the photomultiplier PMT22 gives an average value of 24.5 ^{o}C, with a stability of 0.1 ^{o}C. Therefore, one can conclude that with this cooling system, the variation of the gain of the photomultipliers due to temperature variations is totally negligible.

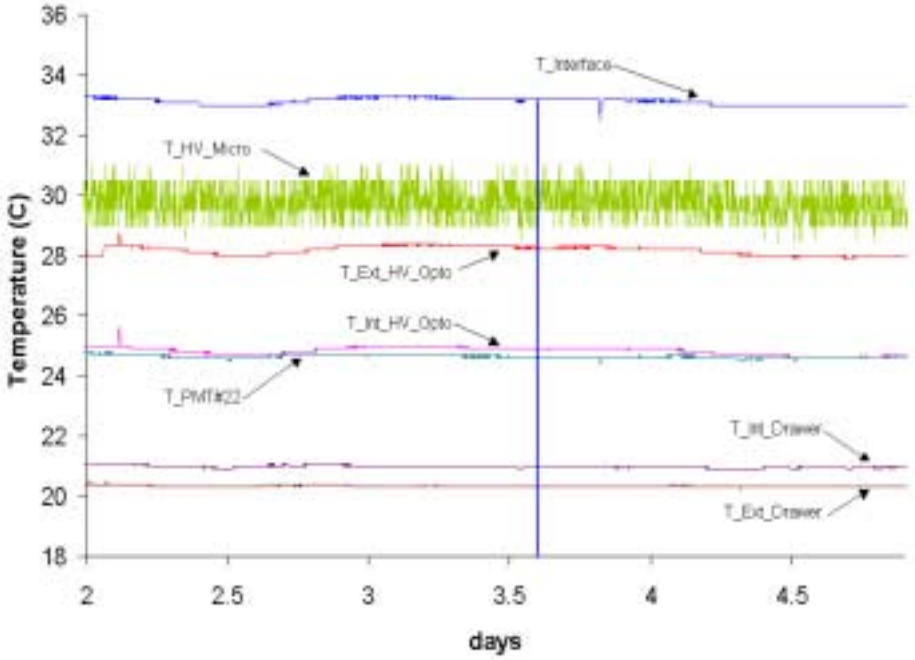

Figure 6.20: *Variation of the temperature of the seven probes located in drawer 2 as a function of time during the September calibration period. One observes the same behaviour for drawer 5.*

6.4.2 Calorimeter performance

6.4.2.1 Water flow variations:

This measurement was made at a constant cooling water temperature of 18 ^{o}C. The water flow was varied between 10 l/h and 60 l/h. At each setting of the flow (10, 20, 40 and 60 l/h) and after stabilization, the temperatures inside drawer 5 were measured. Figure 6.21 shows the variations of the seven temperatures as a function of the flow. In the region 40-60 l/h, the temperatures tend to be almost independent from the flow. One has to keep in mind that this test was done without the finger LV power supplies. The flow will have to be optimized with the finger power supplies installed.

6.4.2.2 cooling water variations:

The cooling water temperature was varied by steps in the range 16 ^{o}C to 22 ^{o}C, at a constant flow of 60 l/h. After stabilization at four values (16, 17, 18, and 22 ^{o}C), the temperatures inside the drawers were measured. The stabilization time was of the order of 1-2 hours. Figure 6.22 represents the variation of the seven temperatures

inside drawer 2 as a function of the cooling temperature. A similar temperature increase rate was found for all the temperature probes, e.g., the temperature close to PMT22 vary by half (3 ^{o}C) the variation of the cooling water (6 ^{o}C). This gives:

$$\Delta T_{PMT} = \frac{1}{2}\Delta T_{Cooling} \tag{6.2}$$

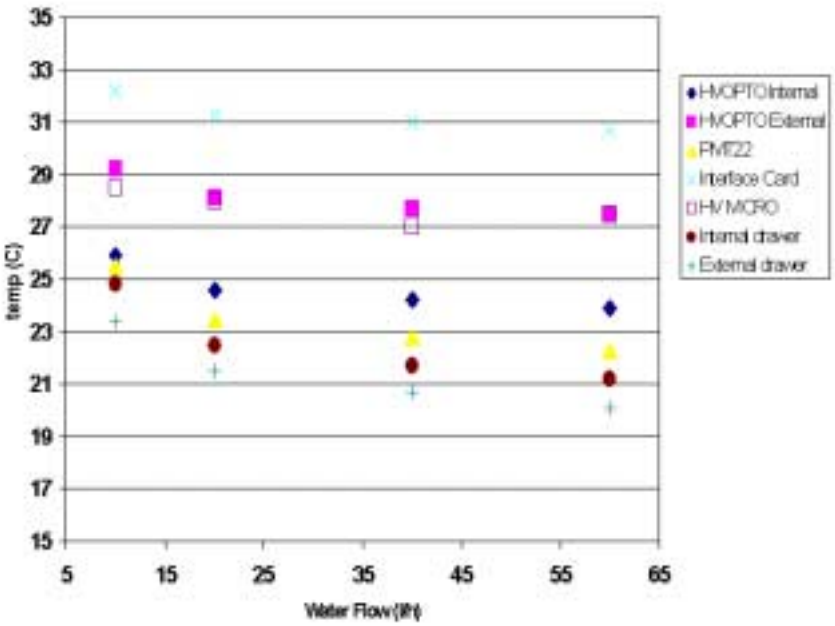

Figure 6.21: *Variation of the temperature of the seven probes located in drawer 5 as a function of the cooling water flow.*

6.4.2.3 Conclusions

The cooling system used for beam and Cesium calibrations has been described. The monitoring system based on the PVSS-II SCADA product has been developed and operating very efficiently during the summer 2001 calibration periods. The stability of the cooling unit was very good, at the level of 0.1 ^{o}C, allowing a very good stability of the electronics located in the drawers. The variation of the gain of the photomultipliers as a function of the water cooling temperature is 0.1% / ^{o}C.

From these studies, we conclude that if the water stability would be the only factor responsible for the PMT gain stability, then in order to ensure a PMT stability of 0.5%, the temperature variations in the PMT block have to be smaller than 2.5 ^{o}C. This corresponds to a temperature variation in the cooling station of 5 ^{o}C. In the calibration setup, all the pipes were isolated. This will most likely not be the case in ATLAS due to space constraints. What remains to be done is the measurement of

the stability of the inlet drawer water temperature using the non-isolated tubes that are expected to be used in ATLAS.

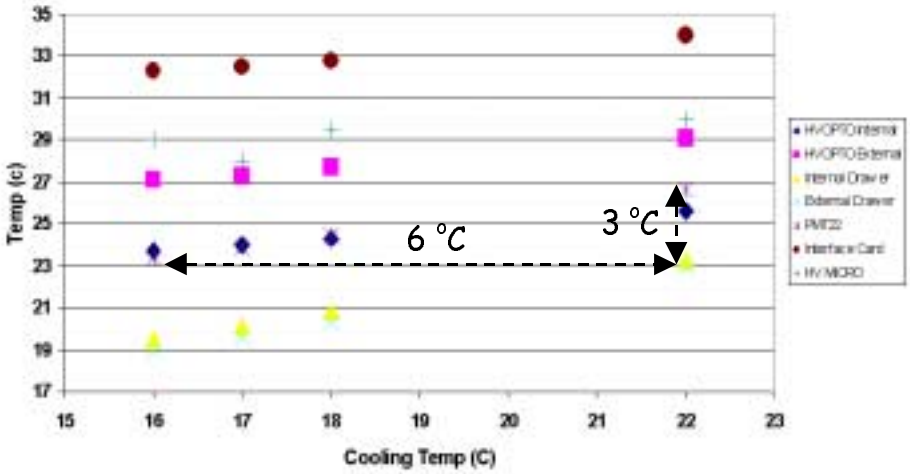

Figure 6.22: *Variation of the temperature of the seven probes located in drawer 2 as a function of the cooling water temperature. One would see the same behaviour for drawer 5.*

Chapter 7

Effects of the DCS controlled parameters on the calorimeter response

During the calibration periods of the modules of the Tile Calorimeter, a systematic study of the effects of the DCS controlled parameters on the calorimeter response has been performed. The photomultipliers (PMT) used in the calorimeter are the most sensitive components of the readout system to the operational conditions, namely the applied HV and the temperature. In this chapter a brief description of the PMT is given. The main requirements for their utilization in the Tile calorimeter are outlined. In the following, the HV and cooling tests performed are described and the analysis procedure is presented. Finally, the results on the energy resolution and linearity of the calorimeter for electrons and pions are shown. The asymmetries between the two PMT used for the double cell readout are studied. The photostatistics of the PMT is also treated and an estimate of the number of photoelectron produced in the PMT is given.

7.1 Photomultipliers

Photomultipliers are electron tube devices which convert light into a measurable electric signal. Figure 7.1 shows the different components of a typical PMT. The photocathode converts photons into electrons by photoelectric effect. This phase is characterized by the so-called quantum efficiency of the PMT, which is defined as the ratio between the number of electrons released and the number of photons on the cathode. The quantum efficiency of the PMT is therefore a function of the wavelength of the incident light.

The electrons created in this phase are focussed by an optical system into an arrangement of electrodes, called dynodes, which multiply the signal at each step. The total charge produced is collected by the anode for its readout.

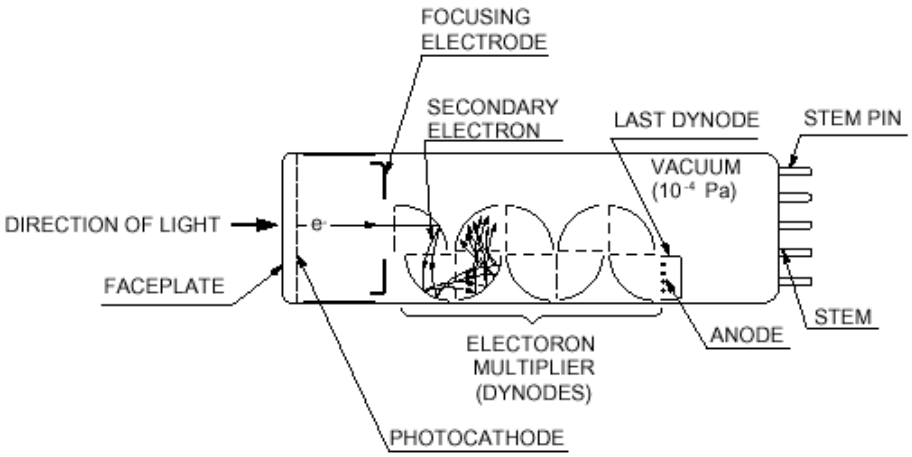

Figure 7.1: *PMT layout.*

The multiplication process is characterized by the gain of the PMT, which is given by the following equation:

$$G = \frac{I_a}{I_k} \tag{7.1}$$

where I_a and I_k are the currents at the level of the anode of tube and the intensity released by the photocathode respectively.

The overall gain of a PMT depends on the number of dynodes in the multiplier section and the secondary emission factor δ, which is a function of the energy of the primary electron. This energy is a function of the voltage difference between the dynodes. If an efficiency of collection of 100% is assumed at all stages of the amplification and that the voltage applied to the PMT is equally distributed among all dynodes, the gain of the PMT can be expressed as follows:

$$G = \alpha V^{\beta} \tag{7.2}$$

where the parameters α and β are usually determined by calibration.

7.1.1 Tilecal Requirements on PMT

PMT constitute an essential part of the readout of the calorimeter and determine the detector performance to some extent. The main specifications of the PMT are derived from the overall physics performance. The main requirements that must be satisfied are:

- The energy deposited by physics events on the cells of the calorimeter at the

LHC will range from 350 MeV for muons up to a few TeV for jets. In order to provide a good linearity of the response of the calorimeter over the full dynamic range, a good linearity of the PMT is needed.

A nominal PMT gain of 10^5 was chosen to cover the whole dynamic range. However, the gain could be significantly reduced to avoid the saturation of the readout electronics at high energies.

- The utilization of wavelength shifting fibers (420 nm $\rightarrow$480 nm) in the readout of the calorimeter cells requires a good quantum efficiency of the PMT at the operating wavelength.
- The rising time of the PMT must allow for the operation at LHC luminosity and provide fast signals to the LVL1 trigger system.
- The PMT must operate in presence of residual magnetic fields up to 20 Gauss.
- A good uniformity of the photocathode is needed in order to have a homogenous conversion of photons into electrons on the whole surface of the PMT. This also applies to the anode to ensure an uniform collection of charge.
- The location of the PMT inside the drawers requires reduced dimensions.

A systematic study of different types of PMT has been performed by the Tilecal collaboration. The results of this analysis can be found in [63, 74]. These measurements led to the selection of the 8-stage PMT, model R7877, from Hamamatsu for its utilization in the Tile calorimeter.

7.2 Calorimeter response

During the calibration periods of the modules of the calorimeter, the effects of the DCS controlled parameters, namely HV applied to the PMT and temperature of the cooling, on the calorimeter response has been studied. A 180 GeV electron beam was hitting the module EBC-24 (referred as module 2 in the previous chapter) at projective η (–1.35), in cell A14 as shown in figure 7.2. This calorimeter cell was read out by PMT 21 and 22, the latter containing a temperature probe.

In addition, online monitoring of the different elements of the calorimeter was performed using the laser and charge injection systems. Several runs with a total number of 50000 events were performed for different settings of the HV and cooling systems. Data from these different subsystems were stored in a *ntuple* at each run. The DCS parameters were monitored by the PVSS-II application and archived into the internal database.

Figure 7.3 shows the charge deposited by physics events, and laser and charge injection systems in cell A14 corresponding to the normal operation conditions of the calorimeter, *i.e.* temperature of the cooling system at 18 ^{0}C, a flow of 60 l/h, and PMT HV values obtained from the calibration with the ^{137}Cs source. Laser and CIS

events were systematically alternated with physics events using periods with no beam.

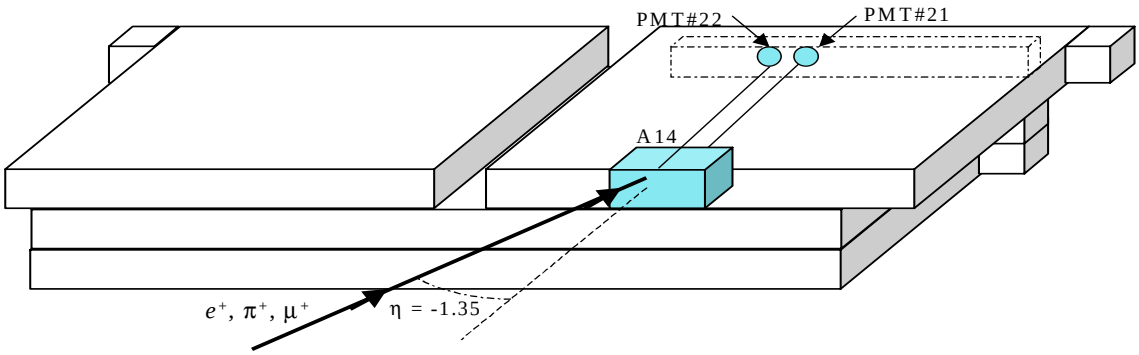

Figure 7.2: *Setup as used during the calibration of the Tilecal modules with particle beam. A 180 GeV electron beam was hitting on cell A14 of the extended barrel module EBC-24, read out by PMT 21 and 22.*

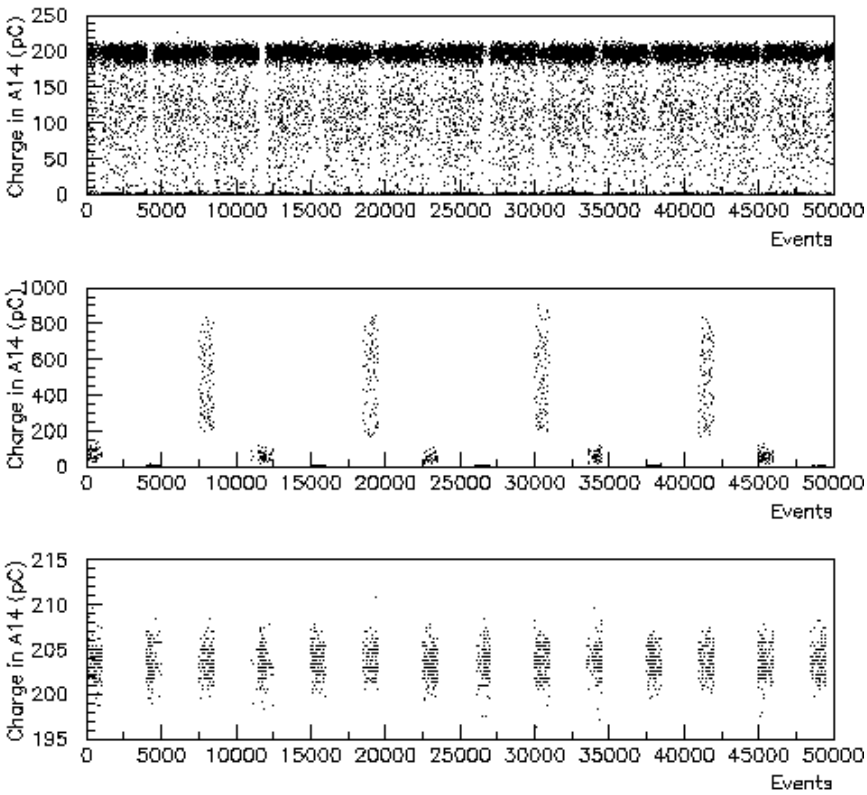

Figure 7.3: *Reconstructed charge in cell A14 for physics, laser and charge injection events.*

The energy deposited in the cell by the physics events range from a few pC up to 220 pC. This is a consequence of the large degree of contamination of the electron beam with pions and muons. As described in the previous chapter, different types of particles release energy in the calorimeter differently. This characteristic is used to perform particle identification with calorimeters. 90% of the cascade originated by electrons is contained in the hit calorimeter cell. Hadronic showers created by pions extend to several cells and therefore, only part of the energy of the incident particle is deposited in cell A14. Muons are *minimum ionizing particles* (m.i.p.), *i.e.* they loose energy in the calorimeter only by ionization and their energy loss per unit length, *dE/dx*, is equal to the minimum for the medium concerned. Therefore, only a small part of the energy of the incident muons is detected by the calorimeter. The analysis of the physics data requires the utilization of adequate cuts which allow to separate the different types of particles. A detailed description of the cuts used in this study is given in the next section.

The laser is equipped with a system of filters which allows to illuminate the PMT with 3 different intensities producing 3 different charges in the readout system. These intensities correspond to the direct laser and to 10 and 100 times attenuated laser intensities. These different signal intensities allow to monitor the linearity of the PMT response in the full dynamic range of the calorimeter as it will be shown in the next sections.

A 100 pC charge, with a precision of ~2%, is induced by the charge injection system in each of the readout channels of the cell. This allows to study the stability of the electronics and isolate effects due purely to the PMT.

7.2.1 Particle separation

7.2.1.1 Beam composition

The separation of different types of particles in the beam has been performed using two different cuts. The first cut is based on the information from two Cherenkov counters installed in the beam line. The second one is based on the characteristic energy deposition pattern of different types of particles in the calorimeter. In the following, the former is referred to as *Cherenkov cut* whereas the latter is called *hadronic cut*. Figure 7.4 shows the beam spectrum as a function of the energy deposited in the whole volume of the module (solid line) and only in cell A14 (dashed line). The energy in cell A14 is mainly deposited by electrons but also by pions releasing a small fraction of their energy in the cell. The total energy deposited in the module allows to identify the three types of particles, centred at different energies. The shower originated by electrons is fully contained in the modules, whereas the hadronic cascade originated by pions is only partially contained. For these reasons the distribution of electrons is centred around 205 pC,

whereas the pion peak is found at lower values. The muon peak is centred around 10 pC and is very close to the pedestal of the readout system. A clear separation of these two signals is required in order to improve the trigger performance to muon events of the calorimeter.

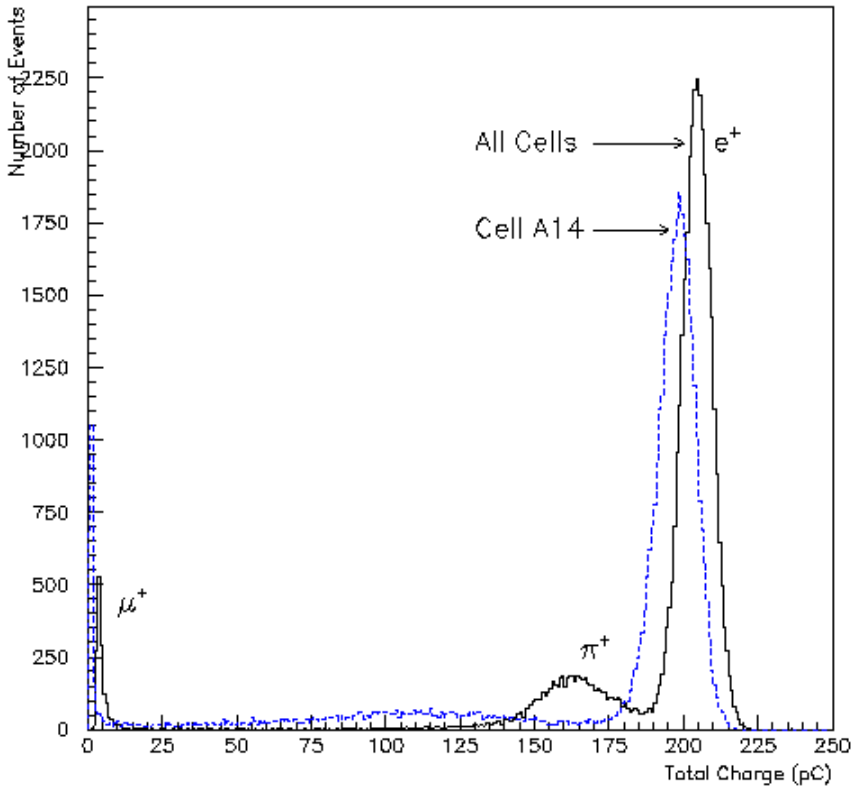

Figure 7.4: *Reconstructed beam spectrum using the energy deposited in all cells of the calorimeter (solid curve) and only in cell A14 (dashed curve). The figure shows the muon and pion contamination of the 300 GeV electron beam. The signal due to muons almost superposes with pedestal events.*

7.2.1.2 Cherenkov cut

Figure 7.5 shows the Cherenkov events corresponding to a run performed under usual operation conditions of the detector. Electrons produce a larger signal on the detector than other particles. However, the Cherenkov counters are optimized for operation at higher energies than the considered in these test (180 GeV). For this reason, bad performance of the second Cherenkov counters were observed during the offline analysis. This impeded a clear separation of the particles requiring to apply a very selective cut in order to isolate only events due to electrons in the calorimeter. The effect of this cut is shown in figure 7.6. Although pions are suppressed, the statistics of the run is significantly reduced.

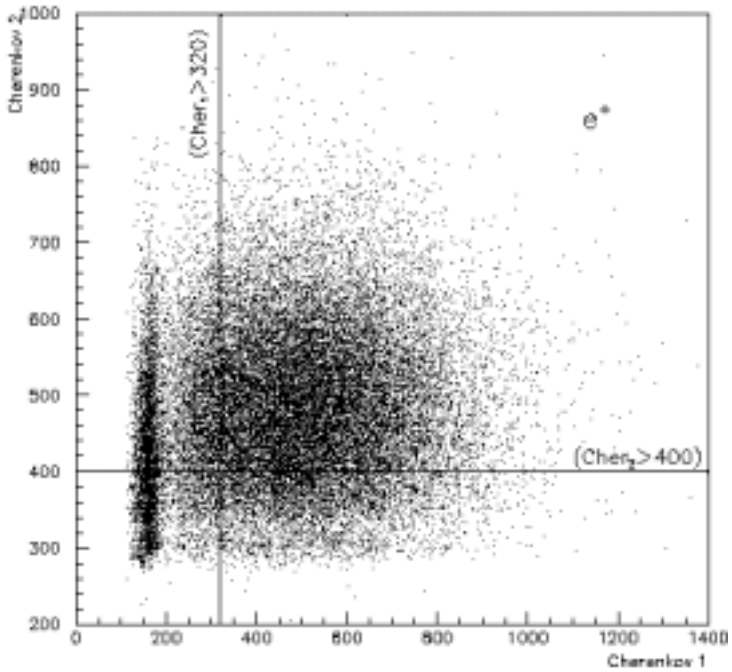

Figure 7.5: *Signal induced by the physics events in both Cherenkov detectors. The plot allows to define a cut isolate electrons in the beam, which produced a higher signal in both counters.*

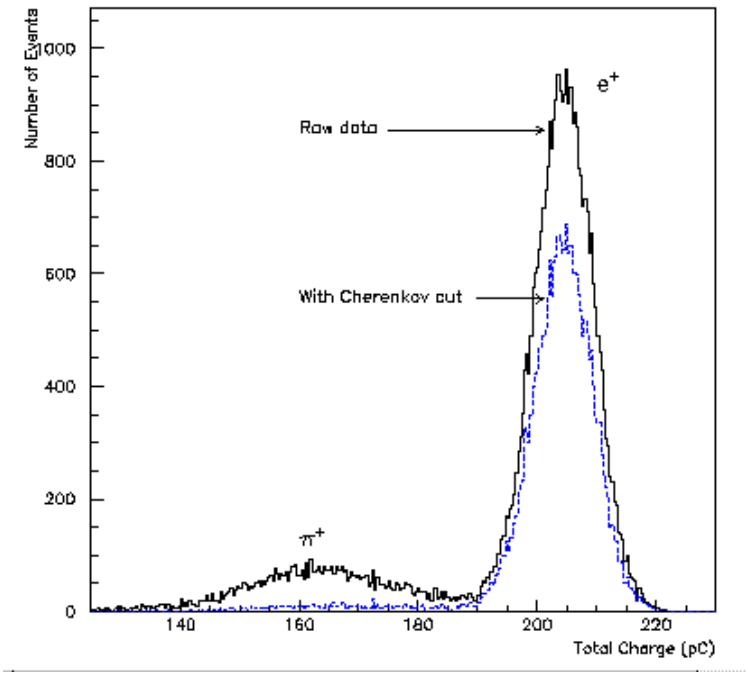

Figure 7.6: *Reconstructed charge using the Cherenkov cut. The plot shows a significant reduction of statistics due to the cut.*

7.2.1.3 Hadronic cut

A second cut based on the profile of the hadronic shower for different types of particles was applied. Figure 7.7 shows the total energy deposited in the calorimeter as a function of the fraction of energy deposited only in sample A. This cut allows a clear identification of the particles. The energy deposited in sample A spreads over the whole range. Around 95% of the shower created by electrons is contained in sample A. The total energy released by muons in the calorimeter is very small whereas the total deposited energy by pions is centred around 160 pC. This latter value is smaller than the total measured charge for electrons since the hadronic shower created by pions is not fully contained in one module of the calorimeter. The cascade originated by pions extends transversely to adjacent modules of the calorimeter. The histogram allows to define the following conditions to characterize events:

- Electrons release around 95% of their energy in sample A.
- The fraction of energy deposited in sample A for pions is below 95% but the total charge measured in the module is above 100 pC.
- The total charge induced in the module by muons is below 11 pC.

Figures 7.8 and 7.9 show the effect of these cuts for electrons and pions respectively. Unlike the Cherenkov cut, the hadronic selection allows a clear separation of the particles without decreasing the number of events of each type. For this reason, the hadronic cut has been applied to the data in the following analysis.

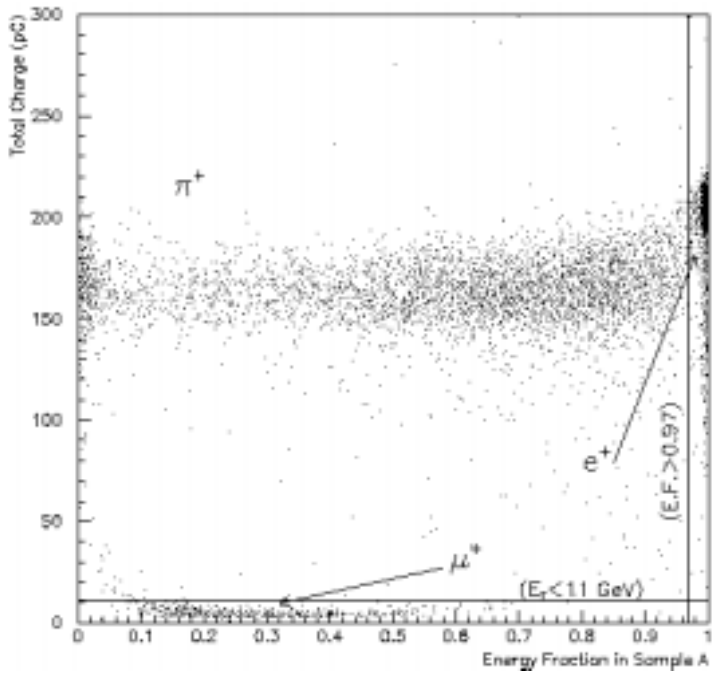

Figure 7.7: *Total reconstructed energy deposited in the calorimeter as a function of the energy fraction deposited in sample A. The histogram shows that the energy due to electron events is practically released in the first sampling layer of the calorimeter.*

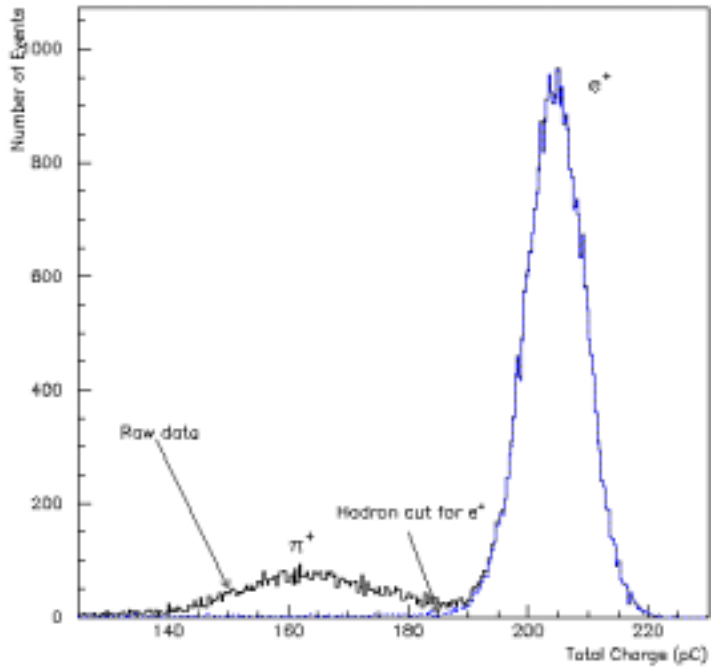

Figure 7.8: *Reconstructed charge deposited by electrons using the hadronic cut compared to the total charge released in the calorimeter by all physics events.*

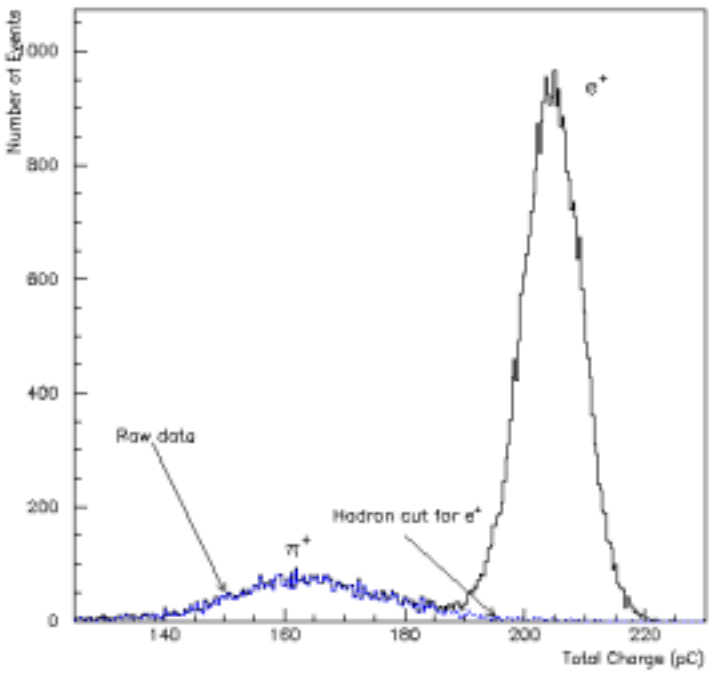

Figure 7.9: *Reconstructed charge deposited by pions using the hadronic cut compared to the total charge released in the calorimeter by all physics events.*

7.2.2 Effect of a HV reduction on the electron signal

7.2.2.1 Scope of the test

During the production of the scintillating tiles used in the calorimeter, the light yield was optimized leading to an increase of ~1.8% of the number of photons produced from the incident particles. Furthermore, in the middle of the production, the polystyrene base material had to be changed from PSM115 to BASF leading to a further increase of ~25% of the total collected charge per GeV in the calorimeter.

The total collected charge in the readout system is a function of the number of photons produced in the Tiles and also of the gain of the PMT of the readout system, *i.e.* of the HV applied to the PMT, according to the following expression:

$$Q_{PMT} = e \cdot N_{pe} \cdot G_{PMT} = e \cdot N_{pe} \alpha \cdot V^{\beta} \tag{7.3}$$

where e is the electron charge, N_{pe} is the total number of photoelectrons and G_{PMT} is the PMT gain.

In order to ensure response uniformity of all cells of the calorimeter two measures are taken during instrumentation:

- In cells where both types of materials are employed, part of the surface of the BASF tiles is masked to reduced the collection of light by the fibers in a 25%.
- PMT with lower quantum efficiency are assigned to cells with higher light yield.

The design requirements called for a conversion factor from energy of the incident particle and the induced charge of 0.8 pC/GeV. However, after the changes mentioned above, a factor of 1.2 pC/GeV for the electromagnetic energy of the shower at 90^0, and of ~1 pC/GeV for the hadronic component, have been determined in recent measurements. Figure 7.10 shows the calibration factor for an extended and a central barrel modules as a function of the tile number after equalization of the cell response using the Cs source for 180 GeV electrons. These plots show a calibration factor of 1.2 pC/GeV for the sampling layers A and B, whereas a factor ~1.13 pC/GeV is found for the sampling region D. This latter result is currently not yet understood and it is being investigated by the collaboration.

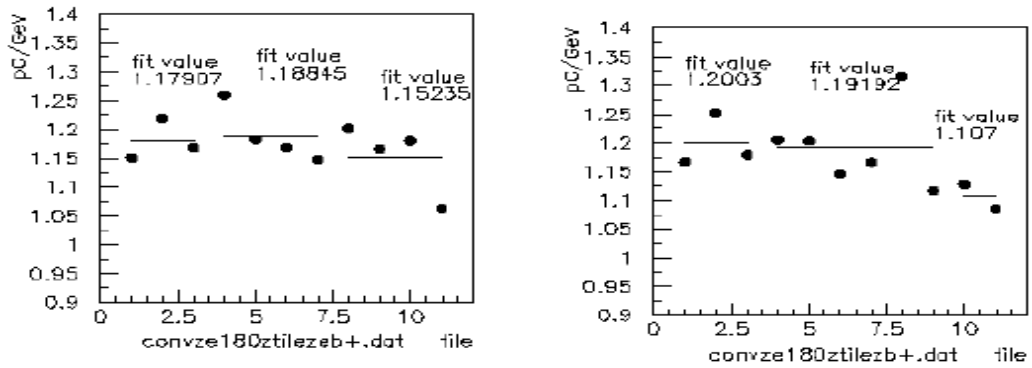

Figure 7.10: *Calibration factors for the different sampling layers as a function of the tile number for: a) an extended barrel module and b) a central barrel module.*

Figure 7.11 shows the HV set after the equalization using the Cs source as a function of the nominal HV (G=10^5) for a number of PMT. The plot indicates that the applied HV must be systematically decreased for most of the PMT with respect to the nominal HV in order to achieve a conversion factor of 1.2 pC / GeV. As a large part of the energy of the incident particles is deposited in the sampling region A, it has been agreed that PMT with nominal HV below 640 V, will be used to instrument cells in this sampling layer of the barrel modules, to avoid the operation of the PMT below 580 V. Table 7.1 shows the typical HV reduction that must be applied to cells in different sampling layers depending on the tile material, determined using the Cs source and from calibration with electron beam.

The maximum detectable energy in the calorimeter is limited by the saturation threshold of the readout electronics. The saturation of the ADC has been found for a total deposited charge of 760 pC, *i.e.* 760 GeV per PMT for hadrons or 1.52 TeV per cell. However, recent simulations show that some jet events at the LHC will release several TeV in a single cell of the calorimeter. Although this type of events must be detected and no precise measurement of the energy is required, the saturation of the electronics must be avoided.

Two different methods have been proposed to decrease the total collected charge. A first method is based in the usage of masks to attenuate the amount of light incident on the PMT. However, the effects of the radiation on the ageing of the masks is unknown and the replacement of the masks during the lifetime of the experiment might be required.

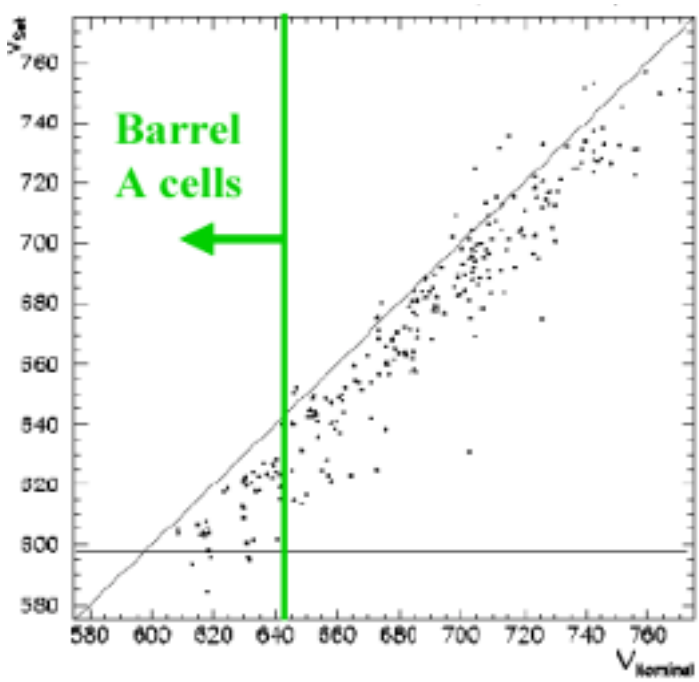

Figure 7.11: *HV set after the equalization of the cell response using the ^{137}Cs source as a function of the nominal HV of the PMT.*

Table 7.1 *Mean HV differences with respect to the nominal values for the two types of tile materials for the Cs calibration and calibration using electrons, e.g. Nominal Voltage = 700 V, set voltage 670 V, then +30 V appears in the table*

		Measurement			**Correction to electron calibration**	
		PSM / BASF MASKED	BASF	BASF - PSM	PSM / BASF MASKED	BASF
Barrel	A	11			12	
	BC	14	38[a]	24	15	37[a]
	D	12[a]	35	24a	6	30
EBA	A	7			6	
	B	15	32[a]	17[a]	13	30[a]
	C10	25	42[a]	17[a]	24	40[a]
	D4	22	39[a]	17[a]	16	33[a]
	D5-6	-4	19	23	-10	13
EBC	A	8			7	
	B	13	30	17	11	28
	C10	16	32	17	14	31
	D4	32	50	17	26	43
	D5-6	-3	22	25	-9	16

a. Predicted value

The second method consists of a reduction of the HV applied and therefore, of PMT gain according to the expression 7.3. However, a substantial reduction of the applied HV may have influence on the normal operation of the PMT. The analysis presented in the following is dedicated to investigate this second method and its repercussions on the calorimeter response, *i.e.* energy resolution and response linearity.

A systematic study of the calorimeter performance as a function of the HV applied to the PMT has been carried out. Table 7.2 shows the nominal HV values, as well as those determined by the Cs calibration, for PMT 21 and 22. The HV applied to the PMT was progressively decreased from the values set after the calibration with the Cs source by 150 V in steps of 25 V. Figure 7.13 shows the history of PMT 21 and PMT 22 during the test. The HV reduction was equally applied to all cells of the module.

Table 7.2 *Nominal HV and HV value after the calibration with the Cs source for the two PMT used for the readout of cell A14. The table also shows the values of the parameters* α *and* β *for PMT 21 and 22.*

PMT	**Nominal HV (V)**	**HV After Cs Calibration (V)**	α **(V^{-1})**	β
21	724 ± 0.2	721.9 ± 0.2	7.87×10^{-16}	7.03
22	704 ± 0.2	698.9 ± 0.2	7.37×10^{-16}	7.07

The values of the parameters α and β have been taken from the Tilecal PMT database and unfortunately their errors are unknown. However, the error in α can be estimated from the following expression:

$$G = \alpha \cdot V^{\beta} = 10^{5} \cdot \left(\frac{V}{V_{nominal}}\right) \tag{7.4}$$

where $V_{nominal}$ represents the nominal HV value of the PMT. Therefore,

$$\alpha = 10^{5} \cdot V_{nominal}^{-\beta} \tag{7.5}$$

and,

$$\frac{\sigma_{\alpha}}{\alpha} = \frac{10^{5}}{\alpha}(-\beta)V_{nominal}^{-(\beta+1)} = -\frac{\beta}{V_{nominal}} \approx 1\% \tag{7.6}$$

The determination of the error of the parameter β is not trivial. However an estimation of an upper quote can be made from the experimental data of the calibration of the PMT. Figure 7.12 shows the distribution of the parameter β for a batch of 5000 PMT. The relative error in the determination of β for the batch of PMT

is 2.5% according to the data shown. This value considers the error due to the calibration procedure but also the tolerance of the PMT. Therefore, the error of the calibration procedure used to determine β must be well below this value. This can be clearly deduced from figure 7.25 since a variation of 1% of the parameter β implies an uncertainty in the determination of the number of photoelectrons of about 25%.

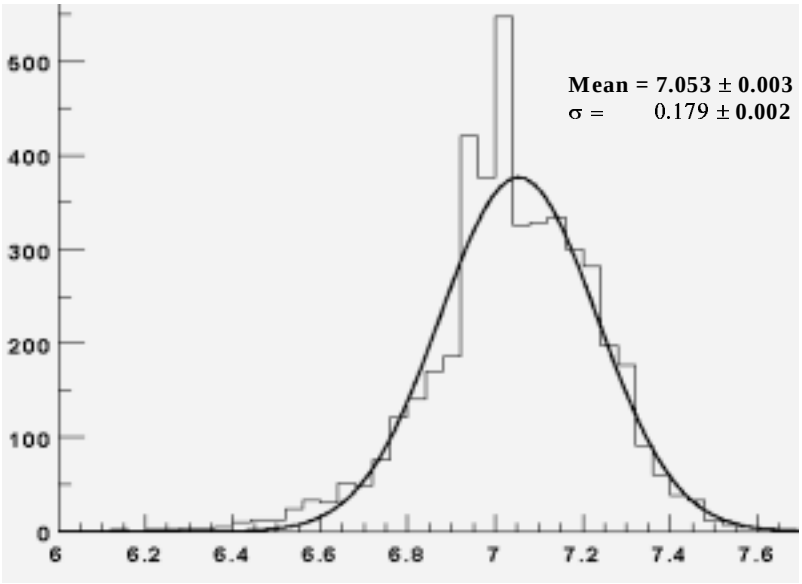

Figure 7.12: *Distribution of the parameter β for a batch of 5000 PMT.*

7.2.2.2 Energy resolution

At each set of values of the HV the total charge in the module, for both electrons and pions at 180 GeV, was reconstructed. In all cases the hadronic cut described above was applied. Figure 7.14 shows the reconstructed charge deposited in the calorimeter by electrons for different HV values. As expected, the mean value of the charge drifts to lower values as a consequence of a reduction of the HV and therefore, of the PMT gain. The mean value of the reconstructed charge and the σ of the distributions shown in this figure were determined by a 2σ gaussian fit. Figure 7.15 shows an example for a run performed at the HV settings obtained from the Cs calibration.

Figure 7.16 and 7.17 show the total reconstructed charge and the calorimeter resolution $\sigma/\langle E\rangle$ as a function of the HV reduction. The errors in the measurements are very small due to the high statistics of the measurements. The error in the resolution has been calculated applying partial derivatives. The size of the points in the plots give an over-estimation of the errors. The behavior of the total charge depends on the applied voltage as expected according to expression 7.2. The values represented in these figures are shown in table 7.3, as well as the calibration

constants obtained in each case. A HV reduction of 25 V provides a conversion factor of 0.88 pC/GeV (*i.e.* sufficient to avoid the saturation of the readout electronics) implying a resolution of a resolution of ~2.6%. The resolution of the calorimeter deteriorates from ~2.5% up to ~5.5% with a decrease of 150 V with respect to the HV obtained by the equalization of the cell response using the Cs source. There are two potential reasons which may explain the deterioration of the energy resolution:

- A HV reduction equally applied to both PMT in a cell introduces asymmetries in the readout system since the dependence of the PMT gain on the HV is a function of the parameters α and β, which are characteristics for each PMT (described in equation 7.3).
- A strong HV reduction influences the proper operation of the PMT.

In the following these two possibilities are studied.

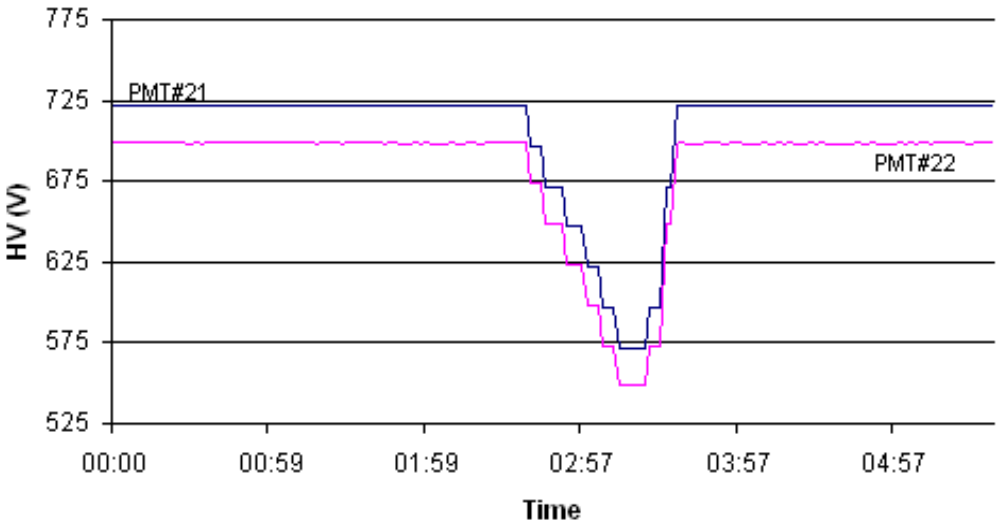

Figure 7.13: *History of the HV applied to PMT 21 and PMT 22.*

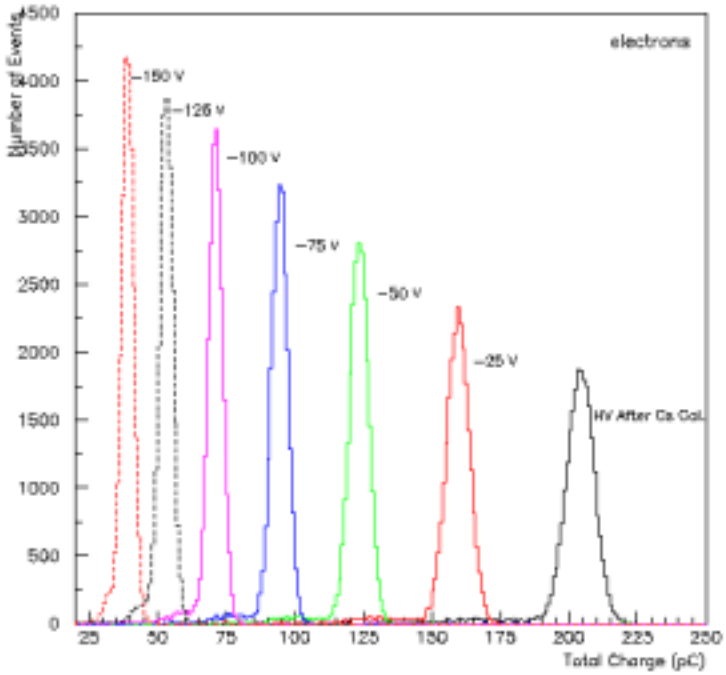

Figure 7.14: *Total reconstructed charge for electrons in sample A for different HV settings.*

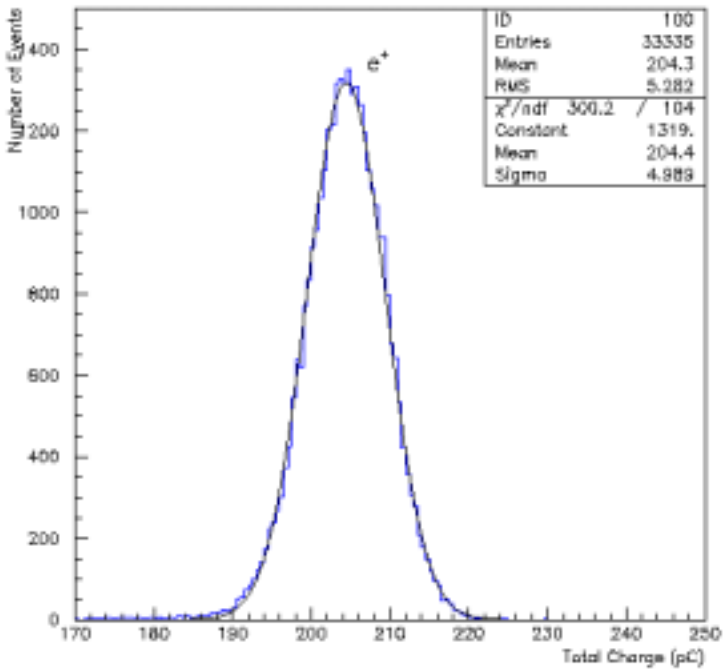

Figure 7.15: *2-σ gaussian fit for 180 GeV electron data at the normal operation conditions of the PMT.*

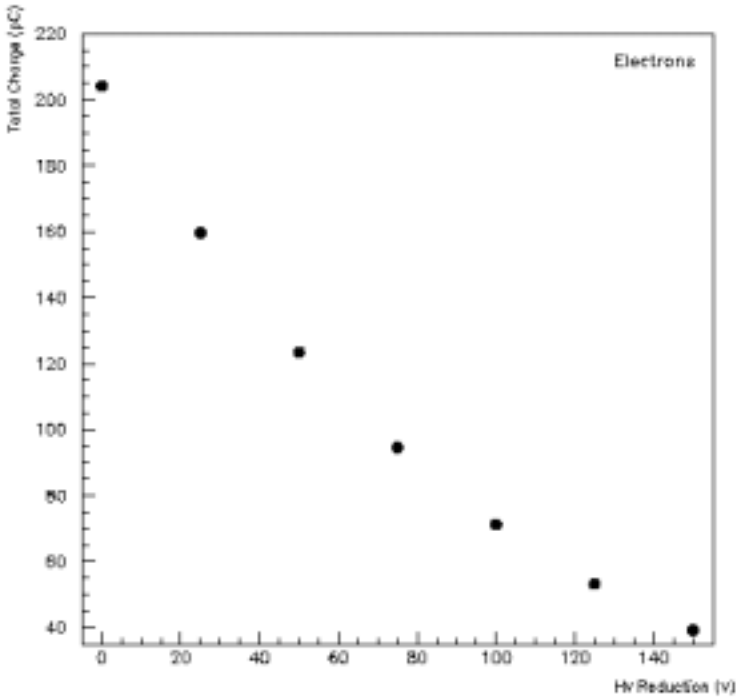

Figure 7.16: *Total reconstructed charge in sample A for electrons as a function of the HV reduction.*

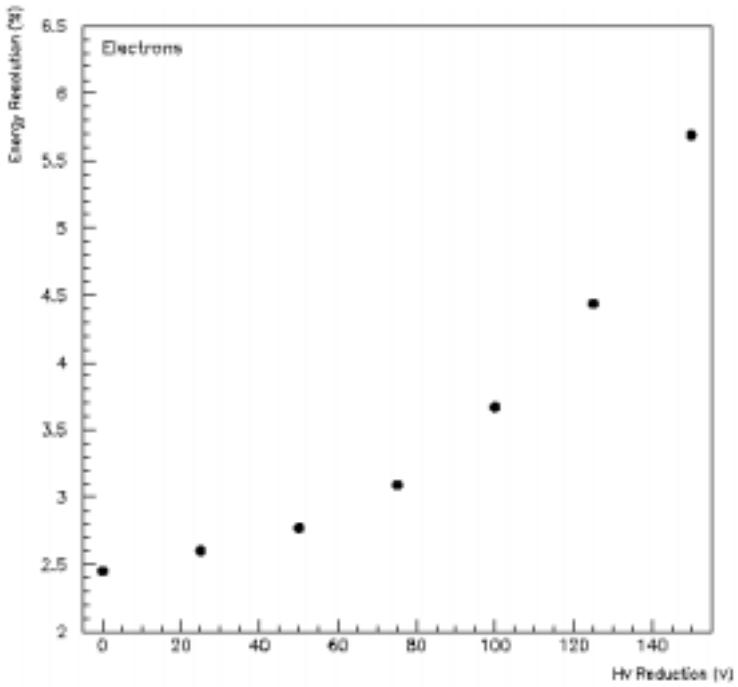

Figure 7.17: *Energy resolution for electrons as a function of the HV reduction.*

Table 7.3 *Mean reconstructed charge in sample A and calorimeter resolution for 180 GeV electrons at different HV reduction values with respect to the HV adjusted with the Cs source.*

HV Red. (V)	$\langle Q \rangle$ (pC)	$\langle \sigma / Q \rangle$	Cal. Factor (pC/GeV)
0[a]	204.20 ± 0.02	2.449 ± 0.017	1.13
25	159.62 ± 0.03	2.596 ± 0.019	0.89
50	123.56 ± 0.02	2.770 ± 0.013	0.69
75	94.59 ± 0.02	3.091 ± 0.019	0.53
100	71.26 ± 0.01	3.671 ± 0.022	0.40
125	53.17 ± 0.02	4.439 ± 0.030	0.29
150	39.18 ± 0.02	5.687 ± 0.035	0.22

a. *i.e.* HV set after the cell response equalization using the ^{137}Cs source.

Asymmetries of the readout system

Figure 7.18 shows the reconstructed charge in each individual PMT as a function of the HV reduction applied. The values shown have been normalized to charge obtained at the equalized HV given by the Cs system. The curves in this plot represent the analytical expression of the normalized charge for each PMT as a function of the applied HV (V) given by the following equation:

$$Q^{i}_{normalized} = \left(\frac{V}{V^{i}_{Cs}}\right)^{\beta} \tag{7.7}$$

where i indicates the PMT number and V^{i}_{Cs} is the HV value for a given PMT obtained from the equalization of the cell response using the Cs source. Considering that $V=V^{i}_{Cs}-R$, where R is the HV reduction applied to the PMT in volts, the normalized charge can be expressed as a function of the HV reduction as follows:

$$Q^{i}_{normalized} = \left(1-\frac{R}{V_{CS}}\right)^{\beta} \tag{7.8}$$

A very good agreement between the experimental data for electrons and the theoretical expressions is found. This result indicates the possibility to recover the resolution of the calorimeter offline by applying corrections based on the β parameter according to the expression 7.3.

The asymmetries introduced by the test method are clearly manifested when considering the ratio of the signal from the two PMT under study. This ratio can be written as a function of the HV reduction as follows:

$$\frac{\langle Q_{21}\rangle}{\langle Q_{22}\rangle} = \frac{\alpha_{21}}{\alpha_{21}}\frac{(V_{Cs}^{21} - R)^{\beta_{21}}}{(V_{Cs}^{22} - R)^{\beta_{22}}} \tag{7.9}$$

where the indices indicate the PMT number, V_{Cs}^{21} and V_{Cs}^{22} are the HV values determined by the calibration with the *Cs* source, and R is the HV reduction in volts. Using the values in table 7.2, one obtains:

$$\frac{\langle Q_{21}\rangle}{\langle Q_{22}\rangle} = 1.065\frac{(721.9 - R)^{7.03}}{(698.9 - R)^{7.07}} \tag{7.10}$$

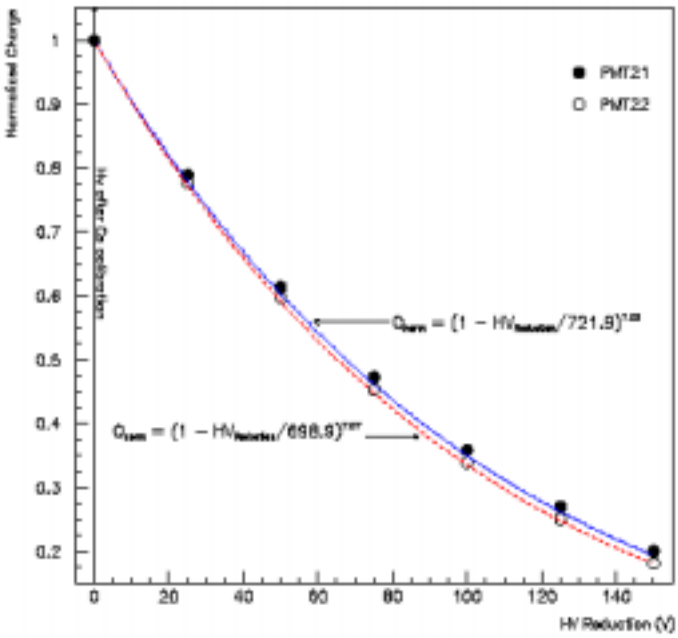

Figure 7.18: *Normalized reconstructed charge in each individual PMT as a function of the HV reduction. The curves in this plot represent the theoretical dependence of the charge on the HV reduction given by equation 7.8 for each PMT.*

Signals from the charge injection system were used to assure that the PMT are the only origin of these asymmetries. Figure 7.19 shows the CIS for a run performed at the operational HV conditions. The multiple peak structure of this histogram is due to the resolution of the ADC (10-bit) used for the digitalization of the signal needed to cover the full dynamic range of the calorimeter.

The ratio between the signal given by both PMT for electrons, as well as the signal of the charge injection system, are presented in figure 7.20 as a function of the HV reduction applied.

The expected ratio of signals between the PMT as function of the HV reduction, given by expression 7.10, is also shown in this plot. A good agreement between experimental data and the theoretical estimation is found at small HV reductions. The plot shows an asymmetry of the readout system of ~15% is found when the HV is reduced 150 V with respect to the values obtained from the calibration with the Cs source. This causes a deterioration of the energy resolution shown in figure 7.17.

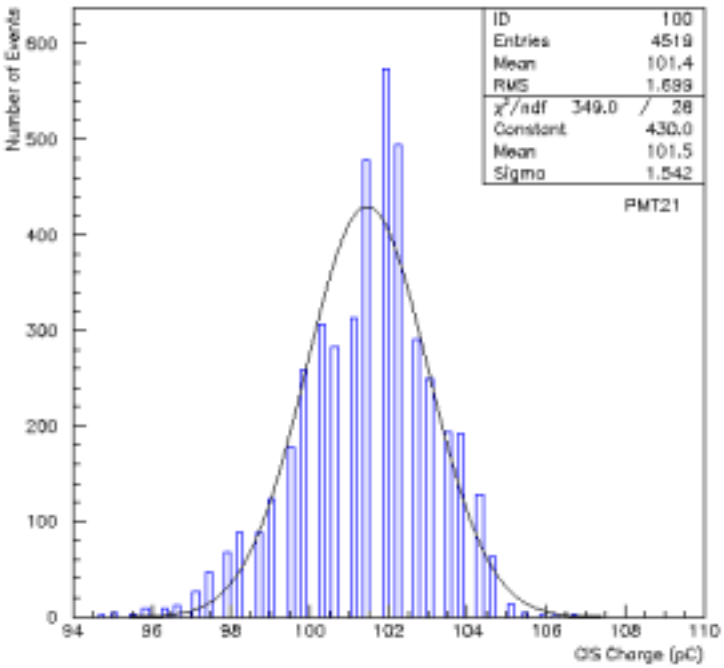

Figure 7.19: *Total reconstructed charge for charge injection events.*

A ratio between signals from both PMT close to 1 is obtained when the nominal HV values ($G_{PMT}=10^5$) are substituted in equation 7.10. This result confirms the accuracy of the calibration method followed to determine the values of α and β of the PMT [74]. An asymmetry of ~4% between both PMT is introduced when the cell response is equalized using the Cs calibration system.

As expected, the signal from the CIS is independent on the value of the HV proving that the effect observed is purely due to the reduction of the gain of the PMT.

Response Linearity

The dependence of the linearity of the calorimeter response, *i.e.* of the gain of the PMT, on the HV settings was studied using the laser calibration system. As shown

in figure 7.3, the laser system allows three different intensities. These simulate events of different energy in the calorimeter. These events are readout by the low and high gain electronics depending on their charge allowing the determination and monitoring of the linearity of the calorimeter.

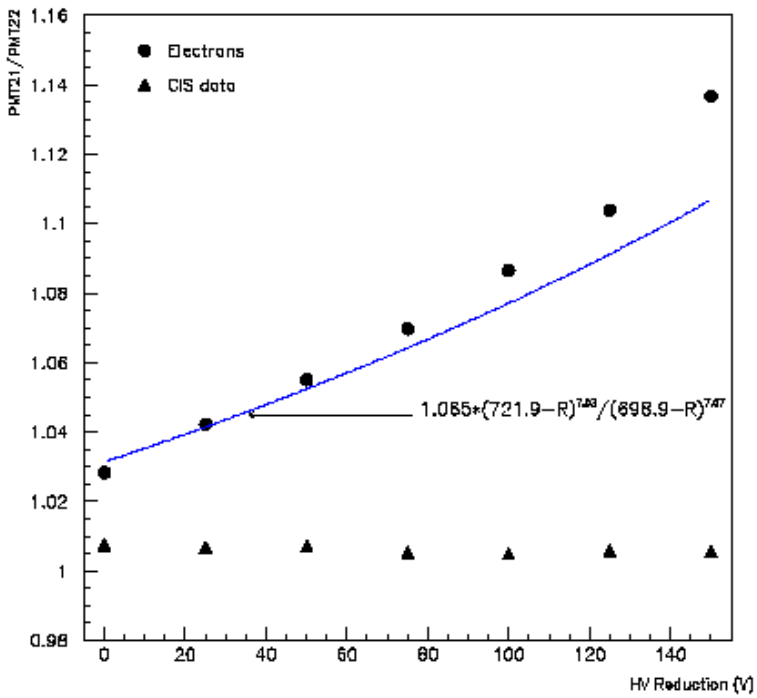

Figure 7.20: *Ratio between the signal induced in PMT#21 and PMT#22 as a function of the HV reduction for 180 GeV electrons and pions. The red curve indicates the dependence of the signal according to expression 7.10 where the HV value given by the Cs calibration is used as reference value. In the blue curve the nominal HV values are taken as reference for the HV reduction.*

In this study, the charge induced on PMT 21 by the direct and 100 times attenuated laser light was reconstructed. In all cases the charge was normalized using the laser signal read by 2 photodiodes of the laser system and the noise or pedestal events were also considered. The linearity of the PMT in the dynamic range covered must verify:

$$\frac{\dfrac{\langle Q^{Laser}_{PMT21}\rangle}{\langle Q^{Laser}_{Phdiode}\rangle - \langle Q_{Pedestal}\rangle}}{\dfrac{\langle Q^{100x}_{PMT21}\rangle}{\langle Q^{Laser}_{Phdiode}\rangle - \langle Q_{Pedestal}\rangle} \times 100} = \frac{HG}{100 \times LG} \approx 1 \qquad (7.11)$$

where,

- $\langle Q_{PMT21}^{Laser} \rangle$ and $\langle Q_{PMT21}^{100x} \rangle$ are the charges induced on PMT 21 by the direct and 100x attenuated laser intensity respectively

- $\langle Q_{Phdiode}^{Laser} \rangle$ is the charge in pC read out by the photodiode.

- $\langle Q_{Pedestal} \rangle$ is the charge due to pedestal events.

HG and *LG* stand for high gain and low gain signals respectively. Figure 7.21 shows the ratio of the signals $HG/(100 \times LG)$ defined in equation 7.11 as a function of the HV reduction. The solid line in this picture represents the fit of the data points to the following function:

$$\frac{HG}{100 \times LG} = aV \tag{7.12}$$

A value of a = 0.98 is found and all points are within the tolerance of the laser system (~2-3%). The results presented here prove the linearity of the PMT response in a certain energy range (180 GeV electrons or ~100 pC per PMT at the nominal HV) for a HV reduction of up to 150 V. However, the response linearity is not ensured at higher energy, and therefore higher charge. Recent studies carried out by the Tilecal collaboration have shown a deterioration of the response linearity of about 4% for a high voltage reduction of 40 V and a total charge of 50 mA (equivalent to ~2 TeV at the nominal HV).

7.2.3 Effect of a HV reduction on the pion signal

The data analysis has also been performed for pions. The results are shown in figures 7.22, 7.23 and 7.24 and table 7.4. Similar behavior of the <Q> deposited for pions and electrons as a function of the HV is found. However no significant variation of resolution of the calorimeter with the HV is observed in this case. Unlike the resolution to electrons, the error bars shown in figure 7.24 are visible due to the lower statistics of the data. A resolution of ~7.4% is obtained at the operational working voltage of the PMT. This value is a factor 3 worse than the resolution for electrons and it is due to the leakage of a part of the hadronic shower produced by pions in the module.

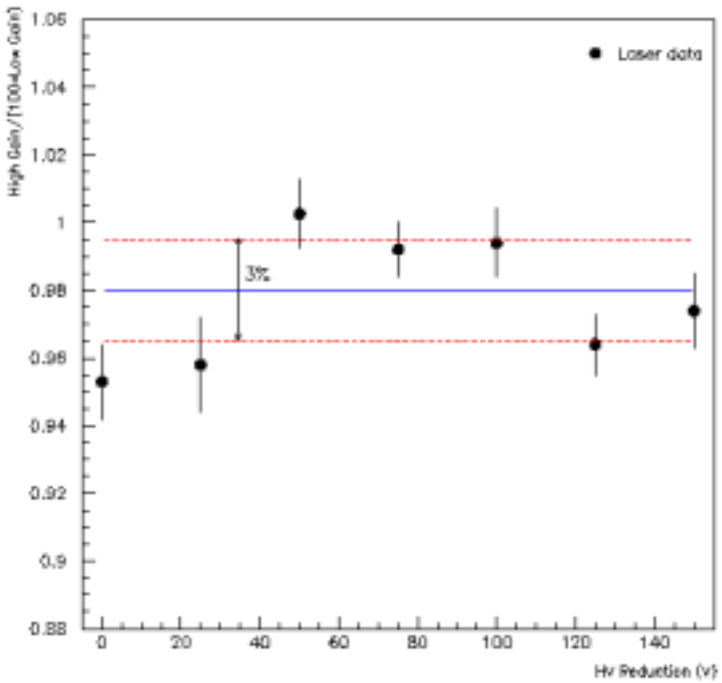

Figure 7.21: *Ratio between high and low gain signal in the calorimeter as a function of the HV reduction.*

Table 7.4 *Mean reconstructed charge for pions and calorimeter resolution for pions at different HV reduction values.*

HV Red. (V)	$\langle Q \rangle$ **(pC)**	$\langle \sigma / Q \rangle$
0	164.34 ± 0.18	7.450 ± 0.104
25	128.4 ± 0.18	7.477 ± 0.101
50	99.68 ± 0.14	7.799 ± 0.102
75	76.19 ± 0.11	7.890 ± 0.107
100	57.81 ± 0.06	7.942 ± 0.104
125	43.29 ± 0.05	7.764 ± 0.104
150	31.97 ± 0.03	7.625 ± 0.088

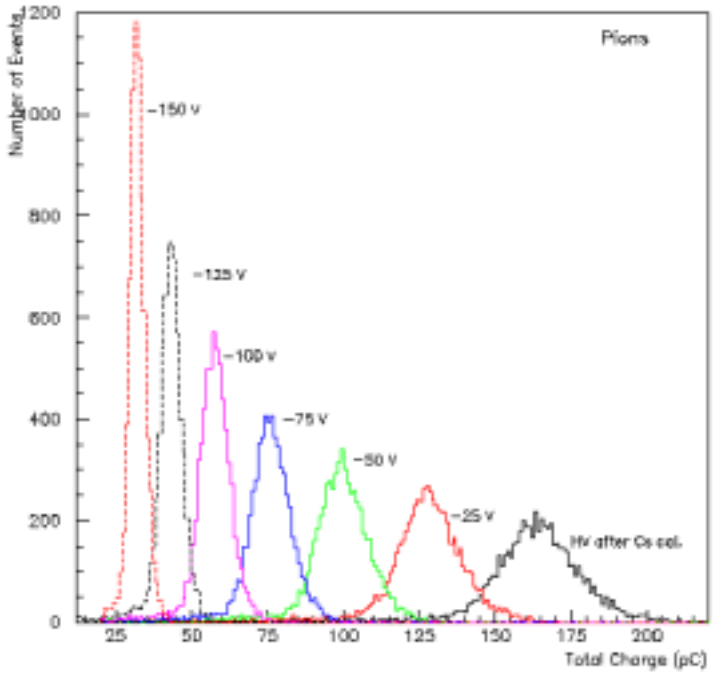

Figure 7.22: *Total reconstructed charge of pions for different HV settings.*

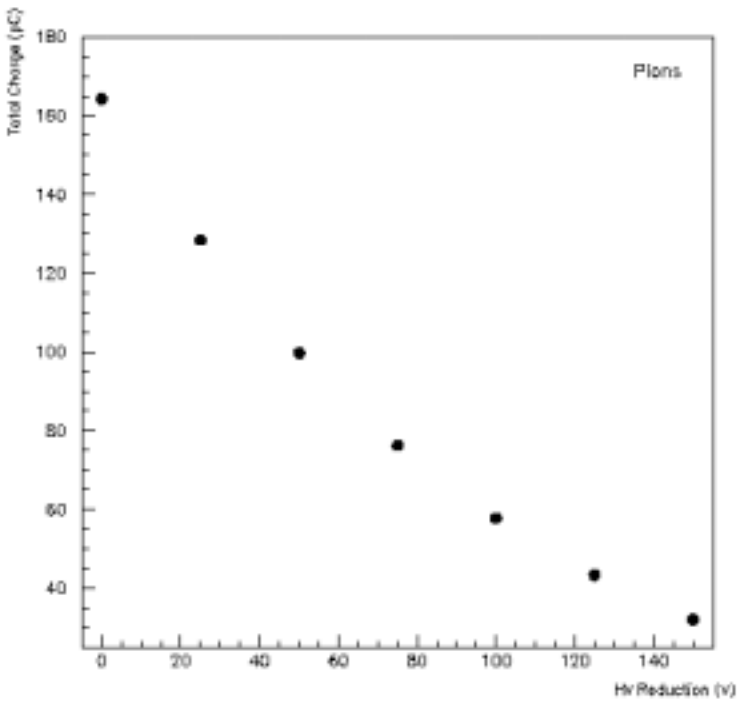

Figure 7.23: *Total reconstructed charge for 180 GeV pions as a function of the HV reduction*

.

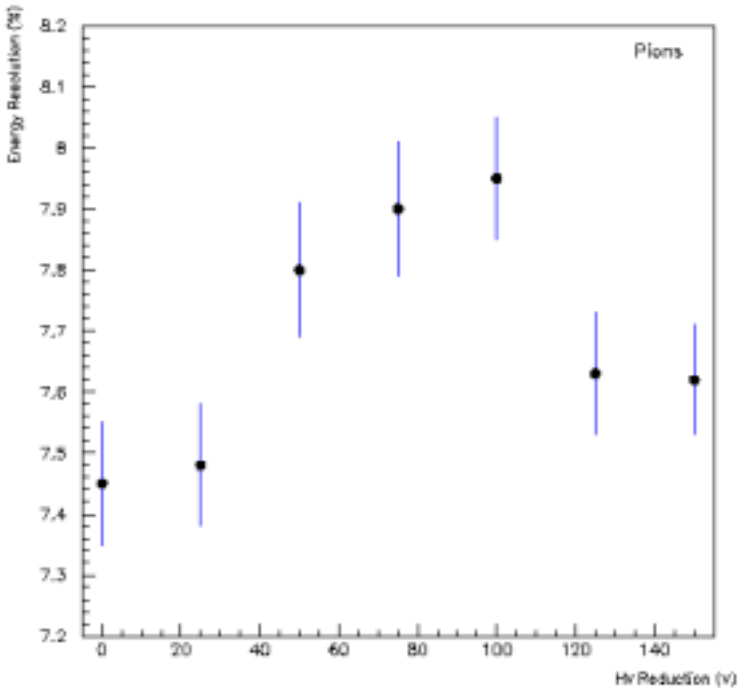

Figure 7.24: *Energy resolution for 180 GeV pions as a function of the HV reduction.*

7.2.3.1 Final decision on HV settings

The results obtained in this study and complementary measurements carried out by the collaboration, have led to the re-definition of the HV settings of the PMT. Table 7.5 shows the final decision taken by the Tilecal collaboration, in which a reduction of 20% of the PMT gain will be applied to cells in sampling A to reduce the total reconstructed charge. In this table, a ~20% increase of the gain of the PMT in D cells is also indicated. A higher signal from D cells will allow to separate the muon signal from the noise improving the trigger capabilities of the detector for this type of particles. The effect of this HV increase on the hadron trigger is negligible since the typical energy deposition in the third sample layer is ~3% of the total energy of jets. Therefore, a gain increase of 20% will lead to an increase of the total jet energy by 0.6%.

The PMT gain will also be increase for cells D4 and C10 by 20%. These types of cells are located just after the gap regions. Preliminary studies performed for 200 GeV jets, show that about 7.5 GeV are deposited in the cells C10 and D4, while about 1.8 GeV are lost in the gap region. An increase of the PMT gain for these cells allows to correct for energy losses in the gap regions.

Table 7.5 *HV Settings after the proposed changes: 20% gain reduction in sample A and 20% gain increase in sample D and cells C10 and D4.*

		PSM/BASF MASKED	BASF
Barrel	A	17	
	BC	15	37[a]
	D	6	30
EBA	A	11	
	B	13	30[a]
	C10	4	20[a]
	D4	-4	13[a]
	D5-6	-10	13
EBC	A	12	
	B	11	28
	C10	-6	11
	D4	6	23
	D5-6	-9	16

a. Predicted value

7.2.3.2 Photostatistics

The data obtained in the HV scan can also be used to determine the number of photo-electrons N_{pe} produced in the PMT depending on the energy of the particles. Previous measurements of the photostatistics can be found in [63, 74]. In these measurements the number of photoelectrons determined was in the order of 64 p.e./GeV.

Figure 7.25 shows the values of the reconstructed charge for 180 GeV incident electrons for each of the PMT here considered as a function of the gain reduction applied. The curves in the plot represent the fit of experimental data to the expression given by equation 7.3. The values of the parameters α and β for each PMT, indicated in table 7.2 have been used.

The curves represent the fit of the experimental data to a linear function. The slope of each fit gives the average value of photoelectrons produced in each PMT. This value is ~6300 for a beam energy of 180 GeV. Assuming that half of the beam energy is read out by each PMT, an average value of 70 pe/GeV is found for this cell equipped with BASF polystyrene. This result is in good agreement with the value determined by the collaboration using other methods. However, the accuracy of this method is strongly determined by the precision of the parameters α and β.

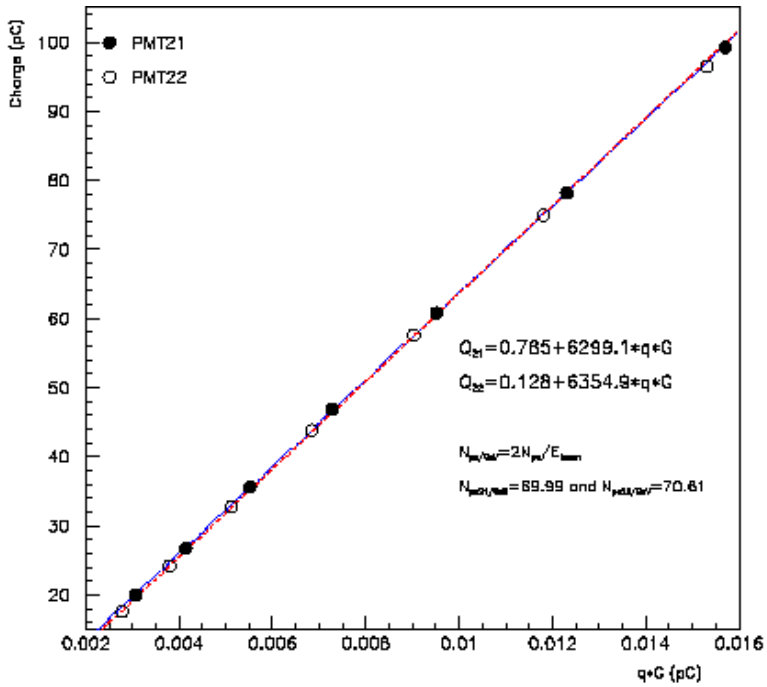

Figure 7.25: *Total charge induced by 180 GeV electrons in each of the PMT as a function of the PMT gain. q represents the electron charge in pC. The curves indicate the fit of the experimental values to expression 7.3.*

7.2.4 Effect of the temperature on the calorimeter response

7.2.4.1 Scope of the test

One of the main requirements of the Tilecal readout electronics is the stability of the output signals. In particular the gain of the photomultiplier has to remain stable within 0.5% during normal operating conditions. Previous measurements in lab [63, 74] showed that the gain of the photomultipliers vary as 0.2%/^{o}C. Since the other components of the readout chain are little affected by temperature variations (within a few degrees), the temperature nearby the photomultipliers has to remain stable within 2.5 ^{o}C.

7.2.4.2 Calorimeter response to electrons and pions

As it has been shown in the previous chapter, the electronics of the modules, *i.e.* drawers and LV system, dissipate ~300 W. The stability of the PMT gain is determined by the operational temperature and therefore, by the stability of the cooling system.

During the temperature test described in section 6.4.2.2, the variation of the gain of the photomultipliers as a function of the temperature was measured using the beam. The temperature of PMT 22 was measured by a 10 kΩ NTC sensor directly mounted onto the PMT block. In this test, the temperature of the cooling system was varied from operational temperature of the PMT 22 was varied by steps in the range 16 ^{0}C to 22 ^{0}C, at a constant flow of 60 l / h, corresponding to a variation of the operational temperature of the PMT from ~23 to ~27 ^{0}C as it has been shown in figure 6.22.

At each value of the cooling water temperature described in the previous chapter, the total energy in the module, for both electrons and pions, was reconstructed. At some point in the test, the cooling unit was switched off in order to further increase the temperature in the drawer. Figure 7.26 shows the variation of the total energy measured as function of the temperature in the PMT block 22, for both electrons and pions. The dashed lines represent a linear fit to the data points. The variation of the total energy and consequently of the gain of the photomultipliers as a function of the temperature in the PMT block is very similar for electrons and pions ($\Delta E/E$ = *0.21%/^{o}C* for electrons and $\Delta E/E$ = *0.23%/^{o}C* for pions). Since in the case of pions, many cells are hit, this shows that the PMT gain variation as a function of the temperature is the same for all the photomultipliers. We can then confirm that:

$$\frac{\Delta E}{E} = 0.2\%/^0C \tag{7.13}$$

This result confirms previous measurements for individual photomultipliers in a test bench [63, 74].

Taking into account that the variation of the temperature inside the PMT block is only half of the temperature variation of the cooling water, according to equation 6.2, the variation of the gain of the photomultipliers as a function of the cooling water temperature is then:

$$\frac{\Delta G}{G} = 0.1\%/^0C \tag{7.14}$$

The reason of the negative slope of the two plots shown above is that changes of the operational temperature cause modifications of the internal structure of the PMT. Although a temperature increase improves the electron extraction by photoelectric effect, the distance between dynodes changes leading to a deterioration of the multiplication process and consequently, to a reduction of the gain of the PMT.

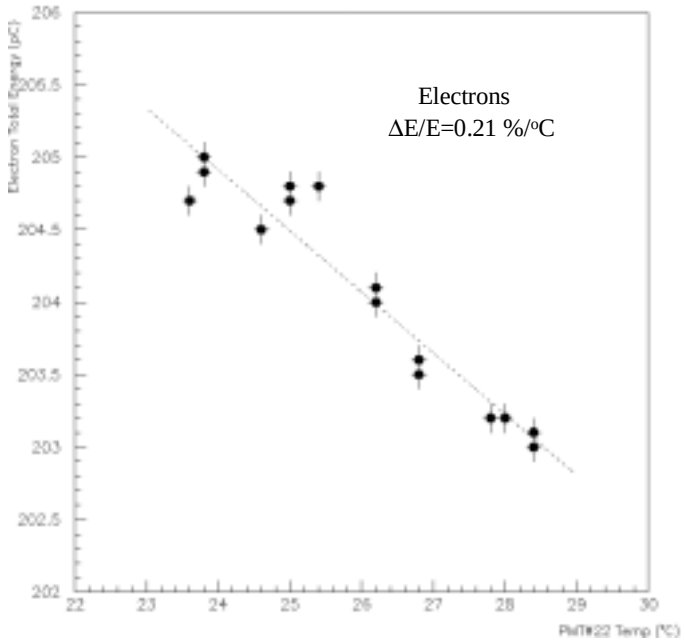

Figure 7.26: *Variation of the total energy measured in the tile calorimeter for 180 GeV electron beam as a function of the temperature in PMT block 22, for electrons.*

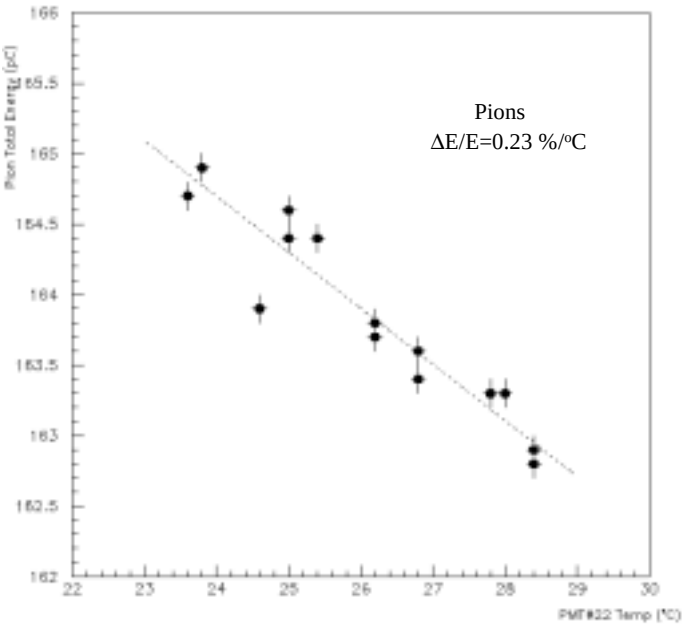

Figure 7.27: *Variation of the total energy measured in the tile calorimeter for 180 GeV pion beam as a function of the temperature in PMT block 22, for pions.*

7.3 Conclusions

In this chapter, the dependence of the calorimeter response on the operational conditions of the PMT, namely the temperature and the applied HV has been determined.

The data analysis shows a high degree of contamination of the electron beam with pions and muons. The characteristic energy deposition pattern of each particle allows a clear identification in the calorimeter. The different techniques applied for the particle separation have been discussed. The so-called hadronic cut provide a more efficient separation without reducing the statistics than the Cherenkov cut.

The results obtained in the HV scan for electrons show the possibility of decreasing the total reconstructed charge in the calorimeter as a function of the energy of the particles, by reducing the HV applied to the PMT. No significative deterioration of the energy resolution is observed for a HV reduction of 25 V.

However, the attenuation of the signal induced by particles in the calorimeter must not limit the trigger capabilities to muons of the detector. The segmentation of the calorimeter allows to improve the resolution to muons by increasing only the HV applied to the PMT of the outermost sampling layer, D.

The study of the linearity of the readout system indicate that the PMT remain in the lineal range at all HV values applied. The deterioration of the energy resolution observed at higher HV reductions seems to be due to the asymmetries between the two PMT used for the cell readout introduced by the test method. A HV reduction equally applied to both PMT induces different gains on the devices which lead to a deterioration of the energy resolution.

No significative deterioration of the energy resolution to pions has been observed.

Data taken during the HV scan for electrons has allowed to estimate the photostatistics of the PMT. A total number of 70 photoelectrons has been determined. The result is in good agreement with previous measurement carried out by the collaboration.

Data corresponding to the cooling temperature scan show a dependence of the variation of the reconstructed signal in the calorimeter on the operational temperature of the PMT, given by the following equation:

$$\Delta E = 0.2\% \, \Delta T_{Cooling} \tag{7.15}$$

This result coincides with previous measurement performed during the characterization of the PMT in a test-bench.

Chapter 8

Conclusions

This thesis work was carried out in the frame of the Detector Control System (DCS) project of the ATLAS experiment at the CERN LHC collider. The requirements and the organization of the DCS are well understood and several prototypes have been implemented with the subdetectors.The ATLAS DCS is based on the experience gained in the development, operation and maintenance of the DCS of the OPAL experiment at the LEP accelerator. The participation in the operation and maintenance of the OPAL control system has served the author of this thesis in gaining practical experience in the field of detector controls.

The DCS will be implemented using well defined building blocks to reduce the design work, to ease commissioning and to minimize the maintenance effort required. For these reasons, commercial components have been selected wherever possible. The work in this thesis has led to the selection of components and technologies and to their validation in real cases. In this thesis work the following topics have been covered:

- Definition of the requirements of the Back-End (BE) system and evaluation of industry technologies for its implementation. The commercial Supervisory Control And Data Acquisition package PVSS-II has been selected for the implementation of the BE of the four LHC experiments in the frame of the Joint Controls Project (JCOP) at CERN. Owing to its openness and flexibility, the system has proven to be adequate for the applications with the subdetectors. The device-oriented nature of PVSS-II facilitates the scalability and integration of small applications developed during the commissioning phase, to the final ATLAS.
- Testing and debugging of the Embedded Local Monitor Board (ELMB). The I/O system ELMB is a cost-effective solution and offers most of the functionality required for the implementation of the Front-End (FE) systems of the ATLAS DCS. The ELMB conforms to the industry standard CAN. CANopen has been implemented as high level communication protocol. The module is well accepted by the community and it is currently being used in many applications with the subdetectors. The utilization of the ELMB in ATLAS will provide standardization and homogeneity throughout the system and permits the utilization of common hardware and software interfaces to SCADA.

- Radiation qualification of the ELMB. The ELMB has been qualified for operation in ATLAS up to the radiation levels expected in the barrel region of the Muon Spectrometer. The different tests, performed according to the ATLAS Policy on Radiation Tolerant Electronics [48], are described. This procedure defines qualification tests for the three main types of radiation effects on electronics: Total Ionization Dose, done with γ radiation, Non Ionizing Energy Loss, carried out with neutrons and Single Event Effects, performed with protons. The results obtained meet the calculated *Radiation Tolerance Criteria (RTC)* at the location indicated. The RTC are calculated from the *Simulated Radiation Levels* given in [48] applying different safety factors which consider uncertainties in the simulation, low-dose rate effects and production tolerance of the components. These tests have helped the understanding of radiation effects on the ELMB and will serve to implement automatic error recovery procedures at both hardware and software levels.
- Evaluation of interfaces BE-FE, which has led to the selection of an OPC-based solution.
- Implementation of a full *Vertical Slice* of the ATLAS DCS comprising the ELMB and SCADA using a custom CANopen OPC server as interface.
- Study of the scalability and of the different system aspects of the ATLAS DCS *Vertical Slice*. A total number of 5000 ELMB nodes in ATLAS is estimated where the MDT subdetector will be the major user with 1200. The ELMB full branch test carried out in this thesis has aimed at defining the CANopen network topology of the MDT detector in ATLAS, which is representative for many applications. In the test, a 200 m long CANbus with up to 16 nodes has been successfully operated from SCADA. The number of I/O channels in this test is of the order of some applications in ATLAS. Studies of the powering of the system, bus load and performance have been performed for different software settings and bus speeds. The system has shown excellent performance with a readout rate of more than 1000 channels in less than four seconds. The results of this test have allowed to identify bottle-necks in the system and have led to a better distribution of the work load among the different elements in the readout chain. In addition, these tests have served to redefine the future bus and node behavior of the ELMB, e.g. implementation of asynchronous transmission in case of values out of predefined range.

  These measurements have proven the principle of the ELMB and the viability of its usage in ATLAS. Although the software of the ELMB will be enhanced to improve robustness of the modules to radiation, the hardware design is essentially ready for mass-production.
- Design and implementation of the DCS for the calibration of the modules of the Tile Hadron Calorimeter with beam particles in summer 2001. This application has served to validate the different technologies and building blocks of the DCS for a subdetector. The DCS has been successfully operated over the three calibration periods. The system has provided most of the functionality required for the final ATLAS detector and has demonstrated the suitability of the components.

- Integration of the different DCS subsystems of the Tile calorimeter, namely cooling, high- and low-voltage systems within a common SCADA framework. A VME-based control system, used for supervision and control of the regulation and distribution of the HV to the PMT used for the calorimeter readout, was interfaced to the DCS. The control system of the cooling and low voltage systems was developed using the elements of the ATLAS DCS *Vertical Slice*. The standard functionality of the ELMB has been extended in order to drive off-board DAC chips needed for the steering of the LV power supplies. The structure of the ELMB software, where the CANopen protocol is separated from the hardware specific routines, has facilitated this work. With this experience a DAC component has been designed as an add-on to the ELMB.
- Development of an interface between the DCS and the monitoring system of the Super Proton Synchrotron (SPS) accelerator to retrieve the beam information.
- Evaluation of a first implementation of the DAQ-DCS Communication (DDC) software in an application with a subdetector. This package provides bi-directional exchange of data, messages and commands between both systems. All DCS parameters relevant for the offline analysis were successfully transferred to the DAQ system online. However, several issues have been identified and reported to the developers, which have allowed the enhancement of the product.
- Determination of the performance of the cooling system using the DCS. The stability of the output signals is determined by the operational conditions of the detector, and in particular, of the temperature of the cooling system. The results show a stability of the cooling system within 0.1 ^{o}C.
- Study of the effects of operational parameters, namely the high voltage and the temperature of the cooling system, on the calorimeter response. Systematic temperature and HV scans were performed during data taking with beam of 180 GeV electrons.
  - cooling tests: Because of the size of the detector, there will be a temperature difference of about 3-4 ^{o}C between bottom and top modules of the calorimeter. Previous measurements, carried out by the Tilecal collaboration, have shown that the gain of the photomultipliers (PMT) used for the cell readout, varies by 0.2% / ^{o}C. For these reasons, the effects of variations of the temperature of the cooling liquid on the operational temperature of the PMT has been determined, confirming the result previously indicated.
  - HV studies: During the production of the modules, the light yield of the scintillating tiles was optimized leading to an increase of ~20% of the total collected charge in the calorimeter. On the other hand, recent simulations show that in the LHC there will be jet events which will release a few TeV in single cells of the calorimeter. These types of events at the current light yield will saturate the readout electronics of the detector. In this thesis, the possibility to reduce the cell signal by decreasing the HV applied and the consequences on the calorimeter response, have been investigated in systematic HV scans.

The data analysis shows a high contamination of the electron beam with pions. Different techniques applied for particle separation for the physics analysis are compared. The results indicate that the gain of the PMT can be significantly reduced by decreasing the HV applied to the PMT by about 25 V, with no significant deterioration of the resolution of the calorimeter. However, a high voltage reduction of 150 V with respect to the usual operational conditions leads to a deterioration of the energy resolution for electrons ranging from ~2.5% to ~7.5%. A good agreement between the electron data for each individual PMT and the expected response is found. In addition, the linearity of the response of the calorimeter as a function of the HV applied was also studied using the laser system. The data indicates that the PMT remain in the linear region up to a HV reduction of 150 V. No significant deterioration of the energy resolution for pions has been observed.

These results indicate that the deterioration of the energy resolution is dominated by a mis-calibration of the two PMT after a 150 V reduction. This HV reduction causes the gain to change differently for each PMT. The resolution can therefore be recovered in the full HV range studied by applying offline corrections to each individual PMT.

As a consequence of this analysis and complementary measurements carried out by the collaboration, it was decided to adjust the HV settings of the calorimeter in order to keep the calibration of 1.1 pC/GeV except for the HV applied to the PMT in the last longitudinal sampling layer. In this particular region, the HV applied to the PMT will be incremented to increase the muon signal and consequently improve the muon trigger capabilities of the calorimeter.

- Study of the photostatistics of the PMT. 70 photoelectrons/GeV has been determined. This result is in good agreement with previous measurements carried out by the collaboration.

This thesis has shown the importance of the DCS for ATLAS because of the complexity of the experiment and the large diversity of components utilized. The work presented here has contributed to the design of the ATLAS DCS and it has permitted the final calibration of the modules of the Tile Hadron Calorimeter.

Appendix A

PVSS-II DLL for HV Interface

Filename: rw_pmt.cpp

```
/*-----------------------------------------------------------------------
 Authors: Fernando VARELA - CERN and USC
          Maurice VASSENT - LPC Clermont
 Last update: 2001/06/21
 Description: DLL used for storage and
          retrival of  all the params of drawers
-----------------------------------------------------------------------*/
#include <vcl.h>
#pragma hdrstop

#include <windows.h>
#include <memory.h>
#include <stdio.h>
#include "MVtype.h"

#define SHMEMSIZE 4096*8
#define SY_OK 0
#define SY_ERROR 1
#define MAXPMT 68
#define MAXPMTSTORAGE 128

// DDL function declarations
extern "C" __declspec(dllexport) int put_pmt(INT16
*DrNbr,UNSINT32 *ts,INT16 *pmt);
extern "C" __declspec(dllexport) int get_pmt(INT16
*DrNbr,UNSINT32 *ts,INT16 *pmt);

// pointer to shared memory
static LPVOID lpvMem = NULL;
// the bloc contains:
//      long int tstamp    time stamp
//      int tmp      in degres C x 10 (ex: 10.5 >> 105 is stored)

int WINAPI DllEntryPoint(HINSTANCE hinstDLL,
                                 //DLL module handle
unsigned long fdwReason,          // reason called
   void*)                         // reserved
{
   // handle to file mapping
   HANDLE hMapObject = NULL;
   BOOL fInit, fIgnore;
    switch (fdwReason)
   {
      // The DLL is loading due to process
      // initialization or a call to LoadLibrary.
       case DLL_PROCESS_ATTACH:
         // Create a named file mapping object.
         hMapObject = CreateFileMapping(
           (HANDLE) 0xFFFFFFFF, // use paging file
            NULL,                       // no security attributes
            PAGE_READWRITE,             // read/write access
             0,                         // size: high 32-bits
             SHMEMSIZE,                 // size: low 32-bits
            "hvpmtdllmem");             // name of map object
         if (hMapObject == NULL)
            return FALSE;
          // The first process to attach initializes memory
         fInit = (GetLastError() !=
                                 ERROR_ALREADY_EXISTS);
         // Get a pointer to the file-mapped shared memory.
         lpvMem = MapViewOfFile(
           hMapObject,               // object to map view of
           FILE_MAP_WRITE,           // read/write access
           0,                        // high offset:  map from
           0,                        // low offset:  beginning
           0);                       // default: map entire file
         if (lpvMem == NULL)
            return FALSE;
          // Initialize memory if this is the first process.
         if (fInit)
            memset(lpvMem, '\0', SHMEMSIZE);
         break;
       // The attached process creates a new thread.
       case DLL_THREAD_ATTACH:
         break;
       // The thread of the attached process terminates.
       case DLL_THREAD_DETACH:
         break;
       // The DLL is unloading from a process due to
       // process termination or a call to FreeLibrary.
       case DLL_PROCESS_DETACH:
          // Unmap shared memory from the process's
                                       // address space.
         fIgnore = UnmapViewOfFile(lpvMem);
          // Close the process's handle to the file-mapping
                                              // object
         fIgnore = CloseHandle(hMapObject);
         break;
       default:
        break;
    }
   return TRUE;
}

/* ----------------------------------------------------------------------
                    users functions
----------------------------------------------------------------------*/
// This fucntion store array values in the WNT shared
                                       //  memory
int put_pmt(INT16 *DrNbr,UNSINT32 *ts,INT16 *pmt)
```

```
{
INT16 drawer;
INT16 *mem_bloc,*cour;
INT32 *mem_st;
mem_bloc = (INT16*) lpvMem;
int i;

cour = pmt;                                  // get data adress
mem_st = (INT32*)pmt;
drawer = *DrNbr;                             // get Drawer number
if (drawer > 255)            // don't go out of shared memory
{
   return SY_ERROR;
}
if (drawer != 0)        // point to the memory storage adress
                                             // for this drawer
{
   mem_bloc += (drawer * MAXPMTSTORAGE);
}
mem_st = (INT32*)mem_bloc;                   // store for  use
mem_bloc += 2;                // skip the time stamp storage
// store arguments
for (i=0;i<MAXPMT; i++)
{
*(mem_bloc++) = *cour++;
}
*mem_st = *ts;                               // store time stamp
return SY_OK;
}

/*
------------------------------------------------------------------------------
 This fucntion retrives array values in the WNT shared
memory
------------------------------------------------------------------------------*/
int get_pmt(INT16 *DrNbr,UNSINT32 *ts,INT16 *pmt)
{
INT16 drawer;
INT16 *mem_bloc, *cour;          // point to the begening of
                                             //shared memory
INT32 *mem_st;
mem_bloc = (INT16*) lpvMem;
int i;

cour = pmt;                                  // get data adress
drawer = *DrNbr;                             // store Drawer number
if (drawer > 255)            // don't go out of shared memory
{
   return SY_ERROR;
}
if (drawer != 0)         // point to the memory adress of this
                                                    // drawer
{
   mem_bloc += (drawer * MAXPMTSTORAGE);
}
                                             // get arguments
mem_st = (INT32*) mem_bloc;
*ts = *mem_st;                               // get time stamp
mem_bloc +=2;                                // point to data storage
for (i=0;i<MAXPMT; i++)
{
*cour++ = *(mem_bloc++);
}
return SY_OK;
}
```

Filename: types.hxx

```
/* ----------------------------------------------------------
     PVSS-II DLL for HV Interface
      2001/05/05
/* ----------------------------------------------------------

typedef signed char            INT8;
typedef signed short int       INT16;
typedef signed long int        MVINT32;
typedef unsigned char          UNSINT8;
typedef unsigned short int     UNSINT16;
typedef unsigned long int      UNSINT32;

/* some Labview arrays and constants*/
typedef struct {
      INT32 length;
      char buf[];
      } **stringHdl;
typedef struct {
      INT32 TblSize;
      INT16 Tblvalue[];
      } IntTbl;
typedef IntTbl ** IntTblHdl;

#ifndef LVTRUE
#define LVTRUE (INT16)0x8000
#endif
#ifndef LVFALSE
#define LVFALSE (INT16)0x0000
#endif
```

Filename: fullHVInterface.hxx

```
#ifndef _TCPEXTERNHDL_H_
#define _TCPEXTERNHDL_H_
#include <BaseExternHdl.hxx>
# ifdef _WIN32
#  define PVSS_EXPORT __declspec(dllexport)
# else
#  define PVSS_EXPORT
# endif

//Include Clermont's data types
#include "types.h"

//Load Clermont's library
extern "C" typedef int (TEMP_GET_PROC)
(INT16 *, INT16 *, INT16 *, INT16 *, INT16 *, INT16 *,
INT16 *,INT16 *);

TEMP_GET_PROC *pGetTemp;
HINSTANCE hInstance;

extern "C" typedef int (PMT_GET_PROC) (INT16 *,
UNSINT32 *, INT16 *);
PMT_GET_PROC *pGetPmt;
HINSTANCE hInstancePmt;

class TCPExternHdl : public BaseExternHdl
{
 public:
  // List of user defined functions
  // Internal use only
  enum
```

```
  {
  F_getTemp=0,
  F_getPmt,
  };
  // Descritption of user defined functions.
  // Used by libCtrl to identify function calls
  static FunctionListRec  fnList[];
  TCPExternHdl(BaseExternHdl *nextHdl, PVSSulong
                funcCount, FunctionListRec fnList[])
               : BaseExternHdl(nextHdl, funcCount, fnList) {}
  // Execute user defined function
  virtual const Variable *execute(ExecuteParamRec
                                  &param);
 private:
  // User define fucntions in DLL
  int getTemp(int drawer, int *temps);
  int getPmt(int drawer, int *PMT);
};
// Create new ExternHdl. This must be global function
named newExternHdl
PVSS_EXPORT
BaseExternHdl *newExternHdl(BaseExternHdl *nextHdl);
#endif
```

Filename: fullHVInterface.cxx

```
// Ctrl extension for HV communication
# ifdef _WIN32
#   include <winsock.h>
# else
#   include  <netdb.h>
#   include  <sys/socket.h>
#   include  <netinet/in.h>
#   include  <errno.h>
#   include  <sys/time.h>
#   include  <sys/types.h>
#   include  <unistd.h>
# endif
#include "fullTileCalHVInterface.hxx"
#include <stdio.h>
#include <string.h>
#include <CharString.hxx>
#include <BlobVar.hxx>
#include <CtrlExpr.hxx>
#include <ExprList.hxx>
#include <CtrlThread.hxx>
#include <IdExpr.hxx>
#include <Variable.hxx>
#include <AnyTypeVar.hxx>
#include <BitVar.hxx>
#include <CharVar.hxx>
#include <IntegerVar.hxx>
#include <UIntegerVar.hxx>
#include <FloatVar.hxx>
#include <TextVar.hxx>
#include <TimeVar.hxx>
#include <DynVar.hxx>
#include <ErrorVar.hxx>
#include <ExternData.hxx>
#include <ErrClass.hxx>
#include <BCTime.h>

// Function description
FunctionListRec TCPExternHdl::fnList[] =
{
// Return-Value   function name      parameter list
true == thread-save
//-------------------------------------------------------------
{ INTEGER_VAR,
"getTemp",
"(int drawer,     dyn_int &temps)"
, true},
{ INTEGER_VAR,
 "getPmt",
"(int drawer,     dyn_int &PMT)"
, true}, };

// Remarks:
// getTemp: Gets a pointer to the drawer number and
returns a points to int array of temps

BaseExternHdl *newExternHdl(BaseExternHdl *nextHdl)
{
 // Calculate number of functions defined
 PVSSulong funcCount = sizeof(TCPExternHdl
                    ::fnList)/sizeof(TCPExternHdl::fnList[0]);

 // now allocate the new instance
 TCPExternHdl *hdl = new TCPExternHdl(nextHdl,
                    funcCount, TCPExternHdl::fnList);
 return hdl;
}
//-------------------------------------------------------------
// This function is called every time we use getTemp in a
// Ctrl script.
// The argument is an aggregaton of function name,
// function number,
// the arguments passed to the Ctrl function, the "thread"
// context  and user defined data.

const Variable *TCPExternHdl
                ::execute(ExecuteParamRec &param)
{
// We return a pointer to a static variable.
static IntegerVar integerVar;

// A pointer to one "argument". Any input argument may
// be an exprssion  like "a ? x : y" instead of a simple value.
 CtrlExpr   *expr;

// A generic pointer to the input / output value
const Variable   *varPtr;

// switch / case on function numbers
 switch (param.funcNum)
 {
//If it is our function
   case F_getTemp:
   {
     // Check for parameter socket (int)
    if (!param.args || !(expr = param.args->getFirst()) ||
        !(varPtr = expr->evaluate(param.thread)) ||
        (varPtr->isA() != INTEGER_VAR))
    {
      ErrClass  errClass(
      ErrClass::PRIO_WARNING, ErrClass::ERR_PARAM,
       ErrClass::ARG_MISSING,
       "TCPExternHdl", "getTemp", "missing or wrong
       drawer number");
      // Remember error message.
      // In the Ctrl script use getLastError to retreive the
```

```
    // error message
    param.thread->appendLastError(&errClass);
    // Return (-1) to indicate an error
    integerVar.setValue (-1);
    return &integerVar;    // error ->return
   }
   IntegerVar  drawer;
   drawer = *varPtr;
   // Input buffer for temperatures
  int tempsArr[7];
  int error = getTemp(drawer.getValue(), tempsArr);
   // Check for parameter data (string or blob)
   // This parameter is an output value (it receives our
   // data),  so get a pointer via the getTarget call.
   if (!param.args || !(expr = param.args->getNext()) ||
      !(varPtr = expr->getTarget(param.thread)) ||
      (varPtr->isA() != DYNINTEGER_VAR))
   {
    ErrClass  errClass(
     ErrClass::PRIO_WARNING, ErrClass::ERR_PARAM,
      ErrClass::ARG_MISSING,
      "TCPExternHdl", "getTemp", "Wrong value for
      temperatures");
    // Remember error message.
    // In the Ctrl script use getLastError to retreive the
    // error message
    param.thread->appendLastError(&errClass);
    // Return (-1) to indicate error
    integerVar.setValue (-1);
    return &integerVar;    // error ->return
   }
 // Convert (and copy) data into DynVar to return
 // dyn_int
 //To be able to call the function in a loop
 ((DynVar *) varPtr)->clear();
 for(int i=0;i<=6;i++)
 ((DynVar *) varPtr)->append(new IntegerVar(
                                                tempsArr[i]));
 //Free memory used by dll.
  FreeLibrary(hInstance);

 // Return 0 if everything is ok
   integerVar.setValue(error);
   return &integerVar;    // error ->return
  } //End of case for function getTemp()

  case F_getPmt:
  {
   // Check for parameter socket (int)
   if (!param.args || !(expr = param.args->getFirst()) ||
      !(varPtr = expr->evaluate(param.thread)) ||
      (varPtr->isA() != INTEGER_VAR))
   {
    ErrClass  errClass(
     ErrClass::PRIO_WARNING, ErrClass::ERR_PARAM,
      ErrClass::ARG_MISSING,
      "TCPExternHdl", "getPmt", "missing or wrong
      drawer number");

    // Remember error message.
    // In the Ctrl script use getLastError to retreive the
    // error message
    param.thread->appendLastError(&errClass);

    // Return (-1) to indicate an error
    integerVar.setValue (-1);
    return &integerVar;    // error ->return
   }

   IntegerVar  drawer;
   drawer = *varPtr;

   // Input buffer for temperatures
   int hvArr[68];
   // Receive data from server.
   // Return value (-1) in case of error
   int errorPmt = getPmt(drawer.getValue(), hvArr);

   // Check for parameter data (string or blob)
   // This parameter is an output value (it receives our
   // data) so get a pointer via the getTarget call.
   if (!param.args || !(expr = param.args->getNext()) ||
      !(varPtr = expr->getTarget(param.thread)) ||
      (varPtr->isA() != DYNINTEGER_VAR))
   {
    ErrClass  errClass(
     ErrClass::PRIO_WARNING, ErrClass::ERR_PARAM,
      ErrClass::ARG_MISSING,
      "TCPExternHdl", "getPmt", "Wrong value for PMT");

    // Remember error message.
    // In the Ctrl script use getLastError to retreive the
    // error message
    param.thread->appendLastError(&errClass);

    // Return (-1) to indicate error
    integerVar.setValue (-1);
    return &integerVar;    // error ->return
   }

  // Convert (and copy) data into DynVar to return
  // dyn_int
  //To be able to call the function in a loop
  ((DynVar *) varPtr)->clear();
  for(int i=0;i<=67;i++)
   ((DynVar *) varPtr)->append(new IntegerVar(hvArr[i]));

  // Return 0 if everything is ok
    integerVar.setValue(errorPmt);
    return &integerVar;    // error ->return
  }//End of case for function getTemp()

  // May never happen, but make compilers happy
  default:
   integerVar.setValue(-1);
   return &integerVar;
 }
 return &integerVar;
}

//-------------------------------------------------------------
//                  Utilitiy functions
//-------------------------------------------------------------
int TCPExternHdl::getTemp(int drawer, int *temps)
{
int error=0;

short drawerS=(short) drawer;
short t1, t2, t3, t4, t5, t6, t7;

hInstance = ::LoadLibrary(
"C:\\ETM\\PVSS2\\2.11.1\\api\\TileCalHVInter-
```

```
face\\rw_temp.dll");

DWORD err = GetLastError();
if(err!=0 && err!=1447)
  cout << "Error from LoadLibrary: " << err << endl;

pGetTemp =  (TEMP_GET_PROC*) ::GetProcAddress(
                                        hInstance, "_temp_get");

err = GetLastError();
if(err!=0 && err!=1447)cout << "Error from GetProcAd-
dress: " << err << endl;

error=(*pGetTemp)(&drawerS, &t1, &t2, &t3, &t4, &t5,
&t6, &t7);

temps[0]=(int) t1;
temps[1]=(int) t2;
temps[2]=(int) t3;
temps[3]=(int) t4;
temps[4]=(int) t5;
temps[5]=(int) t6;
temps[6]=(int) t7;
FreeLibrary(hInstance);
err = GetLastError();
if(err!=0)
  cout << "Error freeing the library 'rw_temp': " << err <<
endl;
return error;
}

//---------------------------------------------------------
int TCPExternHdl::getPmt(int drawer, int *PMT)
{
int error=0;
short drawerS=(short) drawer;
short PMTS[68];

unsigned long int ts;
static unsigned long int tsOld;
hInstancePmt = ::LoadLibrary(
"C:\\ETM\\PVSS2\\2.11.1\\api\\fullTileCalHVInter-
faceNew\\rw_pmt.dll");

DWORD err = GetLastError();

if(err!=0 && err!=1447 && err!=183)
  cout << "Error from LoadLibrary: " << err << endl;
pGetPmt =  (PMT_GET_PROC*)::GetProcAddress(hIn-
stancePmt, "_get_pmt");
err = GetLastError();
if(err!=0 && err!=1447)cout << "Error from GetProcAd-
dress: " << err << endl;
error=(*pGetPmt)(&drawerS, &ts, PMTS);
if(ts != tsOld)
{ tsOld=ts;
  for(int iLoop =0;iLoop <= 67; iLoop++)
    PMT[iLoop] = (int) PMTS[iLoop];}
else
{  for(int iLoop =0;iLoop <= 67; iLoop++)
    PMT[iLoop] = -999999;}
return error;
}

//---------------------------------------------------------
// DLLInit Function for Win NT
// Initialize  winsock
# ifdef _WIN32
BOOL  WINAPI  DllInit(HINSTANCE,
                      DWORD dwReason,
                      LPVOID)
{
 if (dwReason == DLL_PROCESS_ATTACH)
 {
   // Initialize winsock, return FALSE on error
  WSADATA WsaData;
  int err;
  err = WSAStartup(0x0101, &WsaData);
  if (err == SOCKET_ERROR)
    return FALSE;
 }
 else if (dwReason == DLL_PROCESS_DETACH)
   WSACleanup();
 return TRUE;
}
# endif
```

Appendix B

Low voltage motherboard

.

.

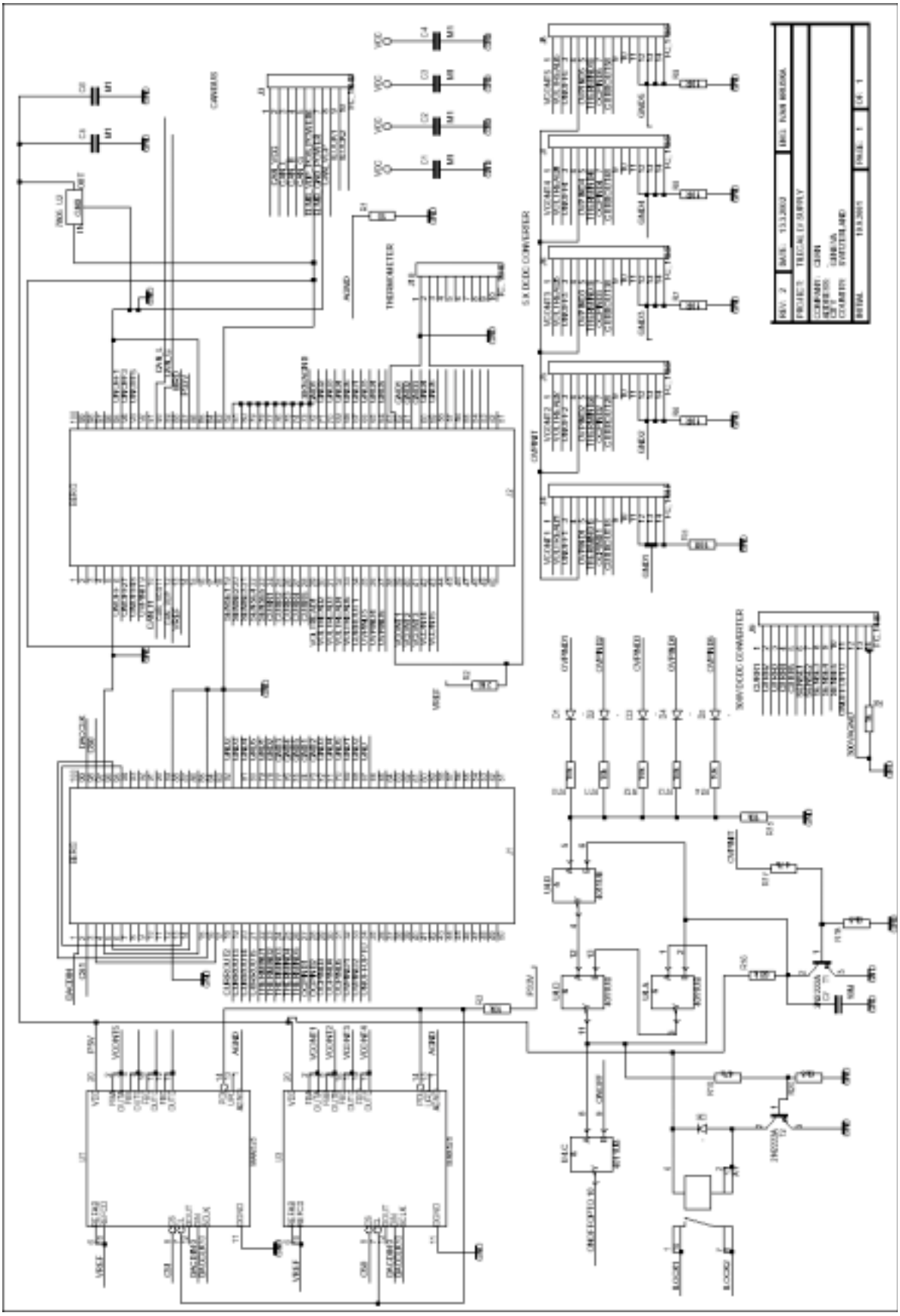

.

List of Figures

List of Tables

Bibliography

[1] ATLAS Collaboration, "*ATLAS Technical Proposal*", CERN / LHCC / 94-43 LHCC / P2, (1996)

[2] ATLAS Collaboration, "ATLAS: Detector and Physics Performance Technical Design Report", CERN / LHC / 99-14, ATLAS TDR 14 (1999)

[3] ATLAS Collaboration, "ATLAS: Detector and Physics Performance Technical Design Report", CERN / LHC / 99-15, ATLAS TDR 15 (1999)

[4] ATLAS Collaboration, "ATLAS Inner Detector Technical Design Report", Vol. 1, CERN / LHC / 97-16, ATLAS TDR 4 (1997)

[5] ATLAS Collaboration, "ATLAS Inner Detector Technical Design Report", Vol. 2, CERN / LHC / 97-17, ATLAS TDR 5 (1997)

[6] ATLAS Collaboration, "ATLAS Pixel Detector Technical Design Report", CERN / LHC / 98-13, ATLAS TDR 4 (1998)

[7] ATLAS Collaboration, "ATLAS Liquid Argon Calorimeter Technical Design Report", CERN / LHC / 96-41, ATLAS TDR 2 (1998)

[8] ATLAS Collaboration, "*ATLAS Tile Calorimeter Technical Design Report*", CERN / LHCC / 96-42, ATLAS TDR 3, (1996)

[9] ATLAS Collaboration, "*ATLAS Muon Spectrometer Technical Design Report*", CERN / LHCC / 97-22, ATLAS TDR 10, (1997)

[10] ATLAS Collaboration, "*ATLAS Magnet System Technical Design Report*", CERN / LHCC / 97-18, ATLAS TDR 6, (1997)

[11] ATLAS Collaboration, "ATLAS DAQ, EF, LVL2 and DCS", LHCC 98-16 (1998)

[12] ATLAS Collaboration, "*ATLAS High-Level Triggers, DAQ and DCS Technical Proposal*", CERN / LHCC / 2000-17, (2000)

[13] Opal Collaboration, "The OPAL Detector at LEP", Nucl. Inst. and Meth., A305, (1991), 275-319.

[14] The OPAL Collaboration, “Search for the Standard Model Higgs Boson in e+e- Collisions at sqrt(s)=192-209 GeV”, CERN-EP-2000-156, Phys. Lett. B499 (2001) 38-52.

[15] The ALEPH Collaboration, “Searches for neutral Higgs bosons in e+e- collisions at centre-of-mass energies from 192 to 202 GeV “, Physics Letters B, Volume 499, Issue 1-2,(2001), pp. 53-66

[16] L3 Collab., M.Acciarri et al.,”Higgs Candidates in e+e- Interactions at $s^{0.5}$= 206.6 GeV”, Physics Letters B, Vol.495, issue 1-2 (2000), 18-25 and CERN-EP / 2000-140; (2000) L3 preprint 228.

[17] A. K. Amundsen et al., "*The control system of the OPAL detector at LEP*", Nucl. Inst. and Meth., A293 (1990), 145-147

[18] Joint Control Project, “The LHC experiments’ Joint COntrols Project, JCOP”, International Conference on Accelerator and Large Experimental Physics Control Systems, Trieste, Italy (1999).

[19] H.J. Burckhart, “Detector Control System”, 4th Workshop on Electronics for LHC Experiments, Rome (Italy), September 1998, p. 19-23.

[20] H.J. Burckhart, “ATLAS Detector Control System: User Requirements Document”, ATLAS DCS-URD1 (1995)

[21] G.Baribaud et al., “Recommendations for the Use of Fieldbuses at CERN in the LHC Era”, Proceedings of the 1997 International Conference on Accelerator and Large Experimental Physics Control Systems, Beijing, (1997), p.285.

[22] H.J. Burckhart, M. Caprini and R. Jones, “Communication DCS-DAQ in ATLAS”, ATLAS DCS-IWN8 (1999)

[23] CAN in Automation (CiA), D-91058 Erlangen, Germany. http: / / www.can-cia.de /

[24] W. Lawrenz, “CAN System Engineering: From Theory to Practical Applications”, Ed. Springer-Verlag New York, Inc, New York (1997)

[25] D. Paret, “Le bus CAN”, Ed. Dunot, Paris (1996)

[26] G. Gruhler and B. Dreier, “CANopen Implementation Guidelines”, STA Reutlingen, Germany (1997)

[27] W.P.J. Heubers, H. Boterenbrood, J.T. van Es, R. G. K. Hart, “CAN field bus for industrial-controls applications in high-energy physics experiments”, ATLAS IWN MUON-NO-228, (1998)

[28] B. Hallgren et al., “*A low-cost I/O concetrator using the CAN fieldbus*” presented at ICALEPS 99 conference, Trieste, October 1999

[29] B. Hallgren and H.J. Burckhart, “Frontend I/O via CANbus of the ATLAS detector control system”, Presented at the LEB98 Workshop, Rome, Italy (1998).

[30] H. Boterenbrood, J. Cook, B. Hallgren, F. Varela, “*Embedded Local Monitor Board ELMB: Hardware and Software*”, ATI-DC-ELMB-0001, CERN (2002)

[31] B. Hallgren, H.J. Burckhart, “Performance measurement of the ATLAS Local Monitor Box with the Liquid Argon subdetector”, ATLAS DCS-IWN5 (1998)

[32] B. Hallgren and H.J. Burckhart, “Review of the Local Monitor Box (LMB)”, ATLAS DCS-IWN7 (1997) http://atlasinfo.cern.ch/ATLAS/GROUPS/DAQTRIG/DCS/LMB/HARDWARE/lmbreview.pdf

[33] V. Filimonov and B. Hallgren, “Magnetic field and temperature tests of the ATLAS Local Monitor Box”, ATLAS DCS-IWN6, (1998)

[34] B. Hallgren, “Description of the ATLAS DCS 1999 TCC2 radiation tests”, http://atlasinfo.cern.ch/ATLAS/GROUPS/DAQTRIG/DCS/TCC2_99/radtests.html

[35] B. Hallgren, “Final test results of the CAN LMB and components after the irradiation”, (1999) http://atlasinfo.cern.ch/ATLAS/GROUPS/DAQTRIG/DCS/TCC2/radtst3.html

[36] H. Boterenbrood, “Software for the ELMB CANopen module”, http://www.nikhef.nl/pub/departments/ct/po/html/ELMB/ELMB15.pdf

[37] A. Daneels and W. Salter, “What is SCADA?”, Proceedings on the International Conference on Accelerator and Large Experimental Physics Control System, Trieste, Italy (1999).

[38] A. Daneels and W. Salter, “Selection and evaluation of commercial SCADA systems for the controls of the CERN LHC experiments”, Proceedings on the International Conference on Accelerator and Large Experimental Physics Control System, Trieste, Italy (1999).

[39] PVSS-II, http://www.pvss.com

[40] OLE for Process Control, http://www.opcfoundation.org/

[41] R. Barillere et al., “Results of the OPC Evaluation done within JCOP for the control of the LHC experiments”, Proceedings on the International Conference on Accelerator and Large Experimental Physics Control System”, Trieste, Italy (1999).

[42] V. M. Filimonov, “Description of the CANopen OPC server”, http://atlasinfo.cern.ch/ATLAS/GROUPS/DAQTRIG/DCS/LMB/ELMB DISTRIBUTION/opccano5.pdf

[43] “ELMB Documentation”, http://atlasinfo.cern.ch/ATLAS/GROUPS/DAQTRIG/DCS/ELMB/ElmbUserGuide.pdf

[44] H. Boterenbrood, H.J. Burckhart, J. Cook, V. Filimonov, B. Hallgren, F. Varela, “Vertical Slice of the ATLAS Detector Control System”, submitted to 7th Workshop on Electronics for LHC Experiments, Stockholm Sweden (2001)

[45] R. Hart and V. Khomoutnikov, “ATLAS DAQ-DCS Communication Software High Level Design”, ATLAS DAQ IWN 165, (2001)

[46] H.Burckhart, R.Hart, R.Jones, V.Khomoutnikov, Y.Ryabov, “Communication between Trigger/DAQ and DCS in ATLAS”, Presented at CHEP'01: Computing in High Energy and Nuclear Physics, Beijing, China, 2001

[47] R. Hart and V. Khomoutnikov, “ATLAS DAQ-DCS Communication Software User Requirements Document”, ATLAS DAQ IWN 164, (2000)

[48] M. Dentan, “ATLAS Policy on radiation tolerant electronics”, CERN ATC-TE-QA-0001, 2000.

[49] M. Huhtinen and F. Faccio, “Computational method to estimate Single Event Upset rates in an accelerator environment”. NIM A450 (2000) 155.

[50] B. I. Hallgren et al., “The Embedded Local Monitor Board (ELMB) in the LHC Front-End I/O Control System”, submitted to 7th Workshop on Electronics for LHC Experiments, Stockholm, Sweden (2001).

[51] H. Burckhart, H.Hallgren, H. Kvedalen, “Irradiation measurements of the ATLAS ELMB”, ATLAS DCS-IWN9, (2001)

[52] J. Cook, B. Hallgren, H. Kvedalen, “Radiation test at GIF and accelerated aging of the ELMB”, ATLAS DCS-IWN10 (2001)

[53] Thermal acceleration factor given by the Arrhenius equation. See for example: http://www.atmel.com/atmel/acrobat/doc1282.pdf

[54] B. Hallgren and H. Kvedalen, “Radiation test of the 3.3V version of the ELMB at GIF”, ATLAS DCS-IWN11 (2001)

[55] J. Cook and B. Hallgren, “Non Ionizing Energy Loss test of the Embedded Local Monitor Box”, ATLAS DCS-IWN14, (2002)

[56] H. Boterenbrood et al., “Single Event Effect test of the Embedded Local Monitor Board”, ATLAS DCS-IWN12, (2001)

[57] F. Varela Rodriguez, J. Cook, V. Filimonov and B. Hallgren, "ELMB full branch test: behavior and performance", ATLAS DCS-IWN13 (2001)

[58] R. Wigmans, "Calorimetry: Energy Measurements in Particle Physics", Ed. Clarendon Press, Oxford (2000)

[59] W.R. Leo, "Techniques for Nuclear and Particle Physics Experiments", Springer-Verlag 1987

[60] A. M. Henriques Correia, "Development of a Lead / Scintillating-fibre Calorimeter for jet detection at LHC. Study of the Z' Vector Boson in the jet decay mode", Ph.D. Thesis University of Lisbon, Lisbon, Portugal (1993)

[61] C. Fabjan, "Calorimetry in High Energy Physics", CERN-EP / 85-54 (1985)

[62] E. Berger et al., "Construction and Performance of an Iron-Scintillator Hadron Calorimeter with Logitudinal Tile Configuration", CERN / LHCC / 95-44, LRDB status report / RD34 (1995).

[63] G. Montarou et al. "Characterization of the Imamates 10-stages R7877 photomultipliers at Clermont for the Tile Calorimeter", CERN TILECAL-No-108 (1997).

[64] ATLAS Collaboration, "*ATLAS Calorimeter Performance*", CERN / LHCC / 96-40, ATLAS TDR 1, (1996)

[65] Z. Ajaltouni et al. "Results from a combined test of an electromagnetic liquid Argon calorimeter with a hadronic scintillating-tile calorimeter", CERN-PPE / 96-178 (1996)

[66] P. Amaral et al., "Hadronic Shower Development in Iron-Scintillator Tile Calorimetry", CERN-99-055 (1999)

[67] S. Constantinescu, S. Dita, A. Henriques, M. Nessi, R. Stanek, "Comparative analysis of the ATLAS Tile Hadronic Calorimeter response to pions and protons", CERN ATL-TILECAL-2001-005 (2001).

[68] Z. Ajaltouni et al., "Response of the ATLAS Tile Calorimeter Prototype to Muons", CERN-PPE / 96-173 (1996)

[69] R. Chadelas, P. Grenier, D. Lambert, P. Rosnet and F. Vazeille for the ATLAS Tile Calorimeter Collaboration, "In-situ high voltage regulation system", ATL-TILECAL-2000-003.

[70] new calculation of SRL in fingers

[71] P. Bonneau, P. Grenier, A.M. Henriques Correia, G. Schlager, F. Varela

Rodriguez, G. Montarou, M. Vassent, “Performance and tests of the cooling system for the ATLAS Tile hadron calorimeter modules calibration”, CERN ATL-TILECAL-2001-006 (2001)

[72] G. Blanchot, P. Bonneau, P. Gris, A. M. Henriques Correia, F. Varela Rodriguez, “Full scale test for the ATLAS calorimeter monophase cooling system”, CERN ATC-TL-ES-0001 (2001)

[73] G. Ambrosini et al., “The ATLAS DAQ and event filter prototype ’-1’ project”, Presented at the International Conference on Computing in High-Energy Physics, Berlin, Germany, (1997)

[74] C. Hebrad, “Etude et caracterisation des photomultiplicateurs du calorimetre a tuiles scintillantes d’ATLAS. Recherche du stop t~1 avec le detecteur ATLAS”, Ph.D. Thesis Universite Blaise Pascal, Clermont-Ferrand, France (1999)